

BAU UND QUALITÄTSSICHERUNG VON MODULEN
UND
STUDIE VON OPTIMIERTEN PIXELSENSORDESIGNS
FÜR DIE ERNEUERUNG DES CMS-PIXELDETEKTORS

Stefan Michael Heindl

Zur Erlangung des akademischen Grades eines
DOKTORS DER NATURWISSENSCHAFTEN
von der Fakultät für Physik des
Karlsruher Instituts für Technologie (KIT)

genehmigte

DISSERTATION

von

Dipl.-Phys. Stefan Michael Heindl
aus Oberndorf am Neckar

Tag der mündlichen Prüfung: 02.12.2016

Referent: Prof. Dr. Thomas Müller, Institut für Experimentelle Kernphysik

Korreferent: Prof. Dr. Ulrich Husemann, Institut für Experimentelle Kernphysik

Stefan Michael Heindl:
*Bau und Qualitätssicherung von Modulen
und
Studie von optimierten Pixelsensordesigns
für die Erneuerung des CMS-Pixeldetektors*
Dezember 2016

ZUSAMMENFASSUNG

Das Tor zum weiten Feld der Elementarteilchenphysik wurde erstmals zu Beginn des letzten Jahrhunderts durch den Wunsch nach einem tieferen Verständnis der fundamentalen Naturprozesse und der elementaren Bestandteile der Materie aufgestoßen. Um diese grundlegenden Fragen beantworten zu können, bedient sich die Elementarteilchenphysik großer Teilchenbeschleuniger, mit denen Teilchen zunächst beschleunigt und dann zur Kollision gebracht werden. Dabei werden zum einen neue unbekannte Teilchen erzeugt und zum anderen die Bestandteile und Eigenschaften der Ausgangsteilchen offengelegt. Die Messergebnisse werden dazu genutzt, die Vorhersagen der zugrundeliegenden Theorie zu prüfen. Im Fall der modernen Elementarteilchenphysik handelt es sich dabei um das Standardmodell (SM), welches alle bekannten Elementarteilchen und ihre Wechselwirkungen beschreibt.

Gleichzeitig gibt es jedoch auch Gründe für die Annahme, dass das Standardmodell nur ein Teil einer noch umfassenderen Theorie ist. In den letzten Jahrzehnten wurden Phänomene wie z.B. Dunkle Materie und Dunkle Energie beschrieben, welche vom Standardmodell nicht erklärt werden können und daher als Physik jenseits des Standardmodells bezeichnet werden.

Der Large Hadron Collider (LHC) der Europäischen Organisation für Kernforschung (CERN) in Genf ist heute mit einem Umfang von 27 km der größte und mit einer Schwerpunktsenergie von 13 TeV auch der leistungsstärkste Teilchenbeschleuniger der Welt. Zwei gegenläufige Protonenstrahlen werden beschleunigt und an vier Stellen des Rings mit einer Rate von 40 MHz zur Kollision gebracht. Jeder der Wechselwirkungspunkte wird von großen Teilchendetektoren umschlossen, welche die bei den Kollisionen entstehenden Zerfallsprodukte nachweisen und speichern. Durch spätere Analyse lässt sich aus den Daten die ursprüngliche Wechselwirkung der Protonen und der an ihr beteiligten Elementarteilchen bestimmen. Zwei der Detektoren sind Mehrzweckexperimente, deren Forschungsprogramm einerseits die Untersuchung und Vervollständigung des Standardmodells und andererseits die Suche nach Physik jenseits des Standardmodells umfasst.

Einer dieser Detektoren ist das Compact Muon Solenoid (CMS) Experiment, ein großer Teilchendetektor mit einer Länge von 22 m, einem Durchmesser von 15 m und einem Gewicht von 14000 t. Zusammen mit dem ATLAS (A Toroidal LHC ApparatuS) Experiment hat die CMS-Kollaboration im Jahr 2012 das Higgs-Boson entdeckt, das letzte noch fehlende Elementarteilchen, welches vom Standardmodell vorhergesagt wird [CMS12], [ATL12]. Diese Entdeckung führte zur Verleihung des Physik-Nobelpreises 2013 an Peter Higgs und François Englert, zwei der Physiker, die den zugrundeliegenden Higgs-Mechanismus bereits 1964 vorgeschlagen hatten. Da das Forschungsprogramm des LHC jedoch nicht nur auf die Suche nach dem Higgs-Boson beschränkt ist, werden sowohl der Beschleuniger als auch die Detektoren ständig weiterentwickelt und verbessert.

Der CMS-Pixeldetektor ist ein Siliziumvertexdetektor, welcher in nächster Nähe zum Wechselwirkungspunkt angeordnet ist und damit den innersten Teil des CMS-Experiments bildet. Teilchen aus den Kollisionen, die einen Pixel durchqueren, erzeugen durch Ionisation Ladungsträgerpaare im Siliziumsubstrat. Diese werden durch ein elektrisches Feld getrennt und die Elektronen fließen über eine kleine Lotverbindung (genannt Bump-Bond) in den Auslesechip, wo sie gemessen werden. Anschließend wird das elektrische Signal des Chips mit Hilfe einer Laserdiode in ein optisches Signal gewandelt und über Lichtleiter nach außen gesendet. Da ein Teilchen stets Treffer in mehreren Lagen des Detektors verursacht, kann mit Hilfe dieser dreidimensionalen Raumpunkte die Flugbahn des Teilchens rekonstruiert werden.

Der aktuelle CMS-Pixeldetektor wurde für eine geplante instantane Luminosität des LHCs von $\mathcal{L} = 1 \cdot 10^{34} \text{ cm}^{-2} \text{ s}^{-1}$ entworfen. Diese wurde im Laufe des Jahres 2016 bereits um mehr als 50% übertroffen und der Detektor arbeitet trotz dieser Steigerung weiterhin problemlos. Allerdings ist für die kommenden Jahre eine weitere Luminositätssteigerung auf Werte bis zu $2 \cdot 10^{34} \text{ cm}^{-2} \text{ s}^{-1}$ geplant und diese würde zu hohen Ineffizienzen des Detektors führen. Die Ineffizienzen werden dabei durch Totzeiten bei der Auslese und durch zu kleine Zwischenspeicher auf den Auslesechips verursacht.

Daher hat sich die CMS-Kollaboration dazu entschieden, den aktuellen Pixeldetektor durch einen neuen Detektor zu ersetzen. Dieser stellt eine Weiterentwicklung dar und verwendet unter anderem einen neuen Auslesechip, bei welchem die genannten Probleme beseitigt worden sind. Der neue Phase-I-Pixeldetektor wird momentan durch eine Kollaboration verschiedener Universitäten und Forschungseinrichtungen gebaut. Seine Installation im CMS-Experiment ist für den Beginn des Jahres 2017 geplant.

In ersten Teil dieser Arbeit wird die Modulproduktion am KIT für den Zentralbereich des neuen CMS-Pixeldetektors vorgestellt. Dies umfasst die gesamte Produktionskette, an deren Ende die fertigen Module stehen. Ein besonderes Augenmerk wird dabei auf die Qualitätssicherung während der Produktion gelegt. Jede Modulkomponente wird im Laufe der Produktion mindestens einmal einzeln getestet und nach der Fertigstellung des Moduls folgen weitere Untersuchungen. Dieser Ansatz wurde gewählt, um eventuelle Probleme so früh wie möglich erkennen zu können. Dies erlaubt zum einen eine schnelle Anpassung der Produktion bei Problemen und verhindert andererseits die Nutzung defekter Komponenten in den weiteren Produktionsschritten.

Für die Tests im Rahmen der Qualitätssicherung wurden drei Teststationen geplant, aufgebaut und betrieben. Außerdem wurde die Testprozedur für die Siliziumsensoren definiert. Die Ergebnisse der Messung der Strom-Spannungs-Kennlinie werden danach in einer zentralen Datenbank gespeichert, so dass diese auch nach mehreren Jahren immer noch abgerufen werden können.

Die erste Teststation dient dem Funktionstest des High Density Interconnects (HDI), einer flexiblen Leiterplatte, mit der auf dem Modul die Daten und die Betriebsspannungen verteilt werden. Mit Hilfe einer Nadeltestkarte werden die einzelnen Leiterbahnen und der Token Bit Manager (TBM) Chip auf ihre Funktionalität geprüft.

Die anderen beiden Teststationen werden für die Untersuchung der fertigen Module genutzt. Die Testprozedur besteht dabei aus elektrischen Tests und einem Test mit Röntgenstrahlung. Während die elektrischen Tests die Funktionalität der Module bei verschiedenen Temperaturen überprüfen, sucht der Röntgentest nach fehlerhaften Bump-Bond-Verbindungen zwischen Sensor und Auslesechip und ermöglicht außerdem die Kalibration der von den Auslesechips gemessenen Signalhöhen. Eine fehlerhafte Bump-Bond-Verbindung verhindert die Erkennung des Teilchendurchgangs im betroffenen Pixel, da der Auslesechip die generierte Ladung nicht mehr messen kann.

Insgesamt wurden am KIT 409 Module für den neuen Pixeldetektor gebaut. Nach den Untersuchungen wurden diese nach Aachen zur Rheinisch-Westfälischen Technischen Hochschule (RWTH) geschickt und dort auf ihre Eignung für den Einbau in den neuen Detektor geprüft. Dies geschah anhand von vorgegebenen Wertebereichen für bestimmte Testergebnisse, die für alle Modulproduktionszentren gleich sind. Das Ergebnis für die Modulproduktion von KIT und RWTH ist mit einem Anteil von 343 (entsprechend 84% der Gesamtzahl) für den Detektor geeigneten Modulen das beste aller fünf Modulproduktionszentren für das Phase-I-Upgrade des Zentralbereichs des CMS-Pixeldetektors und damit die Bestätigung für die exzellente Arbeit, die am KIT und an der RWTH Aachen geleistet worden ist.

Eine weitergehende Untersuchung der Ergebnisse des Röntgentests hat außerdem gezeigt, dass die Gesamtzahl der fehlerhaften Bump-Bond-Verbindungen sehr klein ist. Von über 23 Millionen getesteten Verbindungen waren nur 2750 (oder 0,012%) fehlerhaft.

Der zweite Teil dieser Arbeit befasst sich mit der Untersuchung von optimierten Pixelsensoren für das geplante Phase-II-Upgrade des CMS-Pixeldetektors. Der LHC wird in den Jahren nach 2023 zum HL-LHC ausgebaut mit dem Ziel, noch höhere Luminositäten bis zu $\mathcal{L} = 5 \cdot 10^{34} \text{ cm}^{-2} \text{ s}^{-1}$ zu liefern. Dies bedeutet, dass die Anzahl der gleichzeitig stattfindenden Kollisionen und damit auch die Teilchenrate stark zunehmen werden. Für CMS und die anderen Experimente hat dies zwei Auswirkungen: einerseits erfordert die hohe Strahlenschädigung den Einsatz neuer Materialien, die den erwarteten Bedingungen standhalten können, und andererseits werden ständig so viele Detektorkanäle getroffen, dass es bei der späteren Spurfindung zu Problemen durch Doppeldeutigkeiten kommen kann.

Eine Möglichkeit, die hohe Kanalbelegung zu reduzieren, ist die Steigerung der Granularität der Detektoren. Im Falle des CMS-Pixeldetektors ist diese Steigerung geplant durch eine Verkleinerung der Pixelzellen des Siliziumsensors. Die Fläche der einzelnen Pixel soll dabei mindestens um einen Faktor vier reduziert werden. Dies erfordert die Entwicklung und die Produktion eines neuen Siliziumsensors. Am Anfang dieses Prozesses lassen sich Sensorprototypen jedoch nicht untersuchen, da noch keine Auslesechips mit passender Zellengröße zur Verfügung stehen. Der erste Schritt hin zu einem neuen Sensor ist daher die Untersuchung neuer Layoutideen mit Hilfe von Sensorprototypen, die mit bereits vorhandenen Auslesechips untersucht werden können. Im Falle des CMS-Pixelsensors ist dies die ps146-Auslesechipserie, die auf den Modulen des aktuellen und des neuen Phase-I-Pixeldetektors zum Einsatz kommt. Dieser Ansatz wurde auch für diese Arbeit verwendet.

Die sechs optimierten Pixelsensorlayouts basieren auf den Layouts der Sensoren, die momentan im Zentral- und Vorwärtsbereich des CMS-Pixeldetektors verwendet werden. Ihre Leistungsfähigkeit sowohl in unbestrahlter als auch in bestrahlter Form wurde am Deutschen Elektronen-Synchrotron (DESY) mit Hilfe eines Elektronenstrahls untersucht. Ein Strahlteleskop ermöglichte die Spurrekonstruktion für die einzelnen Teilchen, die die Sensoren durchquert haben, und damit die Untersuchung wichtiger Eigenschaften der Sensoren wie Detektionseffizienz und räumliche Auflösung auf der Ebene der einzelnen Pixelzellen.

Anhand der Ergebnisse konnte gezeigt werden, dass die individuellen Verbesserungen der einzelnen Sensorvarianten die beabsichtigten Ergebnisse liefern. Gleichzeitig gab es keine Varianten, die aufgrund übermäßiger Optimierung nicht nutzbar waren. Vergrößerte Implantatflächen führen zu besserer Treffererkennung und besserer Ladungsteilung mit größeren Trefferclustern. Größere Treffercluster wiederum ermöglichen eine genauere Bestimmung der Trefferposition und damit eine Verbesserung der räumlichen Auflösung. Der negative Einfluss der Strukturen zum Anlegen der Verarmungsspannung, die nur auf den Sensoren für den Zentralbereich vorhanden sind, konnte ebenfalls gezeigt werden.

Das Hauptziel der Sensoruntersuchung war es, das Sensorlayout zu finden, welches am besten für die Anforderungen des Phase-II-Pixeldetektors geeignet ist und daher als Ausgangspunkt für weitere Entwicklungen von Pixelsensoren mit kleinen Pixelgrößen genutzt werden sollte. Die Ergebnisse der Teststrahluntersuchungen lassen jedoch keine eindeutige Schlussfolgerung zu. Sie zeigen vielmehr, dass bei der Entwicklung eines neuen Pixelsensors stets Zielkonflikte zwischen den einzelnen Sensorparametern wie Implantatfläche und Isolationsabstand der einzelnen Pixelzellen auftreten, da sich die Parameter gegenseitig beeinflussen.

PRODUCTION AND QUALITY ASSURANCE OF MODULES
AND
STUDY OF OPTIMIZED PIXEL SENSOR DESIGNS
FOR THE UPGRADE OF THE CMS PIXEL DETECTOR

Stefan Michael Heindl

Zur Erlangung des akademischen Grades eines
DOKTORS DER NATURWISSENSCHAFTEN
von der Fakultät für Physik des
Karlsruher Instituts für Technologie (KIT)

genehmigte

DISSERTATION

von

Dipl.-Phys. Stefan Michael Heindl
aus Oberndorf am Neckar

Tag der mündlichen Prüfung: 02.12.2016

Referent: Prof. Dr. Thomas Müller, Institut für Experimentelle Kernphysik

Korreferent: Prof. Dr. Ulrich Husemann, Institut für Experimentelle Kernphysik

Stefan Michael Heindl:
*Production and Quality Assurance of Modules
and
Study of optimized Pixel Sensor Designs
for the Upgrade of the CMS Pixel Detector*
December 2016

CONTENTS

i	INTRODUCTION AND BASICS	1
1	INTRODUCTION	3
2	THE LARGE HADRON COLLIDER AND THE CMS EXPERIMENT	7
2.1	The Large Hadron Collider	7
2.1.1	Luminosity	9
2.2	The Compact Muon Solenoid Experiment	10
2.2.1	Particle identification in the CMS detector	13
2.2.2	The CMS trigger and data acquisition system	13
2.3	Upgrades to the CMS Experiment	15
2.3.1	The Phase I Upgrade	15
2.3.2	The Phase II Upgrade	16
3	SILICON PARTICLE DETECTORS	19
3.1	Basic properties of semiconductors	19
3.1.1	Energy-band model	19
3.1.2	Indirect semiconductors	21
3.2	Working principle	22
3.2.1	Doping	22
3.2.2	pn-junction	22
3.2.3	Interaction of particles with matter	25
3.3	Position-sensitive silicon particle detectors	27
3.4	Radiation damage in silicon	29
ii	MODULE PRODUCTION FOR THE CMS PIXEL PHASE I UPGRADE	33
4	OVERVIEW OF THE CMS PHASE I PIXEL DETECTOR	35
4.1	The Phase I Pixel Detector	36
4.1.1	BPIX Mechanics and Cooling	37
4.1.2	Material Budget	38
4.1.3	Services and Readout	39
4.2	The Phase I Barrel Pixel Module	40
5	SENSOR TESTING	43
5.1	The Barrel Pixel Silicon Sensor	43
5.2	Testing Method and Equipment	45
5.2.1	Current-Voltage (IV) Measurement	45
5.2.2	IEKP Probe Station	46
5.3	Measurement Results	46
5.3.1	Sensor Acceptance and Classification Criteria	47
5.3.2	Results	48
5.4	Phase I Production Database	52
6	MODULE PRODUCTION	57
6.1	Bare Module Production	58
6.1.1	The RTI Tin-Lead Bumping Process	59
6.1.2	The KIT Bonding Process	60
6.1.3	Bare Module Testing	64
6.2	High Density Interconnect Preparation	70
6.2.1	Token Bit Manager Gluing and Wire Bonding	71
6.2.2	HDI Testing	72
6.3	Pixel Module Gluing	74

6.3.1	Base Strip Gluing	74
6.3.2	HDI Gluing	78
6.3.3	Module Wire Bonding	80
6.3.4	Module Cap Gluing	81
7	MODULE TESTING AND QUALIFICATION	83
7.1	Electrical Test	83
7.1.1	Test Setup	85
7.1.2	Results	87
7.2	X-ray Test	88
7.2.1	Test Setup	89
7.2.2	Results	91
7.3	Module Qualification at Aachen	95
iii	SENSOR LAYOUT STUDY FOR THE CMS PIXEL PHASE II UPGRADE	99
8	SENSOR LAYOUT STUDY FOR THE PHASE II PIXEL DETECTOR	101
8.1	HPK Campaign	101
8.2	Pixel Sensor Layouts	103
8.3	Irradiation	106
9	TEST BEAM MEASUREMENTS	109
9.1	Investigated Sensor Samples	109
9.2	DESY Test Beam	111
9.2.1	The DESY-II Beamlines	112
9.2.2	The DATURA Beam Telescope	113
9.3	EUTelescope Framework and Analysis	115
9.4	The EUTelAnalysisCMSPixel Processor	117
9.5	Results	118
9.5.1	Hit detection efficiency	121
9.5.2	Cluster size	123
9.5.3	Spatial resolution	125
9.6	Conclusions	126
iv	SUMMARY AND OUTLOOK	129
10	SUMMARY AND OUTLOOK	131
	BIBLIOGRAPHY	135
	List of Figures	145
	List of Tables	147

Part I

INTRODUCTION AND BASICS

INTRODUCTION

The scientific field of high-energy particle physics as one of the many disciplines in physics has been formed at the beginning of the last century with the goal to understand the fundamental processes in nature and to explore the elementary constituents of matter. The primary tool of high-energy particle physics to reach that goal are particle collisions. Elementary or composite particles are first accelerated and then brought into collision in order to produce new unknown particles, to reveal their properties and constituents and to verify the predictions and parameters of theory. The underlying theoretical framework of modern high-energy particle physics is the Standard Model (SM), which represents the current knowledge and summarizes all known elementary particles and their interactions. Since it was formulated for the first time in 1961, it has been constantly refined through the last 50 years and today provides high-precision predictions for many phenomena found in nature.

The first particle accelerators have been built in the 1930s and since then the collision energy of the particles has been increased constantly in order to be able to probe new energy realms and to challenge the predictions of the SM. With the need for ever increasing collision energies, the accelerators and also the particle detectors have grown larger and larger in the last decades and today are among the largest and most complex machines ever built.

The design and execution of a state-of-the-art high-energy particle physics experiment today requires deep understanding of both the physics and the technology involved, reaching from the working principle of the basic building blocks of the detector to data acquisition and storage, particle reconstruction algorithms, and finally to the description of the underlying physics processes. This endeavour is only possible by interdisciplinary cooperation of many fields of science like cryogenics, solid state physics, microelectronics and high performance computing. Due to the sheer size of the projects they have also become global efforts with experimental collaborations comprising more than 5000 scientists from numerous countries all over the world.

The world's largest and most powerful particle accelerator is the Large Hadron Collider (LHC) operated by the European Organization for Nuclear Research (CERN) near Geneva in Switzerland. It accelerates protons in its 27 km long ring and brings them into collision at a center of mass energy of 13 TeV at four points of the ring. At each interaction point large particle detectors record the remnants of the collisions. Two of them are general purpose detectors designed for the same measurement program: the search for the Higgs boson predicted by the SM and for possible physics beyond. One of these two detectors is the Compact Muon Solenoid (CMS) experiment, a large particle detector with a length of 22 m and a diameter of 15 m weighing some 14000 t.

Together with the ATLAS (A Toroidal LHC ApparatuS) collaboration that operates the other general purpose detector, CMS has discovered the Higgs boson in 2012 [CMS12], [ATL12]. The discovery led to the award of the 2013 Nobel Prize in Physics to Peter Higgs and François Englert, two of the physicists who have suggested the existence of the particle already in 1964. However, since the research program of the LHC is not only focused on the discovery of the Higgs boson but also on many more open questions that are waiting to be answered, both the LHC and the detectors are undergoing continuous changes and improvements to be able to extend the boundaries of physics knowledge.

The work presented in this thesis focuses on the changes and improvements of the CMS silicon pixel detector during the planned 30 years of operation of the CMS experiment at the LHC. The thesis is thus divided into two parts. After an introduction to the Large Hadron Collider and the CMS experiment in chapter 2 and to silicon particle detectors in general in chapter 3, the first part describes the module production for the new Phase I barrel pixel detector of CMS which will replace the original pixel detector after eight years of operation. The second part presents a study of new silicon pixel sensor layouts for the Phase II upgrade of the CMS pixel detector planned for after 2023.

The CMS pixel detector is a hybrid silicon pixel tracking detector located at the innermost part of the CMS experiment. Its task is to provide information about the trajectories of charged particles emerging from the interaction point by recording high-resolution three-dimensional space points. These space points form a crucial part of the experiment's ability to reconstruct particle trajectories and to identify secondary decay vertices. The current CMS pixel detector has been designed for a planned instantaneous luminosity of $\mathcal{L} = 1 \cdot 10^{34} \text{ cm}^{-2} \text{ s}^{-1}$ and has proven to perform well under these operating conditions. However, the luminosity provided by the LHC has already exceeded this design value by more than 50% during the year 2016 and further increases up to $2 \cdot 10^{34} \text{ cm}^{-2} \text{ s}^{-1}$ are planned for the coming years. Under such conditions, the present pixel detector would be subjected to severe inefficiencies coming from both dead time and insufficient buffering capabilities of the front-end electronics of the pixel detector.

The CMS collaboration has therefore decided to replace the existing pixel detector with a new detector representing an advancement of the current design including a new readout chip which addresses the mentioned inefficiencies. The new Phase I detector is currently being built by a collaboration of many universities and research institutions and its installation in the heart of the CMS experiment is planned during an extended year-end technical stop of the LHC at the beginning of the year 2017.

In this thesis, the production of modules at KIT for the new CMS barrel pixel detector is presented. The complete production chain, starting with the raw materials and ending with the complete module, is described and the different production steps including the necessary equipment are documented in detail. Special attention is paid to the quality assurance during production. All components of a module are tested at least once as individual parts and several times after the module is completed. This strict approach has been chosen to ensure that failures are detected as early as possible in the production. On the one hand it allows to immediately modify the production process if necessary and on the other hand it prevents the further usage of defective components which helps to save other valuable materials. At the end of the production the modules are tested and qualified according to predefined grading parameters to guarantee that only good modules are installed in the new pixel detector.

The first part of this thesis is structured as follows. An introduction to the Phase I pixel detector of the CMS experiment and the Phase I barrel pixel module is given in chapter 4, followed by a description of the barrel pixel silicon sensor, the testing method for determination of its quality and the measurement results in chapter 5. Chapter 6 covers the complete module production from the bare module over the gluing of the different parts to the wire bonding. A description of the testing and qualification procedures of the modules together with an overview of the final results and yields is given in chapter 7.

The second topic of this thesis is the study of new silicon pixel sensor layouts for the planned Phase II upgrade of the CMS pixel detector. After 2023 the LHC will be upgraded to the High Luminosity LHC (HL-LHC) with the goal to provide even higher instantaneous luminosities around $\mathcal{L} = 5 \cdot 10^{34} \text{ cm}^{-2} \text{ s}^{-1}$. This means that the number of simultaneous proton-proton collisions in one bunch crossing will reach average values of 140 and peaks around 200 compared

to 60 in the last years before the upgrade. The high particle rate stemming from the many collisions has two consequences for the HL-LHC experiments including CMS: the performance of the inner detectors will degrade more quickly due to high radiation damage and the large fraction of detector channels hit simultaneously will create high occupancy especially in the tracking detectors. This might lead to misidentified particle tracks due to the ambiguities in the assignment of the hits to tracks in the reconstruction process.

One way to reduce the occupancy is to increase the granularity of the detectors. In case of the CMS pixel detector this is planned for the Phase II upgrade by shrinking the size of the individual pixels in the silicon sensor by at least a factor of four. This requires a complete redesign of the sensor including the production of several prototypes and detailed testing campaigns. For the testing of the prototypes a readout chip with a compatible bump-bonding pattern is required but such a chip is typically not available during the first design phase of a new sensor. The very first step towards a new sensor design is thus testing new ideas in terms of layout and sensor technologies with sensor prototypes compatible to existing readout chips. In case of the CMS pixel detector this is the `PSI46` series of readout chips used both in the modules of the current and the upgraded Phase I detector.

This approach has been chosen for the pixel sensor layout study described in this work. The six different sensor layouts are evolved versions of the sensor layouts currently in use in the barrel and forward pixel detectors of CMS. Their properties and performance have been investigated with an electron beam at the DESY Test Beam Facility in Hamburg, Germany. Using a beam telescope allows precise tracking of the particles traversing the sensor samples, which is necessary to determine important parameters of the sensor layouts like efficiency and spatial resolution on the level of individual pixels.

The second part of the thesis is organized as follows. The silicon pixel sensors and the differences in their individual layouts are described in chapter 8. Chapter 9 first introduces the DESY Test Beam Facility and the software chain used for data acquisition and analysis and then presents the results of the sensor layout study.

Finally, the findings from both parts of the thesis are summarized and a brief outlook on future sensor developments for the Phase II upgrade of the CMS pixel detector is given in chapter 10.

 THE LARGE HADRON COLLIDER AND THE CMS EXPERIMENT

The Large Hadron Collider (LHC), located at the European Organization for Nuclear Research (CERN) near Geneva, Switzerland, is the world's largest and most powerful particle accelerator. It has been designed to accelerate two counterrotating proton beams to a center of mass energy of $\sqrt{s} = 14 \text{ TeV}$ which are then collided at four points of the ring. At each of the four interaction points (IPs) large particle detectors have been built to detect the remnants of the high-energy particle collisions. Two of them are general purpose detectors: ATLAS (A Toroidal LHC Apparatus) [Atl] and CMS (Compact Muon Solenoid) [CMSa]. They are both designed around the same measurement program: the search for the Higgs boson and possible physics beyond the Standard Model. Having two detectors which are using different technologies but aiming at the same targets allows scientists to cross-check important new results before e.g. claiming the detection of a new particle.

Two other smaller detectors are optimized to certain types of physics: LHCb (Large Hadron Collider Beauty) [LHC] and ALICE (A Large Ion Collider Experiment) [Ali]. LHCb is designed to measure CP violation appearing in rare decays of B mesons since CP violation might be partly responsible for the matter-antimatter asymmetry in our universe. ALICE is specialized in observing lead-lead collisions which are created by the LHC in dedicated ion runs. Such collisions might lead to a new state of matter, the quark-gluon plasma, which is believed to exist at extremely high temperatures and densities like shortly after the Big Bang.

More detailed information about the physics program of the four experiments can be found in [Giao4].

2.1 THE LARGE HADRON COLLIDER

The LHC has been designed since the late 1980's and constructed in the years between 1998 and 2008. It is located in a 27 km long circular tunnel about 100 m below the surface which has been constructed for its predecessor, the Large Electron Positron Collider (LEP). LEP was shut down at the end of the year 2000 and then dismantled to allow construction of the LHC in the tunnel. Reusing the existing tunnel allowed for a large cost saving since civil engineering was one of the most expensive tasks of the LEP project but at the same time defined the circumference of the new collider. Together with the superconducting magnet technology available at the time this limited the achievable center of mass energy to a planned value of $\sqrt{s} = 14 \text{ TeV}$.

Compared to its predecessor LEP, which was an electron-positron (lepton) collider, the LHC is designed as a proton-proton (hadron) collider. Leptons are initially preferred since they are point-like particles that deliver clean collisions at a defined energy but they are also light and therefore cannot be accelerated to the same energies as heavier particles like protons. Unfortunately higher achievable energies are today's key to observations of new particles or interactions. A second factor is synchrotron radiation, an electromagnetic radiation which occurs when charged particles are accelerated radially and which reduces the energy of the accelerated particles at every orbit. The total power emitted by a particle with the energy E is given as

$$P = \frac{e^2 c}{6\pi\epsilon_0(m_0 c^2)^4} \cdot \frac{E^4}{r^2}.$$

where m_0 is the rest mass of the particle and r is the radius of the particle accelerator.

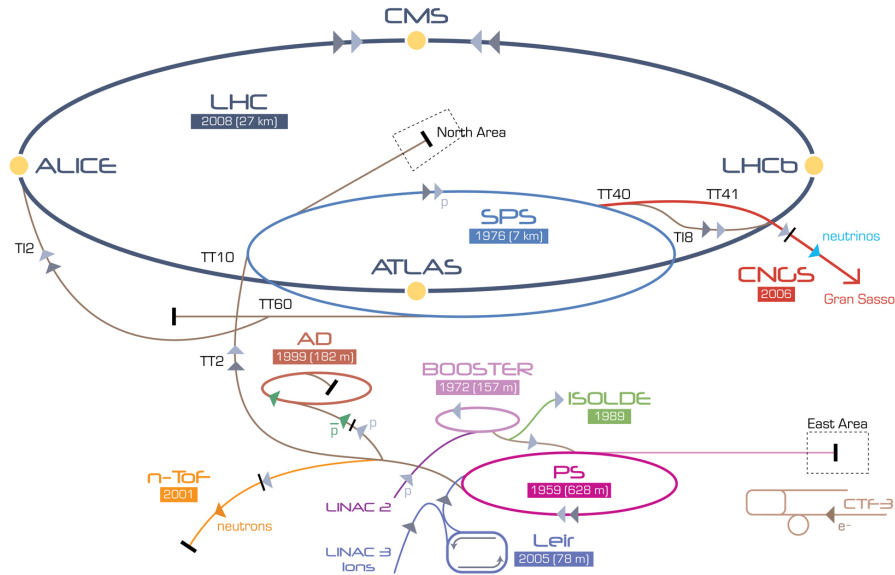


Figure 2.1: The CERN accelerator complex. Protons are accelerated in a linear accelerator (Linac2), the PS Booster, the Proton Synchrotron (PS) and the Super Proton Synchrotron (SPS) before being injected into the LHC at an energy of 450 GeV [Mar13].

Thus it increases with energy to the fourth power and decreases with accelerator radius to the square and rest mass to the fourth power. By comparing the radiated power of an electron and a proton with the same energy, the problem becomes even more clear: $P_{elec} = 1.14 \cdot 10^{13} P_{prot}$. At LEP synchrotron radiation was the limiting factor for the achievable energy of $\sqrt{s} = 209$ GeV. Since protons are about 1800 times heavier than electrons they could be accelerated to energies 1800 times higher to suffer the same energy loss. This is far above the maximum energy defined by the magnetic field of the bending magnets of the LHC.

A possible way to get rid of synchrotron radiation losses would be the usage of a linear collider but only a small number of the accelerated particles actually collide in one crossing and all others are therefore lost. This is not the case with a circular collider where remaining particles can simply collide in the next revolution. This makes it much easier to collect the large amount of data which is required to e.g. observe new particles which are created in very rare processes.

All these points lead to the construction of the LHC as a proton-proton collider with a large discovery potential for new particles and interactions. The messy conditions stemming from the fact that hadrons are composite objects which create many collision products without knowing the real collision energy are accepted and pose high requirements to the analysis of the data acquired by the four detectors at the LHC.

To complement the discovery potential of the machine there is a global effort in the international particle physics community to design and build a new electron-positron linear accelerator in the coming years, the International Linear Collider (ILC). The project has published its Technical Design Report in 2013 [BBF⁺13] and is currently looking for a possible construction site. At the moment, Japan is considered the most likely candidate, as the Japanese government is discussing to contribute half of the costs of the new accelerator.

The LHC is the final accelerator in a complex of five machines located at the CERN site near Geneva. At the beginning protons are created from bottled hydrogen gas which gets stripped of its electrons. Afterwards each of the four preaccelerators increases the energy of the protons before they are injected into the LHC at 450 GeV where they are accelerated to the final energy of 6.5 TeV per beam [Lef09]. A sketch of the CERN accelerator complex is shown in figure 2.1.

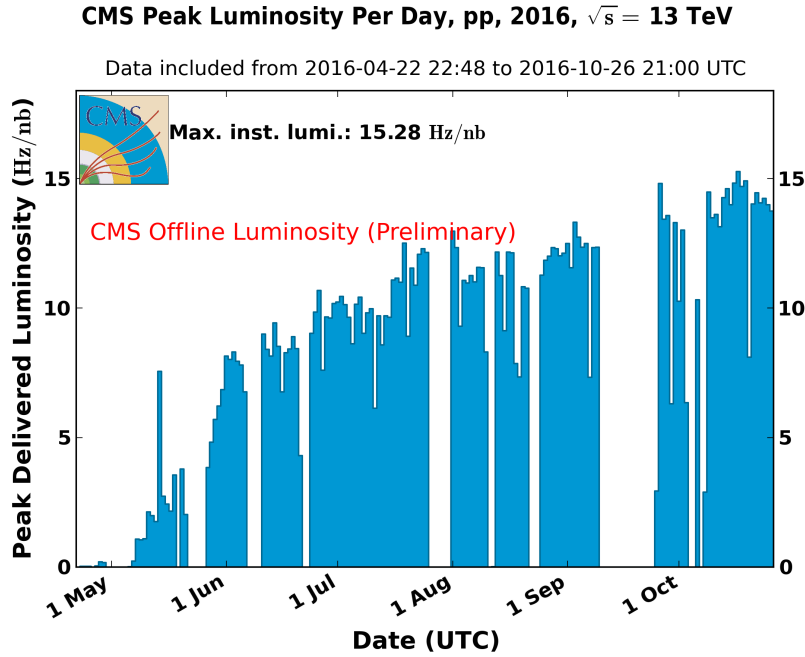


Figure 2.2: CMS Peak Luminosity per day in 2016. The plot shows the development of the peak luminosity delivered to the CMS experiment per day. The LHC design value of $\mathcal{L} = 1 \cdot 10^{34} \text{ cm}^{-2}\text{s}^{-1}$ was reached for the first time on 26 June 2016. Since then, the luminosity has already increased by more than 50% [CMSb].

The sketch also gives the opening dates of the different accelerators. It is obvious that some of them have been constructed already several decades ago like the Proton Synchrotron (PS), which is now operating for more than 50 years. With the advancements in technology new machines have been added over the years and the older ones were kept as preaccelerators. Compared to other possible host sites this is a large advantage for CERN when new accelerators are planned by the international particle physics community.

2.1.1 LUMINOSITY

The luminosity \mathcal{L} is one of the most important quantities for accelerators together with the beam energy. It is a measure of their brightness and defined as the proportionality between the number of events per second and the production cross-section of a certain type of event (which is in turn a measure of the probability that the event occurs) [O⁺14]:

$$\frac{dR}{dT} = \mathcal{L} \cdot \sigma_p$$

The unit of the luminosity is $\text{cm}^{-2}\text{s}^{-1}$. By using the non-SI unit barn ($1\text{b} = 10^{-28}\text{m}^2$) for the cross-section it becomes $\text{b}^{-1}\text{s}^{-1}$.

For the LHC the design luminosity value is $\mathcal{L} = 1 \cdot 10^{34} \text{ cm}^{-2}\text{s}^{-1}$ [BCL⁺04]. It has been reached for the first time on 26 June 2016 [Bra]. Already four months later in October the value had exceeded $1.5 \cdot 10^{34} \text{ cm}^{-2}\text{s}^{-1}$ [CMSb] and further increases up to $2 \cdot 10^{34} \text{ cm}^{-2}\text{s}^{-1}$ are planned for the coming years [DAA⁺12]. The daily peak luminosity delivered to the CMS experiment in 2016 is shown in figure 2.2.

The delivered luminosity is important for the performance of the four LHC detectors since their components have only been designed to be able to cope with the design luminosity value

plus a certain safety margin. In case of CMS, the pixel detector installed at the innermost part reaches its design limitations first [CMS98]. Therefore measures have to be taken to make sure that data taking can continue without losses or interruptions. These measures are described in section 2.3 of this chapter.

To be able to calculate the number of events of a certain process which should have occurred in a defined time of accelerator operation, the integrated luminosity has to be taken into account. It is defined as the integral of the instantaneous luminosity over the operation time:

$$\mathcal{L}_{\text{int}} = \int_0^T \mathcal{L}(t) dt$$

The total number of events of a certain process is then given as $n_{\text{events}} = \mathcal{L}_{\text{int}} \cdot \sigma_p$. The unit of the integrated luminosity is cm^{-2} or b^{-1} .

2.2 THE COMPACT MUON SOLENOID EXPERIMENT

In the beginning of this chapter the four detectors constructed around the interaction points of the LHC were briefly mentioned. Now a more detailed description of the Compact Muon Solenoid (CMS) detector and its silicon pixel tracker is given, since they are of importance in this thesis.

As already said the design of the LHC as a proton-proton collider with both high energy and luminosity poses huge requirements on the experiments. For CMS they can be summarized as follows (compiled from [C+08]):

- Good charged-particle momentum resolution and reconstruction efficiency of their trajectories in the inner tracker
- Good muon identification and momentum resolution and the ability to determine the charge of muons
- Good electromagnetic energy resolution with wide geometric coverage
- Good missing-transverse-energy and dijet-mass resolution
- Full spatial coverage of the interaction point
- Radiation-hard detectors and front-end electronics due to the harsh environment

These requirements drove design and construction of CMS and resulted in an onion-like structure with different subdetectors located in multiple layers around the interaction point while sitting in a magnetic field created by a large solenoid magnet. Since the requirements were the same for all detectors also ATLAS, ALICE and to some extent also LHCb follow that approach.

An overview of CMS with its subdetectors is shown in figure 2.3. Since a spherical geometry is difficult to construct from a mechanical point of view the almost full coverage of the solid angle has been realized by dividing the detector into an elongated barrel part closed with perpendicular endcaps at each side. In total CMS is 21.6 m long, 15 m in diameter and weighs about 14000 t [CMS98]. Compared to ATLAS with a length of 46 m and a diameter of 25 m it is obvious why the experiment is called “compact”. The other two parts of its name stem from the fact that CMS has a high resolution for the reconstruction of muon tracks thanks to its large solenoid magnet with a field strength of $B = 3.8 \text{ T}$.

Collisions take place at a rate of 40 MHz at the interaction point located in the beam pipe at the very center of CMS. Secondary particles originating from the collisions then pass multiple subdetectors where each is designed to measure different important properties of the particles. Starting from the beam pipe these detectors are the silicon tracker (divided into pixel and

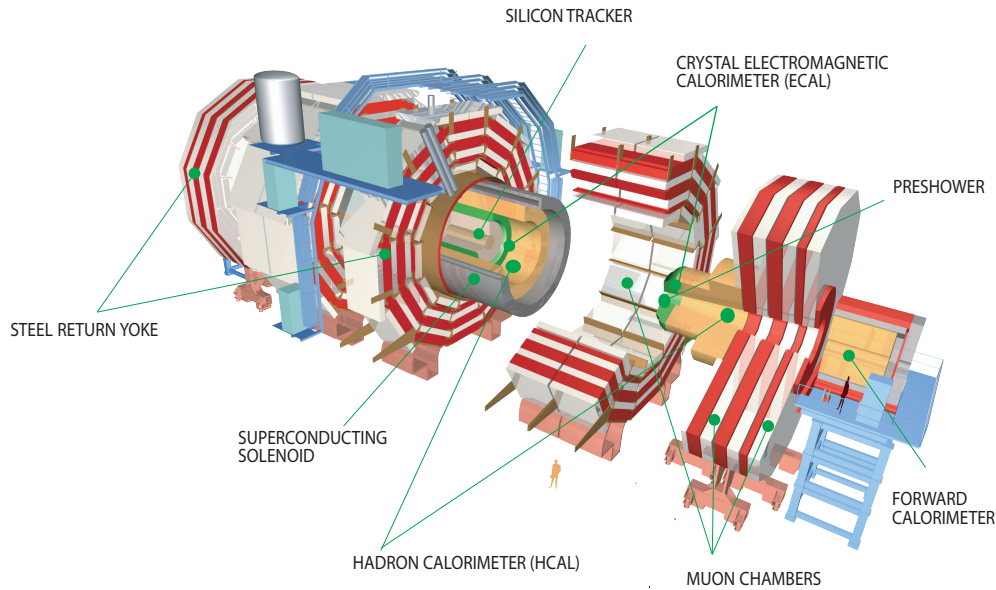


Figure 2.3: Three-dimensional view of the CMS detector. The onion-like structure consisting of several subdetectors in a magnetic field created by a large solenoid magnet is visible. For easier maintenance CMS is constructed in multiple slices which can be pulled apart on hovering air cushions [BC10].

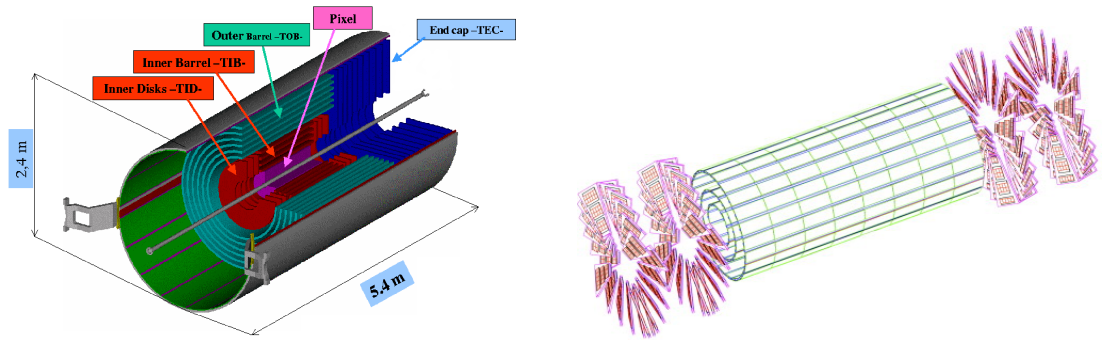
strip detector), the electromagnetic calorimeter and the hadronic calorimeter which are all embedded in the superconducting solenoid magnet. Outside the magnet follow a last layer of the hadronic calorimeter and multiple interleaved layers of muon chambers and iron return yoke. A short description of the different components follows:

MUON CHAMBERS: The high resolution of muon tracks is one of the features of CMS. The muon system is constructed from three different technologies: drift tubes (DT), cathode strip chambers (CSC) and resistive plate chambers (RPC). Each of them is based on the fact that traversing muons ionize the gas inside the detector elements but they have different properties regarding radiation hardness and particle rate. Since the muon chambers are embedded in the return yoke they sit in a high magnetic field which helps to reconstruct the momenta of the muons through bending the tracks.

SOLENOID MAGNET AND RETURN YOKE: The solenoid magnet used in CMS is the largest and strongest superconducting magnet ever used in a particle physics experiment and weighs about 220 t. Its coil of niobium-titanium (NbTi) wire is wound in four layers around a central bore of 6.3 m where it creates a homogeneous field of $B = 3.8\text{ T}$ which is used to bend the tracks of charged particles. Outside the coil in the 10000 t iron return yoke the field strength is still about 2 T.

HADRONIC CALORIMETER (HCAL): The hadronic calorimeter measures the energy of hadronic particles like protons, neutrons, pions or kaons. It is built as a sampling calorimeter consisting of multiple layers of brass¹ and plastic scintillator where incoming hadrons are stopped in the dense brass while producing showers of secondary particles. These secondary particles then produce light in the scintillator which gets detected. Since the HCAL is located inside the magnet bore it is limited in size and thus in energy resolution. To be able to cope with very high energetic showers an additional hadronic calorimeter has been added to the outside of the solenoid acting as a so-called tail catcher.

¹ The brass for the endcap hadronic calorimeter was recycled from old World War II artillery shells donated by the Russian army [Tay11].



- (a) Substructure of the CMS tracker. The pixel detector is placed closest to the interaction point while the surrounding strip detector begins at an inner radius of 20 cm and extends up to 120 cm with its different partitions [Scho3].
- (b) CMS pixel detector consisting of three barrel layers and two endcap disks at each end. Each coloured rectangle marks the position of one pixel module, the basic subunit of the detector [Dom07].

Figure 2.4: The CMS all-silicon tracker and its subcomponents. The tracker comprises an active area of more than 210 m^2 with 76 million readout channels. These values make it the largest silicon tracker used in a high energy particle physics experiment to date.

ELECTROMAGNETIC CALORIMETER (ECAL): The electromagnetic calorimeter measures the energy of particles which only interact electromagnetically like electrons, positrons and photons. They create showers while depositing their energy in the calorimeter material. Since one design target of the CMS detector was the search for the postulated Higgs boson, the energy resolution of the ECAL had to be high in order to be sensitive to the decay of the Higgs boson into two photons ($H \rightarrow \gamma\gamma$). This goal was reached by constructing it from lead-tungstate (PbWO_4) crystal scintillators readout by avalanche photodiodes and vacuum phototriodes.

TRACKER: As its name already implies the most important task of this subdetector is to find particle tracks which can be used to extrapolate the primary and secondary vertices of the interactions and to determine momentum and charge of the particles created in the collisions. Since it is positioned closest to the beam pipe it also faces the harshest operating conditions in CMS: the expected hit rates demand high granularity, the bunch spacing of only 25 ns demands fast response times and the high particle flow demands radiation-hard electronics and materials. At the same time it should be as lightweight as possible to minimize the impact of multiple scattering, nuclear interactions and bremsstrahlung on the outer subdetectors. For the innermost tracker layer at a distance of 4 cm from the beam pipe the calculated hit rate (at design luminosity) is 100 MHz/cm^2 while it decreases to 300 kHz/cm^2 at the boundary to the electromagnetic calorimeter (at 120 cm) [C+08].

Therefore the tracker consists of two subunits, the inner pixel detector and the outer strip detector. Both are all-silicon and together cover an area of more than 210 m^2 while being 5.4 m long and having a diameter of 2.4 m. These values make the CMS tracker the largest silicon tracker used in a high energy particle physics experiment to this day. An overview of the tracker and its partitions is given in figure 2.4.

The pixel detector provides the high granularity required to determine particle tracks at the highest hit rates. It consists of 2 m^2 of silicon in three barrel layers and two endcap disks at each end divided into 66 million pixels with a cell size of $150 \times 100 \mu\text{m}^2$. The exact arrangement is shown in figure 2.4b. Each of the pixels provides a space point in three dimensions for precise particle tracking with a high spatial resolution of $10 \mu\text{m}$ [Dom07]. This allows the reconstruction of secondary vertices created by the decay of relatively long-lived particles from the primary interactions like B mesons.

Starting at a distance of 20 cm from the beam pipe, the remaining tracker volume is filled by the strip detector which is also built in a barrel-with-endcaps configuration comprising ten layers in the barrel and nine layers per endcap (see figure 2.4a). Since the hit rates are significantly lower in this volume, the need for high granularity also decreases and allows the usage of silicon strip detectors. Compared to pixel cells, the strips have the same width but are up to 20 cm long and therefore the 210 m² of silicon in the strip detector consist of only 10 million strips or 13% of the total readout channels [Scho3]. This decreases the achievable spatial resolution especially along the strips but it would not have been possible to equip the full 210 m² with pixel detectors since readout of so many channels, powering and cooling are impossible and pixel detectors are much more expensive. To compensate the bad spatial resolution along the strips one technique used in the strip detector are so-called stereo modules which consist of two silicon strip sensor modules on top of each other while one module is rotated by 100 mrad. By looking at the hit strips on each module their intersection point gives again a three-dimensional space point.

The IEKP took part in the sensor qualification, module wire bonding and assembly of the petals² of one of the two tracker endcaps.

2.2.1 PARTICLE IDENTIFICATION IN THE CMS DETECTOR

Different types of particles create different signatures in the subdetectors of CMS. These different signatures allow identification of the particles by looking at the combined signals of all subdetectors. Figure 2.5 shows a transverse slice of CMS together with examples of the trajectories of five different particles, namely electrons, muons, charged and neutral hadrons and photons. Their signals in the subdetectors are also indicated.

Charged particles like electrons or charged hadrons create hits in the layers of the silicon tracker while neutral particles do not. The tracks are bent by the magnetic field and allow determination of the sign of the charge and the momentum of the particle. The energy of electrons and photons is measured by the electromagnetic calorimeter while hadrons, both charged and neutral, reach the hadronic calorimeter and get measured there. Muons are the only particles that reach the outside of the solenoid magnet and get detected by the muon chambers integrated in the iron return yoke.

Neutrinos are the only established stable particles that cannot be detected directly. Instead their presence has to be confirmed indirectly by measurement of an energy deficit among all other particles. To make this possible the detector has to be constructed hermetic which means that all particles produced in the collisions except neutrinos have to be detected and afterwards reconstructed during data analysis.

A large step forward towards full event reconstruction has been made with the introduction of new so-called particle-flow algorithms into CMS data analysis [Bea13]. Particle-flow algorithms aim at identifying and reconstructing individually each particle arising from the LHC proton-proton collision by combining the available information from all subdetectors.

2.2.2 THE CMS TRIGGER AND DATA ACQUISITION SYSTEM

Since the LHC delivers proton-proton collisions at a rate of 40 MHz respectively every 25 ns, the amount of data produced by the CMS experiment is orders of magnitude too large to be processed and stored with the available computing technology. A typical event recorded by the CMS detector has a size of about 1 MB and thus would result in a total data rate of 40 TB per second. Even if it would be possible to store these large amounts of data the scientific value

² A petal is the major substructure of the strip tracker endcaps, consisting of several detector modules, cooling loops, control electronics and mechanical support. Each endcap is built out of about 100 of such large structures.

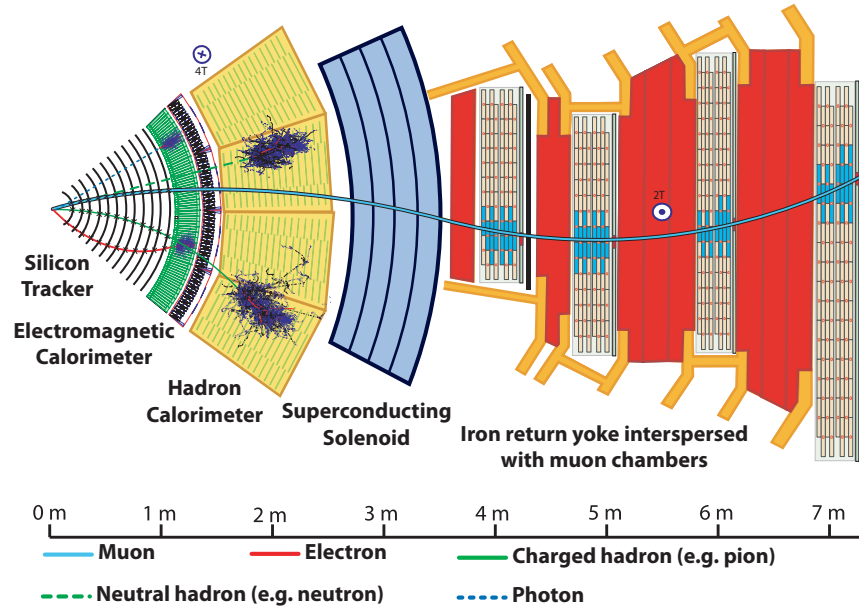


Figure 2.5: Transverse cross section of the CMS detector. The tracks of different traversing particles and their signals created in different subdetectors are indicated by the coloured lines and splashes [Bar11].

obtained from it is questionable because most events that occur only contain low-energetic collisions which are not of interest and any later data selection is also a question of available time if the processing is not done in real time.

It is therefore not only necessary to reduce the total amount of data but at the same time also select those events which contain processes of high interest like inelastic hard scattering. This selection and reduction is done by the so-called trigger system. In CMS it consists of two stages and at the end reduces the event rate to a manageable value of a few hundred Hz.

The first stage is the Level-1 (L1) trigger which is completely implemented in hardware using specially designed ASICs³ and configurable FPGAs⁴ [D⁺oo]. It reduces the initial rate to around 100 kHz and takes its decisions within a maximum latency of 3.4 μ s by applying simplified local reconstruction algorithms to data only from the calorimeters and the muon chambers. The latency time is defined by the depth of the buffer pipelines in the detector front-end electronics where all data has to be stored until a L1 trigger decision is made. It is therefore a trade-off between the required time to take the decision and the length of the pipelines which dictate ASIC sizes, power consumption and cost of the front-end electronics. If no trigger decision arrives within the latency time the oldest data in the pipelines is overwritten and cannot be recovered anymore.

Only after a positive L1 trigger decision the data from all subdetectors belonging to a certain bunch crossing is read out from the front-end pipelines by the data acquisition system and sent to the second stage of the trigger system, the high level trigger (HLT). The HLT is a software-based solution with an output rate of up to 1 kHz running on a large computing cluster with several thousand CPU cores [CRSo2]. It executes a full event reconstruction with algorithms searching for interesting signatures in the allowed latency window of 50 ms. If such a signature is found the event data is sent to storage at the CERN Tier-0 computing center and distributed among the different sites of the worldwide LHC computing grid where it finally becomes

³ Abbreviation for Application-Specific Integrated Circuit.

⁴ Abbreviation for Field Programmable Gate Array.

available for offline analysis. Since the HLT is software-based the trigger signatures are largely configurable and it could also be easily extended when more powerful computing hardware arrives.

2.3 UPGRADES TO THE CMS EXPERIMENT

As already mentioned in section 2.1.1 the LHC is delivering an extraordinary performance and thus it is planned to increase the instantaneous luminosity to twice the design value of $\mathcal{L} = 1 \cdot 10^{34} \text{ cm}^{-2} \text{ s}^{-1}$ in the coming years. The LHC is scheduled to run in its current configuration until 2023 with a total integrated luminosity of 300 fb^{-1} . Afterwards it will be upgraded to the High Luminosity LHC (HL-LHC) with a target luminosity of $\mathcal{L} = 5 \cdot 10^{34} \text{ cm}^{-2} \text{ s}^{-1}$ [HiL14]. This allows for a total integrated luminosity of 3000 fb^{-1} until the planned end of operation around the year 2037.

Together with the performance degradation induced by radiation damage these plans are tough challenges for the operation and data taking of CMS and the other LHC experiments. To cope with these challenges CMS will undergo two major upgrades in the next ten years.

2.3.1 THE PHASE I UPGRADE

The Phase I upgrade of the CMS detector will make sure that the detector is able to cope with both the instantaneous and the integrated luminosity planned for the LHC run until 2023. Together with the luminosity the in-time pile-up⁵ will reach average values around 60 and cause high occupancies in the different subdetectors. This means the number of channels firing simultaneously will reach values which cannot be sustained over longer periods of time because the buffers on the front-end electronics overflow before the L1 trigger decision arrives (see section 2.2.2) and possibly interesting data is inevitably lost.

The planned Phase I upgrade comprises three main areas of work:

UPGRADE OF THE TRIGGER SYSTEM: Most CMS electronics components were designed to operate at a L1 trigger rate of 100 kHz and several subdetectors would need major upgrades to be able to exceed this rate. Since these upgrades are not feasible the higher luminosity and pile-up values planned for the coming years would require a large increase of the current trigger thresholds to keep the rate within the 100 kHz limit [TA13]. This increase would have a negative impact on the physics acceptance of CMS, especially at the electroweak scale where the study of the couplings of the Higgs boson is a priority. To be able to keep the trigger rate within the limit without the need to increase the trigger levels to undesired values where important data gets lost, some parts of the trigger system logic will be upgraded with new electronics technologies: the calorimeter trigger, the muon trigger and the global trigger. This will increase the granularity of the trigger and also its flexibility to be adapted to the rapidly evolving running conditions. In parallel this opportunity will be used to consolidate the many electronics boards currently in use by replacing them with a small number of general-purpose designs housed in modern telecommunications standard (μ TCA) crates.

UPGRADE OF THE HADRONIC CALORIMETER: At the moment the showers in the barrel and endcap parts of the hadronic calorimeter are read out using hybrid photodiodes (HPDs) which show several weaknesses during operation in the magnetic field of CMS. The most significant effect is electrical discharges which appear when the required high voltage for operation (8 kV) is applied [MAD⁺12]. This is a source of noise and additional aging which already triggered the reduction of the operation voltage to 6.5 kV. There is also a large gain divergence seen over all channels in the response to light created by a special LED system for calibration which is not understood at the moment. All

⁵ Pile-up is the number of simultaneous proton-proton collisions in one bunch crossing.

these effects have led to the decision to replace all HPDs with newly developed silicon photomultipliers (SiPMs). This replacement will at the same time allow a much larger segmentation of the HCAL readout which is required for the advanced usage of particle-flow algorithms [Bea13]. In the forward part the existing photomultiplier tubes (PMTs) will be replaced with new multi-anode type tubes which will help to reduce the number of anomalous signals appearing in the current setup.

All parts of the HCAL share a common readout electronics chain with several ASICs which helped to save costs during construction and eases daily operation by minimizing the number of different systems. This successful approach will be kept but improved with new ASICs like the QIE11 flash ADC⁶ chip [BMD⁺14].

UPGRADE OF THE PIXEL DETECTOR: The pixel detector will be completely replaced with a new version with four barrel layers and three endcap disks at each end [DAA⁺12]. New digital readout electronics with larger buffers and higher bandwidth will improve the efficiency at the expected high occupancies, while a new carbon fibre support structure combined with evaporative CO₂ cooling will reduce the material budget in the active tracker volume despite adding a new layer. The new cooling also allows a lower detector operation temperature of -15°C to mitigate the effects of radiation on the silicon sensors. The new pixel detector and its components are described in detail in chapter 4.

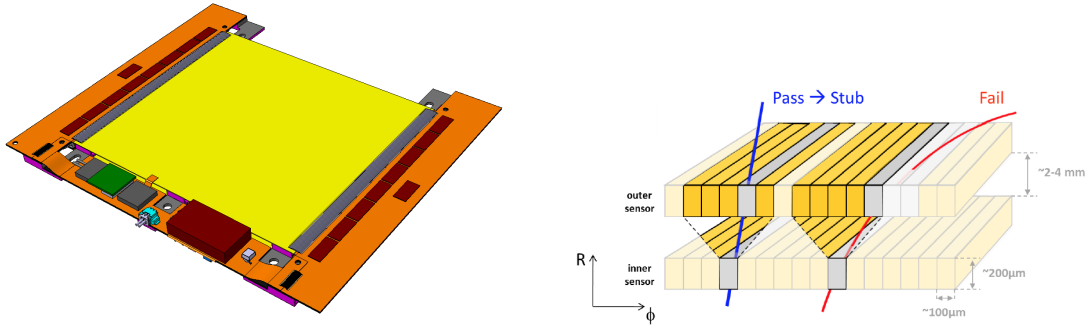
2.3.2 THE PHASE II UPGRADE

The second upgrade will prepare the CMS detector for the challenges of the HL-LHC run with even higher luminosities around $\mathcal{L} = 5 \cdot 10^{34} \text{ cm}^{-2}\text{s}^{-1}$. This means that the impact on CMS will be much more severe than during the current run. Radiation damage to the subdetectors will lead to a progressive degradation of the overall performance of CMS because the dose for one year of HL-LHC running is comparable to the total accumulated dose between the start-up of the LHC in 2008 and the end of Run 3 in 2023.

The absorbed dose and the amount of damage caused are strongly dependent on the location and the construction of the different subdetectors. It is obvious that the tracker and the forward calorimeters are most affected due to their positions closest to interaction point and beam pipe. Damage to the silicon sensors from both ionizing and non-ionizing radiation leads to increased leakage current, trapping of created charge carriers on their drift to the readout electrodes and the need for unsustainably high depletion voltages above 800 V. Radiation will also cause failures in the front-end electronics. In the calorimeters the main problem is the detection of the light signals generated by the particle showers. This light has to be guided from the point of origin in the scintillator material to the attached readout electronics but especially the lead-tungstate (PbWO₄) crystals of the electromagnetic calorimeter lose their transparency with irradiation and therefore the signals get reduced.

Besides radiation damage the second problem will be pile-up which is expected to reach average values of 140 and peaks around 200. This causes very high occupancy in the tracker and might lead to misidentified tracks due to the ambiguities in the assignment of the hits to tracks. To counter these effects the granularity of both the pixel and the strip detector will be increased by more than a factor of four. In case of the pixel detector this increase will mainly be reached by shrinking the size of the pixel cells in a module comparable to the current one while for the strip detector two novel module designs have been created: the 2S module and the PS module. They both consist of a sandwich of two stacked sensors with a separation of several millimeters and are made of either two strip sensors with 5 cm long strips (2S) or one strip and one pixelated sensor with very short strips of 1.5 mm (PS). PS modules are planned for the inner regions of the strip tracker where the occupancy is higher while 2S modules are

⁶ Abbreviation for Analog-to-Digital Converter.



(a) Perspective view of the module. Visible are the two super-imposed silicon strip sensors (yellow), the read-out ASICs (red) and the ends of the Al-CF spacers supporting the sensors (grey) [2SM15].

(b) Working principle of a trigger module. Tracks with lower particle momentum (red) are more curved in the magnetic field and thus miss the search window (yellow) in the outer sensor [BHJ⁺14].

Figure 2.6: 2S module for the Phase II Upgrade of the CMS tracker and its working principle.

used in the outer regions up to the calorimeters. A model of the current 2S module design is shown in figure 2.6a.

The decision to use two silicon detectors for each of the new tracker module designs is driven by another important task: triggering. As already described in section 2.3.1 higher luminosity requires higher trigger thresholds to keep the rate of the L1 trigger below a given value but the relation between threshold and rate is non-linear and flattens out for high thresholds. For the planned HL-LHC luminosity it is therefore not an option anymore [Hal11]. It has been shown that one of the most effective methods to improve the trigger functionality is the exploitation of tracking information at the earliest possible stage.

The natural location to deploy such a track trigger algorithm would be the Level 1 trigger but due to bandwidth limitations it is impossible to read out the whole tracker at a rate of 40 MHz to transfer all hits to the L1 trigger logic. A first step of data reduction in the front-end electronics is thus essential to the track trigger approach and this reduction can be achieved with the new tracker module designs. Both sensors of a module are connected to the same readout ASICs which correlate the hit information and allow a simple discrimination of the transverse momentum. Only if a track passes this discrimination its stub⁷ is sent out to the L1 trigger and processed further. An illustration of the working principle is given in figure 2.6b.

The latency of the L1 trigger will at the same time be increased to 12.8 μs to allow hardware track reconstruction using the stubs from the tracker and new technologies like associative memory [Sab14]. At the end the output rate of the L1 trigger will be of the order of several hundred kHz while the HLT will have a rate of 10 kHz.

The endcap calorimeters will be replaced by a newly designed high-granularity calorimeter (HGC) with an electromagnetic and a hadronic section [CKM⁺15]. Advances in silicon detectors concerning cost per unit area and radiation hardness will for the first time allow the usage of silicon as the active part of a calorimeter. Compared to other more conventional approaches it facilitates much higher longitudinal and lateral granularities which are important for high pile-up scenarios and allow the optimal usage of particle flow algorithms. The design is based on prototypes that have been developed, built and tested for the proposed International Large Detector (ILD) at the ILC [BDJ⁺07].

The HGC comprises an active silicon area of 600 m² divided into an electromagnetic part with tungsten/copper as absorber and a hadronic part using brass. In areas where radiation levels are lower a conventional scintillator-brass design is used.

⁷ Stub is defined as a pair of hits in a sensor doublet from a track with high transverse momentum.

The other subdetectors, which are less affected by radiation damage due to their locations far away from the interaction point, will only be upgraded to be able to take data at higher rates for up to 15 more years. All readout electronics have to be replaced due to the extended L1 trigger latency. A detailed description of all proposed Phase II upgrades to the CMS experiment and its surrounding infrastructure can be found in [\[CKM⁺15\]](#).

SILICON PARTICLE DETECTORS

Position-sensitive particle detectors, also called tracking detectors, are an important component of any modern particle physics experiment because they are able to provide measurements for the determination of particle trajectories, which in turn can be used to deduce basic properties of the particles like momentum, charge and origin. Their performance is vital for all kinds of physics analyses, but especially heavy flavour physics like top quark measurements depend on high resolution reconstructions of secondary decay vertices to allow b jet tagging.

Most particle physics experiments of today use silicon semiconductor detectors because silicon has a number of advantages over other detector concepts like gaseous detectors. First of all, it is available at fairly low cost due to abundant availability in the upper earth crust. Secondly, there is vast experience in industry because silicon-based electronics have become an integral part of our daily life in the decades following the invention of the transistor by Bardeen and Brattain in 1947 [BB48] (though the first transistors were based on germanium and not silicon). Thirdly, the mean ionization energy needed to create electron-hole pairs is much lower in silicon as in gaseous detectors. Since silicon sensors are basically solid-state ionization chambers where incident charged particles interact with the silicon lattice and create electron-hole pairs, this (together with the high material density) results in a large number of charge carriers being produced for every hit.

For silicon about 73 electron-hole pairs per μm of thickness are on average created by a minimum ionizing particle [O^+14]. In a typical sensor with a thickness of $300\ \mu\text{m}$ this leads to a large signal of 22000 electrons. Since silicon also features a high charge carrier mobility, the electrons get collected within a comparatively short time of a few nanoseconds. This is an important feature for detectors used at accelerators like the LHC where collisions happen every 25 ns.

In the following chapter a brief overview of the properties of semiconductors, the working principle of semiconductor detectors and the design of position-sensitive silicon particle detectors is given. In-depth reviews of silicon detectors and their applications can be found in [Har09], [Luto7] and [WRFRo6].

3.1 BASIC PROPERTIES OF SEMICONDUCTORS

Solid materials are classified into three different groups according to their electrical properties where semiconductors are one group while the others are insulators and conductors (or metals). As already deducible from the name the electrical conductivity of a semiconductor lies in between those of insulators and metals.

3.1.1 ENERGY-BAND MODEL

Semiconducting materials are elements in the fourth group of the periodic table out of which silicon and germanium are the most important ones for industrial applications. Both silicon and germanium are crystalline solids where the atoms form a regular lattice structure held together by the interactions of the shell electrons of each atom. Each of those bonds increases

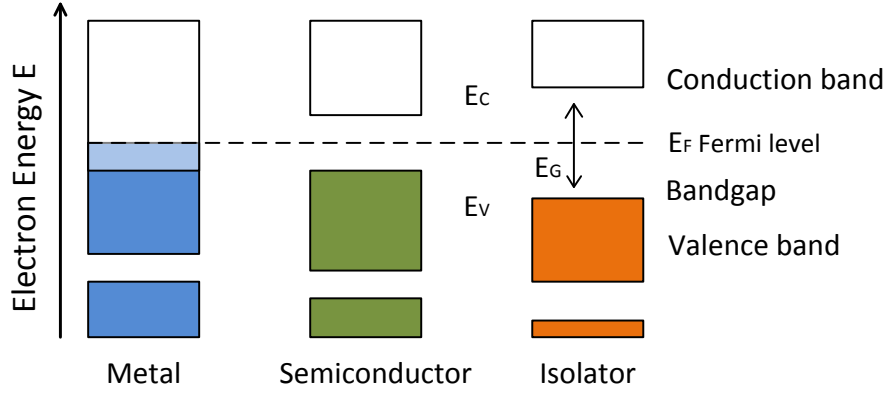


Figure 3.1: Energy band configuration and Fermi energy of conductors, semiconductors and insulators. E_G is the width of the band gap while E_V and E_C are the energy values of the edges of the valence and conduction band. At $T = 0\text{ K}$ the energy states are filled up to the Fermi level (shown by coloring) [IL09].

the energy state density in the material because of small shifts of the energy levels caused by the interaction mechanism. Since solid materials consist of large numbers of atoms there are so many shifts that at the end a continuous band structure is formed which can then be used to describe the electrical properties of the material. This so-called energy-band model allows to divide solid materials into the three groups mentioned at the beginning by looking at their band configurations.

The occupation of the energy states can be described using the Fermi-Dirac distribution since electrons are following the Pauli exclusion principle. The probability to encounter an electron with a given energy E is then defined as

$$f(E) = \frac{1}{e^{[(E-E_F)/k_B T]} + 1} \quad (3.1)$$

with k_B being the Boltzmann constant and T the absolute temperature. The term E_F denotes the Fermi energy at which the probability is 0.5.

At $T = 0\text{ K}$ all energy states up to E_F are occupied. In the energy band model, the highest band which is completely filled with electrons at $T = 0\text{ K}$ is called valence band and the next higher empty band is called conduction band. At temperatures above 0 K some electrons are excited to states above the Fermi energy in the conduction band. Since there are available free states within that band, the electrons can move freely within the crystal lattice and therefore contribute to the conductivity of the material. At the same time other electrons in the valence band occupy the vacant position of the excited electron, make the so-called hole move and also contribute to the conductivity. Hence both electrons and holes are always created in equal numbers.

Figure 3.1 shows the configurations of valence and conduction band in metals, semiconductors and insulators. If the Fermi energy E_F either lies within the conduction band or valence and conduction band overlap the material contains free charge carriers even at $T = 0\text{ K}$. It is then considered a metal or conductor. For both insulators and semiconductors this is not the case and the Fermi energy rather lies in the energy gap between valence and conduction band. For insulators the width of the gap is too large to allow electrons to be excited into the conduction band even at very high temperatures. At $T = 0\text{ K}$ semiconductors exactly behave like insulators but their band gap is much smaller and thus allows thermal excitation of electrons into the conduction band. These electrons are then called intrinsic charge carriers and the material itself an intrinsic semiconductor. The limit between insulators and semiconductors is not exactly defined but most publications draw the line at a band gap width of 3 eV .

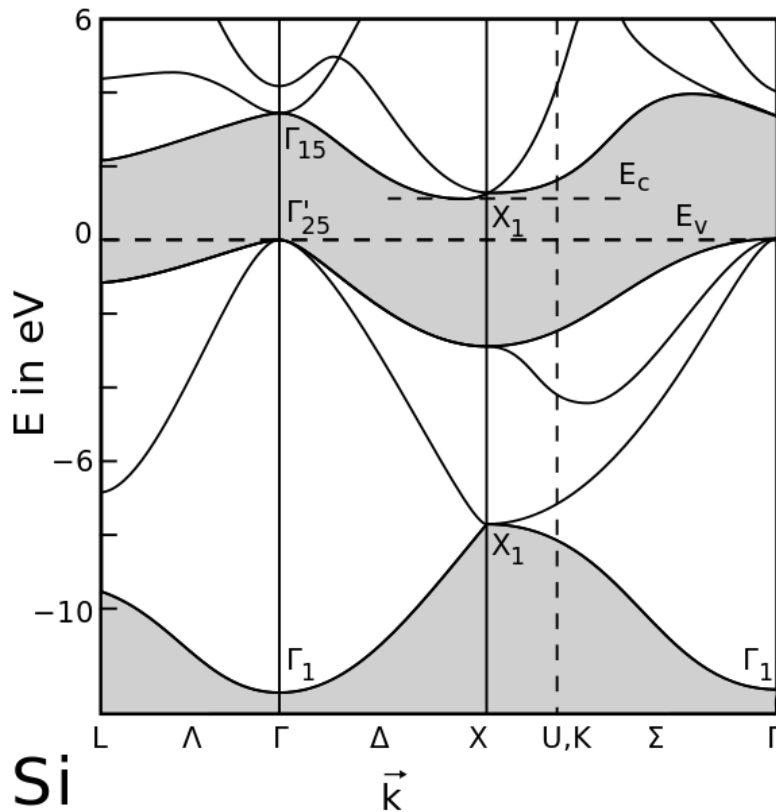


Figure 3.2: Band structure of silicon in the reduced zone scheme. Silicon is a so-called indirect semiconductor since the maximum of the valence band E_V and the minimum of the conduction band E_C are shifted in momentum (or \vec{k} -) space and thus require excitation of a phonon for every transition between the bands in order to conserve energy and momentum [CC74].

3.1.2 INDIRECT SEMICONDUCTORS

The width of the band gap depends on the material. For germanium it is relatively small (0.67 eV) which results in a very low mean ionization energy [Kaso6]. Germanium is therefore the material of choice for spectrometer detectors where energy resolution is important. On the other hand a small band gap also leads to a high number of intrinsic charge carriers at room temperature which create noise. Germanium spectrometers are thus cooled to very low temperatures using liquid nitrogen during operation. For position-sensitive detectors used in particle physics experiments such cooling is not possible due to the low material budget and therefore silicon with a larger band gap of 1.12 eV is better suited for this application. In reality the necessary energies to excite an electron from the valence to the conduction band are even higher because silicon and also germanium are indirect semiconductors.

The band structure of silicon is shown in figure 3.2 where the band gap of 1.12 eV is indicated by the maximum of the valence band E_V and the minimum of the conduction band E_C . It is visible that the two points are shifted in momentum (or \vec{k} -) space which means that transitions between valence and conduction band have to be indirect (hence the classification as indirect semiconductor). To maintain the conservation of energy E and momentum \vec{k} , a phonon has to be excited for every transition of an electron between the two bands and therefore the average energy to create an electron-hole pair in silicon is 3.6 eV, about three times larger than the band gap alone [O⁺14]. Since phonons are seen as vibrations of the crystal lattice the probability for transitions in indirect semiconductors increases with temperature.

3.2 WORKING PRINCIPLE

The conductivity of intrinsic semiconductors at room temperature is still very low and therefore they are not suited for usage in electronics applications like integrated circuits (ICs). In order to modify their conductivity and other properties artificial impurities can be introduced into the crystal lattice. In case of the electric conductivity this process yields increases of several orders of magnitude compared to the intrinsic value.

3.2.1 DOPING

The process to replace atoms in the semiconductor material with other impurity elements is called doping. These impurities create additional energy levels in the band gap close to the edges of the valence or conduction band. Since the energy gap between the bands and the new levels is much smaller than the band gap the probability of the charge carriers to reach the levels is much higher and thus more free charge carriers are created at a certain temperature compared to the intrinsic case.

Silicon as a group IV element in the periodic table with four electrons in the outer shell is usually doped with elements from the third or fifth group. Technically the process is realized either as diffusion at very high temperatures exceeding 1000 K or as ion implantation at energies in the hundred keV range.

Doping with group-V elements like phosphorus, which have five valence electrons, leaves one electron unbound because it is not needed for the bonding to the neighboring silicon atoms in the lattice (cf. fig. 3.3a). Therefore it can be easily excited to the conduction band and participate in the conduction of electric current. Since such elements provide an additional electron to the lattice they are called donors. In the energy band model donors create a new energy level in the band gap close to the conduction band as shown in figure 3.3b.

Group-III elements such as boron only have three valence electrons and leave one bond to the next silicon atoms open. These open bonds are then filled with electrons from other silicon-silicon bonds where they are in turn missing and create a hole which can also contribute to the conduction of electric current (cf. fig. 3.3c). Since such elements effectively take an electron from the lattice they are known as acceptors. In the energy band model acceptors create a new energy level in the band gap close to the valence band as illustrated in figure 3.3d.

Doped semiconductors where the majority of charge carriers stems from the dopant are called extrinsic semiconductors. In contrast to intrinsic semiconductors doping always leads to the fact that one type of free charge carriers, either negative or positive, is more abundant than the other and hence it is called the majority charge carrier. By convention silicon with added donor atoms is called n-doped (or n-type), as electrons are the majority carriers, and silicon with added acceptors is called p-doped or p-type respectively.

3.2.2 PN-JUNCTION

As described in section 3 the signal expected from an incident particle in 300 μm thick silicon is around 22000 electrons but at the same time the number of free charge carriers in intrinsic silicon at room temperature is five magnitudes larger [Harog]. This means that the signal would completely disappear in the background. To be able to detect the signal the amount of free charge carriers has to be reduced drastically. This can be achieved by either cooling the detector to cryogenic temperatures or by depleting the volume of the silicon sensor from free charge carriers using a pn-junction in reverse bias mode. Since cryogenic cooling of large detectors is impractical, all implementations of silicon particle detectors use the reverse-biased pn-junction.

A pn-junction is created by joining p- and n-type silicon together. In reality this is done by different doping of a single silicon crystal. By that joining, a gradient of charge carrier con-

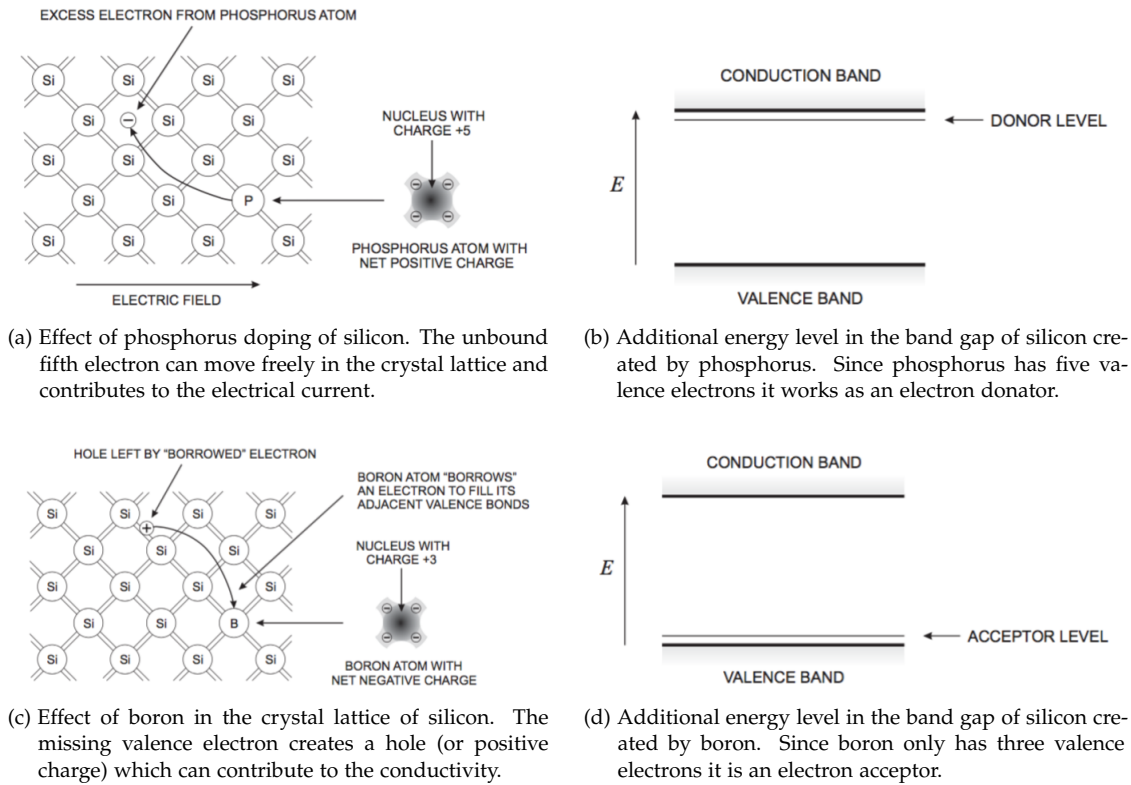


Figure 3.3: Doping of silicon with phosphorus (from group V of the periodic table) or boron (from group III) and the representation in the energy band model [Spi05].

centration between the two types of silicon is formed and free charge carriers start to diffuse through the contact area in order to equalize the concentration. This process is illustrated in figure 3.4. Electrons from the n-doped region drift to the p-doped region where they recombine with the existing holes and at the same time holes from the p-doped region drift to the n-doped region and recombine with electrons. Since the remaining donor and acceptor ions are immobile due to the crystal lattice, a net positive charge develops in the n-type region while a negative charge arises in the p-type region. These charges create an electric field in the boundary region with counteracts the diffusion process until an equilibrium between the forces is reached. In this state a region free of charge carriers around the contact area is formed which is called space-charge region (SCR) or depletion zone. This region is thus suited to be used as a particle detector: electron-hole pairs are generated by incident particles, get separated by the electric field and drift towards the boundary of the SCR where they could be collected by the readout electronics. On the other hand charges created outside the depletion zone are always lost because they immediately recombine with the available charge carriers from the lattice.

The electrostatic potential in the depletion zone is called built-in voltage U_{bi} . It is dependent on the doping concentrations used for the n- and p-type part but normally it is of the order of millivolts and the resulting depletion zone is only a few micrometers wide and therefore inappropriate for the usage as particle detector. However, the application of an external voltage allows to change the width as needed. The polarity required to increase the width is the so-called reverse bias case which is used for detector applications while the polarity reducing the width and allowing the current to flow is the forward bias case. Both cases are the operating modes of one of the most basic electronic components, the diode. A detailed discussion of the basic properties of semiconductor diodes can be found in [Sze85].

The voltage required to increase the depletion zone over the full volume of silicon material used for the pn-junction is called (full) depletion voltage U_{fd} . Since the space-charge region

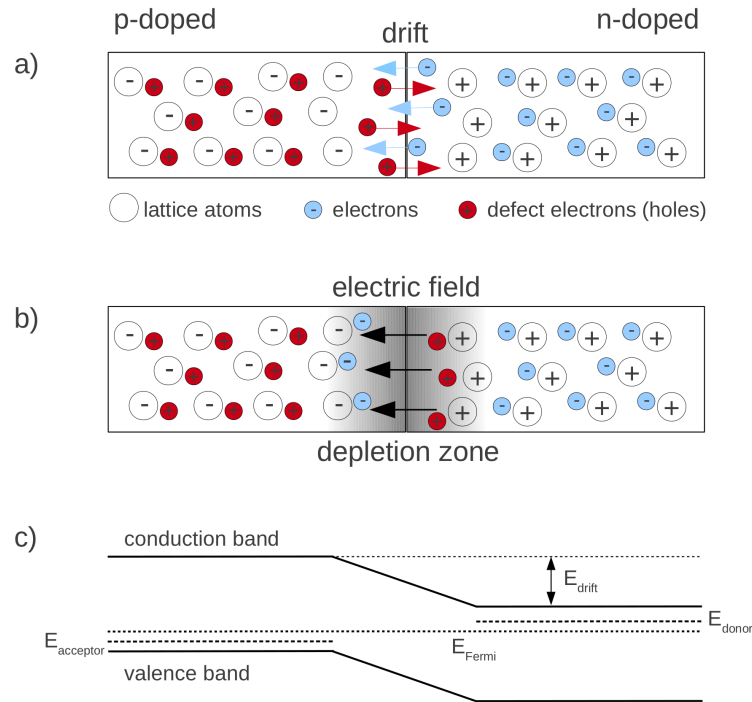


Figure 3.4: pn-junction and formation of the depletion zone [Hos12].

- After joining the two materials: Electrons from the n-doped material drift to the p-doped material due to a gradient in concentration. They recombine with the holes and leave positively charged donor ions at their origins. Holes from the p-doped material at the same time drift to the n-doped region and recombine with electrons leaving negatively charged acceptor ions.
- State of equilibrium: The drift of the charge carriers has come to an end because of the electric field created by the stationary ions. The region around the contact area is free of charge carriers and therefore called depletion zone.
- Representation of the pn-junction in equilibrium in the energy band model: The drift of charge carriers has equalized the different Fermi levels and the bands are shifted by the electric field E_{drift} .

acts as a plate capacitor, the capacitance of a device can be calculated from the width of the SCR. For fully depleted devices that width equals the thickness and the capacitance does not increase any further. By measuring the capacitance for different values of the bias voltage U_{fd} can be found at the kink of the capacitance-voltage characteristic which plots $1/C^2$ over U_{bias} . It is one of the most important design parameters for a silicon sensor since it defines the minimal operation voltage the sensor has to sustain without going into current breakdown.

Normally silicon sensors are operated in the over-depleted mode. This means that the value of the applied bias voltage is set well above U_{fd} (typically to $U_{bias} \approx 2 \cdot U_{fd}$) to create an additional electric field which helps to remove thermally excited electron-hole pairs from the depletion zone. They drift to the connection electrodes and form the leakage (or reverse) current, another important parameter of silicon sensors, since this behaviour directly affects power consumption and noise. As already shown in equation 3.1 the creation of electron-hole pairs and also the resulting leakage current are temperature-dependent. Designing and constructing the detector with an ability to actively cool the silicon sensors thus allows to reduce the leakage current.

Other sources of leakage current are impurities already introduced during processing of the silicon or radiation damage of the silicon lattice. Both add additional energy levels near the middle of the band gap which are responsible for the so-called generation current.

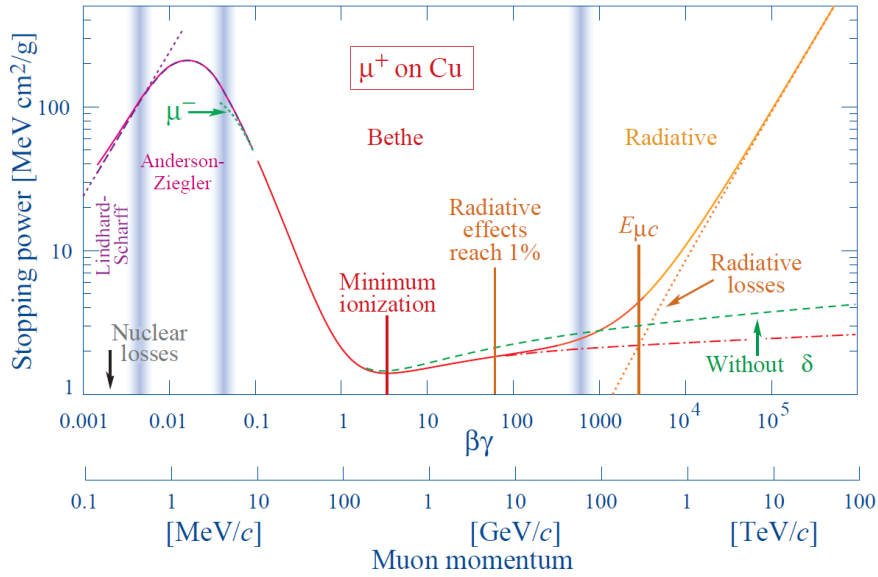


Figure 3.5: Stopping power ($= dE/dx$) for positive muons in copper as a function of $\beta\gamma = p/Mc$ over nine orders of magnitude in momentum. The depicted effect is the fundamental working principle of ionizing particle detectors [O⁺14].

3.2.3 INTERACTION OF PARTICLES WITH MATTER

The functionality of silicon particle detectors is based on the interaction of particles with matter. For tracking detectors only electromagnetic processes play a role which directly implies that neutral particles like neutrons cannot be detected. Due to the interaction, charge carriers are created in the silicon material which can then be detected by the readout electronics.

Depending on the energy and type of the incident particle, different mechanisms contribute to the interaction process. Charged particles interact with the bulk material via ionization processes, while photons have three different mechanisms of interaction with matter depending on their energy. A basic overview of the various types of interactions is given in following sections.

3.2.3.1 Charged particles

Charged particles passing through the silicon sensor lose a part of their kinetic energy due to interactions with the shell electrons of the silicon. The energy loss for particles significantly heavier than electrons is given by the Bethe formula [Bet30]:

$$-\frac{dE}{dx} = 4\pi N_A r_e^2 m_e c^2 z^2 \frac{Z}{A} \frac{1}{\beta^2} \left[\frac{1}{2} \ln \left(\frac{2m_e c^2 \beta^2 \gamma^2 T_{\max}}{I^2} \right) - \beta^2 - \frac{\delta(\beta\gamma)}{2} \right] \quad (3.2)$$

In this equation z is the charge of the incident particle, Z and A are the atomic number and atomic mass of the absorber, $\beta = v/c$ and $\gamma = 1/\sqrt{1-\beta^2}$ are relativistic factors, δ is a density effect correction, I is the mean excitation energy in eV and T_{\max} is the maximum kinetic energy which can be transferred to a free electron in a single collision. The equation shows that the energy loss is independent from the mass of the incident particle. In figure 3.5 the Bethe formula is plotted over its valid momentum range for positive muons traversing a copper absorber. At low momenta various effects that are not yet completely understood contribute to the energy loss while at high momenta radiative processes begin to dominate. The most prominent part of the curve is the minimum around $\beta\gamma = 3$ where the energy deposition of a traversing particle in the absorber is minimal. Particles with momenta of this magnitude are therefore called Minimum Ionizing Particles or MIPs. For electrons in silicon, this value

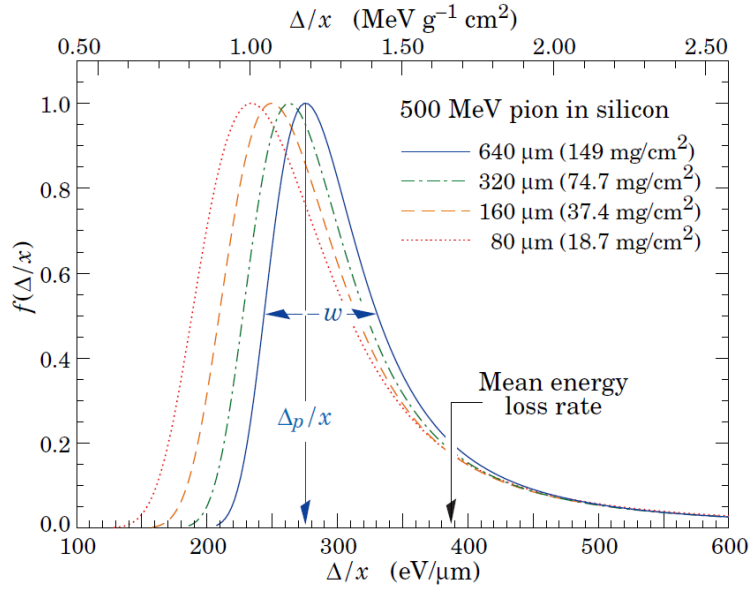


Figure 3.6: Energy loss of a 500 MeV pion in silicon, shown as statistical distribution normalized to one for multiple thicknesses of silicon. Due to statistical fluctuations in the ionization process it is an asymmetric Landau distribution where the most probable value (MPV, the peak of the distribution) of the energy loss is about 30% lower than the mean energy loss and also dependent on the silicon thickness [O⁺14].

corresponds to an energy of about 1.5 MeV and every detector has to be optimized to keep its noise below the energy deposited by such particles to be able to detect them. Other particles with higher ionization power can then be detected without any problem.

Due to statistical fluctuations in the ionization process the energy loss in thin layers of silicon is described with an asymmetric Landau distribution which has a tail towards higher values due to knock-on (or δ -) electrons [Lan44]. An example of such a distribution for the energy loss of a 500 MeV pion in silicon is shown in figure 3.6. The most probable value (MPV) of the energy loss is about 30% lower than the mean energy loss and is dependent on the thickness of the silicon. This knowledge allows a short revisit of the number of 73 electron-hole pairs created per μm of silicon which was given at the beginning of section 3. Minimum ionizing particles have an average energy loss of 390 eV/ μm in silicon which together with the 3.6 eV needed to create an electron-hole pair leads to a result of 108 pairs per μm on average and a most probable value of 73.

The Bethe formula is not valid for light particles such as electrons or positrons since their energy loss is dominated by the emission of Bremsstrahlung. Additionally the energy loss for electrons is different because they are identical to the particles they interact with, the shell electrons of the absorber. Nevertheless they both deposit enough energy in a silicon sensor to be detected.

3.2.3.2 Photons

Photon interactions with matter can be divided into three main mechanisms depending on the energy of the incident photon: the inner photoelectric effect, Compton scattering and pair production. They all have in common that the energy is either partially or completely transferred to charged particles which in turn can then be detected as described in the last paragraph. Figure 3.7 shows the energy dependence of the photon interaction cross section in carbon and the various interaction mechanisms.

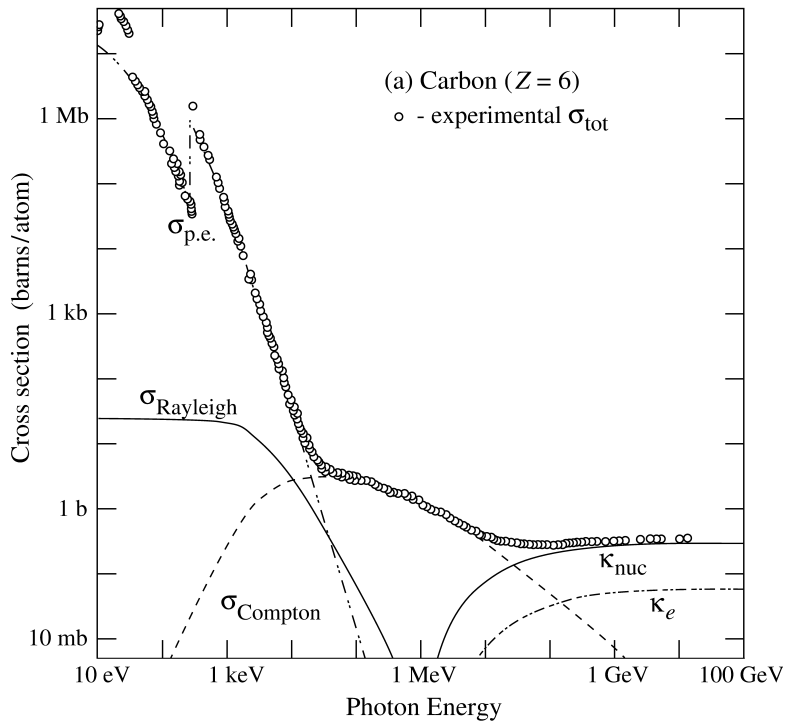


Figure 3.7: Energy dependence of the photon interaction cross section in carbon. The process is dominated by three interaction mechanisms: the inner photoelectric effect at low energies up to 100 keV, Compton scattering at medium energies and pair production at high energies above 50 MeV [O⁺14].

The inner photoelectric effect is the dominating mechanism at energies below 100 keV. By scattering the energy of the photon is completely transferred to a shell electron of the sensor material and the photon is absorbed. The electron is thus excited to the conduction band. This effect is important for the calibration of silicon particle detectors since the radioactive sources or X-ray tubes used to calibrate deliver photons in that energy range.

In the energy range between 100 keV and 10 MeV Compton scattering is the main interaction mechanism. It is based on the scattering of photons on quasi-free electrons where only a fraction of the photon's energy is transferred and the photons have a longer wavelength afterwards. The amount of transferred energy is dependent on the scattering angle and maximal for 180° backscattered photons. The Compton equation gives the energy of the scattered photon E'_ν as a function of initial energy E_ν and scattering angle θ [Com23]:

$$E'_\nu(\theta) = E_\nu \left(1 + \frac{E_\nu}{m_e c^2} \cdot (1 - \cos \theta) \right)^{-1} \quad (3.3)$$

For high energies above 50 MeV pair production becomes the most important interaction mechanism. An electron-positron pair is created from the energy of the absorbed photon if the photon energy is higher than twice the rest mass of an electron ($1.022 \text{ MeV} = 2 \cdot 511 \text{ keV}$). To satisfy conservation of momentum this process requires the presence of an atomic nucleus which receives some recoil.

3.3 POSITION-SENSITIVE SILICON PARTICLE DETECTORS

The basic design of a position-sensitive silicon particle detector is shown in figure 3.8. It is based on multiple pn-junctions whose functionality has already been described in section 3.2.2. They are formed between the p-doped strip implants and the n-doped bulk silicon material. By using a regular pattern of strips and not only a single large implant the device is able

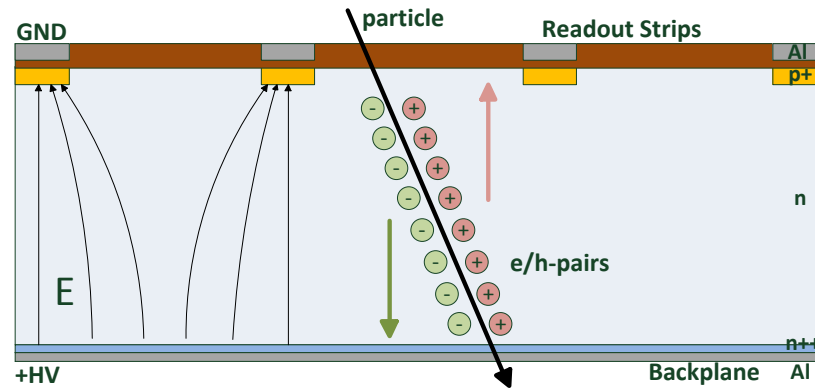


Figure 3.8: Basic design of a position-sensitive silicon particle detector. The pn-junctions are formed between the p-doped strip implants (yellow) and the n-doped bulk silicon (light blue). A positive high voltage is applied to the backplane in order to deplete the bulk material from free charge carriers by operating the detector in reverse bias mode. A traversing particle creates electron-hole pairs along its track by ionizing the silicon atoms. Electrons and holes then get separated by the electric field and induce a current signal in the aluminum readout strips. A position information of the hit is available due to the segmentation of the strip implants [Ebe13].

to give position information on the particle hit at least in the direction perpendicular to the strips. Along the strips the exact position cannot be discriminated. In order to achieve a two dimensional spatial resolution each strip can again be segmented into very short units along its longer dimension where each unit is readout discretely. The resulting device is called a pixel detector comparable to the image sensor of a digital camera.

By applying a positive high voltage to the backside (or backplane) the pn-junctions are operated in reverse bias mode and the bulk material is depleted from free charge carriers. At the same time it forms an electric field which is used to separate the electron-hole pairs created by traversing ionizing particles. Electrons drift to the backplane while holes drift to the strip implants where they can be readout as a current pulse. Typically the readout strips are not directly connected to the strip implants but separated by a thin insulating layer of silicon-dioxide. This design is called capacitive coupling and thus such sensors are called AC-coupled sensors. Capacitive coupling effectively disconnects the inputs of the front-end readout electronics from the leakage current which would be an additional burden for the ASIC design. The currents induced in the insulated readout strips by the drifting charges in the bulk can be calculated using the Shockley-Ramo theorem [Sho38] [Ram39].

A typical silicon strip sensor like it is used in the current CMS strip detector is $10 \times 10 \text{ cm}^2$ in size and the bulk material is $320 \mu\text{m}$ thick. It has about 768 strip implants, each spanning the full sensor length, resulting in a strip pitch of $130 \mu\text{m}$ [Krao4]. The strip pitch is one of the basic design parameters of a silicon sensor since it defines the basic resolution of the sensor. The signals created by traversing particles are normally distributed among several strips according to the Shockley-Ramo theorem and due to the fact that the detector is placed in a magnetic field which not only bends the trajectories of charged particles but also influences the drift directions of the charge carriers created in the silicon sensor. The drift is thus no longer parallel to the electric field but under an angle, the so-called Lorentz angle. While this charge sharing is highly welcome in gaseous detectors (which feature charge multiplication) it might become a problem in silicon since the initial signal gets divided into very small parts which would be lost in the noise distribution. The effect therefore already needs to be taken into account during the design of the detector.

If a particle creates enough charge to reach the readout threshold on at least two strips the position determination of the hit can be enhanced by using either simple center-of-gravity meth-

ods or more complicated algorithms which take the actual shape of the charge distribution into account. In case of the center-of-gravity method this results in a resolution $\sigma_x \propto \text{pitch}/\text{SNR}$ [Luto7]. For typical sensors this value is about $10 \mu\text{m}$. If only a binary hit/no hit signal and no pulse height information is available like it is planned for the future CMS Tracker Phase II upgrade the position resolution is reduced to $\sigma_x \approx \text{pitch}/\sqrt{12} \approx \text{pitch}/3.46$ stemming from geometrical considerations. For the aforementioned sensor this is $40 \mu\text{m}$ or a factor four less compared to the case with analog readout.

3.4 RADIATION DAMAGE IN SILICON

Silicon used in semiconductor particle detectors experiences severe radiation damage during operation due to the traversing particles. Defects are created which influence the properties of the detector and degrade its performance. These defects can be divided into two groups of different damage types: bulk damage and surface damage. Bulk damage is mainly created by hadrons while surface damage is mostly created by photons.

If a particle traverses a silicon detector and interacts with the silicon lattice, defects in the lattice are created by scattering on the lattice atoms. The first atom that is hit is called the primary knock-on atom (PKA) which gets displaced from its lattice position if the energy of the traversing particle exceeds a threshold of about 25 eV . The PKA then leaves behind a vacancy and moves freely through the lattice as an interstitial atom. If it still has sufficient energy, it can create further defects along its path through the lattice or it loses its energy through ionization. Since non-ionizing interactions dominate at low energies, clusters of disordered atoms are formed at the end of the PKA's track. These regions are therefore called cluster defects.

In the energy-band model lattice defects appear as additional energy levels in the band gap and change the electrical properties of the detector. Detailed information about defect formation in silicon and measurements of the energy levels can be found e.g. in [Jun11].

The energy that a traversing particle loses due to displacement of lattice atoms is called non-ionizing energy loss (NIEL). The particle creates damage in the crystal lattice and the NIEL-scaling hypothesis states that the damage increases linearly with the deposited displacement energy [SBD⁺87]. Since most of the energy of the particle is transferred to the primary knock-on atom, the PKA can also create further damage in the silicon lattice. However, this additional damage is independent of the type of the primary particle and its interaction process.

The Lindhard partition function $P(E_R)$ analytically describes the energy loss in non-ionizing processes (like displacement) by a recoiling nucleus of energy E_R . It can be used to calculate the non-ionizing energy loss of different particles in silicon. The displacement damage cross section $D(E)$ expresses the relative displacement efficacy of an impinging particle with energy E , taking into account the various types of interactions between the particle and the silicon lattice atom. It is defined by [VG89]:

$$D(E) = \sum_{\nu} \sigma_{\nu}(E) \int_{E_d}^{E_R^{\max}} f_{\nu}(E, E_R) P(E_R) dE_R \quad (3.4)$$

where the sum is over all possible interactions. The possible reaction by a particle ν is described by the cross section σ_{ν} . The probability to create a PKA due to this reaction is $f_{\nu}(E, E_R)$ depending on the particle energy E and the energy of the recoiling nucleus E_R . The lower bound of the integral E_d is the minimum energy required for displacement of a lattice atom (25 eV in silicon).

A detailed description of the NIEL-scaling hypothesis is given in [Mol99].

In order to be able to compare the damage inflicted by different types of particles at different energies the damage caused by 1 MeV neutrons is taken as reference and the damage

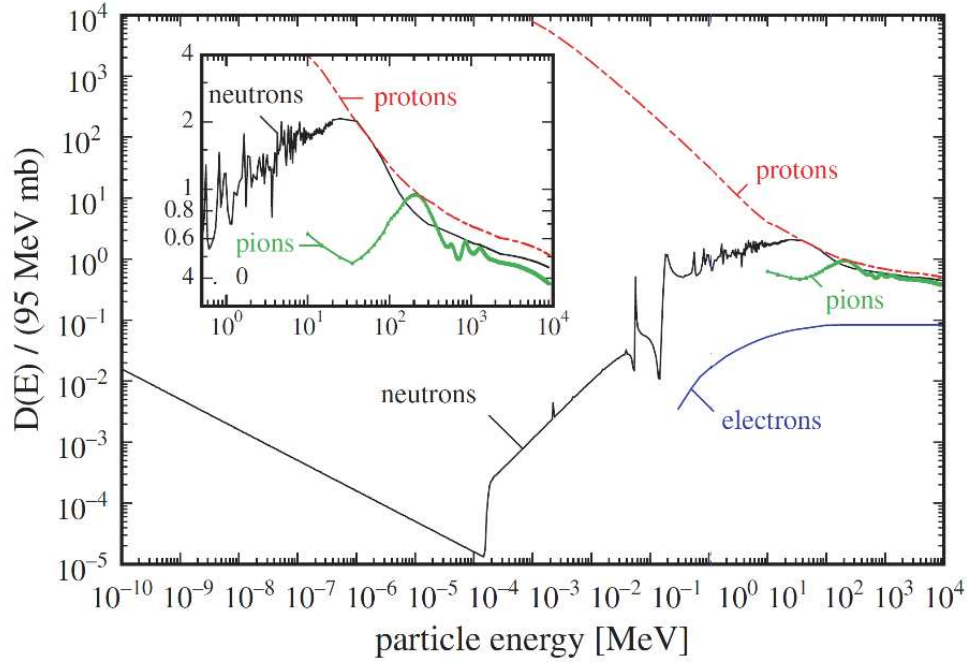


Figure 3.9: Displacement damage functions $D(E)$ for neutrons, protons, pions and electrons in silicon normalized to 95 MeV mb for 1 MeV neutrons. The ordinate therefore represents the damage which is equivalent to 1 MeV neutrons [Lino3].

caused by other particles is scaled to that value. The necessary scaling factor is called hardness factor κ and is defined as follows:

$$\kappa = \frac{\int D(E) F(E) dE}{D(E_n = 1 \text{ MeV}) \int F(E) dE} \quad (3.5)$$

where $D(E_n = 1 \text{ MeV}) = 95 \text{ MeV mb}$. The damage at a given fluence of one particle type can now be compared to the damage done by the corresponding fluence of 1 MeV neutrons and the fluence scaled to 1 MeV neutrons is called the 1 MeV neutron equivalent fluence, F_{eq} :

$$F_{eq} = \kappa \times F = \kappa \times \int F(E) dE \quad (3.6)$$

All given fluences are typically corrected with the hardness factor and stated as 1 MeV neutron equivalent fluences to ensure comparability.

The damage caused by different particle types depending on their energy is shown in figure 3.9. While high energy particles tend to create the same damage, the damage done by low energy protons is much higher than the damage by low energy neutrons.

As already mentioned before radiation damage influences the properties of a silicon particle detector and degrades its performance. It is therefore necessary to study the detector behaviour in an irradiated state. To inflict radiation damage comparable to several years of operation at a high energy particle physics experiment the detector is deliberately irradiated to the expected total particle fluence within a short period of time, typically minutes or hours. This accelerated irradiation is either performed with protons from a particle accelerator or neutrons from a research reactor.

The defects created in the lattice of a silicon particle detector during irradiation are not stable in position and time. While they move through the lattice they can both repair existing defects and recombine with other defects to form new ones. This effect is called annealing.

Since the movement of the defects is highly temperature-dependent they are almost frozen at temperatures below -20°C and thus irradiated samples always have to be stored cold in order to prevent unwanted changes of the sensor properties. In contrast, the annealing processes are strongly accelerated at higher temperatures.

Detailed information about the effects of annealing in silicon sensors can be found in [\[Mol99\]](#).

Part II

MODULE PRODUCTION FOR THE CMS PIXEL PHASE I
UPGRADE

OVERVIEW OF THE CMS PHASE I PIXEL DETECTOR

During the last eight years since the startup of the LHC the pixel detector has shown to be an important part of the CMS experiment. Practically all physics analyses depend on its excellent performance in providing high resolution measurements of the first three space points of the trajectories of charged particles coming from the interaction point inside CMS [Mei14]. The single hit efficiency has been above 99% in the last years and dynamic data loss resulting from buffer overflows in the readout chips (ROCs) will stay below 4% in the innermost layer and even less in the outer ones when running at the design luminosity of $\mathcal{L} = 1 \cdot 10^{34} \text{ cm}^{-2} \text{ s}^{-1}$ [DAA⁺12].

However, the performance of the LHC has also been extraordinary in the last years and some of its design parameters have already been surpassed as shown in section 2.1.1 while further increases are planned for the upcoming years. Since the pixel detector is situated closest to the interaction point, it is most affected by the increase in luminosity and pile-up and its currently high performance will degrade significantly. The current goal of the LHC is to reach twice the design luminosity in the years before 2023 when the machine is shut down for the installation of the HL-LHC upgrades.

The result of both simulations and characterizations of the current readout chip is that such high luminosities would bring the dynamic inefficiencies of the ROCs in the innermost layer to an unacceptable value of 16% [DAA⁺12]. These data losses are mostly attributed to the dead time of the double column drain mechanism and to the insufficient sizes of the data buffers which are needed to store the hit information during the Level 1 trigger latency time and they inevitably lead to decreased tracking efficiency. At the same time higher pile-up leads to higher misidentification rates in track finding because pattern recognition becomes more complicated at higher occupancies.

In order to keep the current performance levels even when the running conditions pose harsher challenges to the detector, the CMS collaboration has decided to replace the pixel detector with a completely new version during an extended technical stop at the beginning of the year 2017. This decision has been made although most of the inefficiencies of the current detector can be attributed to only the readout chip, but a replacement of the ROC would at least have required a replacement of all 1440 detector modules since it is an integral part of the modules. The necessary replacement of the modules offered the opportunity to simultaneously improve the mechanics and cooling of the pixel detector. Building a completely new detector also has the advantage to be able to commission and test it before installation and the current detector can be preserved as spare if anything unforeseen happens during installation.

New requirements based on comprehensive simulations and predictions of future running conditions have been drawn up by the collaboration and thus practically all parts of the detector have either been revised or completely redesigned to be able to fulfil the goals like reducing the dead time of the readout chip, addition of a new barrel layer and endcap disks, and reducing the material budget in the active volume of the tracker [EBH⁺10].

The mechanical layout of the new CMS pixel detector is presented in the next section. It is followed by a description of the Phase I Barrel Pixel Module, the basic unit of the barrel pixel detector. Details on both construction and testing of these modules are given in the next chapters of this thesis.

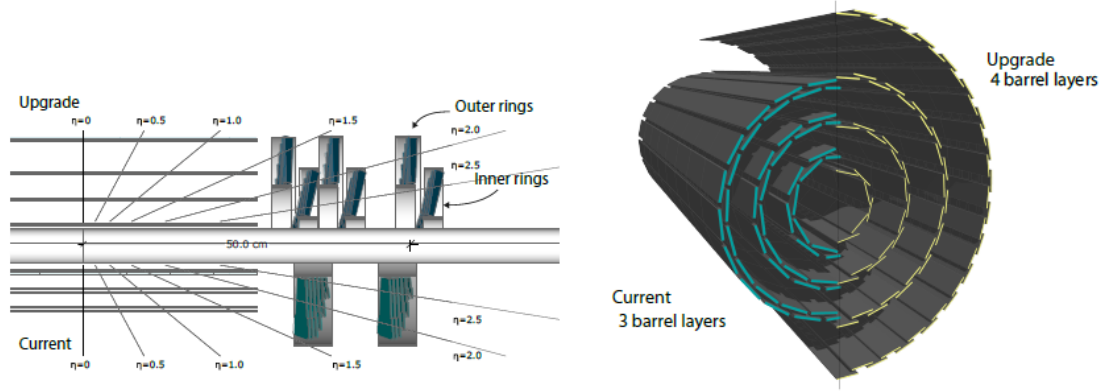


Figure 4.1: Comparison of the layouts of the current and the new Phase I pixel detector. Only one quarter of each is shown since the layouts are point-symmetric to the interaction point [DAA⁺12].
 Left: The Phase I detector features an additional fourth barrel layer and an additional third endcap disk to provide full four-hit coverage up to high pseudorapidities of $|\eta| = 2.5$.
 Right: The new detector layout moves the innermost barrel layer closer to the new beam pipe and the interaction point to improve secondary vertex resolution while placing the new fourth layer into previously unoccupied space in between the pixel and the strip detector.

4.1 THE PHASE I PIXEL DETECTOR

A comparison of the layouts of the current and the new Phase I pixel detector is shown in figure 4.1. The most obvious differences are the additions of both a fourth barrel layer and a third endcap disk at each end but also other adjustments are made. The innermost barrel layer is moved closer to the beam pipe and the interaction point. This improves the resolution of secondary vertices from particles like b quarks and at the same time gives better separation power for vertices from high pile-up events. This move to a radius of 30 mm is only possible because a new beryllium beam pipe with significantly smaller outer radius (22.5 mm compared to 30 mm before) has already been installed in CMS during Long Shutdown 1 in 2013/2014 and CMS is now able to profit from it.

The new fourth barrel layer is placed at a large radius of 160 mm in previously unused space between the pixel and the strip tracker. At this distance the new layer is able to contribute best to the track finding by limiting the extrapolation distance to the first layer of the silicon strip detector. At the same time it can serve as a backup for the first layer of the strip detector should the performance of the strip modules degrade faster than expected in the coming years, since a repair or replacement of those modules is not possible due to lack of access.

An additional third disk is installed at each end of the detector in areas which have already been reserved for a third disk during construction of the first pixel detector, but due to tight schedules and budgetary reasons these disks have not been built and installed eight years ago. All necessary power cables and readout fibres therefore exist and just need to be connected. Hence one of those areas has been chosen for the installation of the so-called Phase I Pixel Pilot Blade system which consists of a spare half-disk equipped with four modules in the new design with the new digital readout chip [Akg15]. The Pilot Blade system was installed during Long Shutdown 1 and allows concurrent running and testing of the new digital chip and all associated back-end electronics under realistic operating conditions. At the same time it is used to test the integration of the new Phase I pixel detector into the CMS experiment as a whole, especially into the central data acquisition system (DAQ), the data quality monitoring (DQM) and the detector control system (DCS).

The following sections and chapters focus on the barrel part (BPIX) of the Phase I pixel detector. A further description of the forward detector (FPix) is omitted since it is not within the

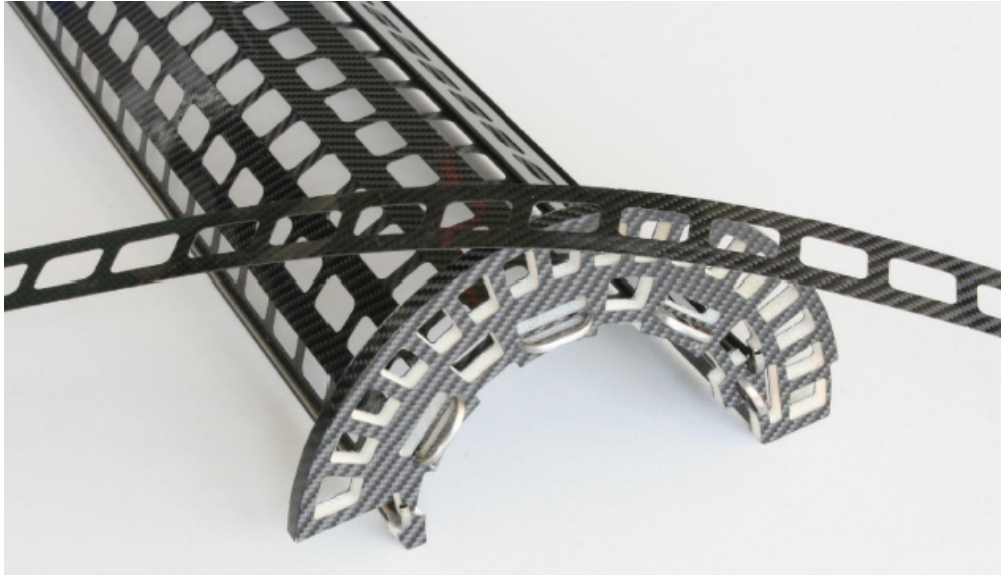


Figure 4.2: Prototype of the new ultra-lightweight BPIX Layer 1 support structure. The ends of the stainless steel cooling pipes are visible protruding from the end-flange made from an Airex foam-carbon fibre sandwich. The facets in the back are glued to the cooling tubes and used to mount the detector modules with small screws. A bare carbon fibre facet with cut-outs to save material is shown lying on the structure. The total mass of the complete structure is only 55 g [DAA⁺12].

scope of this thesis. Detailed information about the upgrade of the FPIX detector can be found in [DAA⁺12].

4.1.1 BPIX MECHANICS AND COOLING

The skeleton of the mechanical structure of the barrel pixel detector layers is formed by the cooling loops made from thin stainless steel pipes running parallel to the beam pipe along the full length of the barrel. These tubes have an outer diameter of only 2 mm with a wall thickness of 100 μm and are held in place by attached end-flanges made from a sandwich structure of Airex foam covered with carbon fibre. Facets also made from carbon fibre with a thickness of 200 μm are glued to the cooling pipes and used to support the modules. Figure 4.2 shows an early prototype of the BPIX Layer 1 support structure.

Each facet is glued to two cooling pipes running in grooves to maximize the surface area available for cooling and the modules are mounted in the same way as in the current detector. Small nuts are glued into holes in the facets and the modules are then screwed down to the facets. Unnecessary material not needed to support the modules is milled away to reduce the mass. This ultra-lightweight construction principle leads to a total mass of the pictured prototype of only 55 g.

The new detector is cooled with an evaporative (or two-phase) CO_2 cooling system which replaces the old mono-phase fluorocarbon system relying just on the heat capacity of C_6F_{14} . Two-phase CO_2 cooling systems have a much higher cooling power compared to older mono-phase systems by taking advantage of the phase transition between liquid and gaseous state and the associated enthalpy of evaporation. This becomes visible by comparing the required energy of 282 J to evaporate one gram of CO_2 with the heat capacity of C_6F_{14} which is only 1.1 J/(g · K) [3M 00]. Therefore the required mass flow to remove a certain amount of heat is drastically decreased and allows the usage of much smaller cooling pipes which contribute less

to the total material budget of the detector. At the same time lower operation temperatures become possible which are beneficial for the lifetime of the new detector.

An additional advantage of CO₂ cooling is the fact that evaporation takes place at much higher pressures compared to other two-phase refrigerants [VCo9]. The high vapour pressure causes the volume of vapour created during cooling to stay low because it is highly compressed and thus makes it flow more easily through small channels. The evaporation temperature is also more stable because the comparatively low pressure drop in the tubing has only a limited effect on the boiling pressure. Last but not least CO₂ has a factor 5000 less global warming potential compared to C₆F₁₄ and is also about 100 times cheaper to source [Int14].

The Phase I pixel detector will not be the first implementation of CO₂ cooling in particle physics. Both the LHCb experiment [LHC] at the LHC and the Alpha Magnetic Spectrometer (AMS-02) experiment [AMS] at the International Space Station cool their silicon trackers with CO₂ and the two systems have proven their performance and reliability in the last years [A+13]. Nevertheless it will be a first for the CMS collaboration and therefore the collaboration has decided to install the new cooling plants already during Long Shutdown 1. They are connected to dummy heat loads and run regularly to gain operation experience before the installation of the new detector. In normal operation the two identical but independent cooling plants are connected to the BPIX and FPIX subdetectors respectively to be able to use different temperature setpoints while in case of failure or maintenance both subdetectors can still be cooled with only one plant.

4.1.2 MATERIAL BUDGET

The addition of a fourth barrel layer and a third endcap disk at each end could easily increase the total material of the pixel detector inside the tracking volume of CMS and with it the probability for multiple scattering of the particle tracks emerging from the interaction point. It was therefore an important goal of the Pixel Phase I upgrade to redesign both the detector and its services like power supply to be lighter than the current system. For the detector itself this resulted in a new ultra-lightweight support structure described above and in a special design of the modules which will be used in the innermost layer (see section 4.2 for details). The new CO₂ cooling system with its smaller cooling pipes and reduced mass flow forms an integral part of the support structure and is one of the main contributions to the reduced material budget.

Another important point is the relocation of services. New longer twisted-pair cables for both data and power distribution allow the connectors and electronics boards to be placed at regions outside the active tracking volume.

The expected results of all these efforts are visible in the plots in figure 4.3. They show a simulated comparison of the material budgets of the current and the new Phase I pixel detector. While the material budget practically stays the same in the barrel region despite adding a fourth layer it is reduced by a factor of up to two in the forward regions above $|\eta| = 1.2$. The relocation of passive services to regions outside the active volume is also clearly recognizable in the shaded bands at $|\eta| \geq 2.5$ where the new detector has a higher material budget than the current one.

Table 4.1 shows a comparison of the total material masses in the simulations of the current and the Phase I pixel detector. Since the relocation of services to areas further out alongside the beam pipe, the masses are given for limited ranges of η and regions outside the active tracking volume have been omitted.

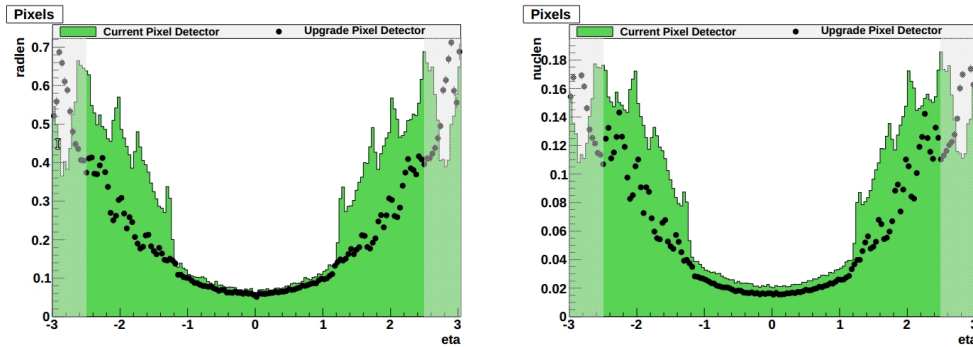


Figure 4.3: Material budget simulation of the CMS pixel detector as a function of pseudorapidity η . The green histogram is the data for the current pixel detector while the black points represent the new Phase I pixel detector. The left plot shows the amount of material in units of radiation length (radlen) and the right plot in units of nuclear interaction length (nuclen). The shaded bands at $|\eta| \geq 2.5$ denote regions outside the active tracker volume. The effort to decrease the amount of material is clearly visible in the regions above $|\eta| = 1.2$ from where services like electronics boards and power supply have been moved further out [DAA⁺12].

Table 4.1: Comparison of the simulated total material weight for both the barrel pixel and forward pixel detector. The ultra-lightweight support structure combined with CO₂ cooling leads to a drastic mass reduction especially in the barrel part of the new detector [DAA⁺12].

Volume	Mass (g)		Difference
	Current detector	Phase I detector	
Barrel pixel ($ \eta < 2.16$)	16801	6686	-60 %
Forward pixel ($ \eta < 2.5$)	8582	7040	-18 %

4.1.3 SERVICES AND READOUT

As already mentioned at the beginning of this chapter the Phase I pixel detector will feature an additional fourth barrel layer and new third endcap disks at each end. These changes increase the active area which has to be equipped with modules and therefore also the number of channels which have to be read out. While the current detector has 66 million pixels the new one comprises 124 million (a plus of 88 %). Since the CMS Pixel Phase I upgrade is designed as a drop-in replacement which is to be installed in a relatively short time of three months during an extended technical stop at the beginning of 2017 most of the services available from and to the outside of CMS cannot be changed and have instead to be reused. This is especially true for the power cables and the optical data fibres.

The cables now have to supply a detector with nearly twice the size than before whereupon the usage of the same powering scheme is impossible since the increased currents would lead to a very high voltage drop and power loss in the cables. Instead a higher voltage is supplied and converted to the required operating voltages by custom designed DC-DC buck converter boards which are located on the detector supply tube just outside the active volume [FFF⁺13]. Like all other electronic components which are placed on the supply tube the DC-DC converter ASIC has to be highly radiation hard and also SEU¹ safe because of the high dose of ionizing radiation in the area from glancing collisions [MAB⁺12].

Also the available optical fibres have to transmit the data of the much larger detector which is additionally subjected to higher particle rates. This is only possible by changing the transmission scheme from a 40 MHz analog level encoded output to a 400 MHz digital output. The new

¹ Abbreviation for Single Event Upset: change of state caused by one single ionizing particle, e.g. in memory cells.

digital readout chips deliver differential electrical signals to the Pixel Optical Hybrids (POHs) located on the supply tube which convert and send the signals over the optical fibres to the Front-end Drivers (FEDs) in the service cavern next to the CMS experiment.

A notable exception is the cooling system which requires completely new tubing due to the change to CO₂ as coolant. The new pipes have already been routed up to the patch panels in CMS during Long Shutdown 1 and only the short distances between the patch panels at each end and the pixel detector have to be connected at the time of installation.

To conclude a comparison of some important numbers for the current and the new Phase I pixel detector is given in table 4.2. It becomes clear that the new detector features nearly twice as many channels as the current one while at the same time construction has been significantly eased by the reduction of necessary module types.

Table 4.2: Comparison of important numbers for the current and the new Phase I pixel detector. The new detector features nearly twice as many channels but consists of much fewer module types which eases construction [DAA⁺12].

	Current detector	Phase I detector	Difference	
Barrel pixel	No. of layers	3	4	+33 %
	Readout channels	48 m	79 m	+65 %
	No. of modules	768	1184	+54 %
	Module types	2	1	-50 %
Forward pixel	No. of endcap disks	2	3	+50 %
	Readout channels	18 m	45 m	+150 %
	No. of modules	672	672	
	Module types	5	1	-80 %
Readout (data encoding)	analog	digital		
Cooling	C ₆ F ₁₄ , mono-phase	CO ₂ , evaporative		

4.2 THE PHASE I BARREL PIXEL MODULE

An exploded view of the basic component of the new barrel pixel detector, the Phase I Barrel Pixel Module, is shown in figure 4.4. The module has a size of 66 mm × 22 mm. Compared to the current one it has exactly the same length but is slightly wider because the new digital readout chips have a larger periphery due to the increased data buffers and thus are longer. The complete barrel detector is equipped with 1184 of these modules. Including spares this requires a production of at least 1400 good modules.

The Phase I barrel pixel module consists of several parts which are described shortly beginning from the bottom. More detailed information is given in the following chapters.

BASE STRIPS: A pair of base strips made from silicon nitride (Si₃N₄) is glued to the bottom side of the readout chips (ROCs). Each base strip has three ears with small holes which protrude from the module and are used to screw the module to the carbon fibre facets of the support structure. Silicon nitride has been chosen to avoid mechanical stress in the module due to thermal expansion because it has a coefficient of thermal expansion (CTE) close to that of pure silicon which is the base material of both the ROCs and the sensor. Since the base strips form the only contact to the support structure and cooling it is important to have a good glue joint to ensure the required heat transfer.

READOUT CHIPS: The sixteen readout chips are bump-bonded to the silicon sensor to be able to readout the signals created by traversing particles. Bump-bonding is a well established connection technique in electronics where solder ball diameters around $70\ \mu\text{m}$ are used to connect packaged ASICs to PCB traces. Such diameters are obviously incompatible with the pixel pitches used in CMS and therefore the processes had to be adapted. In a first step (the bump placement) small solder spheres with a diameter of less than $30\ \mu\text{m}$ are either chemically grown or mechanically placed on the bump-bond pads of the ROC. Afterwards the electrical and mechanical connection to the pads of the individual pixels is done by aligning the ROCs to the sensor and pushing down with a certain force and temperature (the bonding). Finally the completed sandwich is placed in an oven and heated up to above the melting temperature of the solder. This so-called reflow process leads to better aligned and stronger connections due to better wetting of the pads.

In order to be able to connect the ROCs to the readout electronics they are equipped with additional wire bonding pads which are placed at the outer edge and thus protrude from the silicon sensor-ROC sandwich. Wire bonding, another connection technique known from electronics packaging, is used to connect the pads to those on the high density interconnect (HDI) on top of the module. In this process thin aluminum wire with a diameter of $25\ \mu\text{m}$ is welded to the pads at each end using ultrasonic power and force.

SILICON SENSOR: The pixel sensor forms the sensitive element of the module where the signals are created by the traversing particles. It is a 2D-segmented position-sensitive silicon particle sensor as already described in section 3.3. It has 66560 pixels in total and is divided into sixteen fields (2×8) with 4160 pixels each which are bump-bonded to the individual ROCs.

HIGH DENSITY INTERCONNECT: The HDI is a very thin flexible PCB glued to the back-plane of the sensor. It contains the necessary traces to distribute power, clock and trigger signals to each ROC via wire bonds and at the same time routes their data lines back to the token bit manager (TBM) ASIC. The TBM consists of two independent cores of which each one is controlling the readout sequence of the eight ROCs on one half of the module [Bar15]. Their data output is then multiplexed into one 400 MHz stream and sent out as a differential electrical signal to the optical hybrids on the supply tube via a twisted-pair cable. The same cable is used to deliver power and control signals to the module.

The Phase I Barrel Pixel Module for the innermost layer 1 differs in several points from the one described above. Due to the expected high occupancy close to the interaction point it uses a different readout chip called PROC600, which evolved from the ROC and features a new dynamic cluster column drain mechanism better suited for the high rate environment [Hor16]. A different HDI with the provision to mount two TBMs enables an increase in the available bandwidth for sending out hit data. There is also no space on the mechanical support structure to mount the modules with base strips and screws since the width of the facets is too small to fit such modules. Instead the modules are put directly on the facets with the back side of the ROCs and clamped at the ends with small carbon fibre clips which are in turn screwed down in the gaps between the modules along the beam axis. The omission of the base strips also reduces the amount of material used in the first layer. An additional reduction is achieved by thinning down the PROC600 to a thickness of only $75\ \mu\text{m}$ compared to the $175\ \mu\text{m}$ thick ROCs used in the outer three layers [DAA⁺12].

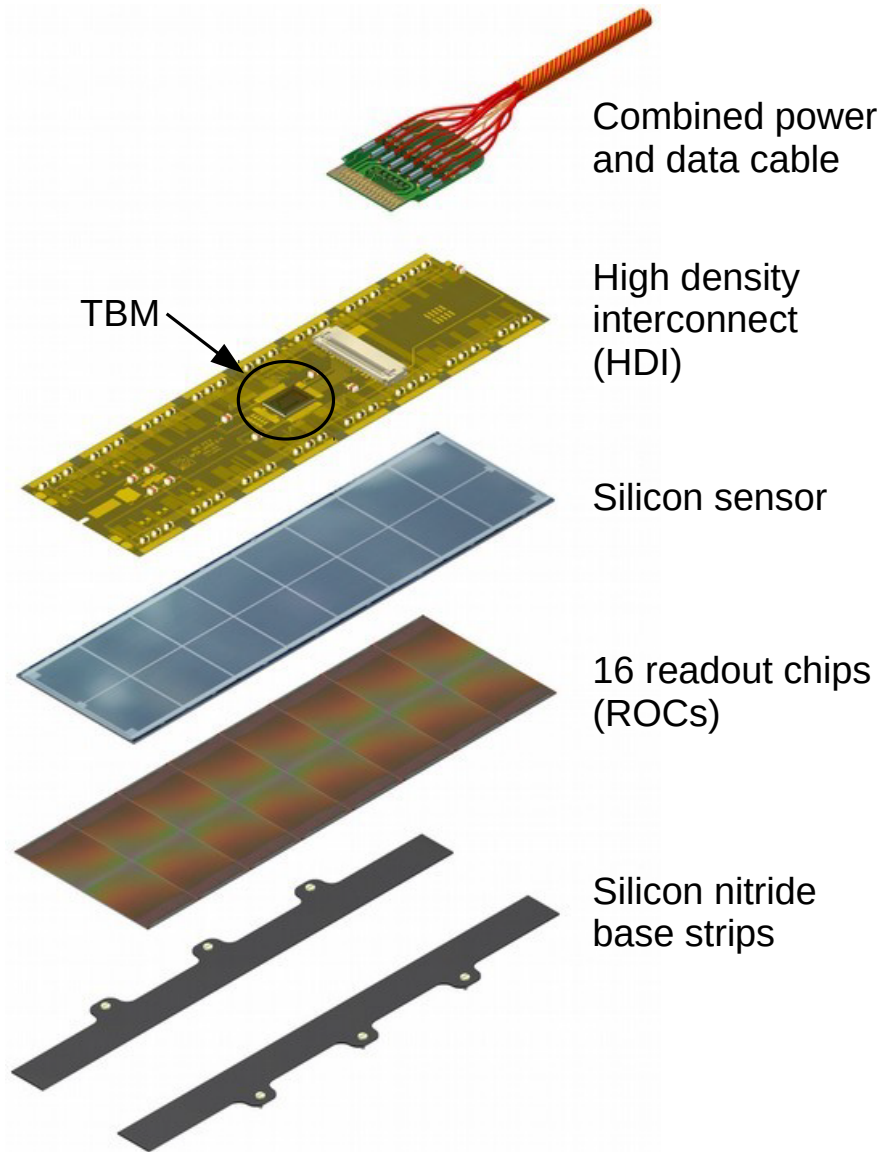


Figure 4.4: Exploded view of the Phase I Barrel Pixel Module for the detector layers 2 to 4. This is the basic component of the new barrel pixel detector and consists of multiple parts which are from bottom up: two silicon nitride base strips used for mounting the module to the support structure, 16 readout chips bump-bonded to the silicon sensor (the active part of the module) and the high density interconnect (HDI), a very thin flexible PCB connecting the ROCs to the token bit manager ASIC (TBM) which controls the readout sequence. A single twisted-pair cable connects the module to the outside world [Erd15].

SENSOR TESTING

The silicon pixel sensor is the sensitive and therefore essential part of the Phase I Barrel Pixel Module described in section 4.2. Due to the relatively short time between the decision to replace the pixel detector and the start of the module production and the high radiation hardness of the sensors currently used in CMS the choice has been made to use the same sensor layout again for the production of the new detector [RBC⁺04].

Redesigning the sensor with e.g. smaller pixels to achieve higher granularity would also have implied a complete redesign of the readout chip since each sensor pixel must be connected to its readout logic in the so-called pixel unit cell of the ROC. This analog circuit requires a certain floor space and cannot easily be changed in size. Additionally the characteristics of the new sensor would have to be verified in detailed testing campaigns of both prototypes and the final sensor including laboratory measurements and beam tests.

The complete design and verification process of a new silicon sensor requires several years which were not available for the upcoming Phase I upgrade but are unavoidable for the future Phase II upgrade since the requirements of the HL-LHC environment can only be met with completely new sensor designs. Work on first sensor prototypes and also a new readout chip has thus already started in 2014 [Sch16], [CGS13].

5.1 THE BARREL PIXEL SILICON SENSOR

As already mentioned above the decision has been taken to reuse the existing sensor design, made by Paul Scherrer Institut (PSI) in Switzerland for the current detector, also for production of the new sensors required for the Phase I pixel detector. This decision directly implied to award the actual production of the new sensor wafers to the same company that already did the production of the currently used sensors, CiS Forschungsinstitut für Mikrosensorik GmbH, since other possible vendors would have needed to be qualified first and the required time for such detailed qualifications was not available. Additionally only CiS is able to reuse their original production photolithography mask set and thus avoided additional costs for the production of new masks.

A picture of the production wafer is shown in figure 5.1. The wafer is four inches (or about 10 cm) in diameter and holds three large pixel sensors suitable for modules. The additional space available is filled with ten smaller sensors usable for single chip assemblies (SCAs) with only one ROC, a double sensor for two ROCs, several diodes and a set of special test structures for process control. Especially the SCA sensors are extremely important since they provide an easy method to create test samples for the evaluation of both sensor and readout chip characteristics. After bump-bonding such samples can just be glued and wire-bonded to small PCBs and connected to the readout electronics without the overhead which is needed for building a full module with HDI and TBM. Examples of important results obtained with such single chip assemblies can be found in [Spa16].

The large sensor for the pixel modules is $66.6 \times 18.6 \text{ mm}^2$ in size and has an active area of $64.8 \times 16.2 \text{ mm}^2$ with 66560 pixels, divided into 16 regions with 4160 pixels each. This segmentation is also visible in the rightmost sensor in figure 5.1. It is produced in an n⁺-in-n technology using n-doped wafers with a thickness of 285 μm sourced from Topsil as bulk ma-

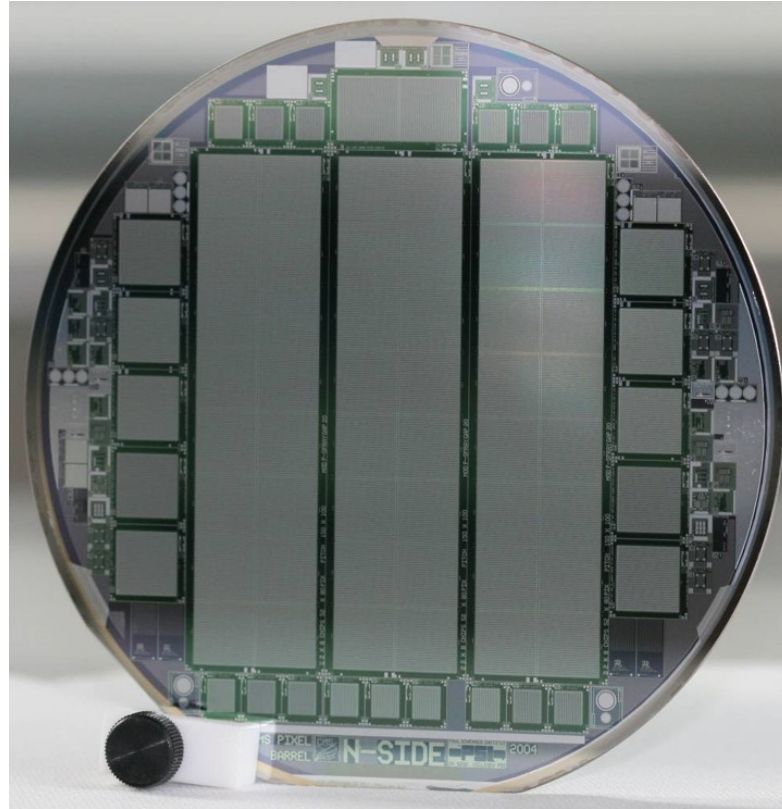


Figure 5.1: CMS wafer with three large pixel sensors for detector modules, designed at PSI and produced by CiS GmbH. The diameter of the wafer is four inches. Additional space around the sensors is filled with ten smaller sensors which are used for single chip assemblies with only one ROC, a double sensor for two ROCs, several diodes and dedicated test structures for process control [Roh13].

material and highly doped n^+ implants. The necessary pn-junction is formed between the bulk and the uniformly p-doped backside [DAA⁺12].

The n^+ -in-n design allows to collect electrons which have a higher mobility compared to holes. This is advantageous because of shorter charge collection times and larger Lorentz drift which results in better charge sharing as described in section 3.3. It also makes the electrons less prone to trapping caused by radiation damage and thus yields higher signals after high irradiation fluences or long LHC run-times. Radiation damage also leads to the effect of type inversion in the n-doped bulk which causes the sensor to deplete from the implant side as opposed to the back side pn-junction before irradiation [PCH⁺92]. This behaviour guarantees a long sensor lifetime by enabling operation in the under-depleted mode.

The usage of n-doped bulk material requires double sided photolithographic processing of the sensor wafers which leads to higher costs compared to single sided sensors made in p-in-n (or n-in-p) technology but also has some advantages like the possibility to add the guard ring scheme to the backside of the sensor which keeps all cutting edges at ground potential. This simplifies the module design and increases the electric strength of the assembled sensor-ROC sandwich because high voltage sparking between sensor and ROCs becomes impossible. Otherwise such sparks could destroy the sensitive electronics in the readout chips [DAA⁺12].

The pixel size of $150\ \mu\text{m} \times 100\ \mu\text{m}$ is optimized for maximum spatial resolution in the magnetic field of CMS. As described in section 3.3 the signal charge is spread among multiple pixels due to the Lorentz force which lets the charge carriers drift under an angle, the Lorentz angle. In CMS this angle is about 22° and together with the sensor thickness of $285\ \mu\text{m}$ it can

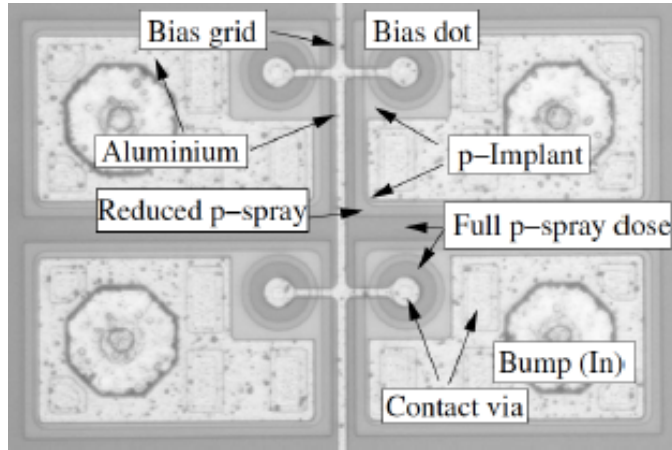


Figure 5.2: Arrangement of four pixels from the CMS pixel sensor. The photographed region is about $300 \times 200 \mu\text{m}^2$ in size. The n^+ -implants of the pixels with the bump bond pads for connection to the readout chip and the bias grid required for testing the sensor before bump-bonding are clearly visible [DAA⁺12].

be calculated that the optimal charge sharing between only two pixels is achieved best with a pitch of $100 \mu\text{m}$ in $r\phi$ -direction [Erd10]. On the other hand the pitch in the other dimension is mostly dictated by the required floor space of the electronics in the pixel cell of the ROC.

As mentioned above the sensor is divided into 16 regions for connection to 16 separate readout chips. Since each ROC has an inactive edge surrounding the matrix of 4160 pixel cells the required surface area on the sensor for bonding is a little bit larger than expected from just the pixel size. Thus the size of the sensor had to be adjusted accordingly and in order not to create inactive areas at the region borders during that process the pixels along the borders have been increased to twice the size ($300 \times 100 \mu\text{m}^2$ or $150 \times 200 \mu\text{m}^2$) and those in the corners to even four times the size ($300 \times 200 \mu\text{m}^2$) of regular ones.

The isolation of the individual pixel implants is implemented by surrounding each one with a so-called moderated p-spray structure. A special punch through biasing grid allows the biasing of the sensor even without having a ROC bump-bonded to it. This is essential for the sensor quality testing done before bump-bonding which is described in the next section. A highly magnified picture of an arrangement of four pixels from the CMS pixel sensor is shown in figure 5.2.

5.2 TESTING METHOD AND EQUIPMENT

To avoid using bad silicon sensors for production of Barrel Pixel Modules or, more accurately, for bump-bonding of sensors with readout chips, the delivered sensors have to be tested beforehand. Only known good material should be bump-bonded since the process is expensive and also time-consuming and the used ROCs cannot be reclaimed if the sensor is found bad after bonding.

5.2.1 CURRENT-VOLTAGE (IV) MEASUREMENT

For the production of the Phase I Barrel Pixel Modules it has been decided to use only one basic but very reliable measurement method known from semiconductor industry to determine the quality of the sensors, namely the measurement of the leakage current and its dependence on the applied bias voltage. It is also known as IV measurement and for standard silicon sensors it is performed by applying high voltage to the sensor backplane while connecting the bias ring on the top side to ground via a high resolution ampere meter. The connection scheme

is slightly different for the CMS pixel sensor due to its double sided processing and will be shown later. This type of measurement also exactly corresponds to the later operation mode of the sensor inside the detector.

5.2.2 IEKP PROBE STATION

The IV measurement described above is performed on one of the two probe stations available at IEKP. These stations have been designed and built by members of the institute using both commercially available components like measurement devices and specially manufactured parts like chuck and housing. They provide a comprehensive set of measurement techniques also used in semiconductor industry.

Samples are placed on the chuck which is equipped with a cooling system based on Peltier elements and allows measurements in a temperature range from -25°C to $+30^{\circ}\text{C}$. It is mounted on a set of motor stages providing three-dimensional movement. Fixation of the samples is provided by small vacuum holes in the chuck surface. Up to four probe needles with a tip diameter of only $2\ \mu\text{m}$ mounted on special micro manipulators can be placed at the same time on different sensor pads to connect them to the measurement devices. A stereo microscope with high magnification and attached camera with LCD screen support the operator when placing the needles. Everything is set up in an electrically shielded dark box since any light shining on a silicon detector sample creates unwanted charge carriers and thus increases the leakage current.

Outside the box the measurement devices are placed in a rack. Essentially these are a Keithley 2410 high voltage supply (up to 1100 V), a Keithley 6485 ampere meter (down to 100 fA) and an Agilent 4284A LCR meter for capacitance measurements. In between the probe needles and the devices there is a purpose-built relay-based switching matrix which implements all possible measurements by routing the voltages and signals to the correct devices.

All components are controlled by a GUI-based software written with National Instruments LabVIEW [Nat16a]. It handles temperature and movement of the chuck, relay settings, read-out of the measurement devices and visualization and saving of the data while the operator only has to select one of the predefined measurements and enter the related parameters. The acquired data is additionally stored in a MySQL database on an IEKP server from where it can be retrieved and plotted afterwards either via a web-based graphical front end or by special analysis tools directly accessing the database.

A detailed description of the probe station, its components and available measurements can be found in [Hof13] and [Erf09]. The structure of the IEKP measurement database and its graphical front end are documented in [Ebe13].

The required setup to perform the IV measurement on CMS pixel sensors is shown in figure 5.3. As mentioned before the connection scheme is different from standard silicon sensors due to the double sided processing. The three sensors from one wafer are placed on a special isolating chuck made from polytetrafluoroethylene (better known as Teflon®) which is put on top of the normal metal chuck of the probe station to avoid short circuits on the implant side of the sensors. The Teflon chuck also has small vacuum holes to hold the sensors in place when the needles are placed on the pads.

Both bias voltage and ground potential are connected on the same side of the sensor since the guard ring structure visible in the right picture of figure 5.3 confines the high voltage to the pixel matrix and the ground is fed to the bias ring on the implant side via the cutting edges of the sensor. The bias ring itself is directly connected to the bias grid shown in figure 5.2.

5.3 MEASUREMENT RESULTS

After the production of a new wafer batch at CiS the IV characteristic of every large pixel sensor is directly measured by the company to determine the quality of the wafers. According to the

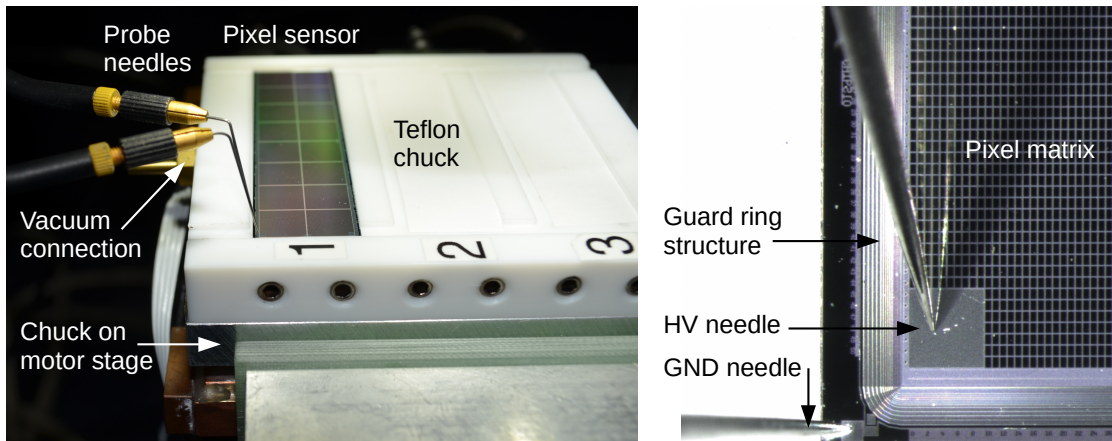


Figure 5.3: IV measurement setup in the IEKP probe station for CMS pixel sensors [Rie14].

Left: Up to three sensors can be placed on the special insulating Teflon jig where they are held in place by vacuum. Two probe needles connect one sensor at a time to the measurement devices.

Right: Highly magnified microscope picture of one corner of the pixel sensor. The high voltage and ground pads of the sensor are connected with probe needles. They are separated by the guard ring structure.

purchasing contract only wafers with a minimum of two good sensors are accepted and paid by the CMS collaboration. As a special incentive to deliver high quality wafers the remuneration of wafers with three good sensors is increased by 17% compared to the expected 1.5-times the price of wafers with only two good sensors.

This purchasing strategy was chosen due to the next step in module production. In order to make the solder balls from the bump-bonding form a good intermetallic connection with the aluminum sensor pads a special under-bump metallization (UBM) needs to be applied on the sensor and this is done in an electroless process by submerging the wafers in different chemical baths. This process has to be paid per wafer since it does not distinguish between good and bad sensors and therefore it would be uneconomical to use wafers with only one good sensor. A side effect of this strategy is the fact that the real number of wafers processed and measured by CiS is not disclosed to the CMS collaboration.

After the initial measurements at CiS the wafers meeting the CMS acceptance criteria are sent to the company chosen for application of the under-bump metallization. In most cases the same company is also contracted to cut the wafers and pick the three pixel sensors and other parts into special transport boxes. After the final shipment to the production centers another IV measurement on the sensors is performed to check for handling errors during chemical processing or cutting or for problems which have occurred during transportation. The results of those measurements determine the sensors which are used for bump-bonding. At KIT it has been decided to remeasure the IV characteristics of all sensors including the ones already classified bad by CiS since first measurement results have shown that some sensors regain a better classification after the second measurement at IEKP. Hence such sensors have been used for bump-bonding.

5.3.1 SENSOR ACCEPTANCE AND CLASSIFICATION CRITERIA

The criteria for both acceptance of CiS sensor wafers by the CMS collaboration and later classification of cut bare sensors after UBM application are defined in the Technical Design Report for the Pixel Upgrade [DAA⁺12]. They are reproduced here:

LEAKAGE CURRENT: The leakage current of a good sensor at the planned operation voltage of -150 V needs to be less than $2\ \mu\text{A}$. The operation voltage is defined as the full depletion voltage plus 50 V . All values have been defined after the analysis of the measurement results from a past prototype production.

$$I(V_{\text{OP}} = V_{\text{FD}} - 50\text{ V} = -150\text{ V}) < 2\ \mu\text{A}$$

SLOW CURRENT BREAKDOWN: A good sensor should not show a slow current breakdown up to the planned operation voltage of -150 V . The definition of slow breakdown is not easy and the collaboration has decided to reuse the same definition as from the production of the current detector. The leakage current at the operation voltage should not be higher than twice the value at operation voltage minus 50 V .

$$I(V_{\text{OP}} = -150\text{ V})/I(V_{\text{OP}} + 50\text{ V} = -100\text{ V}) < 2$$

The criteria are equally important and only sensors fulfilling both of them are classified as good (or “grade 1”). A failure in meeting at least one criterion leads to a bad classification (“grade 0”). As mentioned before only wafers with at least two grade 1 sensors are accepted by CMS and later only grade 1 sensors are used for bump-bonding.

5.3.2 RESULTS

In total 216 wafers with 648 large sensors have been produced by CiS for the Phase I Barrel Pixel Module production at IEKP. They were delivered in four batches over the course of two years and each batch was directly forwarded to PacTech - Packaging Technologies GmbH, the company contracted for application of the under-bump metallization and wafer cutting. At PacTech, one of the 216 wafers was destroyed due to wrong cutting and the remaining 645 sensors were shipped to KIT where one additional sensor was found broken after transport. This means that 644 sensors were available for IV measurement at IEKP. According to the measurements previously done by CiS they should have included 548 grade 1 sensors stemming from 118 wafers with three good sensors and 97 wafers with only two good sensors.

As mentioned before, it has been decided to remeasure all delivered sensors including the ones graded 0 by CiS due to the improving results during measurement of the first batch. For the second and third batch there was also another much more important point why every sensor had to be remeasured: the naming of the individual wafers and with it the naming of the sensors was lost during packaging at PacTech since the company had changed the packaging style without further notice. The individual sensors are not labeled with a complete number including batch and wafer but only their position on the wafer which is embedded in the lithography mask. The application of a complete number during production can not be done with a fixed mask and is therefore omitted. New imaginary names had to be assigned to all 311 sensors of these two batches before IV measurement at IEKP and any comparison with the previously measured CiS results was obviously not possible anymore.

A typical result from the IV measurement at IEKP is shown in figure 5.4. For each of the three pixel sensors from wafer 331154-10 the IV characteristic is measured in steps of 5 volts starting at 0 V . The measurement is stopped when either the voltage reaches -600 V or the leakage current reaches $30\ \mu\text{A}$. Since the sensors are made in an n^+ -in- n design the applied bias voltage has to be negative but to make all the plots easier to read the absolute values of both bias voltage and current are shown instead.

The sensors 331154-10-1 and -2 show the typical and expected behaviour. Starting at 50 V the leakage current stabilizes slightly below $0.5\ \mu\text{A}$ and at around 250 V the sensors break through and the current rises steeply. According to these measurement results and the classification criteria listed above they are both graded as good. The visible kink at the beginning of the flat part of the characteristics can additionally be used to derive the depletion voltage of the

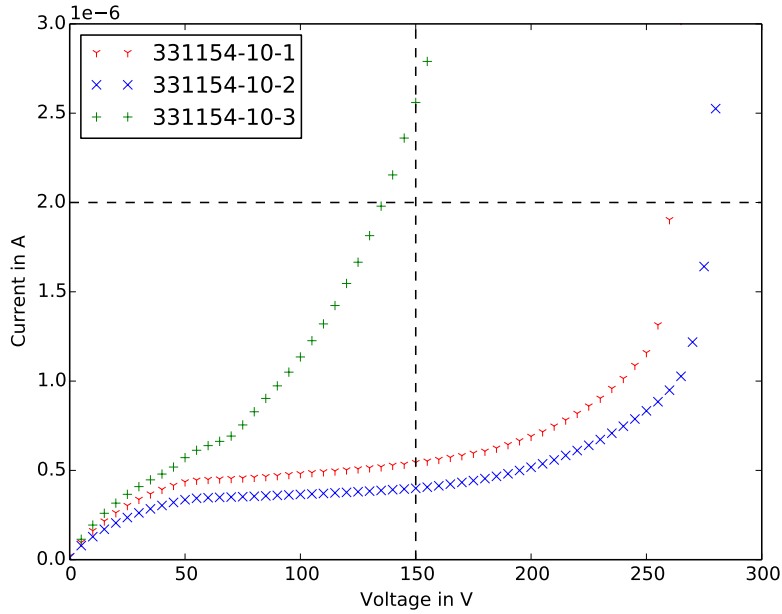


Figure 5.4: IV characteristics of the three CMS pixel sensors from wafer 331154-10. While the sensors 331154-10-1 and -2 are graded 1 and show the typical and expected behaviour with a stable leakage current slightly below $0.5 \mu\text{A}$ and a breakthrough starting at 250 V, sensor -3 is graded 0 since it misses both classification criteria. Its current at 150 V is higher than the allowed $2 \mu\text{A}$ indicated by the two dashed lines and its calculated slope $I(150 \text{ V})/I(100 \text{ V})$ is 2.26 and thus greater than the allowed 2.

sensors which is slightly above 50 V and thus lower than the 100 V assumed in the TDR but this has no effect on the defined specifications. Sensor -3 however is graded as bad since its current at 150 V is higher than the allowed $2 \mu\text{A}$ indicated by the two dashed lines. Additionally it also misses the second classification criterion regarding slow breakdown since its calculated slope $I(150 \text{ V})/I(100 \text{ V})$ is 2.26 and thus greater than the allowed 2.

The IV characteristics of all pixel sensors measured at IEKP are plotted in figure 5.5. The plot contains 533 individual measurement results. The difference compared to the previously mentioned number of 644 sensors available for measurement stems from the fact that not all sensors from the fourth and last batch were remeasured due to time constraints. Bump-bonding of readout chips to sensors had already been stopped due to lack of sensors and in order to restart the production as quickly as possible the new sensors were directly used based on the known CiS measurement results as soon as they became available. This was made possible by another change of the packaging at PacTech for the fourth batch which again included the wafer numbers.

A very large share of sensors has a leakage current of less than $1 \mu\text{A}$ at 150 V as indicated by the wide colored band in the bottom third of the plot. The flat gradient of the band also shows a constant current behaviour in the voltage range between 50 V and 150 V so that all included sensors are graded good. The kink at the beginning allows the deduction of the depletion voltage of the sensors which is in the range between 50 V and 60 V while the breakthrough voltage typically lies above 220 V. The IV characteristics of the bad sensors with grade 0 cover the whole area above the band. While the largest part of them shows very early breakthroughs or even ohmic behaviour a small number passes the current criterion and only gets sorted out due the soft breakdown criterion. Compared to the same plot based on only 168 measurement results from the first sensor batch which was shown in [Rie14] it becomes clear that the cluster-

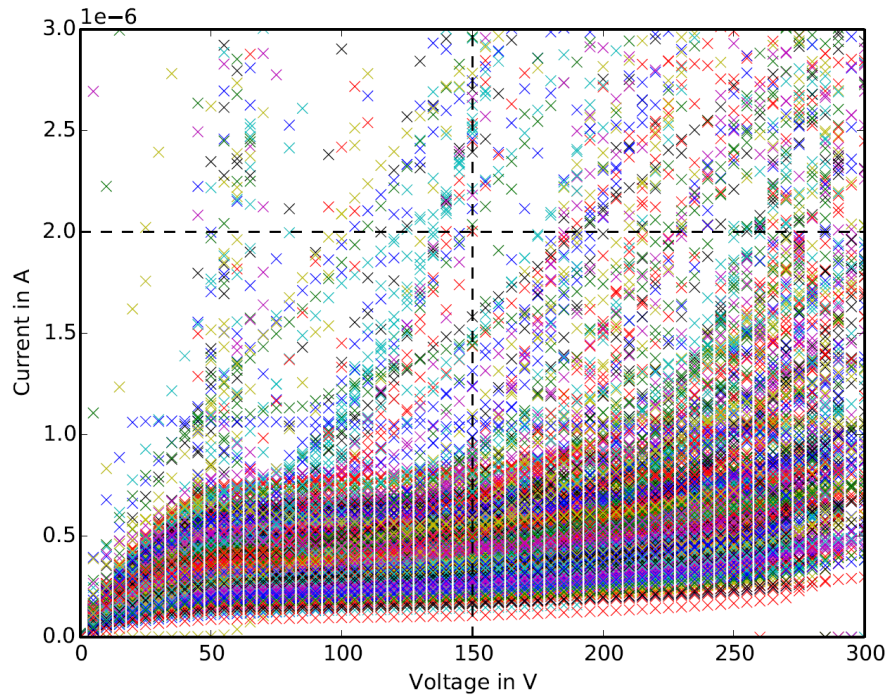


Figure 5.5: IV characteristics of all CMS pixel sensors measured at IEKP. The plot contains 533 individual measurement results. Most sensors have a leakage current of less than $1 \mu\text{A}$ at 150 V and show a constant current behaviour in the voltage range between 50 V and 150 V as indicated by the wide colored band in the lower third of the plot. They are all graded 1. The IV characteristics of the grade 0 sensors cover the whole area above the band whereupon early breakthrough or ohmic behaviour are the main failure modes but a small number of sensors passes the current criterion and only gets sorted out due the soft breakdown criterion.

ing points of the IV characteristics of the bad sensors at the $2 \mu\text{A}$ line around 130 V and 180 V have vanished. This confirms the prior finding that no correlation is present and that the points were just an artifact of low statistics.

The three characteristic numbers from the IV measurement results of the sensors required for classification ($I(100 \text{ V})$, $I(150 \text{ V})$, slope $I(150 \text{ V})/I(100 \text{ V})$) have been extracted from all available data sets and plotted as histograms. The distributions of the current values I_1 at 100 V and I_2 at 150 V are shown in figures 5.6 and 5.7 respectively. Both histograms have comparable shapes and maximum values around $0.5 \mu\text{A}$. Together with the only small increase of the right shoulder in the distribution of the $I(150 \text{ V})$ values this confirms the fact that most sensors have a low leakage current and show a constant current behaviour in the voltage range between 100 V and 150 V which is already visible in figure 5.5.

Only a small number of sensors have leakage currents in the range between $2 \mu\text{A}$ and $10 \mu\text{A}$ while more than 30 sensors have values above $10 \mu\text{A}$ and are thus only shown in the overflow bin. This is compatible with the earlier finding that most bad sensors show either very early breakthroughs or even ohmic behaviour.

Figure 5.8 shows the distribution of the slope $I(150 \text{ V})/I(100 \text{ V})$ which is calculated as an indicator of possible slow breakdown. The maximum around 1.07 is again a confirmation of the fact that most sensors show a constant leakage current behaviour in the voltage range between 100 V and 150 V .

Only a small number of sensors has slope values above the cutoff parameter of 2. Since the slope only gives the proportion between the two current values and does not contemplate the

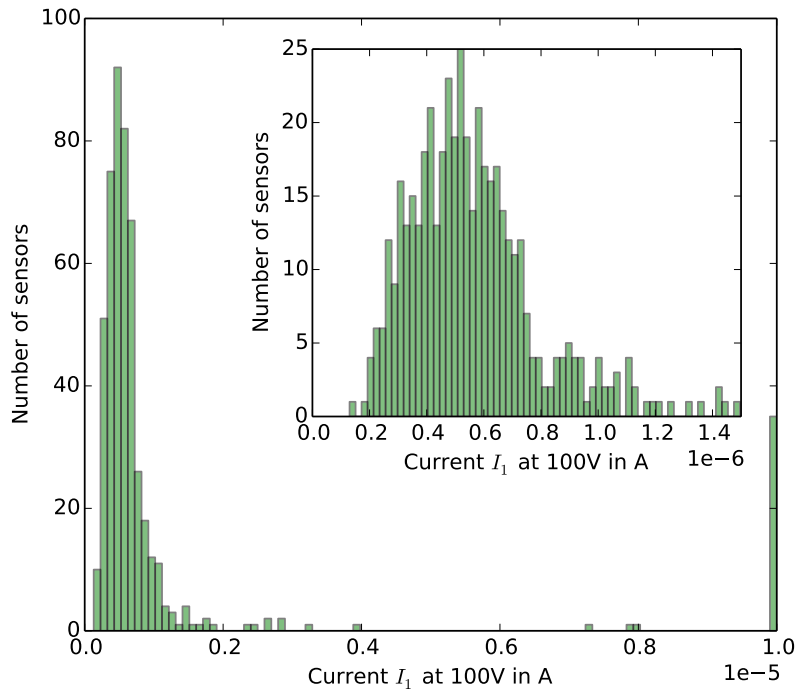


Figure 5.6: Histogram of all I_1 values at $U_1 = 100$ V. The maximum of the distribution is around $0.5 \mu\text{A}$. While the current range between $2 \mu\text{A}$ and $10 \mu\text{A}$ is practically empty more than 30 sensors are in the overflow bin above $10 \mu\text{A}$. This confirms the earlier finding that most bad sensors show either very early breakthroughs or even ohmic behaviour.

absolute values this supports the earlier finding that most sensors are graded bad due to too high leakage currents and not due to possible slow breakdown.

Since each CiS wafer holds three large CMS pixel sensors which are identified as 1, 2 and 3 according to their position (cf. figure 5.1) it is also interesting to study the sensor quality of the different positions. This might uncover systematic problems from mechanical handling during wafer processing at CiS or PacTech. Figure 5.9 shows a histogram of the classification results of the sensors from the 178 measured wafers divided into the three positions. The upper red part of the bars represents the amount of bad sensors with grade 0 while the lower green part is the amount of good sensors with grade 1.

The wafer positions 1 and 2 show a similar share of bad sensors in the range of 21% while for position 3 it is only 14% or two-thirds of the other two. This finding was already shown in [Rie14] where the number of bad sensors at position 3 was only half the one of the other positions. Now with triple the statistics the proportions have come closer but are still different. An explanation of the measured better quality of the sensors at wafer position 3 is not possible since the overall difference is small and does not support the existence of systematic problems during wafer handling. Additionally the distribution might be biased by the purchasing contract with CiS since only wafers with two or more good sensors are delivered to the collaboration and the remaining wafers left at CiS might contain more bad sensors at position 3 but this information is not available for further study.

The final results from the sensor IV measurements performed at both CiS and IEKP are presented in table 5.1. The yields of sensors classified as good from the IEKP measurement results of the four sensor batches are all in the same range around 80% and indicate that the produc-

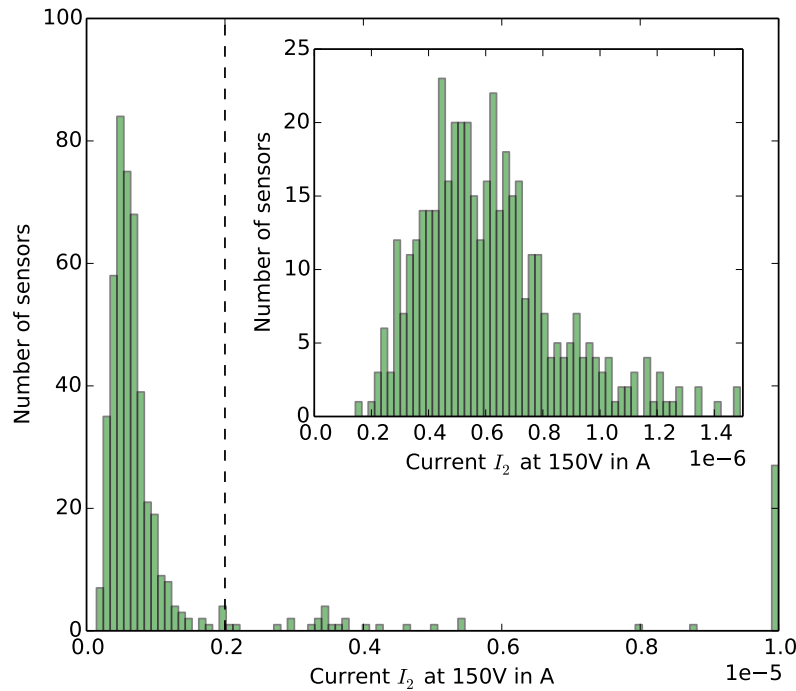


Figure 5.7: Histogram of all I_2 values at $U_2 = 150$ V. The cutoff parameter for classification is indicated as dashed vertical line. The maximum of the distribution is again around $0.5 \mu\text{A}$ but the right shoulder is slightly more pronounced. This confirms the fact that most sensors show a constant leakage current behaviour in the voltage range between 100 V and 150 V.

tion process at CiS is quite mature and stable over several years and that the UBM application at PacTech does not adversely affect sensor quality. Compared to the IV results from CiS about 5.6% of all delivered good sensors have been reclassified as bad after the IEKP measurements.

Small differences in the total numbers of sensors between the different columns can be attributed to the loss of sensors during cutting and shipping. The numbers of batches 3 and 4 are only shown as combined numbers after production since the original naming of the sensors was lost during packaging at PacTech and the individual sensors were indistinguishable afterwards. As already mentioned above the number of sensors from the fourth and last batch which was measured at IEKP is only a fraction of the total number of 165 since most sensors have been directly used for bump-bonding after delivery based on the available CiS results without any additional IV measurement due to time constraints. As an indication the concerned numbers are set in brackets.

Since another IV measurement of the sensor is performed at the beginning of the bare module production (see section 6.1.3) the risk of using bare sensors based on only the CiS results seemed small and this was confirmed by the obtained measurement results. Only six out of the 98 previously untested sensors had to be sorted out due to bad IV characteristics. This corresponds to a fraction of 6% which is compatible with the 5.6% sorted out after the IEKP measurements.

5.4 PHASE I PRODUCTION DATABASE

The production of at least 1400 good barrel pixel modules for the Phase I upgrade of the pixel detector at five production sites is a complex project in terms of material and logistics. As shown in section 4.2 a module consists of multiple components which are sourced from vari-

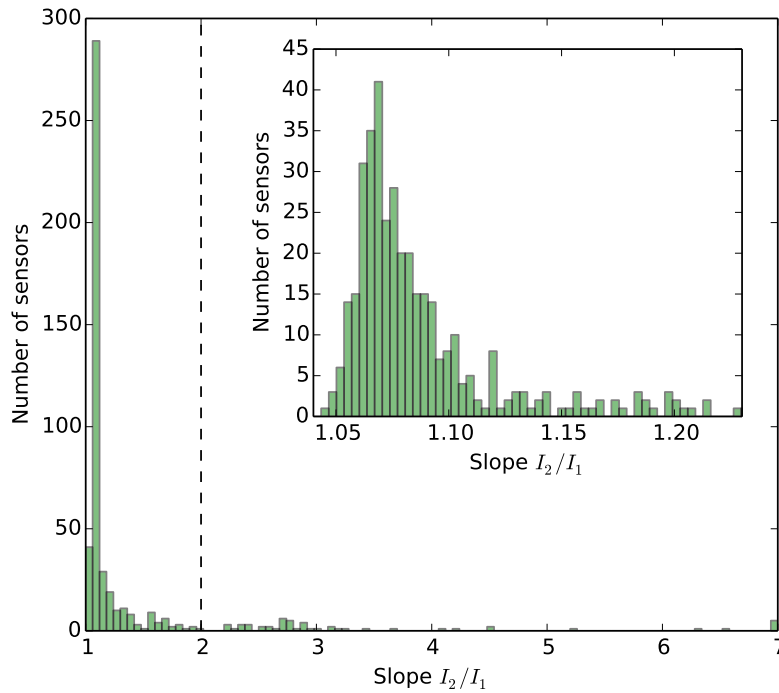


Figure 5.8: Histogram of all slope values I_2/I_1 . The cutoff parameter for classification is indicated as dashed vertical line. The maximum of the distribution is around 1.07. This is again a confirmation of the fact that most sensors show a constant leakage current behaviour in the voltage range between 100 V and 150 V.

ous vendors and combined in several production steps. In order to be able to track both the individual components and the completed modules a dedicated production database¹ has been set up by the University of Pisa. It is based on a MySQL database combined with other freely available open-source software like Python and jQuery and is operated at the Tier 2 computing center of the worldwide LHC computing grid at Pisa. Access is provided by a web-based graphical front end and also through other solutions directly interacting with the database via SQL queries.

Its basic functions include the stock-keeping of the different module components and the tracking of their status which users can flag as bad or destroyed by editing the component properties. If a component gets tested before or during production the measurement results are also uploaded to the database, linked to the component and analyzed automatically. In case of the IV measurements of the silicon sensors described above the complete IV characteristic together with additional information about the measurement environment is inserted and the important values for classification are extracted and the grade is calculated. Special plotting tools are available in the web-based front end which allow a quick comparison of different IV characteristics and other data.

Besides that the database also implements the complete production workflow of a module which is built virtually by adding together all the components. The raw materials are then marked as used and the scripts prevent their further usage. When the new module is finally tested and qualified at the production center the results are uploaded to the database and analyzed automatically with the help of a software called MoReWeb written at Eidgenössische

¹ URL of the web-based graphical database front end: <http://cmspixelprod.pi.infn.it>

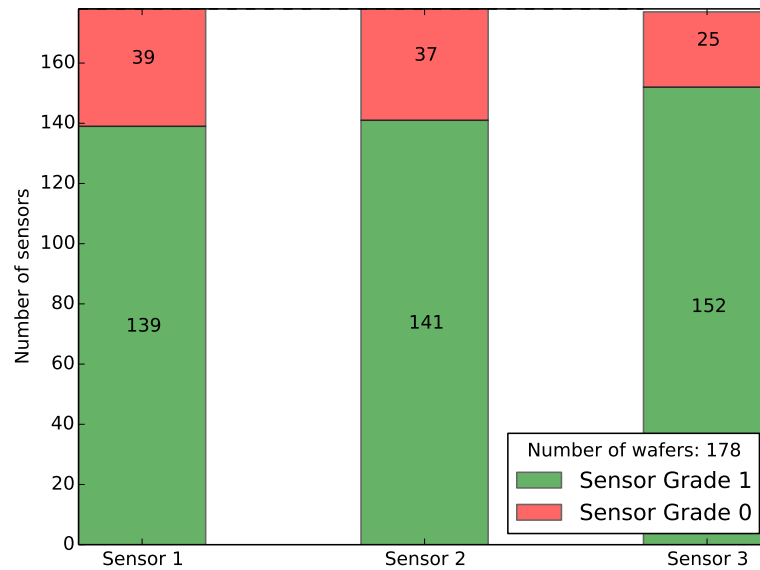


Figure 5.9: Classification of pixel sensors by wafer position. Each CiS wafer holds three large CMS pixel sensors which are numbered 1, 2 and 3 according to their position. After IV measurement of 178 wafers it becomes clear that the positions 1 and 2 show nearly the same ratios between good and bad sensors while the sensors of position 3 are on average of better quality and thus have a higher ratio of good sensors.

Technische Hochschule Zürich (ETH) [Eid16]. MoReWeb analyzes the data and classifies the module according to the global grading parameters defined by the collaboration. Its output is both inserted into the database and made available as a set of webpages containing all the results conditioned in form of tables and plots.

Since the classification by MoReWeb defines the final quality of a module it is important to classify all modules with the same software version and the same set of grading parameters. This is ensured by running the software centrally on the database server and also allows a simple reanalysis of all the data when the grading parameters or the software have changed.

Finally the database also tracks the locations of components and modules and the scripts prohibit the usage of components which are not present at the production center which is trying to use them. Together with the condition that components can be used only once this ensures correct material handling and traceability of the components of a certain module. If parts or modules need to be shipped between production centers a transfer has to be inserted in the database to make sure that the component locations stay up-to-date.

Table 5.1: Yield of CMS pixel sensor IV measurements. The yields of good sensors from the IEKP measurements of the four delivered batches are all in the same range around 80%. Compared to the CiS results about 5.6% of all good sensors have been classified bad after the IEKP measurements. The total number of sensors from the fourth batch measured at IEKP is much lower since most sensors have been directly used for bump-bonding. As an indication the numbers are set in brackets.

Batch	CiS (sensor production)			PacTech (UBM, cutting)			IEKP (IV measurement)		
	Total	Grade 1	Yield	Total	Grade 1	Yield	Total	Grade 1	Yield
1	171	144	84.2 %	168	142	84.5 %	168	134	79.8 %
2	186	162	87.1 %	312	265	84.9 %	311	252	81.0 %
3	126	103	81.7 %						
4	165	141	85.5 %	165	141	85.5 %	(54)	(43)	79.6 %
Sum	648	550	84.9 %	645	548	85.0 %	(533)	(429)	80.5 %

MODULE PRODUCTION

This chapter gives an overview of the barrel pixel module production at Karlsruhe Institute of Technology (KIT) for the Phase I upgrade of the CMS pixel detector. As already mentioned in section 4.2 the new barrel pixel detector consists of 1184 modules and together with spares this requires a production of at least 1400 good modules. The production and qualification of such a large number of modules in a short period of only 18 months is a complex undertaking requiring both qualified personpower and tooling. At the same time it needs to be ensured that possible unforeseen problems do not put the full project at risk. Both points are best respected when the production is not concentrated at a small number of institutes like it was done for the current detector but diversified among multiple institutions. Involving institutions from several countries also allows for easier funding of the project from different national sources.

Therefore it has been decided early in the project to share the production of the new detector among several European universities and research centers while the current barrel pixel detector has been built completely in Switzerland by a consortium consisting of Paul Scherrer Institut (PSI), Eidgenössische Technische Hochschule Zürich (ETH) and University of Zürich. The different institutions involved have organized themselves in four consortia responsible for different parts of the detector. The modules for the first and second layer of the new detector and also all mechanical parts of the support structure are produced by the Swiss consortium mentioned above. One half of the modules for the third layer is made by a consortium composed of CERN, Finnish universities and research institutes and the National Taiwan University (NTU) while the other half is produced by five Italian universities as members of the National Institute for Nuclear Physics (INFN).

The production of the modules for the fourth layer is under the responsibility of a German consortium called D-PIX which consists of DESY, University of Hamburg (UHH), Rheinisch-Westfälische Technische Hochschule Aachen (RWTH) and Karlsruhe Institute of Technology. The 512 modules to produce (plus spares) which are required for that layer are internally shared among two production lines where one is formed by KIT and RWTH and the other by DESY and UHH.

The complete module production chain for the KIT-RWTH line is outlined in figure 6.1. As shown in the diagram the production of the modules is done at KIT while the final qualification and calibration is performed at Aachen. In Karlsruhe two institutes are involved, the Institute for Data Processing and Electronics (IPE) which bonds the readout chips to the silicon sensors and the Institut für Experimentelle Kernphysik (IEKP) which assembles the modules.

For the other production consortia the production chain basically comprises the same steps but especially for the bump-bonding several alternatives have been implemented, ranging from a complete outsourcing to industry to the point of a full in-house process. The solution chosen by KIT lies in between by contracting sensor UBM application and readout chip bumping to industry while performing the bonding process locally at IPE.

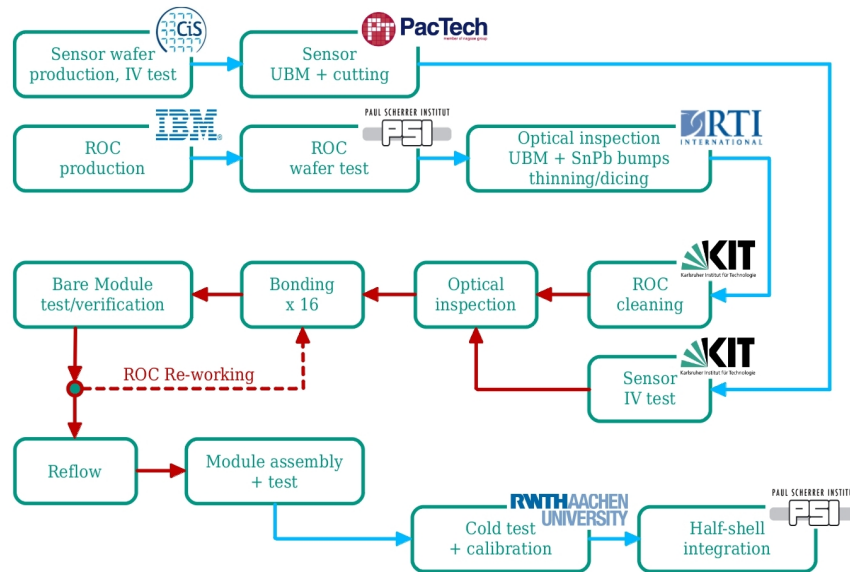


Figure 6.1: Pixel module production workflow for the KIT-RWTH group of the D-PIX consortium. Next to each production step the name of the institution or external company responsible for the step is given. All tasks connected by red arrows are performed at Karlsruhe Institute of Technology.

6.1 BARE MODULE PRODUCTION

The bump-bonded sandwich of sensor and sixteen readout chips is referred to as a bare module in the collaboration. As already mentioned in section 4.2 the production of bare modules is a two-step process consisting of the preparation of the materials and the subsequent bonding. There are many different bump-bonding techniques available on the market that mainly differ in the bump material and the bump diameter. Common bump materials are indium solder, tin-lead solder (SnPb), tin-silver-copper solder (SnAgCu), gold (Au) or copper (Cu) [BCL07]. Each of these materials needs a specially tuned bumping process.

In general, bumping processes can be separated into lithographic and non-lithographic deposition processes. Lithographic processes deposit all bumps in parallel on the pads while the remaining structures on the wafer have to be protected. This protection is applied beforehand with lithographic masks which have to be uniquely produced for each new wafer layout. Since the production of such masks is expensive lithographic bumping processes are typically only used for large-scale productions and not for R&D of new electronics structures. All lithographic processes have in common that the connection between the aluminum pads of the wafers and the bump material is not sufficient because aluminum is barely solderable [BCL07]. In order to reach a good intermetallic connection additional intermediate metal layers have to be applied in further lithography steps. They form the so called under-bump metallization (UBM).

Non-lithographic deposition processes place the bumps serially on predefined positions without the need for any protection of other structures. This makes such processes ideally suited for small scale R&D projects where high flexibility in the bumping pattern and low cost is much more important than high speed. Although the bumping processes themselves are non-lithographic, the complete process chain might still need lithographic steps if a UBM with lithographic application is chosen.

A detailed overview of the available bumping techniques is given in [Hei12] and [Kud14].

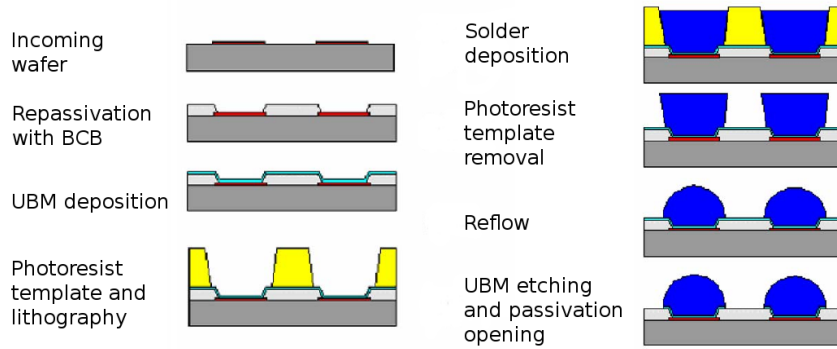


Figure 6.2: RTI SnPb bumping process. The figure shows cross-sectional views of the different steps performed by RTI International to deposit spherical SnPb bumps with a diameter of approximately $30\ \mu\text{m}$ on the readout chips [HLBS03].

6.1.1 THE RTI TIN-LEAD BUMPING PROCESS

For the bump-bonding of the bare modules for the CMS Pixel Phase I Upgrade IPE has chosen a process which is regarded as one of the standard process technologies in high-energy physics applications. The process uses an eutectic mixture of tin and lead as bump material (consisting of 63% tin and 37% lead). In an eutectic composition, the two elements liquefy simultaneously at a temperature lower than the melting temperatures of the single materials. For SnPb this temperature is 183°C . The spherical bumps with a diameter of approximately $30\ \mu\text{m}$ are deposited on the UBM-covered aluminum pads of the readout chips in a lithographic process while the pixel sensors only need a compatible UBM and are not bumped.

Since the material preparation steps like application of the sensor UBM and bumping of the readout chips were not available at KIT and the setup of those steps are either very costly in case of the mentioned lithographic processes or, in case of the non-lithographic serial processes, not perfectly suited for a large-scale production IPE has decided to outsource the complete material preparation to industry.

An overview of the complete bump-bonding process chain chosen by IPE can be found in [CBC⁺16].

As described in section 5.3 the sensor UBM compatible with the chosen SnPb bumps is applied by PacTech in an electroless process called ENEPIG¹ by submerging the wafers in different chemical baths. The UBM layers are thereby deposited on the aluminum pads of the sensors. Electroless processes work without sputtering and thus without any lithographic steps which makes them on the one hand significantly cheaper but on the other hand they always cover all pads on the wafer since they are mask-less processes.

The company selected for bump deposition is RTI International in the USA. After production at IBM the wafers with 244 readout chips each are sent to PSI where the chips are electrically tested and classified. Afterwards the tested wafers are delivered to RTI where the SnPb bumps are placed in an electroplating process. The basic steps of that process are illustrated in figure 6.2 and shortly described in the following list. More details are given in [HLBS03].

1. Repassivation of the wafer with Benzocyclobutene (BCB) to protect the surface. The BCB layer also acts as a stress buffer between the wafer substrate and the bumps. In the areas above the aluminum pads the BCB is first exposed to light and then removed to allow access to the pads.

¹ Abbreviation for Electroless Nickel, Electroless Palladium and Immersion Gold.

2. Deposition of the under-bump metallization (UBM) by electroless plating. Looking from the pad side the RTI UBM consists of a thin tungsten layer which acts as diffusion barrier between pad and UBM, a nickel layer with a thickness of a few μm as wettable metal and a thin surface layer of gold which prevents oxidation of the nickel.
3. Protection of the wafer with a thick layer of photoresist. Openings at the aluminum pads of the chips are created afterwards in a photolithographic process.
4. Electroplating of the bump material (SnPb). The amount of deposited material (and hence the final bump height) is controlled by varying the electroplating current.
5. Removal of the photoresist template.
6. Reflow of the SnPb pillars by heating above the phase transition temperature of the bump material. The reflow reshapes the bumps into truncated spheres with a diameter of approximately $30\ \mu\text{m}$ and ensures a good intermetallic connection between solder and UBM.
7. Etching of the UBM not covered by the bumps and opening of the BCB passivation layer above the wire bond pads in a dry etching process.

After the bumping process a thick layer of photoresist is again applied to the top of the wafer in order to protect the bumps during the following processing steps and also during transport to KIT. As mentioned in section 4.2 the readout chips are thinned down to $175\ \mu\text{m}$ by a subcontractor to reduce the amount of material in the detector. This thinning is performed before the wafers are cut and the readout chips are separated. As a last step before shipment all chips are visually inspected by RTI and marked if problems like residuals from the process or miss-shaped or missing bumps are found.

6.1.2 THE KIT BONDING PROCESS

The flip-chip bonding of the bare modules is performed inside the clean room of the Electronic Packaging Group of IPE since the process requires a clean environment and also clean components. While a clean working environment is ensured by the clean room and proper clothing guidelines, the components of the bare modules are sourced from different companies and might suffer from pollution during transport or handling and thus might need cleaning. Since different types of contaminations require different solvents an elaborated cleaning procedure is necessary. Inorganic pollutions like salts and ionic compounds are typically removed with pure water while organic pollutions are cleaned with acetone.

6.1.2.1 *The KIT Cleaning Procedure*

In case of the readout chips delivered by RTI cleaning is mandatory since the chips are covered with a protective photoresist layer which needs to be removed before usage. A special cleaning procedure was developed at IPE which is tuned to give the best results in terms of remaining residues on the chip while at the same time reducing the necessary manipulation of the delicate bumped chips to a minimum.

35 readout chips are placed on a custom-made plastic tray with the bumped but still protected side up where they are held in place by vacuum additionally secured with a grid made from Teflon strands. The readout chips are then cleaned with a sequence of three different solvent baths. The first bath is ultrapure acetone which dissolves the photoresist and other possible organic contaminants. Since acetone and water are immiscible an intermediate bath of ultrapure isopropyl alcohol (IPA) is necessary to wash away the acetone residuals. The process is completed with a bath of deionized water. In order to speed up the evaporation of the water the tray is finally placed in an evacuated oven heated to 70°C for 15 minutes. The full procedure lasts about 30 minutes and is documented in detail in a manual which can be found in [Kud14].

After the cleaning every readout chip is visually inspected to document the quality of the cleaning and check for any remaining contaminations or bump defects which might affect the later bonding. The inspection is performed with an optical microscope at IPE which features a motorized table and is controlled by a PC. The associated software takes a series of highly magnified pictures for each chip and automatically stitches them together to a single high resolution image of the full chip. In total more than 9000 readout chips have been cleaned and photographed at IPE.

Since the manual analysis of the more than 9000 images would be too time consuming they are instead fed to a custom pattern recognition program which was designed with the National Instruments Vision Development Module [Nat16c]. The software is trained once by an operator and then processes each readout chip image and automatically searches for contaminations, misshaped or completely missing bumps, cracks, etc. Possible problems found are afterwards presented to the operator who finally decides if the readout chip has to be rejected or not.

As mentioned before more than 9000 readout chips have been cleaned and inspected during the bare module production. Out of these more than 90% have been found good for bonding while the main failure modes of the remaining ones were contaminations from handling, residuals from the cleaning process, silicon splinters from the cutting or defects in the BCB passivation layer [Col16]. The last two points are remains from the bumping process at RTI and can therefore not be attributed to bad cleaning.

The silicon sensors are also optically inspected before bonding but in a manual way since an automated inspection is not possible due to the larger size compared to the readout chips. Since the sensors are not bumped they do not have to be inspected to the same detail as the chips and the typical defects like scratches or cracks of the silicon or defects in the PacTech UBM or in the passivation layer are found easier due to their larger size.

6.1.2.2 *Flip-chip Bonding at KIT*

The actual flip-chip bonding is performed with a Finetech FINEPLACER® femto flip-chip bonder manufactured by Finetech GmbH placed on a large anti-vibrational table. An overview of the machine without the additional control and gas distribution modules is given in figure 6.3. The central part is the fully motorized (x, y, z, φ) bonding table. On the right and left side two presentation tables are attached and allow the components for the bonding to be placed and picked up. In the case of the bare module production the cleaned readout chips are placed on the left presentation table in a special type of packaging called Gel-Pak after its manufacturer.

The actual bonding takes place in the central part of the table where the substrate (in our case the CMS pixel sensor) is placed and held in place with the help of vacuum created by a Venturi tube. The bonding area has a size of $100 \times 100 \text{ mm}^2$ and can be heated up to a temperature of 400°C and cooled down by compressed air. The placement arm is located above the bonding table perpendicular to the surface. It features only one degree of freedom for a rotational movement around the x -axis which is used to pick up a readout chip from the Gel-Pak and move it up to a vertical position. In order to be able to pick up the readout chips the end of the arm is equipped with the bond head, a tool which has been custom-made to fit the geometrical dimensions of the chip. The rectangular tool is heatable and features an internal vacuum circuit to hold the chip in place. It is connected to the arm using a special gimbal mounting which helps to first adapt the planarity of the chip to the substrate underneath while keeping it fixed afterwards in the process.

The alignment of the picked up chip and the sensor is performed with the help of a movable camera which runs along the x coordinate of the bonding table. It is connected to a light splitter allowing the simultaneous visualization of the sensor lying on the table and of the readout chip held by the bond head. The usage of such a splitter is crucial for the quality of the bonding process since it allows the alignment to be done automatically by the machine with the help of sophisticated pattern recognition software running on the control PC.

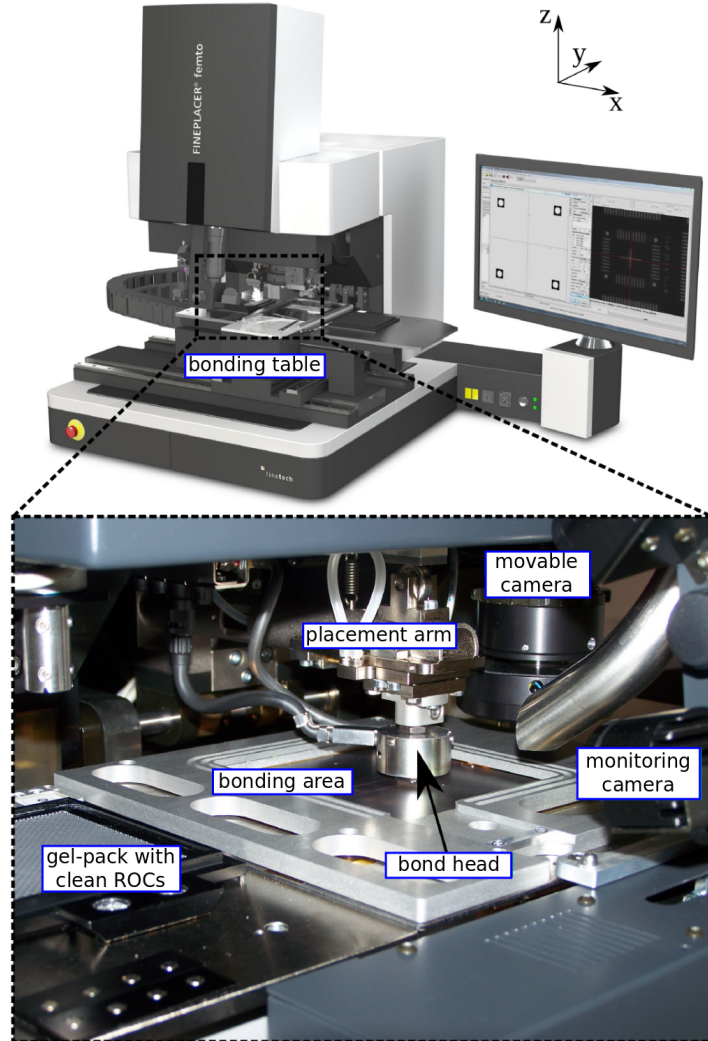


Figure 6.3: Finetech FINEPLACER® femto flip-chip bonder. The picture shows an overview of the machine (top) and a more detailed view of the bonding table and the placement arm with the bond head (bottom) [Fin16].

The bonding area can additionally be covered with a custom-made metal plate which has a cutout in form of the bond head. When the placement arm is in lower horizontal position the bond head closes the cutout and an airtight chamber is formed around the assembly which can be used to perform an in-situ reflow. The machine is therefore connected to a gas module supplying formic acid and nitrogen. While the formic acid creates a reactive atmosphere in the chamber during the reflow process, the nitrogen is used as an inert gas to flush the chamber at both the end of the reflow process and during bonding.

The placement arm can apply bonding forces in the range from 0.5 N to 500 N and the placement accuracy of the machine is better than $\pm 0.5 \mu\text{m}$ while the planarity accuracy is $4 \mu\text{rad}$ according to the technical specifications [Fin16].

The complete procedure for the flip-chip bonding of CMS bare modules developed at IPE is outlined below:

1. Placement of the sensor on the center of the bonding table where it is held in place by vacuum.

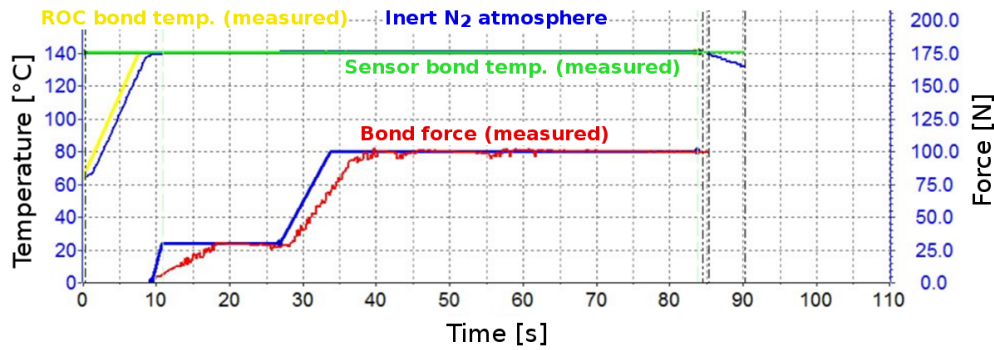


Figure 6.4: Force and temperature profiles as a function of time used for the KIT flip-chip bonding process. The plot shows both the set and the measured values of the bonding force, the temperature of the bond head (holding the chip) and the temperature of the bonding table (supporting the sensor). The bonding of a single chip lasts 85 seconds.

2. Automatic recognition of the two lower sensor corners to define their position in the internal reference coordinate system.
3. Pick up of the readout chip from a Gel-Pak placed on the left presentation table with the placement arm. Since the chip is picked up from the backside which does not feature any visible structures the arm can only be aligned according to the corners of the chip. This is why the quality of the wafer cutting has a large impact on the bonding process and thus needs careful inspection as described above.
4. Flattening of the bond head. Since the readout chip is not picked up flat from the soft Gel-Pak surface it is laid down on a very flat ceramic surface and picked up again to ensure the correct positioning of the bond head.
5. Automatic pattern recognition of unique structures on the bumped side of the readout chip. Their detected positions in the internal coordinate system are compared to those of the sensor corners and an alignment between the two components is performed by movement of the bonding table.
6. Lowering the arm onto the substrate to perform the actual bonding. When the arm has reached the horizontal position the bonding table moves up and applies a user-defined force profile with a maximum force of 100 N while the bond head is heated up to 140°C. The force and temperature profiles as a function of time are shown in figure 6.4. The bonding of a single readout chip lasts 85 seconds.
7. Raising the arm to the initial vertical position. The bond head is cooled down to the initial temperature of 65°C.
8. Repetition of the sequence until all 16 readout chips are connected to the sensor. Since the complete sequence lasts four minutes for one chip, a complete bare module is bonded in about one hour.

6.1.2.3 Module Rework and Reflow

The last step of the bare module production is the reflow procedure which is described here for sake of clarity. Actually it is only performed after the successful testing of the bare module which is presented in the next section since the rework of a module found bad during testing is much easier if the mechanical connection between sensor and readout chips has not yet been reinforced by reflow. A typical rework is the replacement of an electrically bad or even dead

readout chip with a new one. Such chips are most likely damaged during mechanical handling after the electrical test on wafer level at PSI has been performed. The replacement is done by again placing the bare module on the bonding table while heating it to 130°C. The bad readout chip can then be removed either by hand or with the bond head and after the remaining bumps have been sheared off from the sensor, a new chip can be bonded. This procedure has been performed 87 times during the complete bare module production and more than 90% of the reworked bare modules were successfully repaired [Fre16]. It has thus proven to be a valuable tool to reach the required amount of bare modules.

As mentioned before it is possible to perform the reflow process directly on the bonding machine. This opportunity has been used extensively during optimization of the KIT flip-chip bonding process since it is very flexible and no mechanical manipulation of the module is necessary until the end of the complete process. However, regarding the production it would be a bottleneck since the machine is completely blocked during reflow. An additional stand-alone reflow oven has therefore been installed in the IPE clean room which was used for the reflow of the production bare modules. Its large reflow chamber allows parallel reflow of up to twelve modules, which greatly reduces the overall time needed for the reflow procedure.

Detailed information about the optimization of both the bonding and the reflow parameters together with a presentation of the quality control methods like pull testing and X-ray tomography is given in [Col16].

6.1.3 BARE MODULE TESTING

Before the bare modules are finally reflowed and transferred to IEKP for module assembly all produced bare modules have to be tested and classified according to common criteria defined by the collaboration. At KIT this step is performed in the same IPE clean room where the cleaning and the flip-chip bonding of the modules take place. This physical proximity allows a fast feedback on the module quality and quick reaction times if unexpected problems were discovered during the tests.

A dedicated probe station has thus been designed and built which allows the execution of several different tests concerning important parameters of a bare module. These are:

- measurement of the IV characteristic of the sensor after bonding,
- tests of the electrical functionality of each of the 16 readout chips,
- determination of the number of bad or even missing bump bond connections.

A detailed documentation of the hardware setup, the bare module testing procedure and the software including a step-by-step manual can be found in [Hit15].

6.1.3.1 *The Bare Module Probe Station*

An overview of the main components of the probe station is given in figure 6.5. The bare module is placed on an insulated Teflon chuck which is mounted on a set of motor stages providing three-dimensional movement and rotation around the z-axis. Basic alignment of the module is provided by three short pins which serve as a stop during insertion and afterwards the module is fixed with the help of vacuum. The bias voltage for the sensor is supplied by a Keithley 2410 high voltage supply via a tungsten needle mounted on the chuck.

Since the sixteen readout chips are not yet wire-bonded they have to be connected one after another at the bare pads. This is done with a custom needle card with 35 needles, which is fixed to a metal plate above the chuck. This card is just a passive part which relays the data signals and power provided by the so-called digital test board (DTB), a custom-made FPGA-based readout board designed at PSI which is used for all laboratory tests during the production of

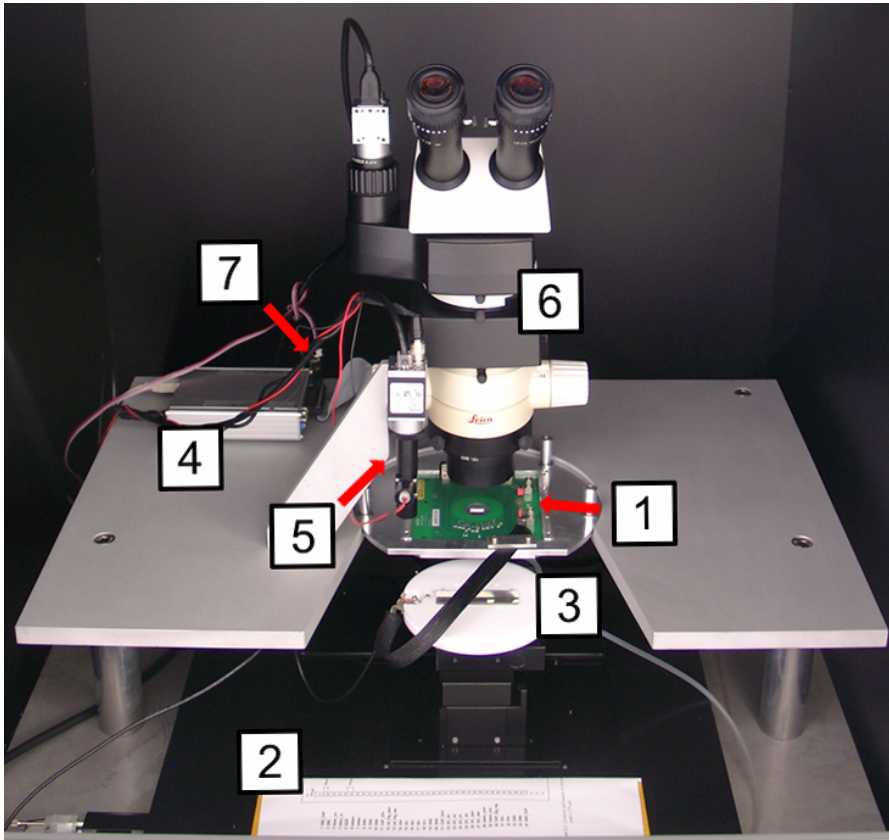


Figure 6.5: Overview of the bare module probe station at IPE. Its indicated main components are: (1) needle card, (2) motor stage, (3) Teflon chuck with HV needle, (4) test board, (5) pattern recognition camera, (6) stereo microscope with camera and (7) temperature/humidity sensor [Hit15].

the pixel modules for the Phase I upgrade [SMP15]. The card is connected to the DTB with a 68-pin SCSI ribbon cable.

A stereo microscope with an attached camera supports the operator while controlling the alignment of the needles to the wire bond pads of the chip under test until the final connection is made by moving up the chuck. A second camera is mounted on a fixed position on the left side of the metal plate holding the probe card. This camera is called the pattern recognition camera since it is used in an automated alignment procedure performed by the software controlling the probe station.

The complete setup is placed inside a metal housing which shields the bare module and the readout chain from electromagnetic noise and light. The housing is placed on an anti-vibrational table which prevents the needles from scratching the bare module due to the inherent vibrations of the machinery in the clean room. Especially the bias voltage circuit connecting the bare module has shown to be very susceptible to noise and a lot of effort was invested in reduction of the noise level. At the end the best conditions have been achieved with the addition of an optimized low-pass filter to the bias voltage line.

All components of the probe station are controlled with a GUI-based software running on a standard PC which is written with National Instruments LabWindows/CVI [Nat16b] and the National Instruments Vision Development Module [Nat16c]. The different measurement steps to test a bare module are predefined and the software automatically performs the alignment, the IV measurement and the electrical test of the readout chips while the operator only has to supervise the sequence and confirm the execution of the steps. At the end the test results are

stored in a format directly suitable for upload to the Phase I production database. For special requirements a manual operation mode allowing access to all parameters is available. Several built-in checks prevent ineligible movements of the motor stages to avoid damage to both the bare module and the needle card when e.g. the card is connected to the pads of a readout chip.

The actual electrical test of the readout chips are performed with pXar (short for pixel Xpert analysis & readout), a software written in C++ for usage with the digital test board [SMP15]. For the GUI and the analysis of the data pXar implements libraries from ROOT [BR97]. All routines necessary for testing both single readout chips and full modules are provided by the software and can additionally be expanded with the addition of user-created tests. This ability is used for the implementation of a new bump bond test specifically tailored to the bump bonding process used at KIT.

pXar itself controls the DTB and its functionality via an USB 2.0 connection to the PC. On the DTB the FPGA firmware implements the basic routines for communication with readout chips or modules and a so-called softcore CPU, a CPU implementation using the FPGA logic blocks which acts like the CPU of a standard PC and is able to execute code written in C++. The individual test routines are executed on that CPU and only the aggregated data is sent to the control PC. This task distribution drastically reduces the required time for testing.

pXar can either be run interactively with GUI or in a command line mode where the tests can be controlled with simple scripts. The bare module probe station software uses such scripts to launch the electrical test of a readout chip after it has been connected.

The complete sequence for testing a new bare module with the KIT probe station is as follows [Hit15]:

1. Placement of the bare module on the chuck and fixation with the help of vacuum.
2. Manual connection of the bias needle to the sensor with the help of tweezers.
3. Automated alignment of the bare module through optical pattern recognition. The individual pads of one readout chip are now located directly under the corresponding needles of the needle card.
4. Connection of the needles to the pads by z movement of the chuck.
5. Measurement of the IV characteristic of the sensor (only for the first chip).
6. Test of the programmability and functionality of the contacted chip by running standard pXar tests.
7. Determination of the number of bad or missing bump bond connections by running a custom test in pXar written by IEKP.
8. Repetition of the steps for the other 15 chips.
9. Unloading of the bare module from the station. Depending on the outcome of the tests the module is either reflowed and sent to IEKP or reworked at IPE.

The electrical tests performed during the sequence include tests of the readout chip as a whole, for example programmability of the DACs² and basic functionality, and also tests of each of the 4160 pixel cells. These tests rely on a special feature of the chip which allows the injection of a built-in calibration signal directly into the preamplifier of a selected pixel cell. This function is illustrated in figure 6.6 and during the bare module test it used to send ten calibration signals into the preamplifier of each pixel cell while reading out the detected hits. For perfectly working pixel cells exactly ten hits are expected while those showing no hits are declared dead. Pixel cells with a high noise level will observe a number of hits which is either

² Digital-to-analog converters are used to steer the behaviour of the chip by creating different reference voltages.

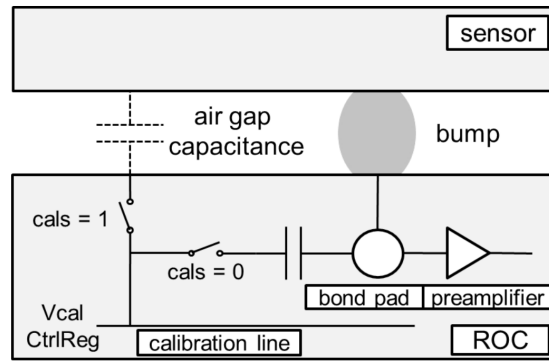


Figure 6.6: Internal calibration mechanism of the ROC. The built-in calibration signal can either be injected directly into the preamplifier (using the setting $\text{cals} = 0$) or capacitively into the sensor above ($\text{cals} = 1$). The induced signal then flows into the preamplifier via the bump connection if it is present [Hit15].

higher or lower than ten. These results are subjected to predefined cuts and classified accordingly. The test at the same time also checks if the calibration signals are detected in the same pixel cell they were injected into. A typical result from such a test is shown in figure 6.7a.

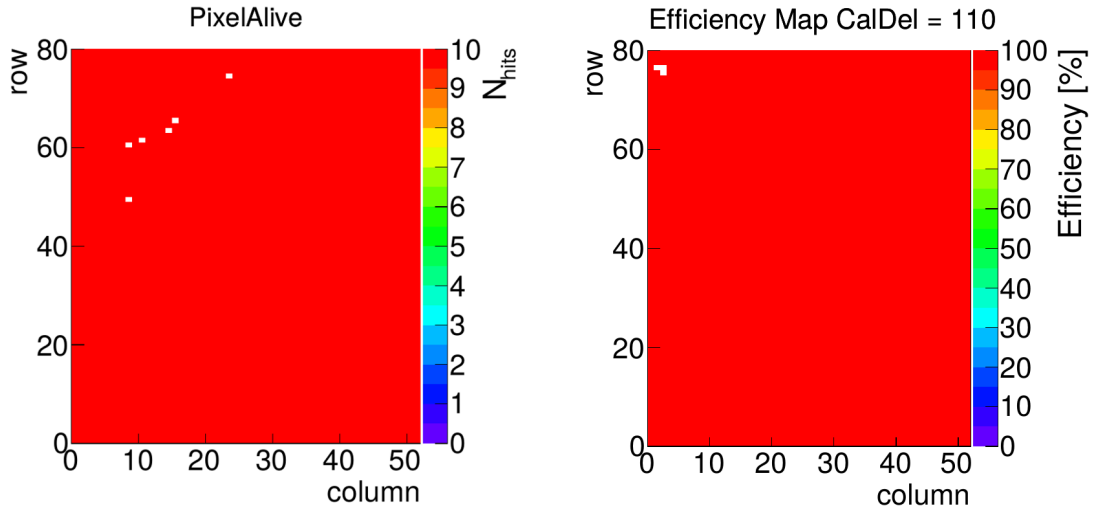
The quality of the bump-bond connections between sensor and readout chip is tested using the same method but this time the signal is injected into the sensor via the air gap capacitance (see fig. 6.6). This type of test is strongly dependent on the separation between sensor and chip which is in turn a direct result of the bump-bonding technology used at KIT. Thus a custom bump-bonding test was developed at IEKP and tuned to the RTI bumping and IPE flip-chipping process. The tuning of the test is performed by comparing the test results to the ones obtained from other tests which are closer to the real operating conditions of the module. Examples of such tests are the creation of charge carriers in the sensor by irradiation with X-rays or charged particles coming from radioactive sources like ^{90}Sr . Ideally every bare module would be tested with such an irradiation method but technical, legal and time constraints made it impossible during the Phase I bare module production at IPE.

The KIT bump-bonding test consists of two steps which are executed one after another. The first step determines the optimal threshold level of the chip which is defined as the lowest threshold for which the noise is still suppressed (or, in more detail, for which less than five out of the 4160 pixels are noisy). In the second step 100 calibration signals are injected into the sensor for each pixel and the hits are read out. This is performed for varying delays between injection and readout to compensate for the inherent differences between the pixel cells of the chip. Afterwards an efficiency map is created by comparing the numbers of received and injected calibration signals for each pixel where pixels with a missing bump connection or defective electronics have a much lower efficiency than good ones. Based on experience from the first bare modules and on crosschecks with results from X-ray irradiations the discrimination cut between good and bad pixels is set at an efficiency of 50% [Hit15]. A typical efficiency map obtained with the KIT bump-bonding test is presented in figure 6.7b.

When a bare module has been completely tested the results are uploaded to the Phase I production database where they are automatically analyzed and the bare module is classified according to the centrally defined parameters. The bare module classification scheme uses three grades A, B and C where C is the worst and only bare modules graded A or B are used afterwards for the production of full detector modules. The classification takes into account several parameters obtained from the measurements at the bare module probe station at IPE:

LEAKAGE CURRENT AND SLOW CURRENT BREAKDOWN:

- Grade A: $I(-150\text{ V}) < 2\ \mu\text{A}$ and $I(-150\text{ V})/I(-100\text{ V}) < 2$



(a) Result of the PixelAlive test from pXar checking the functionality of each pixel cell by injecting ten calibration signals into the preamplifier. Defective pixels like the six ones in the upper left region do not detect any hits during the test.

(b) Efficiency map obtained with the KIT bump-bonding test. 100 calibration signals are injected capacitively into the sensor and the hits are read out. Pixels with missing bump connections like the three ones in the upper left corner show a lower efficiency than the other pixels.

Figure 6.7: Results from both the electrical and the bump-bonding test of a ROC performed at KIT. The plots are obtained from two different readout chips and are thus not related [Hit15].

- Grade B: $2 \mu\text{A} \leq I(-150 \text{ V}) < 10 \mu\text{A}$ or $I(-150 \text{ V})/I(-100 \text{ V}) \geq 2$
- Grade C: $I(-150 \text{ V}) \geq 10 \mu\text{A}$

NUMBER OF DEFECTIVE PIXELS PER ROC:

- Grade A: < 42 defective pixels (1%)
- Grade B: < 167 defective pixels (4%)
- Grade C: ≥ 167 defective pixels

The numbers of defective pixel channels from both the electrical and the bump-bonding test are added here.

DIGITAL CURRENT OF EACH ROC:

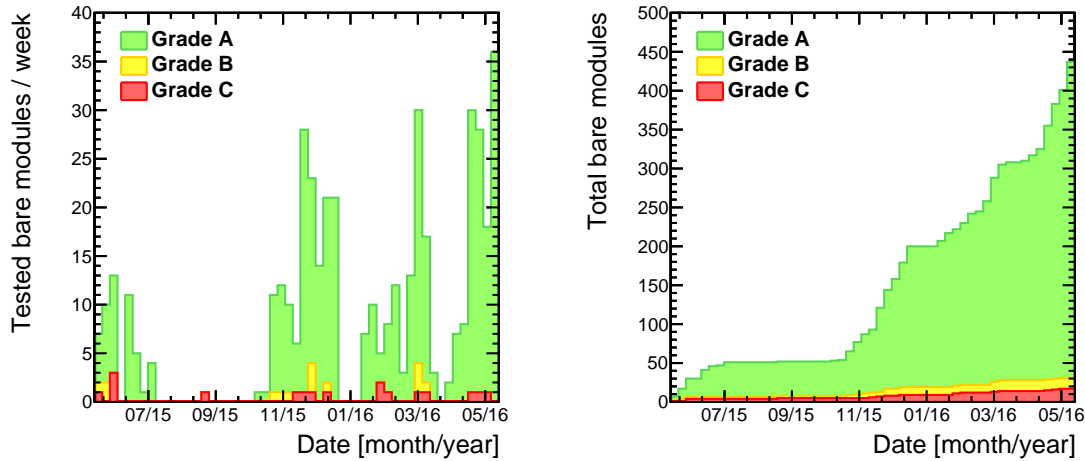
- Grade A: $I_{\text{dig}} \leq 65 \text{ mA}$
- Grade C: $I_{\text{dig}} > 65 \text{ mA}$

High I_{dig} values are a sign for a ROC that has been mechanically damaged during bonding.

The final grade assigned to the bare module is the worst of three single grades from the list above. If a module has been reworked and at least one readout chip has been replaced a “minus” sign is added to the final grade of that module in order to distinguish it from other non-reworked modules.

6.1.3.2 Results

The KIT bare module production at IPE lasted for approximately one year, from May 2015 to May 2016, and during this period 437 bare modules have been produced and tested in total. Out of these 406 (or 92.9%) have been classified as grade A after testing on the bare module probe station, 14 as grade B (3.2%) and 17 as grade C (3.9%). The total yield of good bare



- (a) Weekly rate of bare modules tested at the bare module probe station at IPE. The distinctive periods during which no modules were tested can be attributed to a shortage of readout chips available for bonding.
- (b) Cumulative number of tested bare modules over time. The steeply increasing number of grade A bare modules together with the uncorrelated numbers of bare modules graded B or C are a clear sign of the steadily improving production quality.

Figure 6.8: Production rate and classification of the KIT bare modules. The coloring distinguishes the different classification grades A, B and C [Col16].

modules usable for production of full detector modules obtained by adding up the modules graded A or B is 96.1 % and is a sign of the excellent quality of the KIT bare module production process which has been developed and carefully tuned in the last years.

The bare module production rate expressed as number of tested modules per week is displayed in figure 6.8a where the coloring distinguishes the different grades. The distinctive periods where no bare modules were built and tested can practically all be assigned to interruptions caused by the delayed delivery of bumped readout chips by RTI. Figure 6.8b shows the cumulative amount of tested bare modules as a function of time which closely follows the production. While the number of grade A bare modules increases steeply during the different production periods the numbers of modules graded B or C stay extremely low and are not correlated to the total number of produced modules. This is a clear sign that the quality of the production has steadily improved over time.

The reason for the few modules with grades B or C are mostly related to the silicon sensor since the observed leakage current after bonding had increased to values above $2 \mu\text{A}$ even if the sensor had been tested good before during IV measurement at IEKP. This behaviour was observed mainly at the beginning of the production and a dedicated measure has been introduced in the IPE flip-chip bonding process to detect problematic sensors before the complete bare module is built. After bonding of the first readout chip the incomplete module is directly placed on the bare module probe station and an IV measurement is performed. Only if the result is fine the module is returned and the remaining fifteen chips are bonded, otherwise it is discarded. This procedure helped to save a significant amount of material while only causing a minor increase in the total required bonding time.

Afterwards the completed bare modules show a tendency to keep the good IV behaviour which is a sign of the bad IV characteristic not being related to damage from the bonding process itself. It rather points to questionable results from the IV measurement performed at IEKP before bonding. The IEKP measurement uses a special one-sided connection scheme (cf. section 5.2.1) required by the fact that no readout chips have yet been bonded to the sensor which could provide the ground contact. Instead it relies on the cutting edge of the sensor

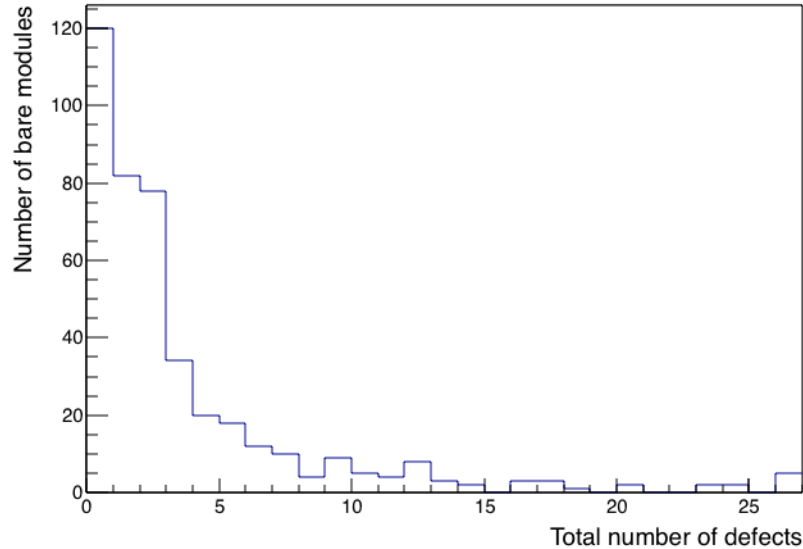


Figure 6.9: Distribution of the total number of defects detected during testing of the bare modules produced at KIT (the last bin includes all modules with more than 25 defects). The number of defects is a combination of missing bump connections found by the KIT bump-bonding test and dead and noisy pixels detected by the PixelAlive test. 30% of all bare modules show exactly zero defective pixels and 90% of the bare modules have less than 11 defects.

to connect the bias ring to ground which might cause discrepancies in the measured current compared to the values obtained at the bare module probe station which uses the intended two-sided connecting scheme.

The quality of the bump bond connections between sensor and readout chips is determined excellent by the KIT bump-bonding test and has also been confirmed by the later X-ray tests (see section 7.2). The average number of defective pixels per bare module (which is the combination of missing bump connections and dead and noisy pixels) varies between four for the grade A bare modules and nine for the other two grades. A distribution of the number of defects for all bare modules is shown in figure 6.9. 30% of all produced bare modules have exactly zero defective pixels and 90% of the bare modules show less than 11 defects while the worst bare module still only has 62 defects (which corresponds to less than 0.1% of the total number of bump bond connections).

475 silicon sensors with grade 1 have been used during the production, out of which 8% had to be sorted out either before bonding due to the results from the optical inspection or after bonding the first readout chip using the procedure described above.

More detailed information and numbers about the results of the KIT bare module production can be found in [Col16].

6.2 HIGH DENSITY INTERCONNECT PREPARATION

The preparation of the High Density Interconnect (HDI) is the next step in the Barrel Pixel Module production. The HDI is a very thin flexible PCB made of polyimide which is optimized for low mass and thus little contribution to the material budget of the detector. It contains the necessary traces to distribute both power and the clock and trigger signals from the token bit manager (TBM) ASIC to the sixteen readout chips of a module and at the same time routes their data lines back. Its basic technology was already used for the modules of the current detector but the design was completely redone to fit the needs of the new readout chips and

the new module connection scheme which now features a single lightweight Molex connector instead of two soldered cables. Additionally it includes several surface-mounted components like capacitors and resistors.

The HDI is produced centrally on large substrates by the same company that already produced the HDIs for the current detector, Hightec MC AG in Switzerland. After production every HDI is optically inspected by Hightec for mechanical defects or bad solder connections and every circuit path is tested for its conductivity with the help of probe needles.

The preparation at the production centers consists of two steps which are described in the next sections. At first the TBM is glued to the HDI and wire-bonded to the corresponding pads. In a second step the electrical functionality of the subassembly is tested. While the gluing is done in the IEKP clean room the wire bonding and electrical testing is performed in the bonding laboratory. Both locations were already used for the production of the modules and petals for the endcaps of the current CMS tracker (cf. section 2.2) and have been upgraded and adapted to the new requirements of the Phase I module production.

6.2.1 TOKEN BIT MANAGER GLUING AND WIRE BONDING

The TBM controls the readout sequence of the readout chips on a module and multiplexes their data output into a 400 MHz stream which is sent out as a differential electrical signal via the attached cable [Bar15]. It has been designed at Rutgers University in the US and is produced in an engineering wafer run by IBM. After production the complete wafers (with more than 1400 TBMs each) are sent back to the US where the colleagues from the FPIX collaboration perform the testing of every TBM. This is done with the help of a specially designed needle card which includes four readout chips and a FPGA to simulate a pixel module. Bad TBMs are marked with ink dots to make sure that they are not used for production. Afterwards the wafers are cut and the singulated TBMs are delivered to the European BPIX module production centers.

For the TBM gluing a dedicated chuck shown in figure 6.10 has been designed and produced at KIT which is also used at the University of Hamburg and supports the parallel gluing of eight TBMs. The HDIs are fixed with Kapton tape to small aluminum handles with vacuum holes (cf. figure 6.11) and a quick measurement of the resistance of the ground plane of the HDI is performed with a Keithley benchtop multimeter before the actual start of the TBM gluing. This measurement has been added during the production since some HDIs were found to have a too high resistance only after being built into full modules at PSI. The resulting voltage drop on the ROC supply lines renders the modules unusable.

The populated handles are then placed on the jig where the HDIs are additionally fixed by vacuum. A bridge which guides the glue application stamp is aligned above the HDIs and the Araldite 2011 two-component glue is applied with the stamp (cf. figure 6.10). Afterwards the TBM is picked up with vacuum tweezers and manually positioned on the HDI. A guided placement tool is not necessary since a placing precision of only ± 0.5 mm is required for this step.

After curing the glue for 24 h the electrical connections between TBM and HDI are established using an industry standard wedge-to-wedge wire bonding technology with a 25 μ m AlSi wire. The HDIs are thus transported to the IEKP bonding laboratory where the Hesse & Knipps BondJet 710 wire bonding machine is situated. Another custom-made chuck is mounted on the machine and allows to fix the HDI while still being attached to the handle. The positions of the wire bonds have been taught only once at the beginning of the production and afterwards the bonding just requires the loading of the program and an optical alignment on four distinct markers on both HDI and TBM before the connections are made automatically.

The quality of bonding is checked by optical inspection of every HDI after bonding and the mechanical strength of the wire bond connections is probed both on sample basis and on

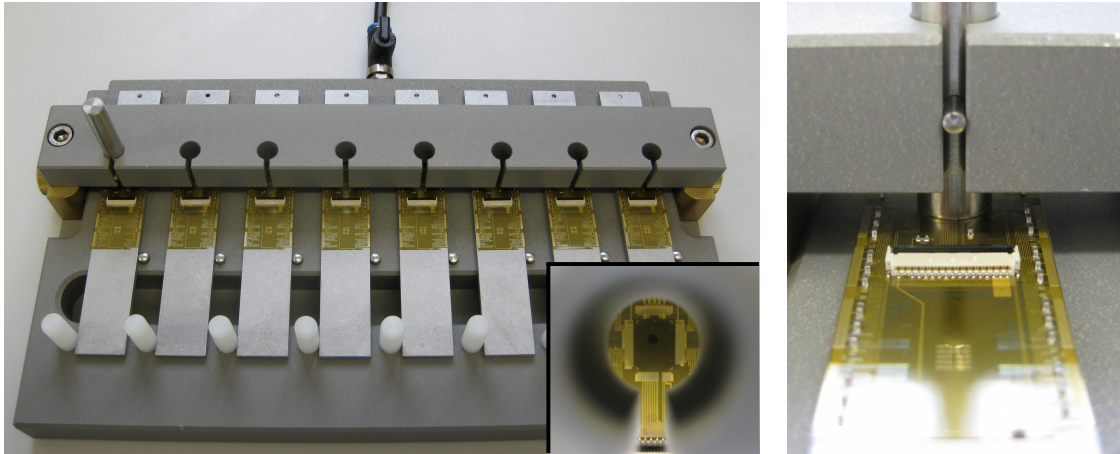


Figure 6.10: TBM gluing chuck designed by KIT. The picture shows an overview of the complete chuck populated with eight HDIs with a magnified detail of the aligned guiding bridge (left) and a close-up view of the stamp depositing glue on a HDI (right).

dedicated test material by pull-testing some of the placed bonds. This method determines the force necessary to either break the wire or lift it off from the pads by pulling the wire upwards with a tiny hook attached to scales. Typically a pull-strength larger than 12 g per bond was obtained, which is very good compared to the theoretical tensile strength of the wire of 15 g according to the manufacturer.

6.2.2 HDI TESTING

After gluing and wire bonding the complete subassembly has to be tested electrically before it can be used for module production since the later gluing of the HDI to the bare module is an irreversible process and a faulty HDI compromises the quality of the whole module and wastes the expensive bare module.

The HDI test setup is located next to the wire bonding machine allowing direct testing of the produced subassemblies. The main part of the setup is a special station equipped with a z-stage holding both a custom-made needle card and a relay board switching the connections to the different needles. The HDI on its handle is placed on the station base plate below the needle card and afterwards the z-stage is slowly lowered until the needles connect the dedicated test pads on the HDI. The complete station and a magnified view of the needle card being in contact position with the HDI are shown in figure 6.11.

The other components of the setup comprise an oscilloscope to check the signal quality, a digital test board to communicate with the TBM, a high voltage power supply to test the resistivity of the HDI high voltage circuitry and several low voltage power supplies to power the equipment. Both the DTB and the relay card are connected to a standard PC running Linux and `psi46test`, another C++ software written for usage with the digital test board. Compared to `pXar`, it is more basic and does not feature a GUI but allows access to low level DTB functions like the adjustment of the generated operating frequency for the attached module. In the HDI test this function is used to reduce the operating frequency to 10 MHz (compared to the nominal 40 MHz) due to the lower signal quality of the needle card connection. A centrally provided script is then executed within `psi46test` to perform the different test steps.

A detailed description of both the test setup and the test procedure is available as an internal CMS note [BM14].

The basic steps of the test procedure are:

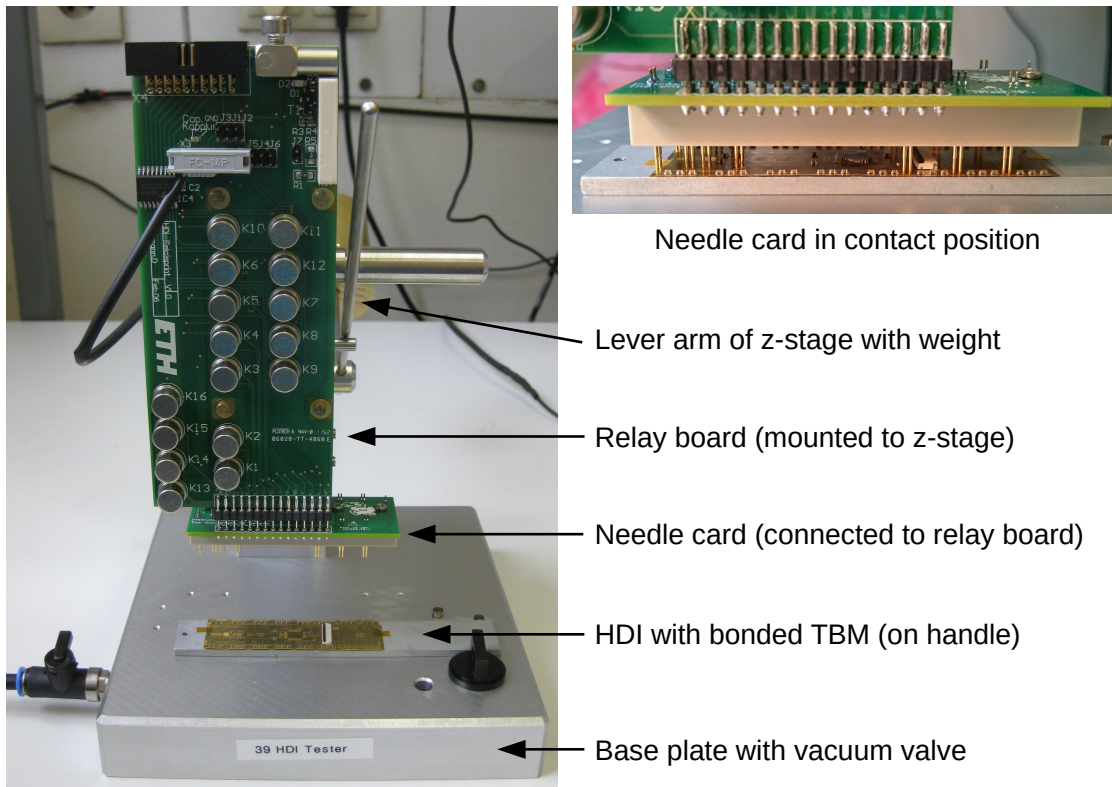


Figure 6.11: HDI test station with needle card and relay board. The picture shows an overview of the complete station with HDI and needle card mounted to the z-stage (left) and a magnified view of the needle card in contact position with the HDI test pads (right).

1. Placement of the HDI on the base plate of the test station and fixation with the help of vacuum.
2. Careful lowering of the needle card until the needle tips are in contact with the test pads on the HDI.
3. Execution of the test script within the psi46test software.
4. Checking of the digital and analog currents drawn by the TBM. The analog current should always be zero.
5. Examination of multiple signal types sent by the TBM to the (not yet connected) readout chips of the first HDI sector. They are received by the needle card and displayed on the oscilloscope where they are visually checked by the operator according to the specifications defined in [BM14].
6. Repetition of the signal examination for the other three HDI sectors by switching the oscilloscope connections with the relay board.
7. Execution of the high voltage test. 600 volts are applied to the HV circuit on the HDI and routed back to the DTB via the needle card and the relay board. The relay board has an integrated series resistance of 100 k Ω and thus the observed current should be around 6 mA. If it is different the HV circuit is most probably damaged and the HDI should not be used.
8. Raising of the needle card and removal of the HDI from the test station.

At the end of the test procedure the HDI is classified with a simple binary pass or fail grade depending on whether all signals and currents have been found correct according to the specifications or not. The results are then added to the Phase I production database and the good HDIs are transported back to the clean room where they are used for module production.

In total more than 2100 HDIs have been produced by Hightec and delivered to the collaboration in multiple batches. KIT has received 486 HDIs out of which 432 have been electrically tested and 420 have passed all tests and were classified as good for module production. This corresponds to a very high yield of 97.2% of good HDIs. The remaining 12 bad HDIs can be divided into two groups where one half showed problems with missing or bad signals on one or more HDI sectors while the other half had problems with the high voltage circuitry.

The 54 untested HDIs have been already sorted out during prior optical inspections performed either before TBM gluing or after wire bonding. They can be divided into three categories of failure modes:

BROKEN SOLDER CONNECTIONS: 24 HDIs showed broken solder connections at at least one pin of the Molex connector pointing to a flawed reflow soldering process. This might also be the source of the high voltage circuitry problems found during electrical testing because systematic checking of each pin with the help of a needle was only introduced after the collaboration was made aware of that problem.

MISSHAPED CUT-OUT: 13 HDIs of the first batch showed a misshaped cut-out at the alignment notch damaging the internal ground plane. This points to bad laser cutting and was corrected for the later batches.

OTHER MECHANICAL DAMAGE OR POLLUTION: The remaining 17 HDIs showed multiple types of mechanical damage like kinks, bends or scratches mostly from packaging or pollution of the wire bond pads caused by the flux used for soldering of the surface-mounted components.

All listed failure modes must have appeared already during production of the HDIs but were not found by the in-house quality control at Hightec.

6.3 PIXEL MODULE GLUING

The final steps of the Phase I pixel module production consist of the joining of the different subassemblies and the wire bonding of the readout chips. Like for the HDI preparation these steps are performed in the IEKP clean room and in the bonding laboratory. An overview of the module gluing line setup at the clean room is given in figure 6.12 where the TBM gluing chuck mentioned in section 6.2 is visible in the foreground. In the background four sets of three different gluing stations each are set up which enable the parallel gluing of four modules. The three different station types are all based on the same design with a vacuum base plate and a z-stage like it is also used for the HDI test station (cf. figure 6.11) but they are equipped with specific attachments and chucks. All gluing stations are connected to a central vacuum vessel mounted between the tables.

A stereo microscope with camera and LCD screen mounted on a movable stand together with a rechargeable battery pack allows the optical inspection and the alignment of the components on all stations. A rotary vane pump providing the vacuum for the necessary fixing and lifting of components is placed outside the clean room to avoid contamination of the room and also disturbance of the operators.

6.3.1 BASE STRIP GLUING

The first step in completion of the module is the gluing of the base strips to the bare module. The base strips are made from silicon nitride (Si_3N_4), a technical ceramic chosen to avoid me-

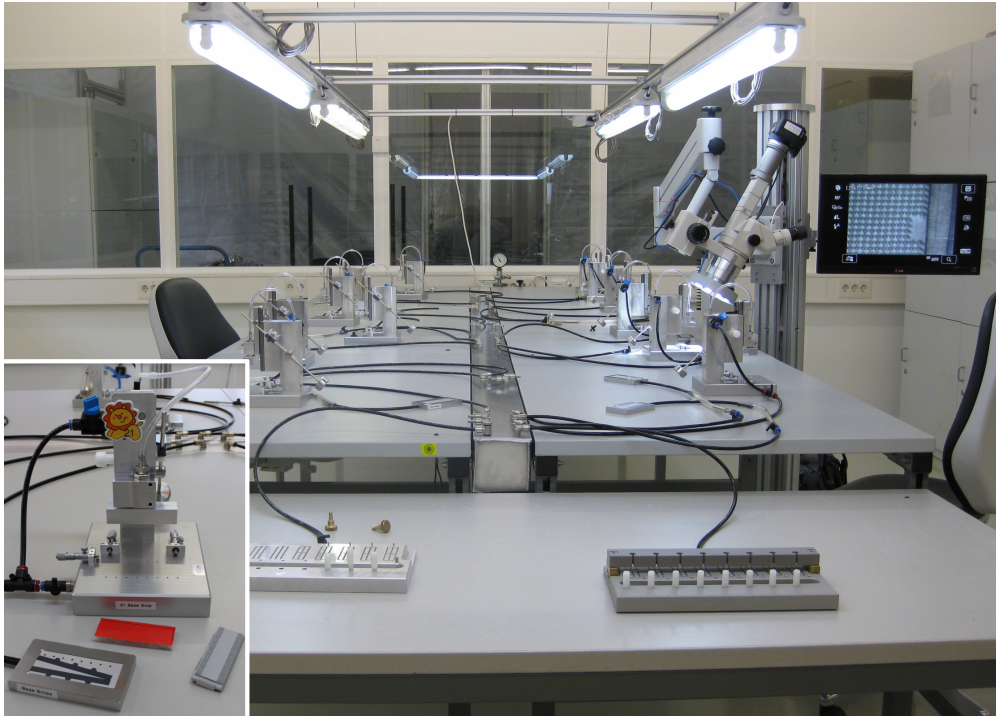


Figure 6.12: Overview of the KIT module gluing line in the clean room together with a magnified inset showing a single gluing station with its accessories. Four sets of three different stations each are set up and enable the parallel gluing of four modules. A movable stereo microscope with camera and screen allows the optical inspection and alignment of the components on all stations.

chanical stress in the module since its coefficient of thermal expansion (CTE) is close to that of pure silicon which is the base material of both the readout chips and the sensor. The silicon nitride wafers are produced by Kyocera Corp.³ in Japan. The base strips are then laser-cut from the wafers at a Swiss company and distributed to the different production centers.

At the production centers the base strips have to be checked for flatness and their thickness has to be measured since first deliveries have shown a deviation from the nominal wafer thickness of $200\ \mu\text{m}$ ordered from Kyocera. To ensure good thermal contact of the modules to the carbon fibre facets of the mechanical structure of the detector the two base strips used for a module have to be of the same thickness to avoid any tilt. At first the flatness is checked by eye with the help of a straightening plate and all base strips bent by mechanical stress from laser cutting are sorted out. Afterwards the thickness of each base strip is measured manually at three points with a micrometer screw and any wedge-shaped base strip is removed. The remaining good base strips are then sorted into $5\ \mu\text{m}$ bins according to their thickness which allows the later gluing of matching pairs.

A distribution of the thicknesses of the base strip pairs used for module production at KIT is shown in figure 6.13. A systematic deviation from the ordered nominal wafer thickness of $200\ \mu\text{m}$ is indicated by the two distinct peaks at $200\ \mu\text{m}$ and $212\ \mu\text{m}$ and also the mean of $207.8\ \mu\text{m}$. Additionally there is a large spread of more than $50\ \mu\text{m}$ between the minimal and maximal values of the distribution. This is a sign of an unreliable wafer production process at Kyocera. Thickness measurements for the bent or wedge-shaped base strips sorted out after checking are not available since they were not recorded.

In total about 1150 base strips have been delivered to KIT and 75% have passed the measurements. At the beginning they were used for gluing studies and afterwards for the module

³ Kyocera Corp. was actually founded as Kyoto Ceramic Company.

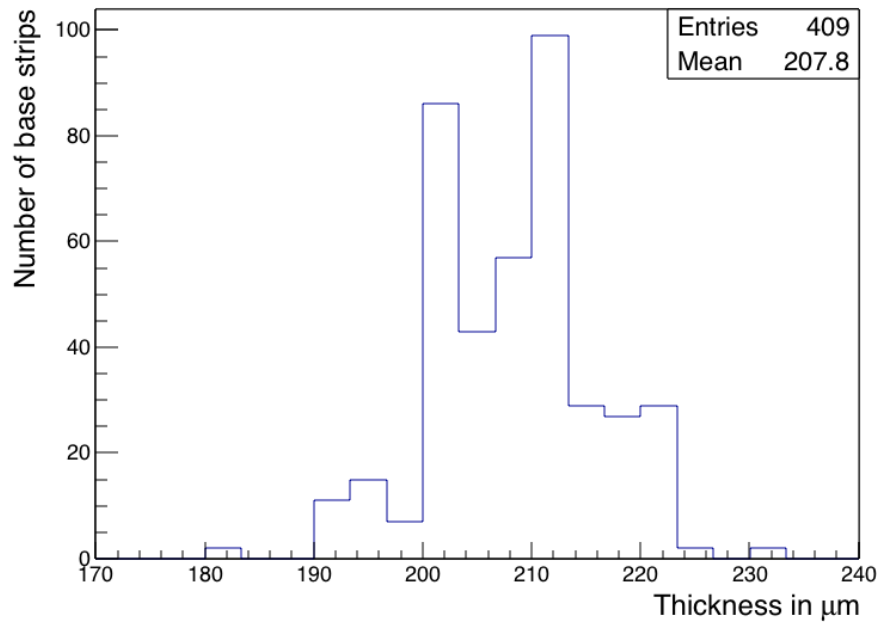


Figure 6.13: Distribution of the thicknesses of the base strip pairs used for production of Phase I pixel modules at KIT. The two distinct peaks at 200 μm and 212 μm and also the mean at 207.8 μm indicate a systematic deviation from the nominal wafer thickness of 200 μm ordered from Kyocera while the large spread of more than 50 μm is a sign of an unreliable wafer production process.

production. The remaining ones have either been misshaped or destroyed during handling.

One of the handling steps that caused the breakup of several base strips is the necessary deburring of the base strips which was introduced after it was found out at KIT that the laser cutting leaves a burr at the edges which cannot be detected during the flatness check because of its small size. It was rather detected during gluing studies performed by several production centers at the beginning of the production. During base strip gluing the base strips have to be held in position with vacuum and despite no detectable leaks, it was shown that glue had been sucked into the very small gap between base strip and vacuum chuck and caused the base strip to adhere to the chuck. A detailed inspection of the base strips at KIT then revealed the existence of the burr. Images of both the problematic base strips and the burr are displayed in figure 6.14.

The deburring is performed by grinding all base strips edges on a ceramic plate dampened with isopropyl alcohol (IPA). After this procedure was adopted by the collaboration the problem of glue being sucked underneath the base strips has not shown up again at the production centers.

The subsequent base strip gluing is performed in a sequence of steps using two different gluing stations. The glue deposition station together with a custom rubber stamp (cf. figure 6.15a) is used to deposit a pattern of Araldite 2011 two-component glue on the base strips and afterwards the bare module gluing station is used to place the bare module on the prepared base strips. The basic sequence is summarized below.

A comprehensive description of the steps including detailed pictures can be found in the Barrel Pixel Module Assembly Manual [Str11] which was originally conceived for the Phase 0 module production but still provides a valid source of information since the Phase I pixel module is just an evolved version of the original one.

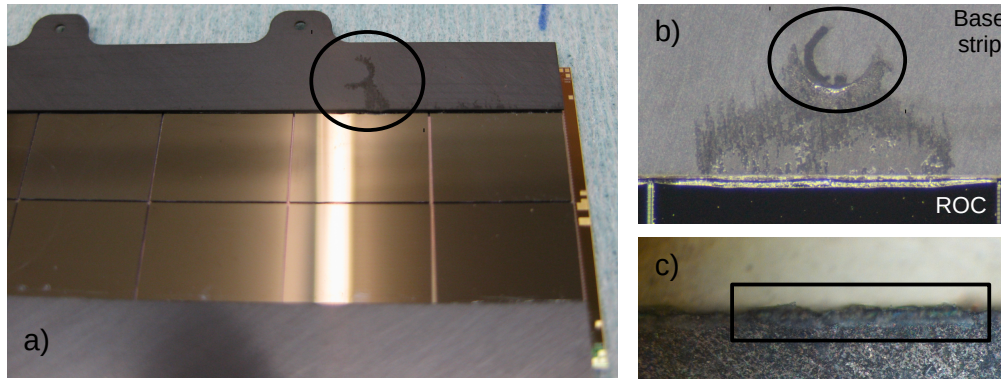
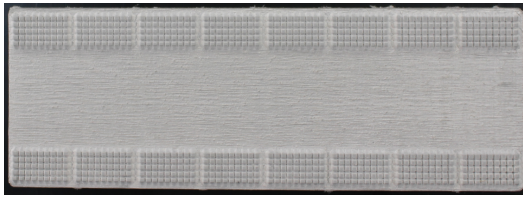


Figure 6.14: Indications and cause of problems during base strip gluing.

- a) View of the bottom side of a problematic bare module adhering to the chuck indicating that glue has been sucked below the base strip.
- b) Magnified view of a different problematic base strip where the glue was even sucked into one of the vacuum openings of the chuck.
- c) Microscope image of a base strip edge. The small depth of field allows the identification of the cause of the problems: a (blurred) burr at the base strip edges due to the laser-cutting.

1. Selection of a base strip pair with matching thicknesses, cleaning with isopropyl alcohol, placement on the associated chuck and fixation with the help of vacuum.
2. Visual inspection (and correction) of the base strip alignment on the chuck.
3. Placement of the base strip chuck on the glue deposition station, lowering of the gluing stamp mounted on the z-stage (without glue) and visual inspection of the alignment.
4. Placement of the bare module on the associated chuck, fixation with vacuum and visual inspection of the alignment.
5. Placement of the bare module chuck on the bare module gluing station, lowering of the suction head mounted on the z-stage and visual inspection of the alignment.
6. Lifting of the bare module with the help of the suction head and removal of the chuck.
7. Placement of the base strip chuck below, lowering of the head with the bare module and visual inspection of the alignment.
8. Lifting of the bare module and removal of the base strip chuck.
9. Dipping of the gluing stamp into the glue basin.
10. Placement of the base strip chuck on the glue deposition station and deposition of the glue pattern on the base strips.
11. Placement of the base strip chuck on the bare module gluing station and lowering of the bare module on the base strips.
12. Removal of the head vacuum after 10 minutes of curing and insertion of a piece of foam material in between head and bare module to distribute the force homogeneously.
13. Removal of the bare module with attached base strips from the station after 24 h of curing and detailed visual inspection of the gluing quality.

Since the base strips form the only contact of the module to the mechanical detector structure it is not only important for the cooling to ensure a good contact between base strips and mounting facet but also a good glue joint between base strips and readout chips. All sixteen



(a) Rubber stamp design used for the entire base strip gluing during production at KIT. It yielded the best results out of several investigated layouts.



(b) Gluing test showing very inhomogeneous glue pattern. While the dotted structure is still perfectly visible at the upper right corner it has vanished completely at the lower left and the glue even spilled over. This is an example of bad alignment of the stamp with respect to the base strips.

Figure 6.15: Rubber stamp for base strip gluing and resulting glue pattern from a base strip gluing test with a glass dummy.

chips together have a power consumption of about 2 W and thus form the main source of heat on the module.

A lot of effort has been invested in the optimization of the glue joint by fulfilling all requirements. These requirements are:

- high filling factor of the glue layer,
- uniform thickness of the glue layer,
- no spill-over of the glue on the chuck or the wire bonding pads of the readout chips.

The optimization process is a complex interplay of the alignment of the base strip gluing station, the design of the rubber stamp used for glue deposition, the depth of the glue basin, the duration the stamp is dipped into the basin and the duration it is left on the bare module to deposit the glue afterwards. Since it is difficult to assess certain properties of the glue joint like the filling factor if a real bare module is glued to a pair of base strips most of the optimizations have been done with glass dummies. The glass dummies are cut to the same size as the footprint of the readout chips on a bare module and replace the bare module in the gluing tests. In order to save valuable production material the very first tests have even been done not with glue but with hand cream which can be wiped off easily.

A typical result from a glass dummy gluing test done with real glue is shown in figure 6.15b. While the dotted structure of the gluing stamp is still visible at the upper right corner it has vanished completely at the lower left corner and the glue even spilled over the base strip edge. Such a result can be attributed to bad alignment of the stamp with respect to the base strips.

6.3.2 HDI GLUING

After the base strips are safely attached to the bare module the next step on the way to a complete module is the gluing of the HDI to the sensor side of the bare module. This is again performed in a sequence of steps using the same glue deposition station as before but equipped with a different rubber stamp and the HDI gluing station to place the HDI on the prepared bare module. During the single steps special attention needs to be paid to the wire bonds connecting the TBM to the HDI to make sure that they do not get crushed. The HDI needs to be perfectly aligned to the cut-outs in the vacuum suction head of the gluing station made both for the wire-bonded TBM and for the Molex connector (cf. figure 6.16). The basic steps are listed below:

1. Visual inspection of both the bare module (with base strips) and the HDI.

2. Placement of the HDI on the HDI gluing station, lowering of the suction head mounted on the z-stage and visual inspection of the alignment.
3. Lifting of the HDI with the help of the suction head and removal of the handle.
4. Placement of the base strip chuck with the bare module on the HDI gluing station, lowering of the HDI and visual inspection of the alignment.
5. Lifting of the HDI and removal of the base strip chuck from the station.
6. Placement of the base strip chuck on the glue deposition station, lowering of the glue stamp mounted on the z-stage (without glue) and visual inspection of the alignment.
7. Dipping of the gluing stamp into the glue basin.
8. Deposition of the glue pattern on the sensor side of the bare module.
9. Placement of the base strip chuck on the HDI gluing station and lowering of the HDI on the sensor.
10. Removal of the head vacuum to allow a better adaption of the HDI to the glue.
11. Removal of the completed module after 24 h of curing and placement on the module handle.

A detailed visual inspection of the gluing quality follows and the module is also scanned in high resolution for future reference with the help of a repurposed flat bed scanner.

In case of the HDI gluing the quality of the glue joint is equally important as for the base strip gluing even if the power consumption of the TBM is low and does not require a perfect cooling contact. Instead the wire bond pads at the edges of the HDI need to be well supported since any cushioning of the pads can reduce the bonding quality. The basic requirements to the glue joint between HDI and sensor are therefore the same as listed above and also on this topic a lot of time has been invested into the optimization.

Since the HDI is rather expensive and the inherent transparency of its Kapton base material is counteracted by the electrical circuits and the surface-mounted components the gluing tests have been performed with pure Kapton film and silicon dummies as replacements of the original components.

A result of such a gluing test is shown in figure 6.16. While the dotted structure of the gluing stamp is still visible along the center of the HDI it has vanished at the edges where the wire bond pads are located. The bad fill factor in the central region is attributed to a bumpy Kapton surface and thus a bad contact due to bending of the Kapton in the vacuum openings when it is sucked to the pictured suction head. The same effect is observed on real modules since the HDI flex print is equally thin and also gets bent during lifting. Even an immediate removal of the head vacuum after placement of the HDI on the sensor is not able to create a perfect glue joint in the central region.

Since the gluing below the wire bond pads is unaffected and a perfect glue joint in the central region of the HDI is not necessary the results were deemed adequate and the gluing of the modules was performed in that way.

At the end of the gluing of the different subassemblies in the IEKP clean room the module is placed on an aluminum module handle similar to the HDI handle (cf. figure 6.11) before it is transported to the bonding laboratory. Two nylon pins protruding from the handle surface fix the module at the base strip holes to prevent lateral movement.

After wire bonding an additional plastic cover is placed on the module which pushes down the base strip ears and both secures the module against lift-off and protects the delicate wire

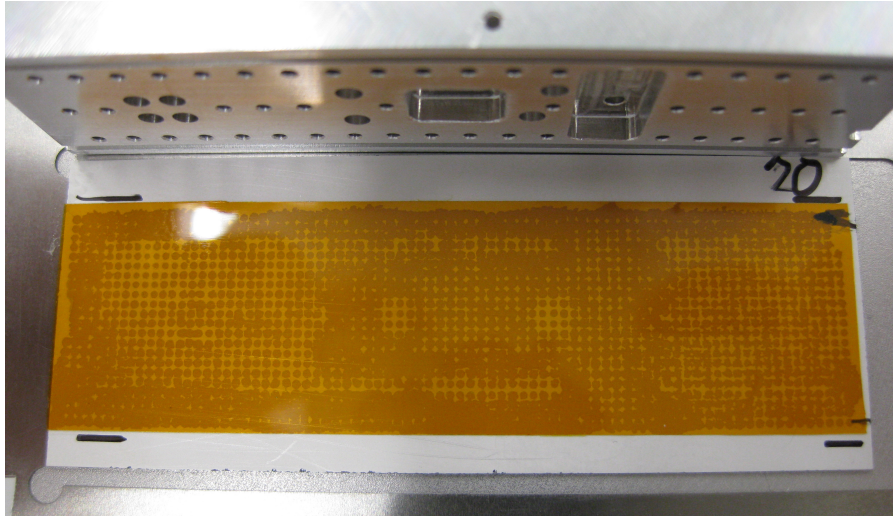


Figure 6.16: Results from a HDI gluing test performed with a Kapton film and a silicon dummy replacing the original components. The dotted pattern of the gluing stamp is still visible below the Kapton in the central region but has vanished at the edges. This result is attributed to bending of the Kapton in the vacuum openings when it is sucked to the suction head shown above.

bonds. The complete handle with cover was designed at KIT in a way that allows the module to stay on it during all tests and qualifications without any need for direct handling until the final mounting on the mechanical structure of the detector is done at PSI. More than 1050 of these handles have been manufactured at the IEKP workshop and also distributed to the production centers at Hamburg and CERN.

6.3.3 MODULE WIRE BONDING

At the IEKP bonding laboratory the electrical connections between HDI and readout chips and sensor are established with the same wedge-to-wedge wire bonding technology that is used for the HDI-TBM bonding (cf. section 6.2). At first three bonds for the sensor bias voltage are placed between the high voltage pad of the HDI and the silicon sensor and then the readout chips are connected to the pads on the HDI by 560 bonds.

The total time needed to bond a complete module is 30 minutes equally distributed between the prior alignment and dust removal performed by the operator and the automated placement of the wire bond connections by the machine. At the end the quality of the bonding is visually checked with the help of a stereo microscope available at the bonding machine. Bonds showing problems like lift-offs are manually removed and replaced. A completely bonded pixel module with attached sacrificial cable for testing and qualification is shown in figure 6.17.

During the production it was found that the number of bonding problems depends on the relative humidity (RH) in the laboratory originating from the weather conditions outside. Above 45% RH the number of bonds with lift-off problems on the HDI side increased steeply and made successful bonding impossible. The installation of an air dryer helped to stabilize the relative humidity in the room below 40% and to decouple the achievable bonding quality from the environmental conditions.

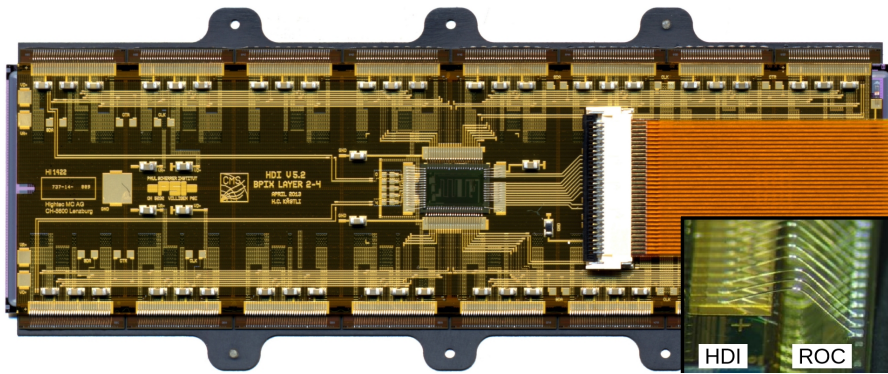


Figure 6.17: Completely wire-bonded KIT Phase I pixel module and magnified detail of the bond loop shape. The 560 wire bonds connecting the 16 readout chips are visible at the long edges of the HDI while the bias voltage connection of the sensor is provided by the three bonds connecting the sensor at the upper right corner. The sacrificial cable used during testing and qualification is already attached.

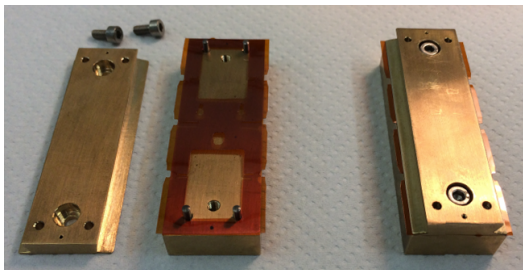
6.3.4 MODULE CAP GLUING

The final module cable replacing the sacrificial one visible in figure 6.17 is a thin and flexible twisted-pair cable since the cabling from the modules to the Pixel Optical Hybrids (POHs) on the supply tube needs to fit into tight spaces and around sharp corners. The downside of this flexibility is the fact that such a cable can accidentally move and damage the wire bonds of the modules it is routed along on its path to the POH. In order to protect the module and especially the wire bonds after the installation on the detector mechanics each module is equipped with a cap made from a 75 μm thick Kapton film which is glued to the surface-mounted capacitors on the HDI.

Since the final designs of the protection cap and the necessary mounting tools were not available during module production, direct mounting of the cap at KIT was not possible. Instead all produced modules have been equipped with the cap in one go after the delivery to ETH Zürich. Personnel from KIT and RWTH stayed in Zürich for three weeks to perform both the cap gluing and the reception testing of their modules.

The first step of the cap mounting procedure is the preparation of the cap itself since it is delivered from the company as a flat piece of cut Kapton film whose edges still need to be folded downwards to effectively protect the wire bonds between readout chips and HDI after mounting. The folding is performed manually with the help of a chuck which is shown in figure 6.18a. Afterwards the mounting of the cap is performed with the same type of gluing station used for module production but equipped with a new vacuum suction head to hold the cap. Silicone-based glue is stamped on the upper sides of the capacitors on the HDI and the cap is slowly lowered with the help of the z-stage of the gluing station until it sits on the module. A KIT pixel module with the protection cap in place is shown in figure 6.18b.

After curing the glue for about one hour the module is placed in the ETH test setup to perform the final reception test. The result of this last test (combined with the qualification results obtained before) determines if the module is mounted on the detector mechanics after shipment to PSI, if it is kept as possible spare or if it should not be used at all due to non-recoverable damage. The basic test procedures used for module testing and qualification are described in section 7.



(a) Preparation of the Kapton module cap. The edges of the initially flat cap have to be folded downwards with the help of a special chuck after delivery from the company.



(b) KIT module with placed cap. The folded edges now protect the wire bonds connecting readout chips and HDI.

Figure 6.18: Preparation of the module protection cap and KIT pixel module with cap. The module is now ready for final testing and mounting on the detector mechanics.

MODULE TESTING AND QUALIFICATION

After gluing and wire bonding the functionality of the modules produced at KIT has to be tested. This is done in two steps. First the modules are tested electrically and the good modules are then checked for dead bump bond connections by inducing signals in the silicon sensor through X-rays. Only modules which pass both steps are packaged and shipped to RWTH Aachen as shown in the production workflow diagram in figure 6.1. In Aachen the complete qualification and the final classification of the modules according to the grading parameters defined by the collaboration is performed.

7.1 ELECTRICAL TEST

The electrical test of the modules is performed at IEKP in the pixel laboratory where a dedicated test station has been set up at the beginning of the production. The test sequence consists of three steps of standard tests defined in pXar: Pretest, Full Test and IV measurement. The sequence is executed twice at temperatures of -20°C and $+17^{\circ}\text{C}$.

The Pretest is executed first and verifies the functionality of the readout chips as a whole. Since each readout chip is initialized in a safe state by the internal power-up reset circuit, it has to be programmed in order to be functional. Being able to communicate with the chip is thus of prime importance. The communication is tested by trying to program DACs of the chip, especially the VANA DAC which controls the analog power consumption of the chip by adjusting an internal voltage regulator. If the chip is programmable, the analog current drawn by the chip (from the DTB) should change measurably and the current is then optimized to the target value of 24 mA defined by the design specifications of the ROC.

Afterwards the reverse communication direction for receiving hit data from the module is established. This is done by configuring the TBM with correct settings for its internal delays which adjust the phases of the different parts of the 400 MHz data signal. Only if the settings are chosen correctly, the output data can be identified by the deserializer implemented in the FPGA of the DTB. The optimal settings are found by scanning a subset of all possible combinations derived from previous measurements of the TBM since a scan of the complete phase space is very time consuming and typically does not yield better results.

The subsequent Full Test performs comprehensive tests of the 4160 individual pixel cells of each chip. It consists of seven steps which are described below.

The final IV measurement checks the quality of the silicon sensor after the handling steps performed during module production.

A subset of the Full Test, namely the PixelAlive test and the KIT bump-bonding test, is already used for the bare module test performed at IPE during module production (see section 6.1.3).

PIXELALIVE TEST: The PixelAlive test checks the functionality of the electronics in the pixel cells of each readout chip. It uses the chip's built-in calibration signal (cf. figure 6.6) to send ten calibration signals into the preamplifier of each pixel cell while reading out the detected hits. For perfectly working pixel cells exactly ten hits are expected while those showing no hits are declared dead. Pixel cells with a high noise level will observe

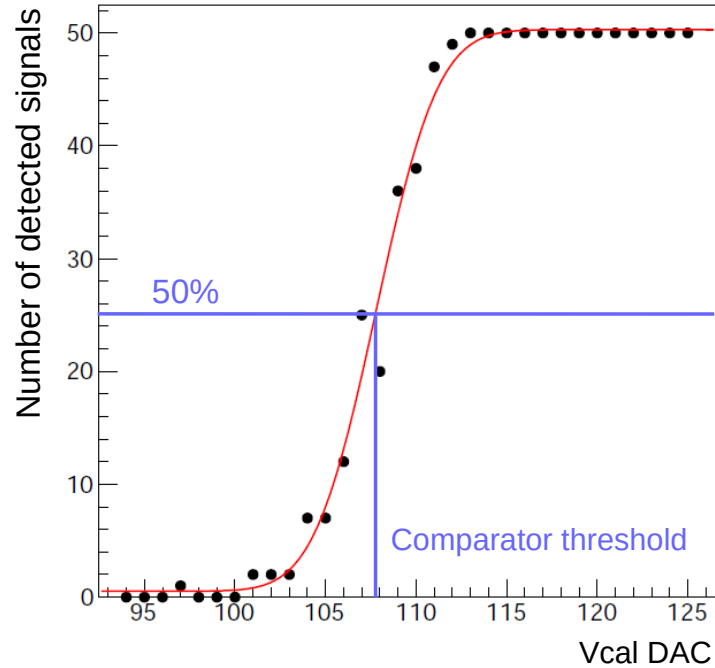


Figure 7.1: Result from the SCurve test of a single pixel. 50 calibration signals are injected for every V_{CAL} DAC value, the number of detected hits (black dots) is recorded and fitted with an error function (red line). The width of the fitted function then gives an estimate of the noise. In addition the comparator threshold can be derived from the point where 50% of the injected pulses are detected.

a number of hits which is either higher or lower than ten. These results are subjected to predefined cuts and classified accordingly. At the same time the test also checks if the calibration signals are detected in the same pixel cell they were injected into.

KIT BUMP-BONDING TEST: The KIT bump-bonding test checks the quality of the bump-bond connections between sensor and readout chip by using the same method as the PixelAlive test but this time the signal is injected into the sensor via the air gap capacitance between readout chip and sensor. A custom KIT bump-bonding test is used since the test is strongly dependent on the separation between sensor and chip which is different for each bump-bonding technology.

SCURVE TEST: The SCurve test measures the noise of the pixels by using the so-called S-curve method. Gradually increasing calibration signals (defined by the V_{CAL} DAC value) are injected into the pixel cell while a fixed threshold is maintained and the detected number of hits is plotted against the height of the injected signal.

Ideally the resulting curve would be a step function since all signals below the threshold should not be detected while all signals above should. In reality the resulting curve is S-shaped and the width of the rise is a measure of the noise. The curve is thus fitted with an error function whose width gives an estimate of the noise in units of V_{CAL} DAC under the assumption of a Gaussian noise distribution. Additionally the curve can be used to derive the comparator threshold by looking at the V_{CAL} DAC value for which 50% of the injected signals are detected. A typical S-curve and the associated fit obtained from this test are shown in figure 7.1. The conversion between internal V_{CAL} DAC units and electrons is discussed only in section 7.3 but the mean pixel noise for a fully depleted sensor is around 140 electrons [Spa16].

TRIM TEST: The Trim test adjusts the thresholds of the individual pixel cells of a ROC since a uniform charge threshold across all pixels is important for the interpolation of the center of a hit cluster. Setting only the global threshold of the chip via the $V_{THRCOMP}$ DAC does not lead to a uniform value because of variations in the transistors from processing. Additionally the threshold of each pixel can be lowered compared to the global value with the help of four so-called trim bits. The absolute charge threshold of a pixel Q_{thr} is thus given by

$$Q_{thr} = Q_{comp} - (15 - \text{trim bits}) \cdot Q_{scale}$$

where Q_{comp} is the global threshold set via the $V_{THRCOMP}$ DAC, Q_{scale} is the gain value of the trim bits defined via the V_{TRIM} DAC and trim bits is the setting of the four trim bits (a value between 0 and 15).

The process of finding optimal settings for both the two global DACs and the individual trim bits of each pixel to balance the threshold differences is called trimming and is performed in several steps. After successful trimming the typical RMS of the threshold distribution of all pixel cells of a ROC is around 1 V_{CAL} DAC [Spa16].

PHOPTIMIZATION TEST: The phOptimization test adjusts the pulse heights of the pixel cells in such a way that the available range of the ADC of the ROC is used optimally. This is performed by optimizing the $PHSCALE$ and $PHOFFSET$ DACs which are responsible for scaling respectively shifting of the signal.

GAINPEDESTAL TEST: The GainPedestal test performs a gain calibration of every pixel by injecting calibration signals covering the full range of V_{CAL} DAC values. The recorded pulse height is then plotted as a function of the height of the injected signal and the distribution is fitted to obtain an analytic description of its shape. The standard implementation in pXar uses an error function to describe the linear rise while the flat part representing the saturation at high charge values is normally outside the ADC range after a successful phOptimization test.

The inverse of the error function is later used to convert ADC values of recorded signal heights into V_{CAL} DAC values.

READBACk TEST: The Readback test checks the readback function of the ROC which allows the inspection of several chip parameters like external supply voltages, internal regulated reference voltages and DAC settings. The parameter of interest is selected via the $READBACk$ DAC and then transmitted back by the ROC as a special payload in the normal event data output. In case of the electrical test of the modules the readback function is configured to return the digital supply voltage while a scan of the DTB output voltage is performed and the linear dependence between the two values is verified. This also allows the calibration of the analog chip current.

7.1.1 TEST SETUP

The test setup used to perform the electrical tests of the modules is shown in figure 7.2. Up to two modules can be tested in parallel on the chuck which is equipped with a cooling system based on Peltier elements and allows measurements in a temperature range from -25°C to $+30^{\circ}\text{C}$. The chuck is placed in a light-tight box with an insertable barrier which further reduces the inner volume since the box is flushed with dry air to prevent condensation. The DTBs are set up outside the box in order to both reduce the number of necessary feedthroughs and to allow active cooling with a fan during testing. A Keithley 2410 high voltage supply is connected to the DTBs and provides the bias voltage for the sensors.

The connection between the modules with attached sacrificial cables and the SCSI ribbon cables of the DTBs is made possible with a special adapter which was designed and produced by KIT for the entire collaboration. Since the Molex connectors only have a specified number

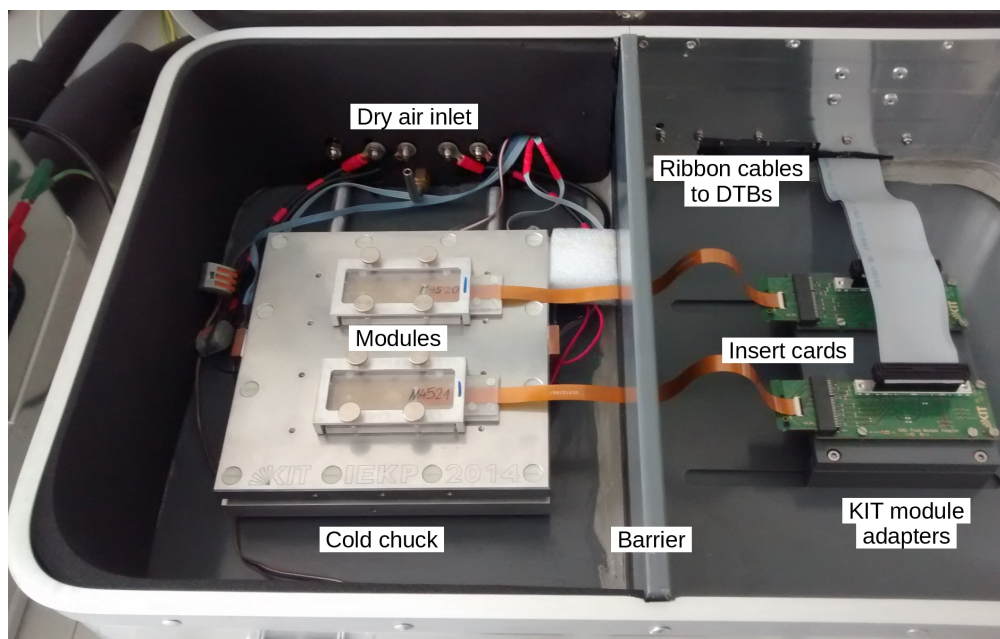


Figure 7.2: Test setup used for electrical tests of modules produced at KIT. Up to two modules can be tested in parallel on the cold chuck which is placed in a light-tight box. The box is additionally flushed with dry air to prevent condensation. The connection of the modules to the DTBs outside the box is performed via special two-piece adapters which were designed and produced by KIT.

of ten mating cycles, a two-piece solution has been chosen for the adapter in order to allow longer usage of the more expensive parts like the SCSI connector. It consists of a small passive insert card which only routes the signal lines from the Molex connector to the card edge and a larger adapter with the appropriate edge card connector, SCSI connector for the DTB ribbon cable and additional surface-mounted components for impedance matching of the differential data lines (cf. figure 7.2). The passive insert card is cheap to produce compared to the adapter and thus allows every module to be equipped with its own card. This approach reduces the necessary number of mating cycles of the Molex connector to the absolute minimum.

The test setup is controlled by a PC running Linux and the necessary software packages to operate the different parts of the setup (pXar for module testing and LabVIEW for temperature control of the chuck). A special Python script written at KIT is used to automate the module tests. The script is called *eComodoro* and it mimics the functionality of a software package named *eComandante* written at ETH Zürich for the same purpose. Since the test setup in Zürich is completely different in terms of the components it was easier to implement an own solution instead of adapting the existing software.

To run an automated electrical test, the names of the modules and other test parameters like bias voltage are modified in the configuration file of *eComodoro* and the test temperature of -20°C is entered in the LabVIEW program. *eComodoro* then parses the file, creates the necessary directory structures and files, and executes two instances of pXar which run Pretest, Full Test and IV measurement consecutively. Afterwards the temperature setting is changed to $+17^{\circ}\text{C}$ and *eComodoro* is run again.

A single electrical test lasts 90 minutes for both modules and thus two modules are completely tested in less than four hours including the time needed for mounting and cooling. This allows a throughput of four modules during normal working hours.

The electrical tests are then analyzed with a local installation of MoReWeb, the software which

is also used by the production database to classify the modules (cf. section 5.4). MoReWeb separately classifies both the electrical test results and the IV characteristic of a module according to a large number of parameters defined by the collaboration and finally creates a set of webpages containing all the results in form of tables and plots. It reports three different grades: one for the electrical test, one for the IV measurement and a combined result (which is the worse of the latter two).

7.1.2 RESULTS

In total 409 modules have been produced at KIT and tested electrically in the setup described above. The result of the tests according to MoReWeb is as follows:

- 235 grade A modules (57.5 %)
- 147 grade B modules (35.9 %)
- 17 grade C modules (4.2 %)
- 10 non-graded (broken) modules (2.4 %)

The main failure mode for the grade B modules is the insufficient scaling of the sensor leakage current with temperature. The relation between two leakage current values of a silicon sensor measured at different temperatures T_1 and T_2 is given by [Chi13]:

$$I(T_2) = I(T_1) \cdot \left(\frac{T_2}{T_1}\right)^2 \cdot \exp\left(-\frac{E_g}{2k_B} \left[\frac{1}{T_2} - \frac{1}{T_1}\right]\right) = I(T_1) \cdot f_s$$

where $E_g = 1.2 \text{ eV}$ is the effective band gap of silicon and k_B is the Boltzmann constant. For the temperatures used for the electrical test ($+17^\circ\text{C}$ and -20°C) the scaling factor in the formula has a calculated value of $f_s = 44$. The IV measurement is graded B by MoReWeb if the real factor obtained from comparing the two IV characteristics is less than 20.

For the 137 modules graded B due to insufficient scaling of the leakage current (corresponding to 93.2 % of all grade B modules), factors down to even 1 have been observed. This means that the leakage current of the CiS sensors does not scale according to the above formula for low temperatures and the currents measured at -20°C are much higher than expected. Although the sensor design is exactly the same as the one used for the current detector this feature was not observed during the former module production since the modules were not tested at low temperatures at that time. A possible explanation are surface currents which begin to dominate the total leakage current for low temperatures but this has not yet been confirmed definitively.

The remaining 10 grade B modules either showed problems with the leakage current (current values above $2 \mu\text{A}$ or slope values above 2 for $T = +17^\circ\text{C}$) or more than 1 % of missing bumps were detected on at least one readout chip by the KIT bump-bonding test. The grading parameters for the IV measurement results and the bump bonding defects are identical to the ones used for bare module testing (cf. section 6.1.3).

Out of 17 grade C modules 15 have severe problems with at least one ROC (sometimes combined with very high leakage current) and the remaining two have a non-working TBM. Since the TBMs are tested on the HDI before usage this result seemed dubious and the TBMs were replaced with new ones which then showed exactly the same problem. This supports the claim that the TBMs themselves were fine and are instead put in an undefined state by non-working ROCs on the modules sending garbage data.

The 10 broken modules which could not be tested successfully at all either have problems with non-programmable ROCs which cause the Pretest to fail or with a disconnected bias voltage pin of the Molex connector due to bad soldering. This mainly happened in the first half of the production when the collaboration was not yet aware of this failure and thus the HDIs were not yet specifically checked.

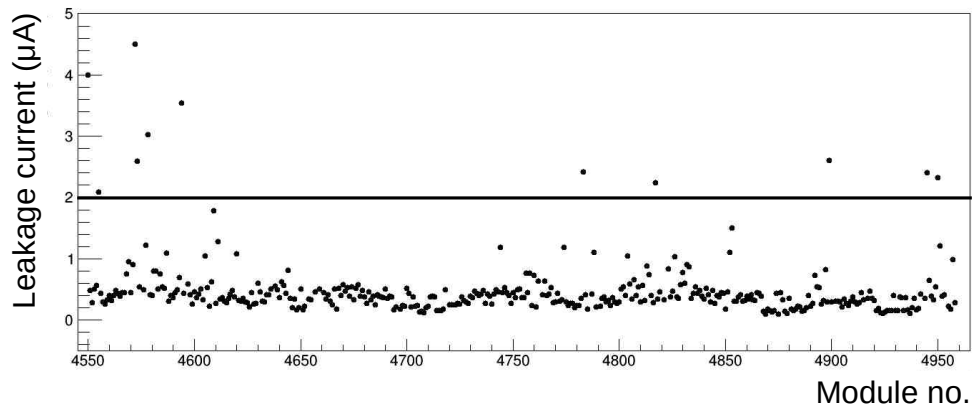


Figure 7.3: Distribution of the leakage currents at -150 V measured at $+17^\circ\text{C}$ during the electrical test of the KIT modules. The black line at $2\ \mu\text{A}$ defines the maximum allowed value for grade A modules. 379 modules (corresponding to 95.2% of all measured modules) have a leakage current below that value with a mean of $0.47\ \mu\text{A}$ and only 19 modules (4.8%) have a value above. These results show that the sensor quality is not systematically degraded by production [Tas16].

During the electrical test the IV characteristic of the silicon sensor is recorded for every module. The measured values at the default operating voltage of -150 V can be used to check the quality of the modules after handling over the course of the production. A distribution of the measured leakage current values of the KIT modules is shown in figure 7.3.

379 modules (corresponding to 95.2% of all measured modules) have a leakage current below $2\ \mu\text{A}$ with a mean of only $0.47\ \mu\text{A}$ and are thus graded A in terms of leakage current. The remaining 19 modules can be grouped in 14 modules with grade B (3.5%) and 5 modules with grade C (1.3%) with a maximum current of $40\ \mu\text{A}$ on one module. Detailed inspection revealed a small hole in the HDI of that module which causes a short circuit between the internal ground plane and the sensor. Besides the small spread around the mean value the only recognizable feature is a tendency towards lower leakage current values for increasing module numbers. This effect was already seen during the IV measurements of the bare sensors.

7.2 X-RAY TEST

The modules found good after the electrical test are then irradiated with X-rays to crosscheck the results of the KIT bump-bonding test with the result of a test method which is closer to the real operating conditions of the modules. As already described in section 6.1.3 the necessary charge carriers can be created in the sensor by irradiation with X-rays or by charged particles coming from a radioactive source like ^{90}Sr .

The basic test principle is to wait until a certain number of hits has been detected in each pixel of the module and then to check if there are still pixels left which have not seen any hit. Since this is statistically unlikely these pixels are either not connected to their pixel cell in the ROC or the associated pixel cell is electrically dead. These pixels are therefore counted as defective.

At IEKP irradiation with X-rays has been chosen to evaluate the bump bond quality since the available ^{90}Sr sources only have a limited opening angle of the electrons created by β^- decay. Thus the source either needs to be placed high above the module to illuminate it completely or the module needs to be scanned with the source. Both possibilities are impractical



Figure 7.4: X-ray setup used for irradiation of modules produced at KIT. The backward-facing primary beam of the X-ray tube is used to create a secondary beam of characteristic X-rays by illuminating the silver target. The modules are placed on the cold chuck on the bottom of the shielding box and get irradiated by the secondary beam.

because a large distance reduces the available rate and the scanning needs a setup equipped with a motor stage.

7.2.1 TEST SETUP

The test setup in the X-ray laboratory used to irradiate the modules is shown in figure 7.4. In order to create a spot size large enough to illuminate two modules in parallel the backward-facing primary beam of the X-ray tube is only used to create a secondary beam of characteristic X-rays which covers a large part of the bottom of the shielding box. This is done by irradiating a silver target mounted in the back of the box. The K_{α} line of the characteristic X-rays of silver has an energy of 22.2 keV which corresponds to a mean charge of 6156 electron-hole pairs created in silicon [DKI⁺03]. A cold chuck identical to the one used in the setup for the electrical test (cf. figure 7.2) is placed on the bottom of the box in the secondary beam and stabilizes the temperature of the modules which get irradiated.

Since the shielding box is not air-tight it is not possible to flush its complete volume with dry air and thus only measurements at temperatures above the dew point are allowed to avoid condensation. The test setup is controlled by a PC running Linux and the necessary software packages to operate the different parts of the setup (pXar for data acquisition with the pixel modules and LabVIEW for control of both the X-ray generator and the chuck temperature).

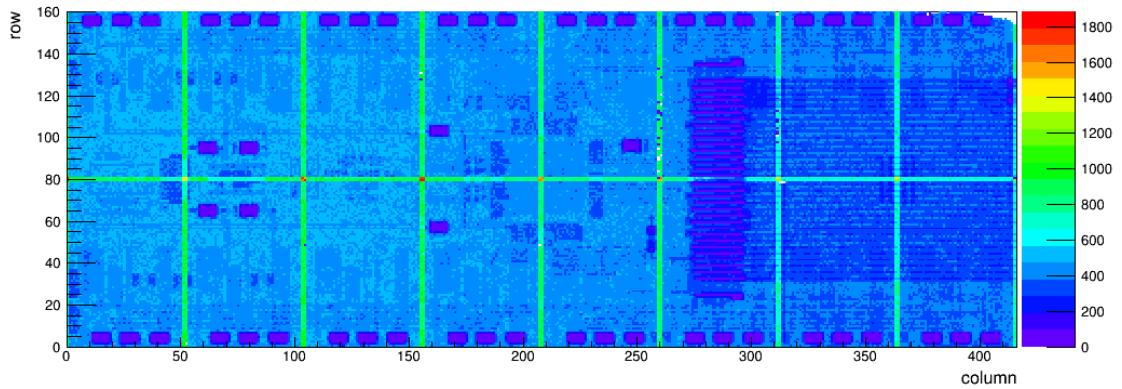


Figure 7.5: Hitmap of KIT module M4682 after irradiation with X-rays. Several defective pixels with no hits are seen in the upper right corner. The complete module has detected 27 million hits which corresponds to an average number of 412 hits per pixel. Pixels below the surface-mounted components of the HDI see less hits due to shielding while the number of detected hits in the larger pixels at the ROC borders is twice the average.

In order to achieve the highest possible rate and thus the shortest time to accumulate the necessary statistics the X-ray tube is run at the maximum allowed power of 2000 W. Hit data is then acquired with pXar from both modules in parallel for 30 minutes. This duration is a compromise between adequate hit statistics in all pixels and the necessary time to take this data since the real time needed for 30 minutes of data acquisition is about a factor three longer (1.5 hours). This is due to the fact that during data acquisition the events are only stored in the onboard memory of the DTB and not directly transferred to the PC. When the memory is full the acquisition has to be stopped and the data has to be downloaded to the PC. This process takes longer than the actual time needed to fill the memory.

Since data is stored by pXar in form of Root files the included hitmap can be analyzed directly with the help of a Root script. The script takes the hitmap and compares the number of hits seen by each pixel with a maximum number of allowed hits for a non-working pixel, which is defined by the user. Typically this cut is set at zero since defective pixels should not see any hits. All pixels below the cut are summed up for each ROC and compared to the grading parameters defined by the collaboration. These are:

- Grade A: < 42 defective pixels (1%)
- Grade B: < 167 defective pixels (4%)
- Grade C: \geq 167 defective pixels

Based on the results for the individual ROCs a grade is automatically assigned to the complete module and displayed.

An example of a hitmap of a module with several defective pixels in the upper right corner is shown in figure 7.5. After 30 minutes of data acquisition during irradiation with X-rays the module has seen about 27 million hits which corresponds to an average number of 412 hits per pixel. The pixels below the surface-mounted components of the HDI see less hits due to shielding while the larger pixels at the ROC borders have about twice the average number of hits. Together these effects create a hitmap of the module which allows the identification of all major features of a module (cf. figure 6.17).

Table 7.1: Results from the electrical and X-ray tests of the modules at KIT. The last column represents the combined results from both tests. 27 modules were shipped to Aachen before X-ray irradiation due to time constraints.

Grade	Electrical Test	X-ray Test	Combined
A	235	355	233
B	147	9	147
A+B	382	364	380
C	17	6	17
Non-graded (defective)	10	12	12
Sum	409	382	409
Yield	93 %	95 %	92 %

7.2.2 RESULTS

In total 370 modules have been investigated with X-rays at KIT. The result obtained by grading the number of defective pixels per module according to the parameters listed above is as follows:

- 355 grade A modules (96.0 %)
- 9 grade B modules (2.4 %)
- 6 grade C modules (1.6 %) with up to 300 detected defects on one ROC

The remaining 39 modules which have not been irradiated can be divided into two groups. The first group of 12 modules could not be tested due to electrical problems like non-working ROCs or disconnected bias voltage pins in the Molex connector and was therefore not incorporated in the numbers above while the 27 modules of the second group were shipped to Aachen before X-ray irradiation due to time constraints. The results from both the electrical and the X-ray tests of the built modules performed at KIT are given in table 7.1.

A distribution showing the total number of defects obtained by X-ray irradiation for the KIT modules is shown in figure 7.6. Two-thirds of the modules have less than four detected defects. Together with the maximum of the distribution at zero defects this is a sign of the excellent quality of the bump bonding of the KIT modules.

Since the modules have been checked three times for defective pixels altogether (during bare module testing, during the electrical test of the full module and finally by X-ray irradiation), it is now possible to check the correlation between the results of the KIT bump-bonding test on both the bare modules and the full modules and the defects obtained from X-ray irradiation. The procedure follows the outline given in [Hit15]. In order to provide figures of merit for the quality of the KIT bump-bonding test, two types of errors are defined:

- Undetected X-ray defects (false negative errors): pixels which were detected as defective from X-ray irradiation were qualified as functional by the bump-bonding test.
- Overestimated defects (false positive errors): pixels which were detected as functional from X-ray irradiation were qualified as defective by the bump-bonding test.

For a bump-bonding test it is especially important to have a low number of undetected defects since it has to reliably detect the actually present defects on a module. The number of overestimated defects could on the other hand be larger as long it does not lead to a downgrading of too many modules.

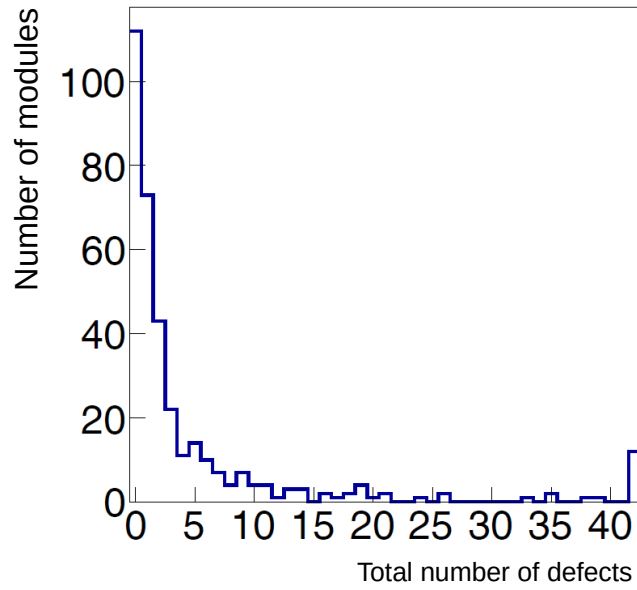


Figure 7.6: Distribution of the total number of defects detected by X-ray irradiation of KIT modules (the last bin includes all modules with more than 40 defects). The number of defects found is a combination of missing bump connections and dead and noisy pixels. Two-thirds of the modules have less than four detected defects. Together with the maximum at zero defects this is a sign of the excellent quality of the bump bonding of the KIT modules.

Distributions of the errors of the KIT bump-bonding test on both the bare modules and the full modules are shown in figure 7.7. The number of undetected defects is low for both module types which is a sign of the good reliability of the KIT bump-bonding test. The number of overestimated defects is higher but still small compared to the total number of 65560 pixels on a module.

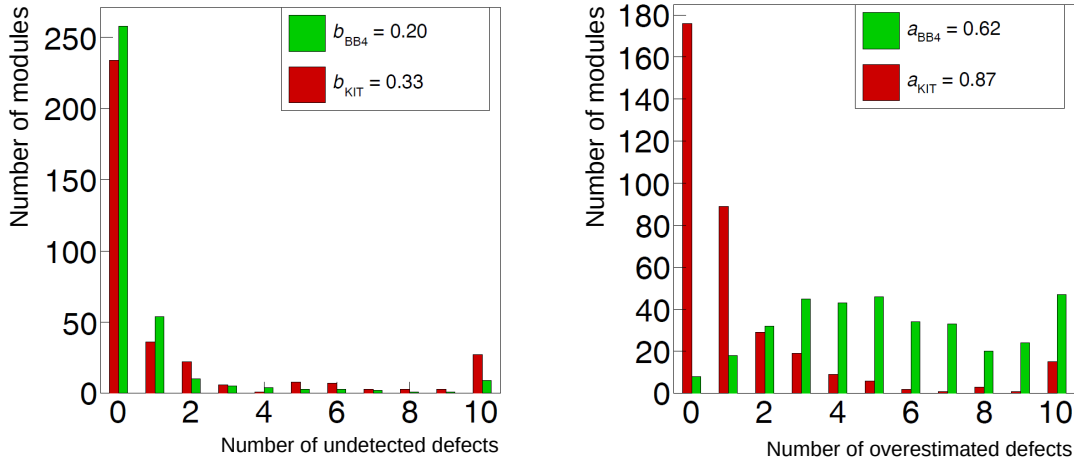
The percentage of overestimated and undetected defects can now be defined as:

$$\begin{aligned} a &= \frac{N_{\text{overestimated}}}{N_{\text{defects}}} \\ b &= \frac{N_{\text{undetected}}}{N_{\text{defects}}} \end{aligned} \quad (7.1)$$

where $N_{\text{overestimated}}$ is the cumulative number of overestimated defects, $N_{\text{undetected}}$ is the cumulative number of undetected X-ray defects and N_{defects} is the cumulative number of defects detected with the bump-bonding test on all modules. In case of the KIT bump-bonding test the figures of merit are:

$$\begin{aligned} a_{\text{bare module}} &= 87\% \\ a_{\text{full module}} &= 62\% \\ b_{\text{bare module}} &= 33\% \\ b_{\text{full module}} &= 20\% \end{aligned} \quad (7.2)$$

It becomes clear that the KIT bump-bonding test works better on full modules than on bare modules. This might be attributed to both the noise conditions, which are worse during the bare module test with the needle card, and to the reflow process, which is performed only after the bare module test and leads to a reshaping of the bumps and a better connection between readout chips and sensor. The signal injected by the test via the air gap capacitance can thus be detected better on a full module. The numbers also show that the test delivers the



(a) Undetected X-ray defects: pixels detected as defective from X-ray irradiation were qualified as functional by the bump-bonding test.

(b) Overestimated defects: pixels detected as functional from X-ray irradiation were qualified as defective by the bump-bonding test.

Figure 7.7: Comparison of the results from the KIT bump-bonding test on both the bare modules (red) and the full modules (green) with the results from X-ray irradiation. Overflow values are included in the last bin. The number of undetected defects is low for both module types which is a sign of the good reliability of the KIT bump-bonding test. The number of overestimated defects is on the other hand higher but still small compared to the number of 65560 pixels on a module. This desired conservative estimate has no consequences for the grading of the modules since modules only get downgraded if more than 656 pixels are found defect during testing.

desired conservative estimate since the percentage of overestimated defects is larger than the percentage of undetected X-ray defects for both module types.

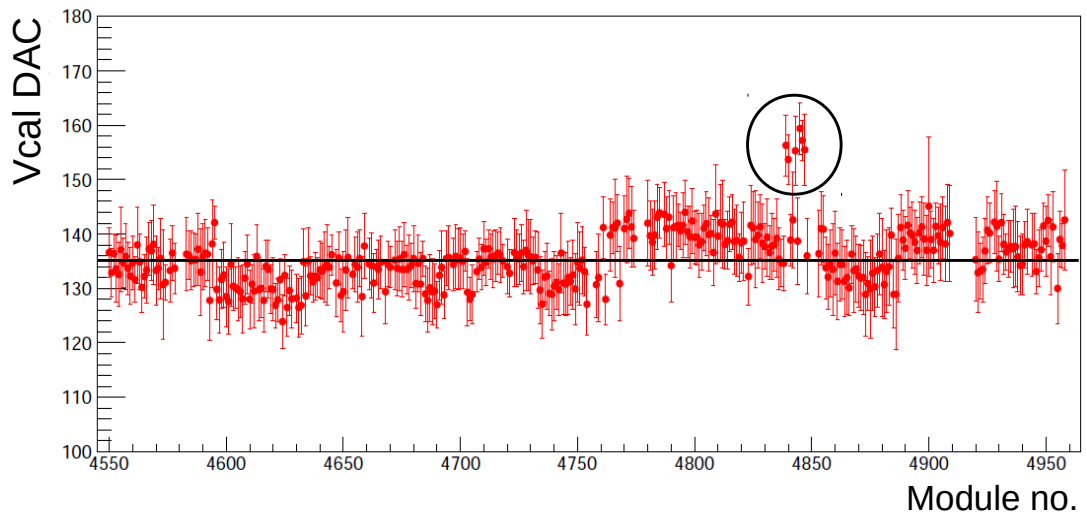
For comparison the standard PSI bump-bonding test was also included in the electrical test of the full modules produced by KIT and its figures of merit have been calculated:

$$\begin{aligned} a_{\text{full module, PSI}} &= 40 \% \\ b_{\text{full module, PSI}} &= 70 \% \end{aligned} \quad (7.3)$$

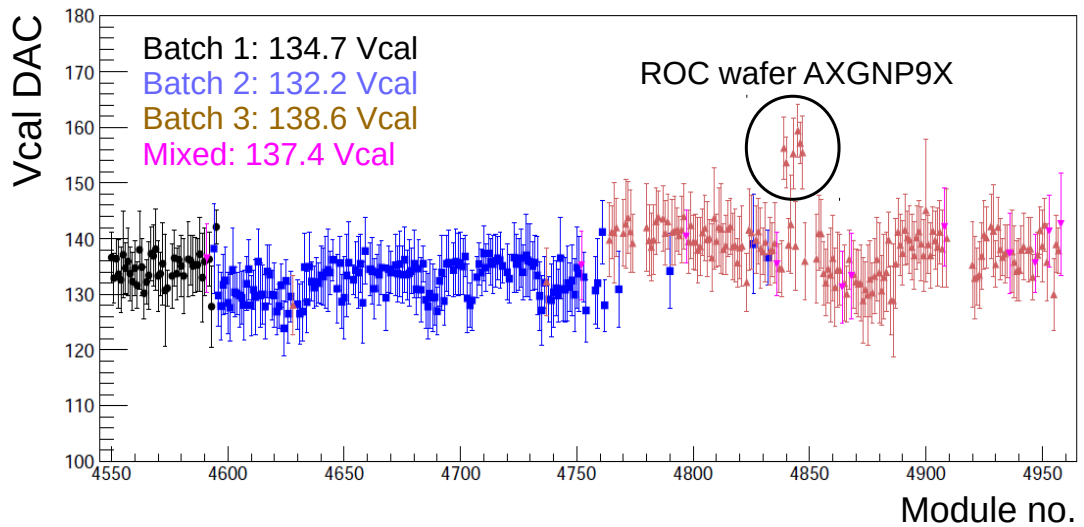
The numbers are worse than the ones of the KIT test and show that the PSI test does not find 70% of the defects detected by X-ray irradiation. This is contrary to the requirements defined above and emphasizes the need for a bump-bonding test tuned to the adopted bonding process. The results delivered by the PSI test were actually even worse at the beginning of the production when the decision has been made to implement an own KIT bump-bonding test and only reached the current level when the test implementation was changed sometime during production.

While the figures of merit of the different tests give the impression that the test results are far away from the real number of defects obtained from X-ray irradiation the picture changes if absolute numbers are taken into account. In total the test results of 350 modules have been analyzed which corresponds to a number of 23 296 000 tested pixels. Out of these only 2750 (or 0.012%) are defective according to the X-ray results and the worst result from the KIT bump-bonding test is 8025 detected defects on all bare modules (0.034%). This equals to an average of 23 detected bump bond defects on each module. Since the sixteen ROCs of a module could together have up to 656 defects and the module would still be graded A it becomes clear that the test does not lead to any unwanted downgrading.

A side effect of using characteristic X-rays to irradiate the modules is the fact that the de-



(a) Distribution of measured pulse height values. No large overall spread but some steps are recognizable and the mean value of 135.4 V_{CAL} DAC units indicated by the black line is within the standard deviation of practically all modules. Only six modules between the numbers M4839 and M4847 are distinctive outliers with a mean value of 156.6 V_{CAL} DAC.



(b) Distribution of measured pulse height values grouped into the three ROC batches used at KIT. The mean values of the different batches and of the small number of mixed modules are given in the plot. The visible steps in the distribution are compatible with the different batches but the six outliers can only be explained by checking the usage of the individual ROC wafers. The result is that all these modules were produced with ROCs from one single wafer named AXGNP9X which was most likely produced by IBM with anomalous process parameters.

Figure 7.8: Distributions of measured pulse height values obtained from irradiation of KIT modules with monochromatic X-rays from the K_{α} line of silver [Tas16].

finer energy of the monochromatic X-rays of the K_{α} line of silver can be used to check the uniformity of the measured signal heights of the KIT modules. The X-ray photons with an energy of 22.2 keV interact with the silicon via the inner photoelectric effect in which they get absorbed and a mean charge of 6156 electron-hole pairs is created in the silicon sensor (see section 3.2.3). The associated pulse height distribution recorded by the individual ROCs is a Gaussian distribution which is then fitted. The maximum of the fit gives the mean deposited energy in V_{CAL} DAC units (since the pulse height data from the ROC is automatically converted into units of V_{CAL} DAC by pXar).

This analysis has been done for all 370 modules which have been irradiated with X-rays and the mean of the signal heights measured by the 16 ROCs on a module is shown in figure 7.8a. No large overall spread but some steps are recognizable. The mean value of 135.4 V_{CAL} DAC units is within the standard deviation of practically all modules. Only six modules between the numbers M4839 and M4847 are distinctive outliers with a mean value of 156.6 V_{CAL} DAC.

One possible explanation of the visible steps in the measured signal height in figure 7.8a and also the outliers might be a dependency from the IBM ROC production batch since different production periods always give slight variations in electronics. KIT has altogether received wafers from three of these batches. Normally only ROCs from the same wafer have been used to produce a single bare module at IPE but in order to maximize the yield some bare modules were produced with ROCs from multiple wafers. They are called mixed modules in the following.

Figure 7.8b shows the mean of the measured signal heights grouped into the three ROC batches used at KIT. The visible steps in the distribution can now be explained with the different ROC batches but still not the outliers. Thus the usage of the individual ROC wafers of the third batch has been checked and the result is that all six modules were produced with ROCs from one single wafer named AXGNP9X. The most probable explanation for the fact that the ROCs from this wafer are distinctively different from all the others are anomalous process parameters during production at IBM which have not been detected.

Since the pulse heights of the sixteen individual ROCs of every irradiated module are also available, a check for systematic differences between the measured pulse heights of the sixteen ROC locations on a module becomes possible. The existence of such differences would either be a sign of HDI problems or a hint at mechanical problems caused during the bonding or later during handling of the bare or full module. The corresponding distribution of the mean pulse height for every ROC position grouped by ROC batch is shown in figure 7.9.

Besides the expected shift between the three ROC batches, no other systematic differences are recognizable. This is another sign for the excellent quality of the KIT module production.

7.3 MODULE QUALIFICATION AT AACHEN

As already mentioned before the good modules are sent to RWTH Aachen where a complete qualification and the final classification of the modules according to the grading parameters defined by the collaboration are performed. The qualification is divided into three parts:

ELECTRICAL TEST: In total three electrical tests with a scope identical to the KIT test described in section 7.1 are performed, the first two tests at a temperature of -20°C and the last one at $+17^{\circ}\text{C}$. In between the two tests at -20°C an additional thermal cycling consisting of ten cycles between -25°C and $+17^{\circ}\text{C}$ is inserted to check the modules for infant mortality caused by mechanical problems present from module production.

X-RAY CALIBRATION: Afterwards the modules are calibrated to define the conversion factor between the measured pulse height distribution of a signal given in V_{CAL} DAC units and the created signal charge in electrons. This is performed in the same way like

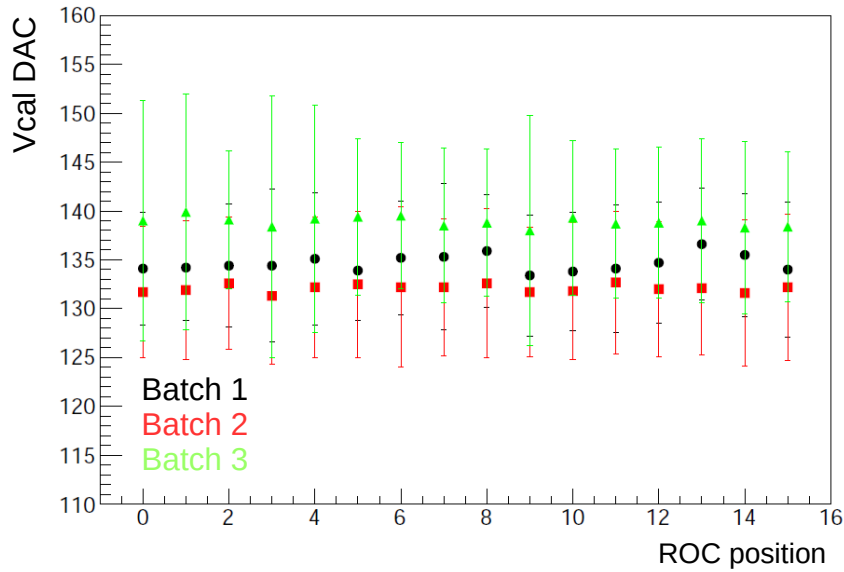


Figure 7.9: Distribution of the measured pulse height values for the sixteen individual ROC positions of the KIT modules (grouped by the three ROC batches). The visible shift between the three ROC batches is expected (cf. figure 7.8b) and no other systematic differences are recognizable [Tas16].

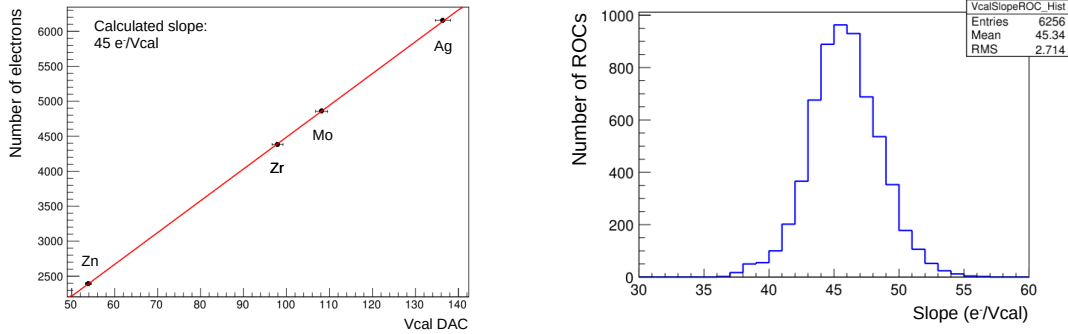
the check for defective pixels is done at KIT. The monochromatic K_{α} line of the characteristic X-rays of a target material is used to create a known number of electron-hole pairs in the silicon sensor of the module and the measured pulse height distribution is fitted to get the mean deposited energy in V_{CAL} DAC units.

If this is done for multiple targets with different energy values of the K_{α} lines the calculated number of electrons can be plotted against the mean deposited energy obtained from the measured pulse height distribution and a straight line can be fitted to the points since a linear correlation between the two values is expected. The resulting slope of the straight-line fit is the sought conversion factor. An example of such an energy calibration of a module performed in Aachen with four X-ray targets (zinc, zirconium, molybdenum and silver) is given in figure 7.10a.

HIGH RATE TEST: The last test of the complete qualification is the high rate test again performed with X-rays. This time the modules are placed in the continuous spectrum of the direct beam of the X-ray tube to achieve the highest possible hit rates while the detection efficiency of the ROCs is checked by injecting calibration pulses directly into the preamplifiers of the pixel cells and counting the detected hits. This test emulates the later operation mode of the modules in the CMS environment where a high background rate is present. Each module is tested at three rates of 150 MHz, 100 MHz and 50 MHz which correspond to the expected rates (plus an additional safety margin) in the detector layers 2, 3 and 4.

A distribution of the slope values obtained from the X-ray calibration of all modules is shown in figure 7.10b. The mean of 45.3 electrons per V_{CAL} DAC is compatible with the results from the other production centers.

The final results of the KIT-RWTH module production for the Phase I upgrade of the CMS pixel detector are shown in table 7.2. They are obtained by combining the results from the



- (a) Example of an energy calibration performed with four X-ray targets (zinc, zirconium, molybdenum and silver). The slope of the straight-line fit is the factor for the conversion of measured VCAL DAC values into electron charge. For this module it is 45 electrons per VCAL DAC.
- (b) Distribution of slope values from the X-ray calibration of all modules at RWTH Aachen. The calculated mean of 45.3 electrons per VCAL DAC is compatible with the results from the other production centers.

Figure 7.10: Example for an energy calibration with four X-ray targets and distribution of the slope values from all modules calibrated at RWTH Aachen [Lip16].

Table 7.2: Final results of the KIT-RWTH module production. The last column represents the combined results from both the complete qualification and classification of the modules at RWTH Aachen and from the reception test at ETH Zürich. The indicated full module yield of 84 % is the highest among all five module production centers in the collaboration.

Grade	Electrical Test	X-ray Test	Reception Test	Combined
A	153	339	344	140
B	225	9	33	203
A+B	378	348	377	343
C	13	43	3	48
Non-graded (defective)	18	18	18	18
Sum	409	409	398	409
Yield	92 %	85 %	95 %	84 %

complete qualification and classification of the modules performed at RWTH Aachen and from the reception test done at ETH Zürich.

The total number of modules tested in Zürich is smaller than the number of modules qualified at Aachen since several modules which have been graded C before were not shipped. Those modules are unrecoverably damaged due to non-working ROCs, soldering problems at the Molex connector or very high sensor leakage currents.

Out of the 409 modules which were built at KIT 343 have been graded A or B after the final qualification and the reception test. This number corresponds to 84 % of the total number of modules built and surpasses the initial requirement of the collaboration of 307 good modules (consisting of 256 modules for installation and 20 % spares) by 12 %. The overall module production yield of the KIT-RWTH group of 84 % is the highest among all five module production centers in the collaboration and thus the ultimate confirmation of the excellent work done both at KIT and RWTH Aachen.

Part III

SENSOR LAYOUT STUDY FOR THE CMS PIXEL PHASE II
UPGRADE

SENSOR LAYOUT STUDY FOR THE PHASE II PIXEL DETECTOR

As already mentioned in section 2.3 the Phase II upgrade will prepare the CMS detector for the challenges of the HL-LHC run with ultimate luminosities around $\mathcal{L} = 5 \cdot 10^{34} \text{ cm}^{-2}\text{s}^{-1}$. For the CMS pixel detector which is located closest to the interaction point the main challenges from the HL-LHC running conditions are radiation damage and pile-up. While the radiation damage caused by the high particle flux only leads to a progressive degradation of its ability to detect charged particles over time, the high pile-up with average values of 140 simultaneous proton-proton collisions and peaks around 200 is present as soon as the delivered luminosity has reached the planned goals and causes very high occupancy in the pixel detector layers. A consequence of this high occupancy are misidentified tracks due to the ambiguities in the assignment of the hits to tracks.

In order to counter this problem the granularity of the pixel detector will have to be increased by more than a factor of four. This increase will mainly be reached by shrinking the size of the pixel cells of the sensor in a module with a design comparable to the Phase I module which was described in section 4.2.

This shrinking requires a complete redesign of the silicon sensor. As stated in the beginning of chapter 5 the design and verification of a new silicon sensor is a process which takes several years including the production of several prototypes and detailed testing campaigns and thus has to be started long before the planned installation date of the new detector.

Additionally the testing of the new sensor design requires the availability of a readout chip which is compatible with the bump-bonding pattern of the new layout and of the associated readout system including software. This is typically not the case during the first design phase of a new sensor since the work on the new readout chips runs in parallel.

The very first step towards a new sensor design is therefore the testing of new ideas in terms of layout and sensor technologies with sensor prototypes which are compatible with existing readout chips. In case of the CMS pixel detector this is the PSI46 series of readout chips designed by PSI which is used both in the modules of the current Phase 0 and the upgraded Phase I detector. The main difference between the older PSI46V2 chip (of Phase 0) and the new PSI46DIGV21-RESPIN chip (of Phase I) is the change of the data output scheme from a 40 MHz analog level encoded output to a 160 MHz digital output. For both chip variants the necessary readout systems are available from the module production periods.

This approach has been chosen for the pixel sensor investigations described in this work.

8.1 HPK CAMPAIGN

All silicon pixel sensors used in this study were ordered by the CMS collaboration in the scope of its campaign to identify the baseline sensor technology for future CMS tracking detectors (or, for short, HPK campaign) [Hof11]. This campaign was launched to find radiation hard sensor materials for the Phase II upgrade of the CMS tracker by comparing sensors and test structures from wafers with different doping types, bulk materials and thicknesses. In order to ensure comparability between all wafers only one lithography mask set has been used and only one vendor has been chosen to manufacture all wafers, Hamamatsu Photonics K.K. (HPK),

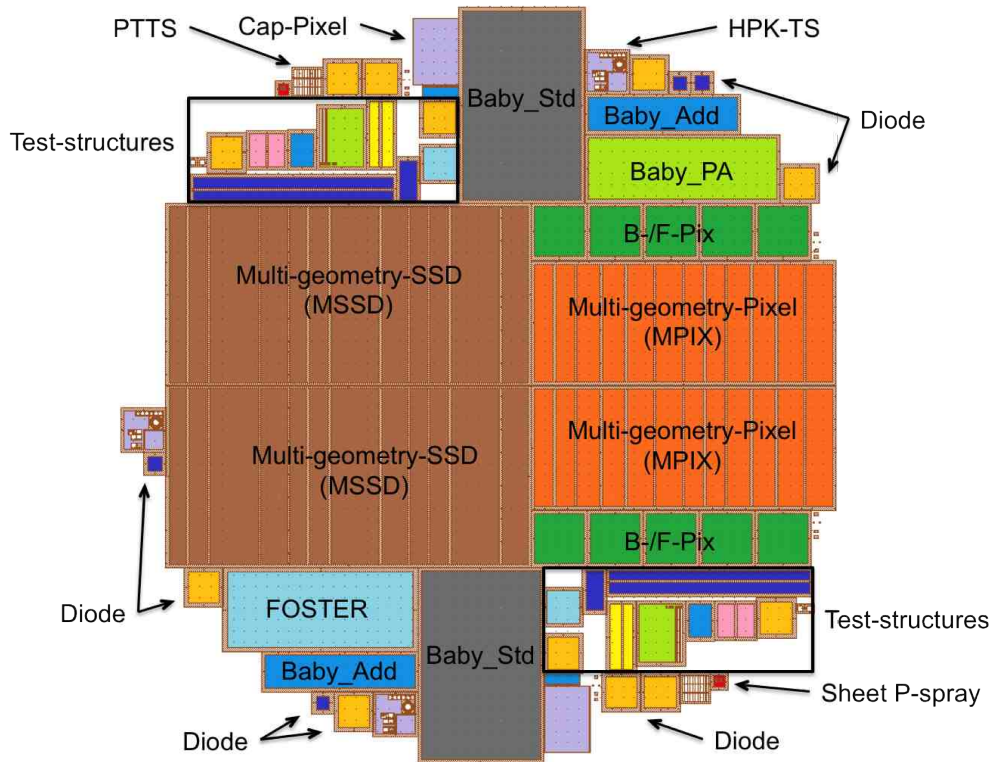


Figure 8.1: Layout and naming of the HPK campaign wafer. The wafer comprises 28 different sensors and test structures including 6 pixel sensors compatible with the PSI46 series of readout chips (labeled as B-/F-Pix, dark green). Since several structures including the pixel sensors are placed twice the wafer altogether contains 67 individual structures [Hof13].

hence the name of the campaign. In total the campaign consisted of 144 wafers in 24 different material variants [Hof13].

The layout of the wafer and the naming of the different structures is shown in figure 8.1. It includes six pixel sensor layouts with a bump-bonding pattern compatible to the PSI46 series of readout chips. The layouts of the two sensor types currently in use in the barrel and forward pixel detector of CMS have been used as a starting point for the design and four out of the six layouts are similar to the barrel pixel sensor while the remaining two are similar to the forward pixel sensor. They are thus named BPix and FPix respectively. The different variations of the layouts are further differentiated by an additional letter where the BPix sensors range from A to D and the FPix ones from E to F.

Since the sensor layouts are compatible with the PSI46 series of readout chips their basic design is equal to the small sensors on the standard CiS wafers. It thus consists of 4160 pixels with a regular size of $150\ \mu\text{m} \times 100\ \mu\text{m}$ and enlarged pixels at the outer edges of the matrix. In contrast to the silicon sensor of a full module the sensor layouts of the HPK campaign only have 4160 pixels since they are made to be bump-bonded to a single readout chip. As mentioned in section 5.1 such assemblies are called single chip assemblies (SCAs) and provide an easy method to create test samples for the evaluation of sensor or readout chip characteristics. After bump-bonding such samples are just glued and wire-bonded to small PCBs and then connected to the readout electronics without the overhead needed for production of a full module with HDI and TBM.

Since the focus of the investigations in this work is directed on the comparison of the different available layout variations of the pixel sensors all samples have been taken from the same base material, $320\ \mu\text{m}$ thick p-doped wafers made of Float Zone silicon. Since the PSI46 series of

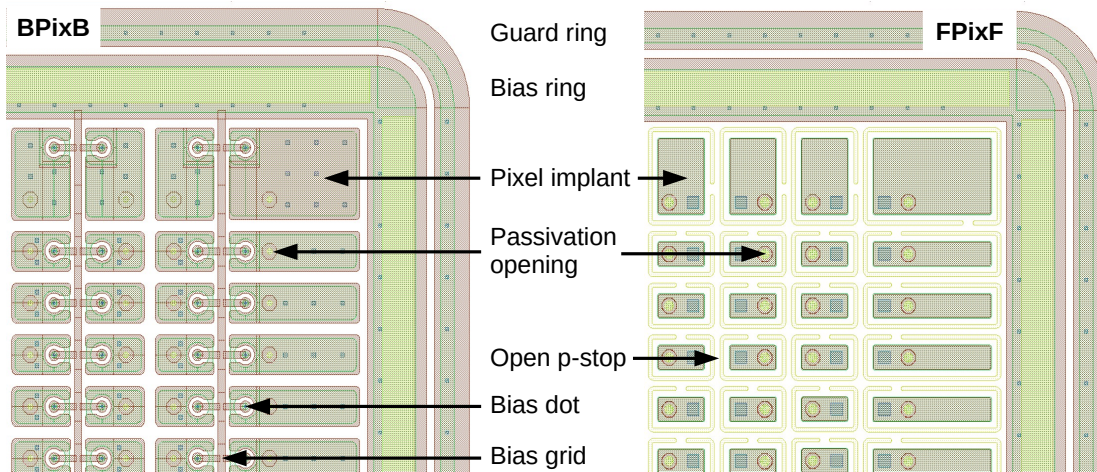


Figure 8.2: Layouts of the BPixB and the FPixF pixel sensors from the HPK campaign wafer. The main differences between the two layouts are the biasing scheme and the pixel isolation technique. While the BPix layout contains a bias grid connecting each pixel to the bias ring via the bias dot and thus uses the cheaper p-spray isolation, the FPix layout has no bias grid and relies on the conductive accumulation layer underneath the silicon oxide to bias the pixels via the openings in the p-stop rings.

readout chips is only able to read out and amplify electron signals the bulk doping is given and the other two parameters were chosen to be as close as possible to the standard CiS sensor used in both the current and the Phase I pixel detector. Float Zone silicon has also been the standard material for the production of semiconductor sensors for years due to its high purity. More information about the different types of silicon bulk material can be found in [Har09].

8.2 PIXEL SENSOR LAYOUTS

In the following the two basic sensor layouts for BPix and FPix and their variations are described. A comparison of the two layouts is shown in figure 8.2. Only a detail of one corner of the pixel matrix is given which also shows the different implant sizes of the border pixels (cf. section 5.1). For both layouts the pixel matrices are surrounded by an outer guard ring which protects the pixels from the bias voltage applied to the back side of the sensor and an inner bias ring which is needed to bias the pixels by allowing the connection of the ground potential. Also visible is the opening in the passivation layer where the bump for the connection to the ROC is placed. In contrast to CiS the HPK wafers are produced in a single-sided process which means that the cutting edges of the sensors are always on high potential and might cause high voltage sparking between sensor and readout chip.

The main differences between the BPix and the FPix layouts are the biasing scheme and the technique used for pixel isolation. Both points are strongly connected with each other since not all biasing schemes are possible with all isolation techniques. Several studies with irradiated sensors and accompanying T-CAD¹ simulations have also shown that the used isolation technique and its parameters are crucial points for the functionality and the long-term operation of silicon sensors. Detailed results from these studies can be found in [Pri16].

The two isolation techniques used for the pixel sensors are open p-stop for the FPix layout and p-spray for the BPix layout. A short description of the techniques and their impacts on the layouts follows:

¹ Abbreviation for Technology Computer Aided Design, a software tool that models semiconductor device operation.

Table 8.1: Differences of the HPK pixel sensor layout variations. BPixB and FPixF are the reference layouts which are closest to the original ones used in the CMS pixel detector. The implant area of the BPix layouts is dependent on the size of the bias dot.

Layout	Implant area (μm^2)	Bias dot isolation (μm)	P-stop width (μm)
BPixA	6040 (+10 %)	14 (-22 %)	-
BPixB (ref.)	5486	18	-
BPixC	4833 (-12 %)	22 (+22 %)	-
BPixD	6492 (+18 %)	10 (-44 %)	-
FPixE	8979 (+91 %)	-	5 (-38 %)
FPixF (ref.)	4704	-	8

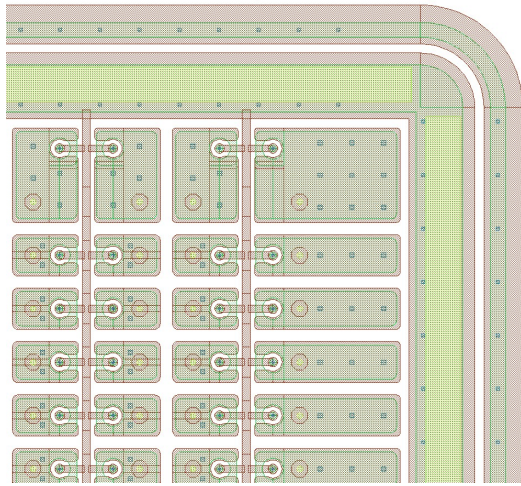
OPEN P-STOP: Instead of a closed isolation ring around every pixel implant, the layout of the FPix sensor includes open p-stop rings which surround the individual pixel implants. These rings and their openings are visible in the right picture of figure 8.2 as light green lines. The usage of open p-stop rings allows the biasing of the pixels and thus also the testing of the sensor without an additional bias grid which connects each pixel to the bias ring. They are instead connected by the conductive accumulation layer underneath the silicon oxide [BBH⁺02]. Since this layer would at the same time short-circuit adjacent pixels, the open p-stop rings have been designed in a way that neighbouring pixel cells always have at least one closed section of the ring in between themselves.

P-SPRAY: As it is visible in the layout of the BPix sensor in the left picture of figure 8.2, the sensor has been designed with a bias grid to allow the biasing of the pixels. The bias grid is connected to both the bias ring and the individual pixels via the so-called bias dot. Therefore the biasing is always ensured and the p-spray isolation technique can be used to isolate the pixels which is cheaper than p-stop since it is applied uniformly onto the wafer and does not need additional lithographic steps. The drawback of this approach is that the pixel implants are connected to the p-spray layer and form an additional lateral pn-junction. To anyway guarantee a high breakdown voltage the applied p-spray dose has to be controlled carefully [Pri16].

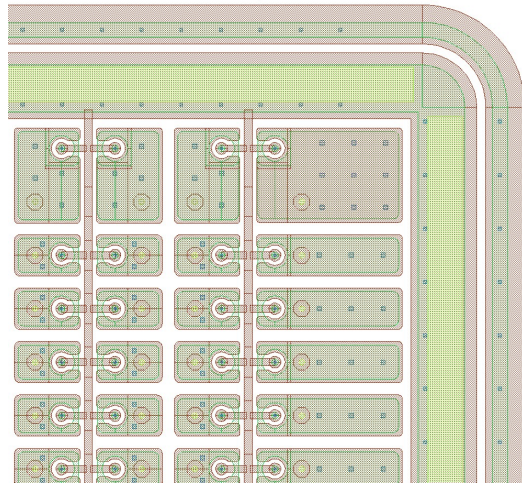
After the basic differences between the two layouts are clarified, it is now possible to explain the layout variations which are differentiated by an additional letter. Details of all six pixel sensor layouts of the HPK campaign wafer are shown in figure 8.3. BPixB and FPixF are the reference layouts which are closest to the original ones used in the CMS pixel detector and the remaining four are variations of them.

The differences of the four variations are clearly visible in the pictures of figure 8.3. For the three BPix sensors they consist of different implant sizes and varying isolation distances between the bias dot and the implant. While the BPixA and BPixC layouts only have a smaller respectively larger isolation distance of the bias dot compared to the reference layout, the BPixD layout is more aggressive and features a maximized implant size together with a minimized bias dot isolation distance. The FPixE layout also is a more aggressive variant of the reference version with a maximized implant size and thinner open p-stop rings. Detailed figures regarding the properties of the four variations and their differences from the BPixB and FPixF reference layouts are given in table 8.1.

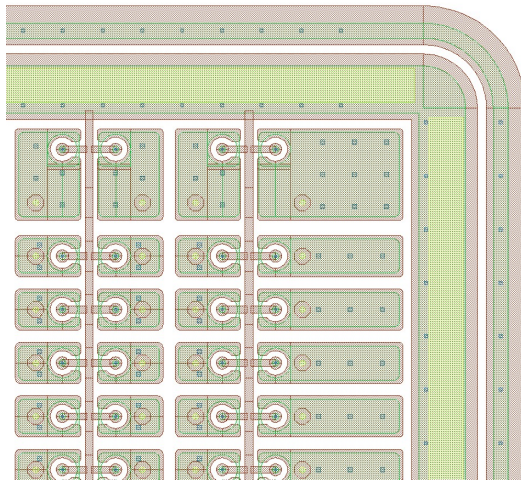
While a maximized implant size is desirable due to the better charge collection in the gap regions caused by the improved electric field configuration, larger implant sizes and the accompanying smaller bias dot isolation distances respectively thinner p-stop rings also lead to higher electric fields at the edges of the structures and possibly earlier breakdown.



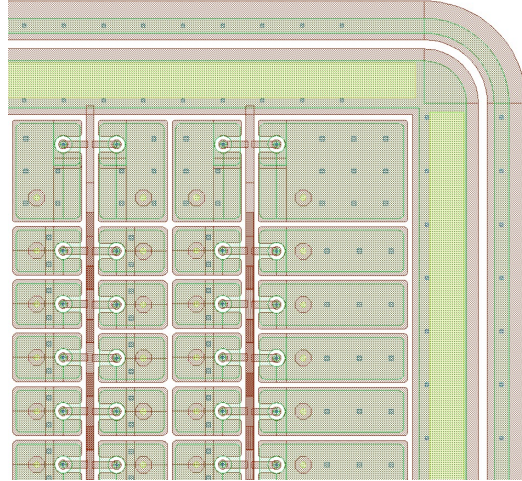
(a) BPixA layout. Improved variant with smaller isolation distance of the bias dot.



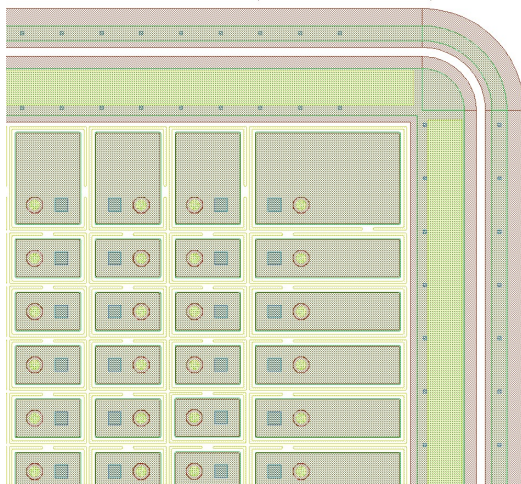
(b) BPixB layout. Reference layout closest to the one used in the barrel pixel detector.



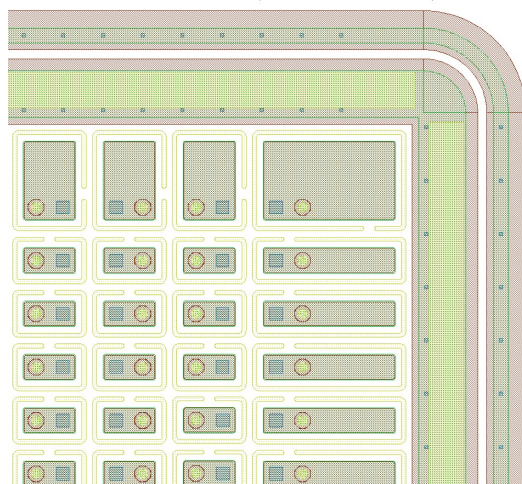
(c) BPixC layout. Conservative variant with larger isolation distance of the bias dot.



(d) BPixD layout. Aggressive variant of the reference layout with maximized implant size and minimized isolation distance of the bias dot.



(e) FPixE layout. Aggressive variant of the reference layout with maximized implant size and thinner open p-stop rings.



(f) FPixF layout. Reference layout closest to the one used in the forward pixel detector.

Figure 8.3: Layouts of the six pixel sensor designs from the HPK campaign wafer. BPixB and FPixF represent the reference layouts which are closest to the original ones used in the CMS pixel detector and the remaining four are variations of them.

8.3 IRRADIATION

As already mentioned in the beginning of this chapter the CMS pixel detector will be subjected to very high particle fluences during the HL-LHC run which cause high radiation damage in the detector components. The innermost layer will be most affected due to its position at a distance of only 3 cm from the interaction point where the fluence will reach values of $2 \cdot 10^{16} \text{ n}_{\text{eq}} \text{ cm}^{-2}$. Further out the fluence rapidly decreases to a value of $3 \cdot 10^{15} \text{ n}_{\text{eq}} \text{ cm}^{-2}$ at a radius of 11 cm [CKM⁺15]. The latter value is similar to the one expected for the innermost layer of the Phase I pixel detector described in the first part of this work. The comparison of the two values demonstrates the challenge of the HL-LHC with a factor 7 higher fluence at the same detector position.

It is therefore mandatory to investigate the performance of the pixel sensor layouts after irradiation. While it would be desirable to irradiate the HPK samples to fluences comparable to the ones given above this is not possible in reality since the sensors are bump-bonded to the PSI46V2 readout chip which is only usable up to irradiation fluences around $3 \cdot 10^{15} \text{ n}_{\text{eq}} \text{ cm}^{-2}$ and the operation of ROCs irradiated to such values already requires manual adjustments to the standard operation procedures [R⁺10]. It has therefore been decided to irradiate the samples to a fluence of $1.2 \cdot 10^{15} \text{ n}_{\text{eq}} \text{ cm}^{-2}$, a value where the ROC is still known to work.

The only solution to irradiate the sensors to higher fluences while still being able to read out the signals would be an irradiation of the sensor before the bonding to the readout chip is performed. Since standard bonding processes like the one used at IPE for the production of the bare modules for the Phase I upgrade (cf. section 6.1.2) always involve high temperatures around at least 140°C for certain periods of time this is not possible due to annealing (cf. section 3.4). The annealing caused by a short period of one minute at 140°C is comparable to several weeks at room temperature and the properties of the irradiated sensors would completely change already during bonding.

Since bonding of highly irradiated sensors is nevertheless an interesting topic for the development of radiation-hard silicon sensors for the HL-LHC experiments, the IPE has started to investigate other possible bump-bonding processes without the need for high temperatures during the bonding phase in the last years after the Finetech FINEPLACER® femto flip-chip bonder was installed. Good results have been achieved with gold-stud bump bonding which uses readout chips with standard SnPb solder bumps and sensors with gold-stud bumps [Kud14]. The idea is that the gold-stud bumps penetrate inside the soft solder bumps during the bonding process and form a sticky connection between ROC and sensor. Since no flat UBM on the sensor has to be connected to the ROC, high temperatures that are necessary to melt the solder bumps can be avoided.

First results from investigations of highly irradiated pixel sensor samples made with gold-stud bump bonding can be found in [Sch15].

The irradiation facility used to irradiate the samples is operated by the Zyklotron AG (ZAG), a private company located at Campus North of Karlsruhe Institute of Technology. ZAG operates two cyclotrons, the Karlsruher Kompaktzyklotron (KAZ) and the Karlsruher Minizyklotron (MIZ), of which the KAZ is used for the irradiations. It provides protons with an energy between 15 and 40 MeV and a beam current of up to 100 μA . For irradiations of silicon devices, the energy and the current are however limited to 23 MeV and 2 μA due to heating of the samples [Die16]. Higher values would cause unwanted annealing already during irradiation. The hardness factor κ of the 23 MeV protons is 2 (cf. equation 3.6) [Die03].

The actual preparation of the samples and the execution of the irradiation are performed by IEKP. The setup used is shown in figure 8.4. The samples are fixed to an aluminum frame which is placed inside a thermally insulated cooling box in front of the exit window of the proton beam. The front side of the box only consists of two thin Kapton foils in order not to

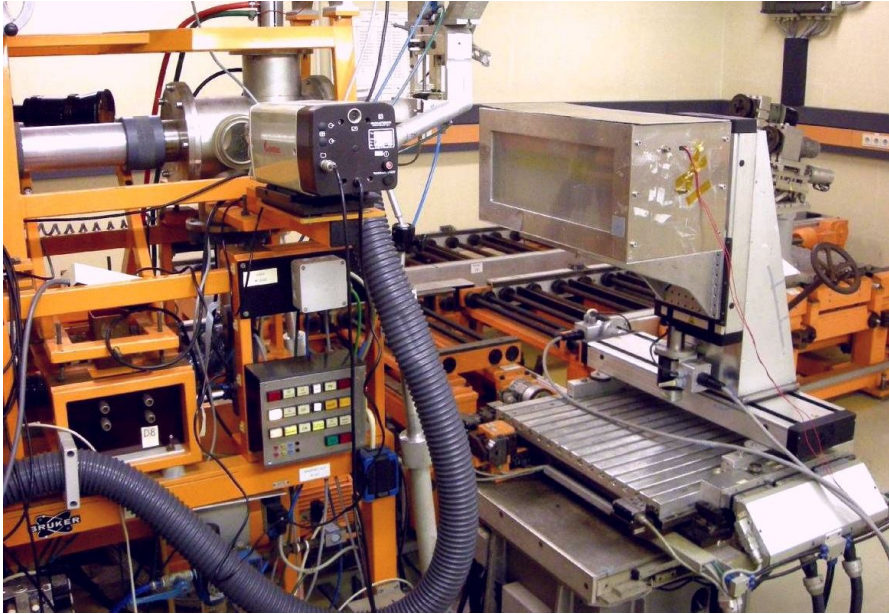


Figure 8.4: IEKP irradiation setup at the Karlsruher Kompaktzyklotron (KAZ). The protons with an energy of 23 MeV exit the stainless steel beam pipe in the upper left part of the picture and hit the silicon samples in the cooling box on the right. Since the beam spot only has a diameter of 4 to 8 mm the box is mounted on a controlled xy-stage and the samples are scanned with the beam [Die16].

reduce the proton energy. The inside of the box is actively cooled to -30°C with the help of cold gaseous nitrogen to prevent annealing of the samples. Since the beam spot only has a diameter of 4 to 8 mm the box is mounted on a programmable xy-stage and the samples have to be scanned with the beam to be irradiated homogeneously. The scanning procedure also allows the irradiation of multiple samples in one session.

The irradiation fluence of a sample is directly dependent on the number of scans, that is the number of times the beam is hitting a certain point on the sample, when the other parameters like beam current and scanning speed are kept constant. For typical values a fluence of $2 \cdot 10^{13} \text{ n}_{\text{eq}} \text{ cm}^{-2}$ is achieved per double scan (down and back up) [Die16]. After irradiation dosimetry measurements are performed with the help of nickel foils which are attached to the samples during the irradiation procedure. The activity of ^{57}Ni undergoing β^{+} decay is measured by ZAG with a germanium detector system. The estimated uncertainty of the irradiation fluence is 15%.

TEST BEAM MEASUREMENTS

Test beams are particle beams which allow the assessment of the properties and the performance of particle detectors. Using test beams provides a unique opportunity for detector development since the detector samples are operated in conditions that resemble the later use case in a particle physics experiment as closely as possible. The results from such tests thus provide additional information which cannot be obtained from simulations or laboratory tests.

Test beam facilities are operated by several research institutions distributed over the world like the European Organization for Nuclear Research (CERN), Fermi National Accelerator Laboratory (FNAL) and Deutsches Elektronen-Synchrotron (DESY) and usually the parameters of the test beams like particle type, energy, direction and time structure are known properties. This knowledge can be used to choose the test beam with the best parameters for a planned detector characterization.

The performance of the pixel sensor layouts from the HPK campaign wafer which were described in the previous chapter has been investigated at the DESY test beam in Hamburg. Since DESY is a member of the German D-PIX consortium and involved into the production of detector modules for the Phase I upgrade of the CMS pixel detector, the local CMS group has large experience in the operation of the PS146 series of readout chips in both the laboratory and the test beam. Besides that the CERN test beam was not available during the time of the beam test due to the LHC Long Shutdown 1 which comprised the complete CERN accelerator complex and therefore also the test beams.

Before the DESY test beam, its infrastructure and the associated software chain for data acquisition and analysis are described in detail, the investigated sensor samples are introduced.

9.1 INVESTIGATED SENSOR SAMPLES

Since there are six different sensor layout variations, it was planned to have 24 samples prepared, four for each variation. To be able to distinguish them easily, the samples are named according to the official naming of the structures on the HPK campaign wafer which provides their most important properties at a glance. The four different parts of the naming are explained with the help of the following example:

FZ320Y_02_BPixB_1

The first block indicates the bulk material (Float Zone silicon), its active thickness (320 μm) and the pixel isolation technique (Y for p-spray, while P stands for open p-stop). The second block is the wafer number in the batch of wafers with the same basic properties (in this case the second FZ320Y wafer) and the third block describes the actual structure. The last block enumerates the structure position on the wafer if a structure is present multiple times.

Since this study is focused on the investigation of the different layout variations, both the bulk material and the active thickness are fixed and the sample names always start with FZ320. Also the pixel isolation technique is predetermined by the layouts (cf. section 8.2) and thus all BPix sensors are taken from FZ320Y wafers and all FPix sensors from FZ320P wafers. To get the necessary number of samples the sensors are taken from four wafers (01 to 04) and from

up to two positions (1 and 2).

The preparation of the samples was done by PSI since bump bonding at IPE was not yet available at the time when the samples were produced. An additional problem was that all structures of the HPK wafers were delivered already cut and without any UBM since bump bonding is not needed for any of the structures except the pixel sensor layouts. As mentioned in chapter 6 most UBM deposition processes in industry work with lithography masks which are made for complete wafers and thus cannot be used for the HPK sensors. Other processes without lithography like the electroless ENEPIG process of PacTech were not yet qualified at that time.

The PSI bump-bonding process has been developed for the production of the modules for the current CMS pixel detector and is based on indium solder bumps [BGG⁺06]. It is a complete in-house process but also needs lithographic steps to deposit a UBM consisting of titanium, nickel and gold on both the sensor and readout chip pads which allows the wetting of the aluminum pads with indium. For the mass production of the bare modules for the CMS pixel detector the UBM has been applied on complete wafers but for the HPK samples the cut sensors had to be reassembled to a wafer-like structure in order to be able to use the existing lithography masks. This work was extremely complicated and time-consuming since exact alignment is necessary to ensure a correct UBM deposition.

After the UBM deposition the bonding of the sensor to the `PS146V2` readout chip and the final reflow were performed. While standard single chip assemblies with double-sided `CiS` sensors would now have been ready for wire bonding an additional production step had to be included for the HPK assemblies to ensure a high dielectric strength of the sensor-ROC sandwich. As mentioned in section 8.2 the HPK wafers are produced in a one-sided process which means that the cutting edges of the sensors are always on high potential and might cause high voltage sparking between sensor and readout chip.

The spark protection is provided by a thin layer of a polymer called Parylene® since the dielectric strength of Parylene is very high (up to 5 kV for a film thickness of 25 µm). Parylene is applied by chemical vapor deposition and thus covers the complete surface area of the assemblies. To still be able to wire bond the assemblies after deposition the bond pads of the ROC and the HV pad of the sensor have to be protected. This is done by masking them with Kapton tape. The effectivity of the Parylene coating has been tested at PSI with one of the samples in a destructive test. The assembly was able to stand voltages of up to -600 V which is sufficient for operating also the irradiated samples.

After removal of the Kapton tape masks the assembly is glued to the carrier PCB and the wire bonding to the pads on the PCB is performed. An example of a single chip assembly on a carrier PCB comparable to the HPK pixel sensor samples used in the test beam is shown in figure 9.1. The single chip assembly itself is visible in the center with the sensor on top. Three wire bonds connect the bias voltage to the sensor while the ROC below is connected with 35 bonds visible in the front. The box header in the back is used to connect the PCB to the test board for readout. A special feature of the PCB is the option to either supply the sensor bias voltage via the test board and the box header or via the Lemo connector on the left. The selection is done by soldering the red wire to the pad associated to the chosen method. Supplying the bias voltage via the Lemo connector is necessary when (irradiated) samples have to be operated at bias voltages higher than 500 V since the box header and the test board itself are not rated for higher values.

As mentioned in the beginning it was planned to have 24 samples which means four of each layout out of which two would have been irradiated. One pair of each layout type, consisting of an unirradiated and an irradiated sample, would then have been investigated while the remaining samples would have been kept as spares. Unfortunately nine samples were already

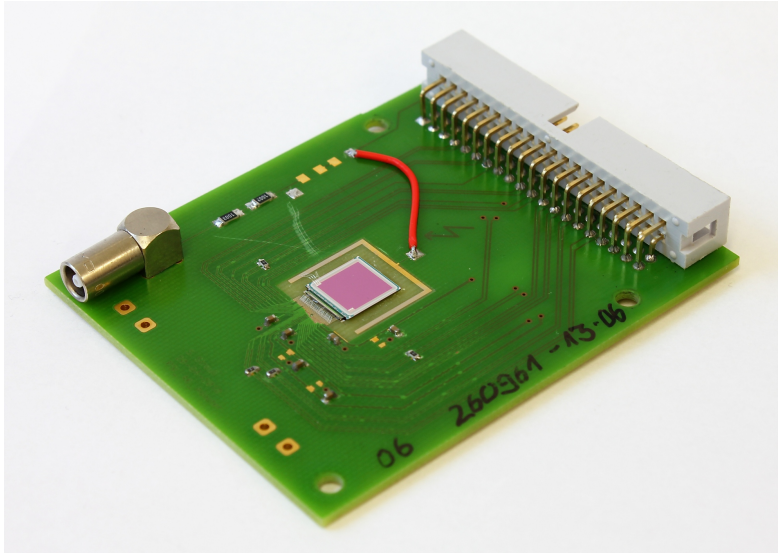


Figure 9.1: Example of a single chip assembly on a carrier PCB comparable to the HPK pixel sensor samples. The box header at the back is used to connect the wire bonded ROC to the test board for readout. The bias voltage for the sensor can either be supplied via the test board or the Lemo connector on the left if higher voltages are necessary which the test board cannot stand.

lost after preparation. A quick functionality test at PSI showed various reasons like bad IV characteristics of the sensor, bad bump bonding or a non-working ROC. One chip was damaged during the masking of the wire bond pads with Kapton since this requires using tools on the chip surface.

Fifteen samples were shipped to KIT out of which eight have been irradiated with protons to a fluence of $1.2 \cdot 10^{15} \text{ n}_{\text{eq}} \text{ cm}^{-2}$. Afterwards the chips have been tested again and another six samples were lost (four irradiated and two non-irradiated ones). Three out of the four irradiated samples had problems with the ROC and one sample had a bad IV characteristic while for the non-irradiated ones there was a dead ROC and a sensor short circuit.

The nine samples remaining for investigation at the DESY test beam facility are listed in table 9.1. Only two pairs consisting of an unirradiated and an irradiated sample, which are necessary to obtain comparable results, are available and both pairs are from the FPix base layout. According to the layout variation they are named “E” respectively “F”.

The sample FZ320Y_03_BPixC_1 has not been used in the DESY beam test since it has about 2500 defective bump bond connections leaving more than half of the sensor unconnected and there is another BPixC sample with the same sensor layout available. The missing connections drastically reduce the statistics compared to a fully working sample.

9.2 DESY TEST BEAM

As mentioned in the beginning of this chapter test beam measurements are widely used to assess the characteristics and performance of particle detectors. On the one hand they provide a unique opportunity to operate the detectors in an environment as close as possible to the later operation in a particle physics experiment and on the other hand they allow a more sophisticated study of the detectors compared to laboratory tests or simulations. Some important parameters like efficiency and spatial resolution can only be evaluated correctly with reference tracks of the particles traversing the detector sample. This task is fulfilled by a so-called beam telescope which tracks the particles via their hits in multiple consecutive planes of position-sensitive detectors and later provides the track information to the analysis.

Table 9.1: HPK sensor samples available for investigation at the DESY test beam. Only two pairs consisting of an unirradiated and an irradiated sample are available for testing and both are from the FPix base layout. During the beam test a shorter name was assigned to the investigated samples which is also listed.

HPK sample name	DESY name	Fluence ($n_{eq} \text{ cm}^{-2}$)	Pair
FZ320Y_04_BPixA_1	chip 62	0	-
FZ320Y_02_BPixC_1	chip 61	0	-
FZ320Y_03_BPixC_1	-	0	-
FZ320P_02_FPixE_2	chip 60	0	E
FZ320P_02_FPixF_1	chip 63	0	F
FZ320Y_01_BPixB_1	chip 66	$1.2 \cdot 10^{15}$	-
FZ320P_01_FPixE_1	chip 64	$1.2 \cdot 10^{15}$	E
FZ320P_01_FPixE_2	chip 67	$1.2 \cdot 10^{15}$	E
FZ320P_01_FPixF_2	chip 65	$1.2 \cdot 10^{15}$	F

9.2.1 THE DESY-II BEAMLINES

The DESY Test Beam Facility offers three beam lines with electron or positron beams with an energy of a few GeV and medium rates of up to 1 kHz. It is one of the two users of the DESY-II synchrotron whose main purpose is the top-up injection of particles into the PETRA-III synchrotron light source. DESY-II has a circumference of 293 m and a maximum beam energy of about 6.3 GeV. It circulates one particle bunch at a time at a revolution frequency of 1.024 MHz and the duration of one acceleration cycle is 80 ms [BGGH].

The beam generation scheme for the test beams is shown in figure 9.2. Due to the high number of particles per DESY-II bunch, the test beams are generated via a twofold conversion. A carbon fibre target is moved into the DESY-II primary beam and the electrons (respectively positrons) generate Bremsstrahlung photons which exit the synchrotron tangentially. They are then converted back into electron-positron pairs in a copper or aluminum converter target. A dipole magnet works as a spectrometer to select either electrons or positrons and also enables the momentum discrimination of the particles delivered to the test beam area. A final collimator in front of the area only allows the passage of the desired particles with the selected energy and blocks the remaining particle spectrum. The momentum discrimination also reduces the instantaneous rate and allows tracking of single particles in the final beam. In total three test beam areas are available, each featuring its own independent beam extraction and momentum selection equipment.

The energy of the DESY-II synchrotron varies with time. With a rate of 12.5 Hz, the beam energy is ramped up to the nominal value of 6.3 GeV and back down to the injection energy of 450 MeV. Therefore electrons (or positrons) only reach the test beam area when the primary beam energy is higher than the test beam energy chosen by the user and the test beam is also modulated by a frequency of 12.5 Hz.

A side effect of the modulation is the fact that the particle rate for the test beam is small (≈ 1 Hz) for high selected energies around 6 GeV since the primary beam only reaches this energy for a short period in the whole acceleration cycle. To get reasonable rates of the order of several hundred Hz, the particle energy has to be chosen below 5 GeV. However particles with lower energy have a higher chance to undergo multiple scattering in either the detector sample or the beam telescope which impairs the analysis results. The selection of the beam energy at the DESY Test Beam Facility is thus a compromise between particle rate and multiple scattering.

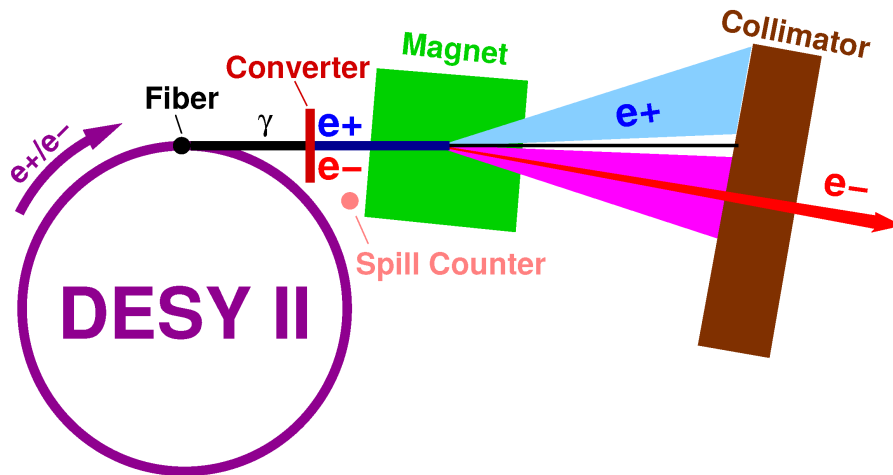


Figure 9.2: Schematic of the test beam generation at DESY. Circulating electrons or positrons hit a carbon fibre target inside the DESY II synchrotron and emit Bremsstrahlung photons which are then converted back into electrons and positrons by hitting a secondary converter target. A dipole magnet deflects the particles and enables the selection of both particle type and energy for the test beam while a collimator blocks the remaining particle spectrum [DES16].

9.2.2 THE DATURA BEAM TELESCOPE

As mentioned before the precise tracking of the particles traversing the detector sample is essential for the determination of important parameters of the sample. Most beam telescopes used for this task consist of multiple planes of well-known and characterized silicon pixel or strip detectors which provide good spatial resolution. Ideally the resolution of the telescope should be better than the one of the sample.

The beam telescope provided by the DESY Test Beam Facility is an EUDET telescope named DATURA¹. The EUDET research project conducted detector R&D towards the International Linear Collider (ILC) and was supported by the European Union in the 6th Framework Programme structuring the European Research Area [A⁺12]. EUDET ended in December 2010. One of its activities was the development of infrastructure for test beams including the EUDET beam telescope, the associated data acquisition software EUDAQ and the data analysis framework EU Telescope. Until today seven incarnations of the EUDET telescope have been built and also distributed to other test beam facilities at CERN and SLAC.

The DATURA telescope is a six-planes pixel detector telescope divided into an upstream and a downstream arm with three planes each and a measured average pointing resolution of $(3.24 \pm 0.09) \mu\text{m}$ [JSB⁺16]. The detector sample, the so-called device under test (DUT), is mounted in between the two arms to ensure good track finding and easy interpolation of the telescope tracks to the corresponding DUT position. Each of the six planes consists of a high-resolution Monolithic Active Pixel Sensor (MAPS) named MIMOSA26 which is produced in a $0.35 \mu\text{m}$ CMOS process. The MIMOSA26 sensor has 1152×576 pixels with a pitch of $18.4 \times 18.4 \mu\text{m}^2$. Its active area of $21.1 \times 10.6 \text{mm}^2$ is thinned down to a thickness of only $50 \mu\text{m}$ to reduce material budget and multiple scattering.

The MIMOSA26 pixel detector is read out in a rolling-shutter mode at a frequency of 80 MHz with a total integration time of $115.2 \mu\text{s}$ [HGBB⁺10]. Rolling-shutter mode means that the individual rows of the pixel matrix are read out one after another. This takes longer than parallel readout but allows the relocation of a large part of the pixel cell electronics to the insensitive areas of the sensor outside the pixel matrix and thus the reduction of the pixel size. The readout uses adjustable discriminators in the chip periphery for zero suppression of the data and

¹ Acronym for DESY Advanced Telescope Using Readout Acceleration.

correlated double sampling (CDS) to remove offsets in the individual pixel charges. CDS is performed by subtracting samplings of two successive frames recorded by the detector.

The long integration time is a drawback and makes the telescope unsuitable for high rate measurements since it also records further particles traversing the telescope after the trigger has been issued by the first particle but does not provide any time-of-arrival information for the individual hits. For a beam energy of 5.2 GeV the track multiplicity in the DATURA telescope per event respectively readout frame is around 2.5 [Spa16].

Since the DUTs are based on the `PSI46V2` readout chip which has a trigger window of only 25 ns defined by the LHC clock of 40 MHz, they only record the first particle which caused the trigger to be issued. In order to be able to select the corresponding track from the multiple telescope hits, an external timing reference is required. This is provided by an additional reference sample (called REF) also based on the `PSI46V2` readout chip which is mounted behind the downstream arm of the telescope. It therefore has the same timing characteristics as the DUT and both samples are synchronized by operating them with the same externally generated clock. Later in the analysis the telescope tracks are first matched with the REF detector in order to select the particles which are in the correct time frame and then the selected tracks are compared to the DUT measurements to evaluate the efficiency. Since the REF measurements are independent from the DUT and only reduce the total number of tracks, no additional bias is introduced by this method.

The complete telescope is mounted on a robust mechanical structure. Each MIMOSA26 sensor plane is encased in an aluminum housing with cut-outs for the beam which are covered with thin Kapton films (cf. figure 9.3). A water chiller ensures a constant operation temperature of the sensors of 18°C. The housings are movable on rails which enable individual shifting of the telescope planes to accommodate different DUT setups. Since the total material budget of the telescope only amounts to 300 μm of silicon sensor and 300 μm of protective Kapton film, it is ideally suited for measurements at test beam energies of a few GeV.

The telescope setup used for the investigation of the HPK pixel sensor samples is shown in figure 9.3. The DUT is placed between the upstream and downstream arms of the telescope on a Peltier element inside an thermally insulated box made of foam material to cool the irradiated samples. The heat generated at the back side of Peltier element is dissipated by water cooling. To prevent condensation on the samples the inner volume of the box is flushed with dry air.

The readout of the telescope planes and the DUT is triggered by four scintillators that are placed in front and at the end of the setup. Each scintillator is equipped with a silicon photomultiplier (SiPM) which amplifies the scintillation light and generates a signal for further processing by the EUDET trigger logic unit (TLU). The TLU is a programmable trigger logic based on a commercial FPGA board and an additional custom-made coincidence unit with four discriminators and is programmable from a standard PC via a USB connection [Cus]. It generates and distributes the common trigger signal to the telescope, the DUT and the reference sample (REF). The TLU is also able to handle trigger veto conditions like busy signals since the integration time of the telescope is very long compared to the revolution frequency of the synchrotron. When the telescope readout has been triggered, its busy signal is raised and the TLU vetoes any new trigger until the readout is finished and the busy signal is lowered again.

The `PSI46V2` readout chip used for the samples is normally operated at the LHC in a beam-synchronous mode running on the 40 MHz machine clock. At the DESY Test Beam Facility this creates problems since the required 40 MHz are not a multiple of the 1.024 MHz clock of the DESY-II synchrotron and thus the DESY-II clock cannot just be multiplied and used. Instead a detector clock signal is created by an external pulse generator which is triggered by the DESY-II clock. The pulse generator delivers 39 pulses with a length of 24.9 ns each for every DESY-II

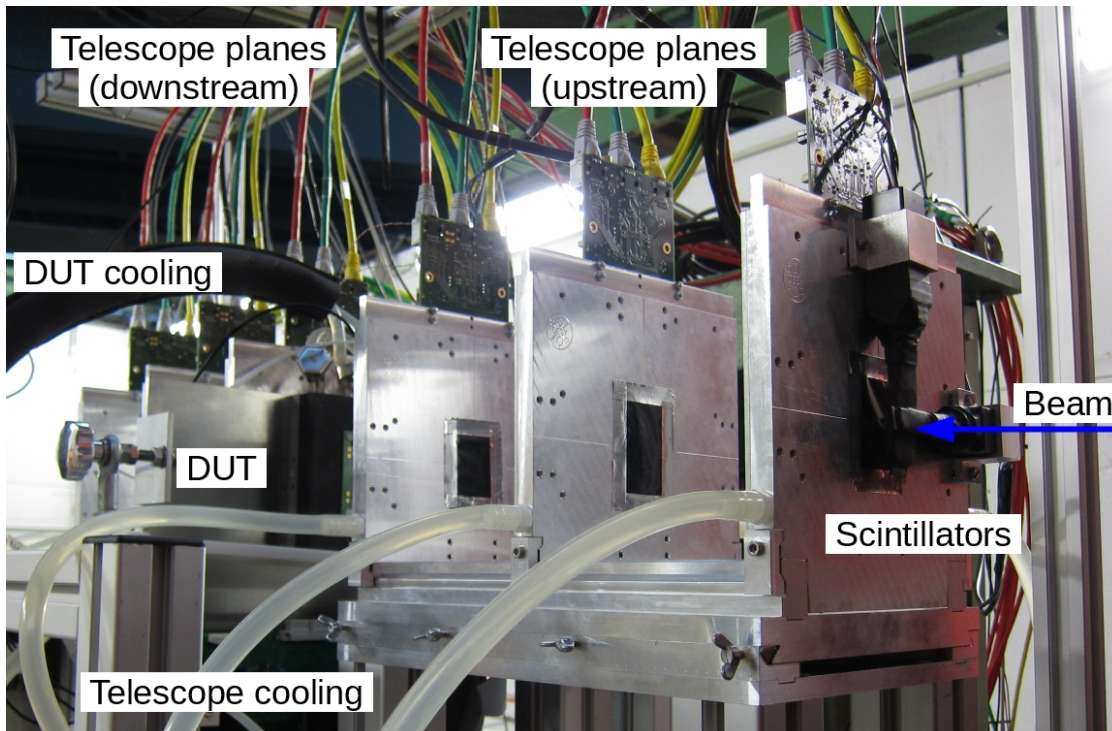


Figure 9.3: DATURA telescope setup used for the investigation of the HPK pixel sensor samples. The DUT is placed in between the upstream and downstream arms of the telescope and cooled by a Peltier element. Scintillators in front and at the end of the telescope generate the trigger signal. The additional REF sample used as timing reference is hidden by the downstream planes of the telescope.

clock cycle and thus emulates a ≈ 40 MHz clock for the operation of the test board and the ROC.

Additionally the DESY-II clock is resynchronized to the 50 Hz of the power grid before the injection of every new bunch and during these resynchronization periods the clock cycle is interrupted for several periods. This interruption causes the PLL² of the internal clock distribution circuit on the test board FPGA to fail and the data taking is corrupted.

A solution to this problem was found during the test beam. PSI provided a new firmware for the test board without the embedded PLL. Since the PLL was used in the clock distribution circuit of the test board to create an internal 80 MHz clock signal out of the external 40 MHz clock it is now necessary to directly supply a 80 MHz clock signal to the test board.

9.3 EUTELESCOPE FRAMEWORK AND ANALYSIS

The analysis of the test beam data is implemented in the EUTelescope framework which in turn is a group of Marlin processors used for analysis and reconstruction of data taken with pixel beam telescopes. EUTelescope has been developed in the context of the EUDET research project and is embedded in the ILCSoft framework. The ILCSoft framework is being developed by the International Linear Collider (ILC) community and combines several data processing tools used for detector development for the ILC [GE]. Its core elements are the event based Linear Collider I/O (LCIO) data format, the Geometry API for Reconstruction (GEAR) markup language and the Modular Analysis & Reconstruction for the LINear collider (Marlin) event processor. Marlin is responsible for the consecutive execution of the analysis subroutines called

² Abbreviation for phase-locked loop, a system that generates an output signal whose phase is related to the phase of an input signal.

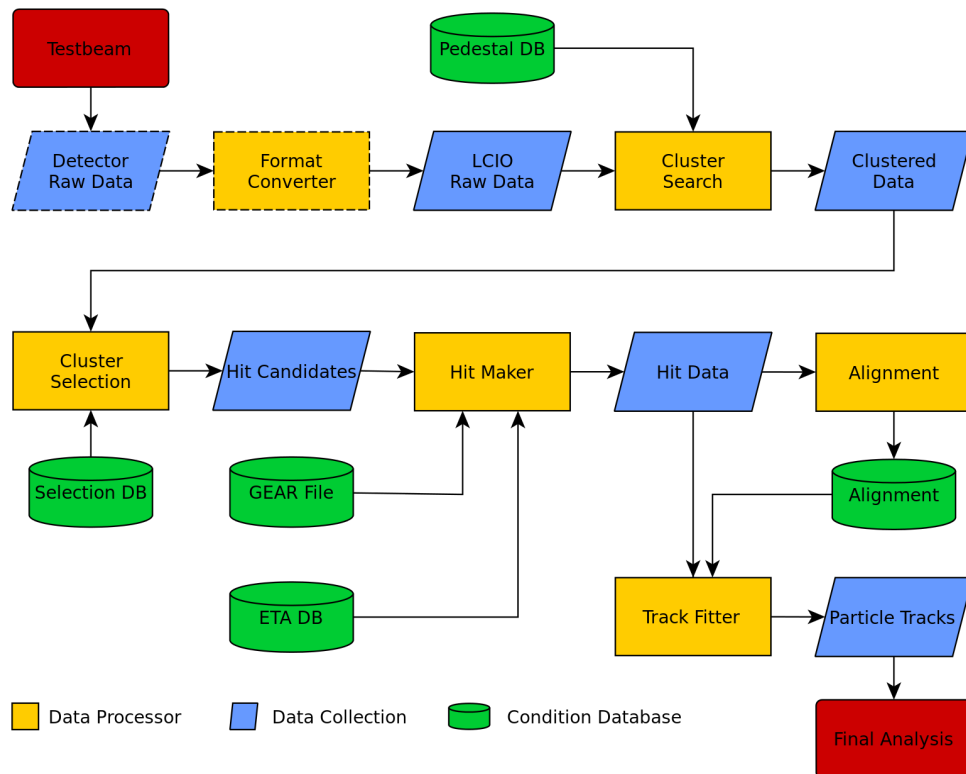


Figure 9.4: Data analysis workflow in the EUTelescope framework. Several individual Marlin processors are used to reconstruct the particle tracks in the telescope necessary for the final analysis of the DUT data. Each processor generates its own data collection which is stored in the LCIO file format. External databases are loaded to obtain important information about the telescope geometry and created to store the alignment constants [EUT].

processors which are controlled by their own sets of parameters stored in Extensible Markup Language (XML) files called steering files. The modular structure with independent processors allows the composition of analysis chains for a wide range of applications.

The Marlin processors provided by the EUTelescope framework are used to analyze the data of the DATURA telescope. An overview of the data analysis workflow is given in figure 9.4. Individual processors first convert the raw data of each telescope plane into the LCIO data format, find noisy pixels that have to be excluded from further analysis, cluster the remaining hits in each layer, align the telescope planes and finally reconstruct the particle tracks through the telescope. The results of each intermediate step are stored in a new LCIO file.

The LCIO data format is an event based data format which stores every trigger decision together with all corresponding detector data under one consecutive event number. Each event entry consists of an event header and the actual event data. The header contains information about the detector, the timestamp and the run number and remains unchanged during the analysis. The event data on the other hand is stored in different types of data collections specific to the individual processors. The entries of each collection are labeled with a unique hexadecimal ID which connects the otherwise independent collections and allows easy cross-referencing between the information.

The DATURA telescope geometry is described using the Geometry API for Reconstruction (GEAR) markup language which implements all information about the telescope like geometry of the individual planes, properties of the materials or size of the pixel cells. For event reconstruction the necessary information can be obtained from the GEAR file by the individual Marlin processors used in the analysis chain.

The starting point of the track reconstruction is the conversion of the zero-suppressed raw data from the telescope into the LCIO file format with a TrackerData collection. Zero-suppressed data excludes all pixels from the telescope which do not contain any hit information and thus keeps both the file size and the necessary processing time minimal. Since traversing particles might have hit more than one pixel, the raw hits cannot be used for transformation into geometrical space points. Instead the clustering processor is used to find adjoining pixel hits and perform a simple geometrical interpolation of the cluster center since the MIMOSA26 pixel sensor only provides binary hit data and no pulse height information (cf. section 3.3). At this point also clusters containing noisy pixels are removed from the data collection.

Afterwards the geometrical description of the telescope is obtained from the GEAR file by the HitMaker processor and used to transform the local coordinates of the clusters into the global telescope reference frame. These hits are then used by the Alignment processor to align the individual telescope planes to each other since the alignment in the GEAR file obtained from user measurements always includes a certain degree of uncertainty. Finally the Track Fitter processor connects the hits in the aligned planes to find the final particle tracks necessary for the analysis of the DUT data.

9.4 THE EUTELANALYSISCMSPIXEL PROCESSOR

The last step of the EUTelescope analysis chain is the EUTelAnalysisCMSPixel processor which has been written by the DESY CMS group for the analysis of data from single chip assemblies with readout chips from the PSI46 series and which is now included in the official EUTelescope distribution. It combines the particle tracks from the analysis of the telescope data with the data from both the reference sample and the DUT to determine the performance of the DUT.

This is done by first decoding the events included in the raw data files from both the DUT and the REF chip with the help of the CMSPixelDecoder, a generic decoding class for PSI46-type pixel detector readout chips [Spa15]. Afterwards the ADC values of the hits are converted into internal VCAL DAC units using calibration data from an electrical test of the sample (cf. section 7.1). The VCAL DAC values are again converted into an electron charge deposited in the sensor with the help of the conversion factor derived from X-ray calibration (cf. section 7.3). The hits are then clustered and the position of the cluster center is calculated with the center-of-gravity method (cf. section 3.3).

A coarse prealignment of the DUT and REF detectors is performed by a simple extrapolation of the upstream respectively downstream triplets³ to their positions. The intersection point with the detector plane is calculated and the residual between DUT or REF hit and track impact is minimized. The prealignment alone is sufficient for the REF detector since the tagging of the telescope tracks does not require a high alignment precision.

In a second step the DUT sample with applied prealignment shifts is aligned precisely using the MILLEPEDE-II algorithm which implements a global minimization approach [BKM11]. MILLEPEDE-II is capable of fitting several thousand parameters and millions of tracks simultaneously and is therefore also used in the alignment of the CMS silicon tracker. The calculated alignment constants are stored and upon the next execution of the analysis processor, they are applied to the data. It was shown that the alignment constants typically converge already after the second execution of the analysis.

After the complete alignment of the setup, particle tracks reconstructed from the telescope data are extrapolated to the expected hit positions in the DUT and REF planes to check if the traversing particle has been detected. As mentioned above the telescope has a much larger integration time and sensor area than the DUT and the reference sample. Thus only a few of the particle tracks in the telescope are detected and only tracks with a hit in the REF plane are

³ A triplet is a part of a complete particle track consisting of three hits in the planes of one telescope arm.

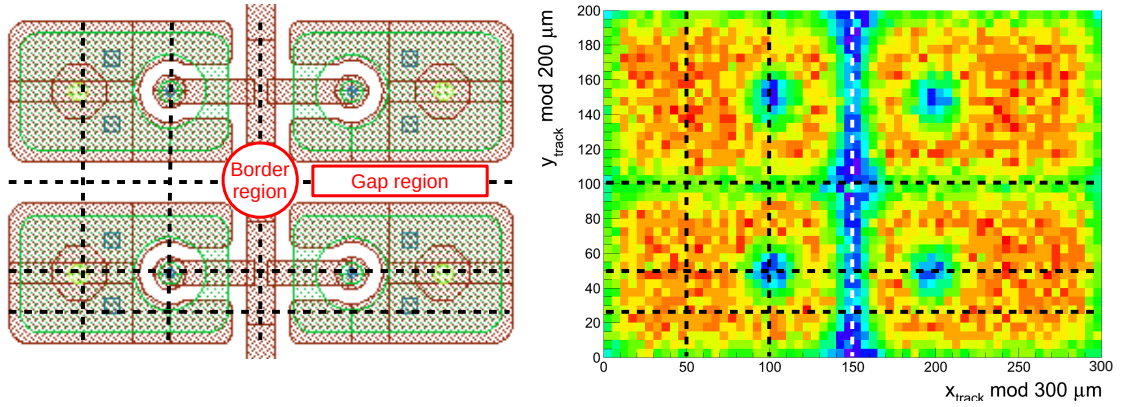


Figure 9.5: Definition of the profile cuts and the regions used during data analysis. The dashed lines indicate the positions of the 1D profiles that have been created to better quantify the performance of the sensor layouts. The red boxes mark additional regions in between the pixel cells where the performance is also evaluated. Since the fiducial region of the pixel array only consists of identical multiples of the basic 2×2 building block (left), all pixel data from one measurement is folded into one building block during analysis to increase statistics (right).

considered as detectable tracks for the DUT. This allows the definition of the DUT detection efficiency as follows:

$$\text{Eff}_{\text{DUT}} = \frac{\text{Tracks with both REF and DUT hits}}{\text{Tracks with only REF hit}} \quad (9.1)$$

The analysis further distinguishes between hits in the DUT without restrictions (DUT hits) and hits with a corresponding hit in the reference sensor (linked hits) which include a complete track through the telescope and both detector samples. A second distinction is made between hits in the entire pixel matrix of the DUT and hits only in the inner pixel grid which forms the fiducial region. The edge pixels are excluded from that region since they have a different electric field configuration, charge collection behaviour and spatial resolution due to their enlarged size.

9.5 RESULTS

As mentioned in section 8.2 the differences of the HPK pixel sensor variations lie in the layout of the pixel cells of the sensor. It is therefore necessary to study the performance of the sensor samples on the level of the individual pixel cells. Since the sensor area comprises in total 4160 pixel cells and the available measurement time at the test beam is limited, the average hit statistics is low in a single pixel cell of the sensor and does not allow the study of individual pixel cells. This problem is solved by taking advantage of the layout of the fiducial region of the pixel array of the sensors. The layout only consists of multiples of the same basic building block of 2×2 pixel cells which allows the folding of all data from one measurement into one single 2×2 block. This method increases the available statistics for one pixel cell by a factor of 1000 and thus makes the study of individual pixel cells possible.

The left-hand side of figure 9.5 shows the basic sensor building block with a size of $300 \times 200 \mu\text{m}^2$ consisting of 2×2 cells while on the right an example of the associated folded measurement results is plotted. The folding is always indicated by “mod” in the axis labels. The main features of the building block like the four pixel implants with the isolated bias dots connected by the central bias line are clearly visible.

In order to be able to better quantify the performance of the individual pixel cells several cuts in the form of one-dimensional profiles are extracted from the two-dimensional measure-

Table 9.2: Naming and positions of the one-dimensional profile cuts of the basic 2×2 sensor building block used for the analysis of the test beam data.

Profile name	Position	Pixel cell feature
xm50	$x = 50 \mu\text{m}$	Unstructured (reference)
xm100	$x = 100 \mu\text{m}$	Bias dots
xm150	$x = 150 \mu\text{m}$	Bias line
ym25	$y = 25 \mu\text{m}$	Unstructured (reference)
ym50	$y = 50 \mu\text{m}$	Bias dots
ym100	$y = 100 \mu\text{m}$	Gap and border regions

ment result plots. They are both taken from the unstructured region of the pixel cells and from selected regions with features like the bias dots, the bias line, the gap region between two pixels and the border region between four pixels. This allows a comparison of the results at the positions of the structures with the reference values from the unstructured region. The six profile cuts, the gap region and the border region used in the analysis are indicated in figure 9.5 and the names and positions of the profile cuts are given in table 9.2.

The following analysis results are presented in this thesis:

SPATIAL HIT DETECTION EFFICIENCY: The reconstructed particle tracks from the beam telescope allow the creation of high resolution hit efficiency plots for the individual layouts whereby the impact of the structures like the bias dots or the bias line on the efficiency becomes visible. The efficiency value is calculated according to equation 9.1.

CLUSTER SIZE: Charge sharing between several adjoining pixels requires the clustering of the hit data. Since the `PSI46V2` readout chip not only records hits, but also the associated pulse heights of the signals, the clustering algorithm can profit from this information during the calculation of the cluster center which directly improves the spatial hit resolution. The average cluster size is an indicator of the usability of this method.

SPATIAL RESOLUTION: The spatial resolution of the DUT is one of the most important parameters besides the hit detection efficiency. To first order, it is given by the width of the distribution of the residuals. The residual is the calculated distance between the interpolated penetration point of the telescope track in the DUT and the hit position assigned by the clustering algorithm. However, the width of the distribution is folded with the intrinsic resolution of the beam telescope. Since the pointing resolution of the telescope is very high (cf. section 9.2.2), no unfolding has been performed. The values for the resolution are then compared to the theoretical values assuming only binary readout which are calculated by $\sigma \approx \text{pitch}/\sqrt{12}$ (cf. section 3.3). The measured values should be better due to the available pulse height information.

The analysis results are taken from both unirradiated and irradiated samples which were mounted perpendicular to the electron beam during the measurements at DESY. The resulting incidence angle of 0° is best suited for the study of the performance of the different pixel sensor variations since other values would always lead to additional charge sharing due to geometrical reasons. All unirradiated samples were operated with a bias voltage of -150 V which corresponds to the default operating voltage also used for the modules of the CMS pixel detector. The irradiated samples were operated with a bias voltage of -450 V . This value was chosen according to the results of the prior electrical tests of the samples which were performed with bias voltages up to -600 V . The results showed that the sensors are already fully depleted at -450 V and the potential risk of breakdown of the samples is strongly reduced at this value

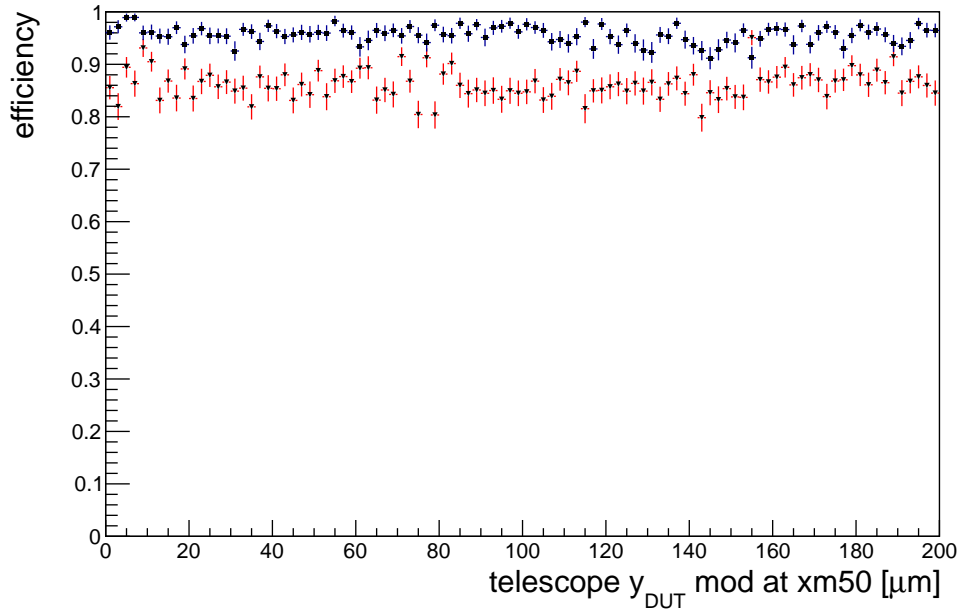


Figure 9.6: Illustration of the test board clock problem on the basis of two hit detection efficiency profiles of the unstructured region (xm50) of chip 62. The only difference between the two measurements is the clock scheme. It is clearly visible that the efficiency at 40 MHz (indicated by triangles with red error bars) is lower than at 80 MHz (squares with blue error bars).

compared to operation at -600 V.

One problem encountered during data analysis is the effect of the test board clock signal on the data (cf. section 9.2.2). It is illustrated in figure 9.6 for chip 62, an unirradiated BPixB sample. The plot shows two one-dimensional profiles of the hit detection efficiency in the unstructured region (xm50) of the pixel cells. The only difference between the two measurements is the test board clock scheme, no other parameters were changed. It is clearly visible that the efficiency at 40 MHz is lower than at 80 MHz. This drop is attributed to the clock shift interrupting the PLL in the internal clock distribution circuit of the test board while running with the 40 MHz clock.

To be able to compare the measurements taken with the 40 MHz clock with the ones taken with the 80 MHz clock (without PLL) the decision has been made to rescale the results from all 40 MHz runs to the expected nominal values from the results of the 80 MHz runs.

A second problem is the validity of the recorded data for both the telescope and the HPK samples. Since there was no direct data quality monitoring (DQM) available during the test beam, this could only be checked afterwards during analysis. Out of the eight samples (see table 9.1), chip 60 has no valid data at all because it was measured as the very first DUT with only the 40 MHz clock and the clock settings were not optimized either. For chip 64 there are problems with the calibration of the ROC. Apparently the comparator threshold was set too high and thus lower signals generated by the traversing particles are cut off. This limits the analysis to the hit detection efficiency because the other results like average cluster size are dependent on the threshold setting.

9.5.1 HIT DETECTION EFFICIENCY

The hit detection efficiency of the pixel sensor layout samples is determined by the number of track-related hits in both the DUT and the reference sensor divided by the total number of tracks with at least a corresponding reference hit (cf. equation 9.1). Depending on the exact hit position and the sensor layout the efficiency varies within a certain range. However, since the implant always covers a big part of the pixel cell area the overall efficiencies for all measured unirradiated pixel sensor layouts are between 96 % and 99 % and there are no outliers meaning that all sensors show comparable performance. This result was expected since the design process of the HPK pixel sensor layout variations used the layouts of the two sensor types currently in use in the barrel and forward pixel detector of CMS as a starting point and these sensors have already proven their quality both during the operation at the LHC and in laboratory tests [AAB⁺08].

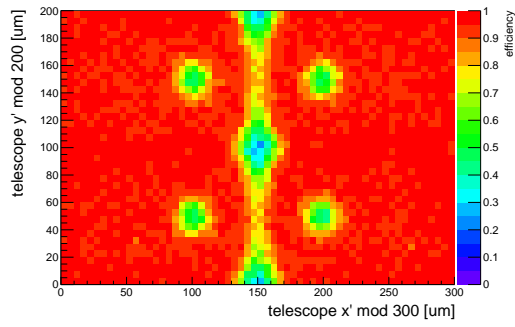
Only if the hit detection efficiencies of the different sensor layouts are analyzed for the single pixel cells, it is possible to locate inefficient regions caused by the individual features of the layouts. Therefore spatial resolved efficiency plots like the ones shown in figure 9.7 have been created for all measured pixel sensor samples. The highest efficiencies are typically associated to particle tracks that traverse the implant areas of the pixel cells. All charge that is created in the sensor bulk below is collected by the implant which gives a high signal and a high detection probability. If a track on the other hand traverses the sensor in between two implants, the effective charge per pixel is reduced due to charge sharing and due to charge flowing into the biasing circuit. Therefore the resulting signals might not be able to exceed the comparator thresholds of the ROCs, stays undetected and thereby reduces the efficiency in that particular region.

Figure 9.7a shows the hit detection efficiency of the unirradiated BPixA sample (chip 62). As described before, only the structured regions of the pixel cells without implant like the bias dots and the central bias line exhibit a lower efficiency. The border regions where four neighboring pixels meet are regions with even lower efficiency. The inefficiency at these regions is a result of both the missing implant and the bias line above which influences the electric field responsible for the collection of the generated charge. Additionally the generated charge might partly drain via the bias line. For the unirradiated FPixF sample (chip63, see figure 9.7b) only the inefficiency at the border regions is visible but the efficiency drop is lower than for the BPix sample. This is due to the fact that the FPix layouts do not feature a biasing circuit which influences the electric field configuration.

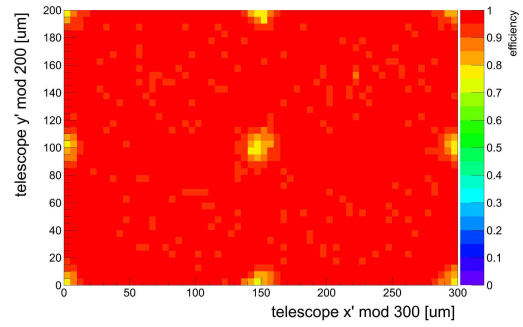
For the BPixA sample the efficiency drop does not occur at the border regions without bias line because the BPixA layout features larger implant sizes compared to the FPixF layout which improve the charge collection (cf. table 8.1).

After irradiation the hit detection efficiency changes noticeably. A comparison of an unirradiated BPixA sample (chip 62) and an irradiated BPixB sample (chip 66) is shown in figures 9.7a and 9.7c. The effect of irradiation is clearly visible in the two plots. While the efficiency of the irradiated sample is only about 7 % lower in the unstructured region of the pixel cells, it is strongly affected in the bias dots, the central bias line and towards the gap regions between the pixel cell implants. These efficiency drops are the results of the reduction of the signal charges which might fall below the comparator thresholds of the ROCs. The reduction is caused both by charge sharing (see table 9.4) and by radiation damage (cf. section 3.4) which leads to charge trapping in the band gap and changes of the electric field configuration [SFK⁺12]. Comparable results from a test beam campaign of irradiated strip sensors with multiple strip geometries are shown in [Nür13].

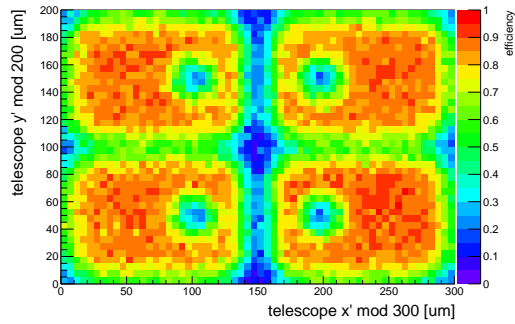
Figure 9.7d shows the efficiency of an irradiated FPixF sample (chip 65). Since the FPix layouts have no bias dots and associated bias lines their efficiency is not affected and only the drop towards the gap and border regions between the pixel cell implants is visible.



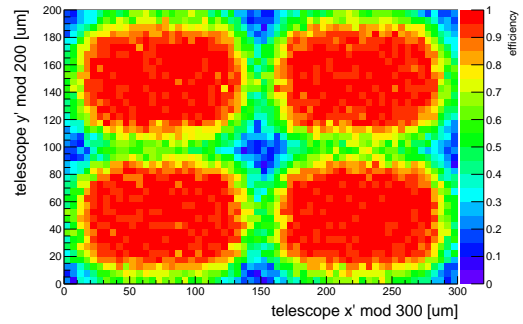
(a) Efficiency of the unirradiated BPixA sample (chip 62). The efficiency is very high in all regions except the bias dots, the central bias line and especially the border region between the four pixels.



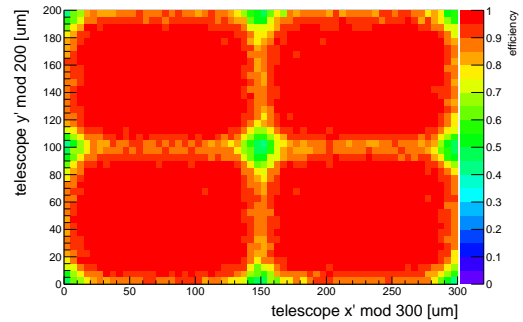
(b) Efficiency of the unirradiated FPixF sample (chip 63). Since the FPix layouts have no bias dots and associated bias lines their efficiency is not affected. Only the drop in the border regions between four neighboring pixels is visible but much less pronounced than in the BPix samples.



(c) Efficiency of the irradiated BPixB sample (chip 66). While the efficiency is only 7% lower in the unstructured region of the pixel cells compared to the unirradiated sample, it is strongly affected in the bias dots, the bias line and towards the gap regions between the pixel cell implants.



(d) Efficiency of the irradiated FPixF sample (chip 65). Compared to the unirradiated sample, the efficiency in the unstructured regions of the pixel cells did not decline at all and only the drop towards the gap regions between the pixel implants is visible.



(e) Efficiency of an irradiated FPixE sample (chip 67). The drop towards the gap regions is much reduced compared to the irradiated FPixF sample. This is an effect of the larger implant size of the FPixE layout.

Figure 9.7: Hit detection efficiencies of both unirradiated and irradiated HPK pixel sensor samples. A reduction of the efficiency is clearly visible in the irradiated samples. The irradiated FPix samples in general and especially the FPixE sample show better results than the irradiated BPixB sample.

Table 9.3: Hit detection efficiencies of the pixel cell structures of the HPK pixel sensor layouts. The values are given as percentages of the efficiency of the unstructured regions of the pixel cells. The FPix layouts have no bias dots and no bias lines and thus the values at the bias line region are identical to the ones in the gap region. The statistical uncertainty of the values is 6%.

Layout	DESY name	Efficiency compared to unstructured region			
		Bias dot	Bias line	Gap region	Border region
BPixA	chip 62	55 %	82 %	100 %	27 %
BPixC	chip 61	44 %	71 %	100 %	23 %
FPixF	chip 63	-	100 %	100 %	80 %
BPixB (irradiated)	chip 66	33 %	27 %	68 %	11 %
FPixE (irradiated)	chip 64	-	92 %	92 %	49 %
FPixE (irradiated)	chip 67	-	92 %	92 %	45 %
FPixF (irradiated)	chip 65	-	59 %	63 %	13 %

While the hit detection efficiencies are equally high for the two FPix layout variations in the unirradiated case, this changes for the irradiated samples. A comparison of irradiated FPixF and FPixE sensor layouts is shown in figures 9.7d and 9.7e. The FPixF layout is the reference layout which is closest to the original FPix sensor layout while the FPixE layout is an aggressive variant of the FPixF design with a 91 % larger implant and a 38 % thinner p-stop ring.

The large efficiency drop of the reference layout towards the gap regions is mitigated by the larger implant size of the FPixE layout. The larger implant both reduces the width of the gap and minimizes the changes of the electric field configuration in the remaining gap after irradiation.

The hit detection efficiencies for all measured samples at the unstructured regions of the pixel cells and also at the structures, the gap region and the border region have been extracted from the measurement results with the help of one-dimensional profile cuts of the efficiency plots shown in figure 9.7. The values are given in table 9.3. To be able to compare the results of the different layouts and also the unirradiated and irradiated samples the values are given as percentages of the efficiency of the unstructured regions of the pixel cells.

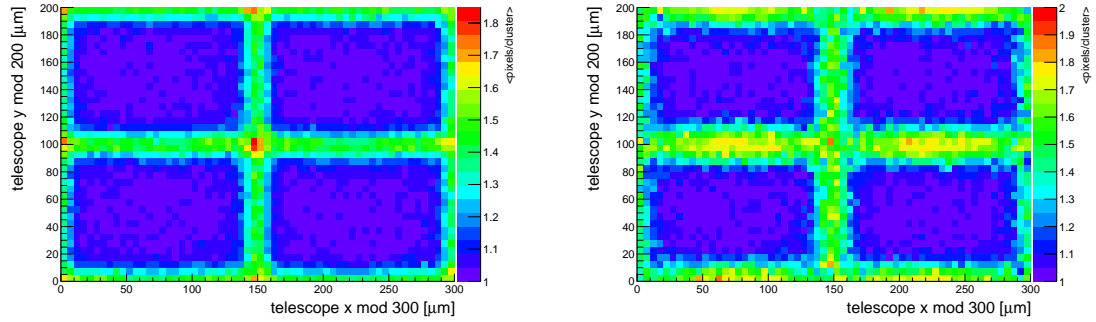
For the different BPix layout variations it becomes clear that the larger bias dot isolation of the BPixC layout (compared to the BPixA layout) results in a worse efficiency in the bias dot region and also in the bias line region which are both caused by the smaller implant size (see table 8.1).

For the FPix layout variations the values confirm the findings from above. The FPixE layout benefits from the larger implant and shows much better efficiencies in the gap regions and especially in the border region where four neighboring pixels meet.

9.5.2 CLUSTER SIZE

Charge sharing between adjoining pixels leads to hit clusters instead of single hits in the pixel sensor. Figure 9.8 shows a comparison of the measured average cluster sizes in an unirradiated and an irradiated FPixF sample.

Particles that hit the pixel cells at the position of the implant mostly create one pixel clusters due to the configuration of the electric field while particle hits in between two neighbouring pixels are more likely to share the generated charge between the pixels and thus produce two pixel clusters. This probability is reflected in the plots in figure 9.8 by the increased cluster sizes



(a) Cluster sizes of the unirradiated FPiXF sample (chip 63). In the gap and border regions the cluster sizes are larger due to charge sharing. (b) Cluster sizes of the irradiated FPiXF sample (chip 65). Compared to the unirradiated sample, the cluster sizes in the gap and border regions have increased due to the changes of the electric field configuration.

Figure 9.8: Comparison of the average cluster sizes of unirradiated and irradiated FPiXF layouts. Particles that hit the pixel cells at the implant positions mostly create single pixel clusters while hits in between two implants are more likely to share the generated charge and produce two pixel clusters. The largest clusters are thus created in the border regions where four neighboring pixels meet.

Table 9.4: Measured average cluster sizes of the HPK pixel sensor layouts. While the cluster sizes are close to 1 in the pixel implant area, the values are larger in the gap and border regions due to charge sharing. Irradiated samples show larger cluster sizes than the unirradiated ones due to changes of the electric field configuration. The statistical uncertainty of the average cluster sizes is 0.13.

Layout	Name	Cluster size				
		Pixel implant	Bias dot	Bias line	Gap region	Border reg.
BPixA	chip 62	1.02	1.09	1.1	1.28	1.36
BPixC	chip 61	1.01	1.05	1.07	1.29	1.25
FPiXF	chip 63	1.04	-	1.42	1.49	1.83
BPixB (irrad.)	chip 66	1.1	1.28	1.28	1.8	1.9
FPiXE (irrad.)	chip 67	1.15	-	1.82	1.87	2.18
FPiXF (irrad.)	chip 65	1.06	-	1.7	1.77	1.88

in the gap regions between the pixels. Even larger clusters are created in the border regions where four neighboring pixels meet.

For the irradiated sample, the cluster sizes are increased compared to the unirradiated one. This is due to the changes of the electric field configuration caused by radiation damage.

The average cluster sizes for all samples with valid data at both the unstructured regions of the pixel cells and at the structures, the gap region and the border region have been extracted from the measurement results with the help of one-dimensional profile cuts of the cluster size plots. The values are presented in table 9.4.

The average cluster sizes are close to 1 for particle hits in the implant region of the pixel cells and increase for the gap and border regions due to charge sharing. For the BPix samples the average cluster size in the gap region with the bias line is lower than in the other gap regions. This is a sign that the bias line influences the configuration of the electric field. Parts of the created charge might also flow into the bias grid instead of the pixel cells and the remaining charge is not able to exceed the comparator threshold of the ROCs.

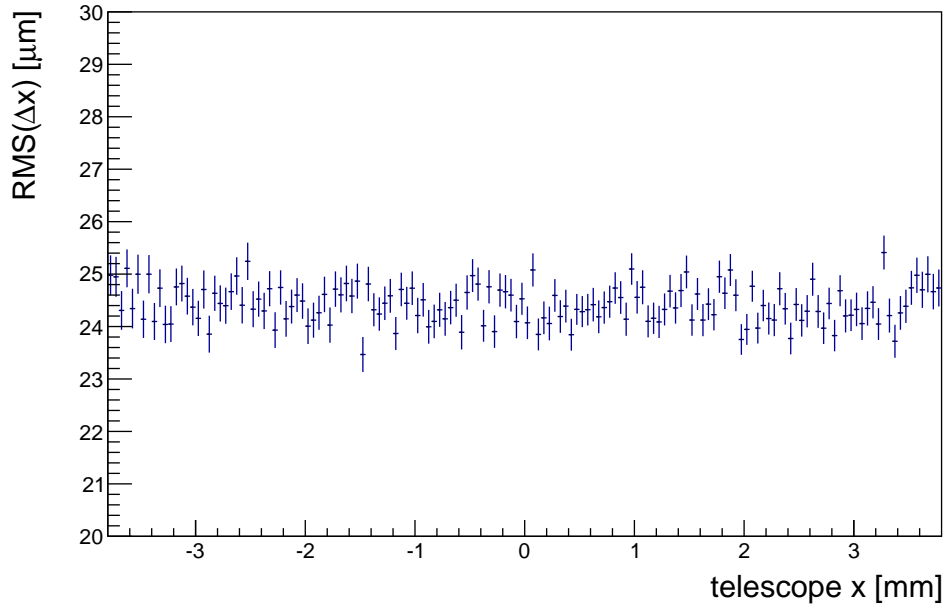


Figure 9.9: Spatial resolution of the unirradiated BPixB sample (chip 62) in x -direction of the telescope planes. The mean value is $24.6 \mu\text{m}$. Due to the mounting scheme of the DUT the x -direction of the telescope planes corresponds to the shorter dimension of the pixel cells which is $100 \mu\text{m}$. The measured value is 15 % better than expected resolution for binary readout of $\approx 29 \mu\text{m}$.

For the irradiated FPixE sample the cluster sizes in the gap and border regions are larger than for the irradiated FPixF sample. This can be attributed to the larger implant size of the FPixE layout which supports the charge sharing by increasing the amount of gathered charge and thus the probability to reach the comparator threshold.

9.5.3 SPATIAL RESOLUTION

The distribution of the mean spatial resolutions of the unirradiated BPixB sample (chip 62) in x -direction of the telescope planes is shown in figure 9.9. The mean value of the resolution taken from the distribution is $24.6 \mu\text{m}$. Due to the mounting scheme of the sensor samples in the DUT position the x -direction of the telescope planes corresponds to the shorter dimension of the pixel cells. The associated pixel pitch is $100 \mu\text{m}$ and thus the expected resolution for binary readout is $\sigma \approx 100 \mu\text{m}/\sqrt{12} \approx 29 \mu\text{m}$. The measured value of $24.6 \mu\text{m}$ is 15 % better than this value which underlines the importance of the availability of the pulse height information. Together with the charge sharing the pulse height information allows a more accurate hit position calculation in the clustering process which improves the resolution.

The mean values of the resolutions in both x - and y -direction of the pixel cells have been extracted from the analysis results of all pixel sensor samples with valid data and are shown in table 9.5. All values are better than the expected resolutions for binary readout ($\approx 43 \mu\text{m}$ in x -direction and $\approx 29 \mu\text{m}$ in y -direction).

The different layout variations do not show any noteworthy differences in resolution. However, all irradiated samples show 10 % better resolution values in x -direction and 12 % better resolution values in y -direction compared to the unirradiated ones. This can be attributed to the larger cluster sizes reported above which additionally improve the hit position calculation in the clustering process.

Table 9.5: Measured average resolutions of the HPK pixel sensor layouts. All values are better than the expected resolutions for binary readout ($\approx 43 \mu\text{m}$ in x and $\approx 29 \mu\text{m}$ in y). There are no large differences between the layouts but the irradiated samples show better values compared to unirradiated ones since the larger cluster sizes improve the hit position calculation. The statistical uncertainty of the average resolutions is $0.8 \mu\text{m}$.

Layout	DESY name	Resolution x (μm)	Resolution y (μm)
BPixA	chip 62	35.4	24.6
BPixC	chip 61	35.6	24.8
FPixF	chip 63	35.5	24.0
BPixB (irradiated)	chip 66	32.1	21.8
FPixE (irradiated)	chip 67	32.0	21.2
FPixF (irradiated)	chip 65	31.6	20.8

9.6 CONCLUSIONS

The first conclusion from the results presented in the last section is that the individual changes of the different HPK sensor layout variations show the expected effects and that there are no unforeseen surprises like non-working layouts. Such problems could be caused by too aggressive sensor designs which cannot be operated either due to early current breakdown caused by very high electric fields or due to short-circuits between the individual pixel cells caused by a too low value of the pixel isolation.

Increased implant areas realized by larger implant sizes and smaller bias dot isolation distances or thinner p-stop rings (cf. table 8.1) lead to the desired effects of better hit detection and better charge sharing. The resulting larger cluster sizes allow a more accurate hit position calculation which improves the spatial resolution. At the same time the changes do not lead to unusable sensors and thus are not too aggressive. The negative influence of the bias structure only present on the BPix sensor layouts on the charge collection is also verified.

The main goal of the sensor layout study was to identify the pixel cell layout which is best suited for the needs of the Phase II pixel detector and should therefore be taken as the starting point for future sensor developments with smaller pixel sizes. From the results one could easily conclude that the FPix sensor layout in general and especially the aggressive FPixE variant is the sought layout.

The simple feature-less layout of the pixel cells without bias dots and bias lines yields a homogeneous hit detection efficiency over the entire pixel cell with only small drops in the border regions where four neighboring pixels meet (cf. figure 9.7b). After irradiation, these drops also extend to the gap regions between two neighboring pixels but it has been shown that this effect is mitigated by the maximized implant size of the FPixE layout variation (cf. figure 9.7e).

Also the hit clusters are larger in the gap regions between the pixel implants both before and after irradiation compared to the BPix layouts. The hit position calculation in the clustering process profits from larger cluster sizes and thus the average spatial resolution is better for the FPix layouts.

In contrast, the efficiency of the BPix layouts is influenced by the structure used for the biasing of the individual pixel cells. This structure consists of the bias dots and the bias lines. While the bias dot reduces the efficiency in the otherwise homogeneous pixel cell due to the missing implant area, the bias line severely influences the efficiency in the gap region where it is located since it has a negative effect on the electric field configuration.

In the border regions where four neighboring pixels meet the combined effects of the bias line and the missing implant lead to a severe drop of the efficiency. In contrast to the FPix sample, there is no inefficiency in the border regions without bias lines because the implant is larger (cf. figure 9.7a). After irradiation the efficiency drop at the bias structures increases and additional inefficiencies at the gap regions appear (cf. figure 9.7c). Overall, the efficiency of the irradiated BPixB sample is worse than the one of the irradiated FPixE and FPixF samples.

However, such a conclusion does not take into account the benefits of the bias structure of the BPix layouts. It allows the reliable measurement of the IV characteristic of the silicon sensor before the bump-bonding of the readout chips is performed and thus the determination of the sensor quality. This is very important since only known good sensors should be bump-bonded since the process is expensive and time-consuming and the used ROCs cannot be reclaimed if the sensor is found bad only after bonding. A secondary effect of the bias structure is the protection of the ROCs in case of an event like beam loss in the LHC which creates an unwanted amount of charge in the sensor. The charge could then drain via the bias lines instead of flowing into the ROCs and destroying the sensitive input amplifiers.

As mentioned in section 8.2, the open p-stop structure used for the pixel isolation of the FPix sensor layouts should provide the same functionality. Yet there are large deviations between the IV characteristics of the bare sensors and the complete single chip assemblies after bump-bonding as shown in [Sch15]. The leakage currents of the SCAs are up to a factor of 10 higher than those of the bare sensors and the breakdown voltages are significantly lower. This has been attributed to an incomplete depletion of the pixel cells. Especially the cells in the middle of the pixel matrix are less accessible by the accumulation layer which is needed to connect the individual cells to the bias ring.

Another result of the IV measurements both before and after bonding in [Sch15] is the fact that the breakdown voltage of the reference FPixF layout, which is closest to the original FPix sensor layout, is higher than the breakdown voltage of the aggressive FPixE layout with maximized implant size and thinner p-stop rings. This confirms the problems of the higher electric fields at the edges of the pixel cell structures which were already mentioned in section 8.2 and might lead to earlier breakdown.

While from the point of view of hit detection efficiency, a homogeneous pixel cell with a maximized implant size would be desirable, quality assurance requires a sensor which is reliably testable and from the point of view of detector operation the sensor has to have a sufficient breakdown voltage that allows safe operation in the experiment also after several years of irradiation. The design of a new pixel sensor layout is therefore always a trade-off between implant size, pixel isolation scheme and biasing scheme which is not easy to solve.

The sizes of the pixel implant and the isolation scheme can only be optimized through detailed T-CAD simulations and evaluation of sensor prototypes but there are ideas how to enable a reliable IV measurement without the need for a biasing circuit which causes inefficiencies and is not needed during later operation in the experiment. One idea is to put an additional aluminum grid on the top side of the sensor which connects the bump bond pads of all pixel cells. This grid could then be used for biasing during the measurement of the IV characteristic of the sensor and afterwards removed by chemical etching. Only after the removal the good sensors would be bump-bonded with readout chips.

This idea has not yet been realized and it is unclear whether the etching process and the additional handling steps influence the quality of the sensors. It is also not yet defined if the testing should occur before or after cutting since the removal of the metal grid is more complicated on individual sensors than on complete wafers. On the other hand the cutting could introduce additional problems which are not detected if it is performed only after testing. It might therefore be easier to concentrate on the improvement of the functionality of the open p-stop structures of the FPix sensor layouts.

Conclusions from the sensor layout study itself also lead to advice for future test beams with the goal to improve the quality of the detector samples, the measurement data and the results. Samples should only be produced from known-good sensors and readout chips with proven and regularly used bump-bonding processes. The measurement setup at the test beam should be well understood and allow the in-situ calibration of the detector samples. A fast feedback of the data quality either through online monitoring or immediate analysis of the recorded data is mandatory to be able to quickly intervene if problems occur. All these points have not yet been available for the study.

While both a better measurement setup and the direct monitoring of the data quality have been realized in the last years through the usage of the newest version of the PSI46 readout chip (called PSI46DIGV21-RESPIN) and a complete integration of the readout into the EUDAQ data acquisition framework [Spa16], it was not possible to bump-bond additional detector samples which would have been necessary for a new test beam campaign.

The missing UBM on the already cut pixel sensors from the HPK campaign only allows for bumping processes which do not need UBM since the UBM application on single sensors is not feasible. Therefore the gold-stud bumping available at IPE which was already discussed in section 8.3 is a suitable process. However, the placement of gold studs on the HPK pixel sensors was not successful due to the very small opening in the passivation layer above the bump-bond pads of the pixel cells. The contact area between gold stud and aluminum pad is too small and the gold does not stick to the pad.

Part IV

SUMMARY AND OUTLOOK

SUMMARY AND OUTLOOK

Today's particle accelerators and the associated experiments are planned and built in huge interdisciplinary efforts and the collaborations behind the largest projects comprise more than 5000 scientists from numerous countries all over the world. Both the accelerators and the detectors undergo continuous changes and improvements during their planned operation periods of several decades in order to make use of technological progress and to adapt new developments in the field of high-energy physics. This thesis focuses on the planned upgrades of the silicon pixel detector of the Compact Muon Solenoid (CMS) experiment, one of the particle detectors at the Large Hadron Collider (LHC), the world's largest and most powerful particle accelerator.

The first part of this thesis is dedicated to the module production for the Phase I upgrade of the CMS silicon pixel detector, the innermost part of the CMS experiment. The task of the pixel detector is to provide information about the trajectories of charged particles emerging from the proton-proton collisions at the center of CMS. It has proven to perform well under the current operating conditions despite the fact that the LHC has already exceeded its design luminosity by more than 50%. However, further increases up to $\mathcal{L} = 2 \cdot 10^{34} \text{ cm}^{-2} \text{ s}^{-1}$ are planned for the upcoming years and under these conditions, the present detector would be subjected to severe inefficiencies and data losses due to readout-induced dead time and insufficient buffering capabilities of the readout chips of the detector modules.

In order to overcome these limitations, the CMS collaboration has decided to replace the existing pixel detector with a new detector, which is currently being built by a collaboration of many universities and research institutions. The new Phase I pixel detector constitutes an advancement of the present design comprising a new readout chip which addresses the inefficiencies and other improvements like a reduced material budget. Its installation in the experiment is planned during an extended year-end technical stop of the LHC at the beginning of the year 2017.

In the last two years, 409 modules for the new CMS barrel pixel detector have been produced at KIT and tested at RWTH Aachen. This thesis covers the complete production chain of the modules, starting from the raw materials and ending with the fully tested modules. Special attention was paid to the quality assurance during production and to the testing of the modules. For this task three dedicated test setups have been designed, built and operated. An additional point was the test procedure of the bare silicon sensors. The IV measurement parameters and the upload to the central production database for long-term storage have been defined.

The first test setup is used for electrical functionality tests of the High Density Interconnect (HDI), a flexible PCB responsible for the routing of the data and power lines on the barrel pixel module. With the help of a needle card the test station checks the integrity of all traces and also the functionality of the Token Bit Manager (TBM) chip.

The other two setups are used for testing the complete modules. The testing procedure consists of both electrical and X-ray tests. While the electrical tests confirm the functionality of the modules at $+17^\circ\text{C}$ and -20°C , the X-ray test checks them for missing or defective bump-bond connections. Additionally the X-ray test allows the calibration of the pulse height signal measured by the ROCs. A problematic bump-bond connection prevents the charge created in the silicon sensor from being read out and thus the hit will stay undetected.

After testing the modules are packaged and shipped to RWTH Aachen where they are qualified according to predefined grading parameters to ensure that only good modules are installed in the new pixel detector. For the 409 KIT modules the final results of the qualification are excellent. 343 (or 84 %) of the modules are ready for the installation in the new CMS pixel detector. A detailed analysis of the X-ray test results revealed that the total number of defective bump-bond connections is very small. Out of 23 296 000 tested pixels only 2750 (or 0.012 %) are defective while the grading criteria would allow up to 1 %.

The overall yield of the KIT-RWTH module production of 84 % is the highest among all five module production centers in the Phase I Barrel Pixel Upgrade Collaboration and thus the ultimate confirmation of the excellent work done both at KIT and RWTH Aachen.

The second part of this thesis focuses on the study of optimized silicon pixel sensor layouts for the Phase II upgrade of the CMS pixel detector. After the year 2023 the LHC will be upgraded to the High Luminosity LHC (HL-LHC) with the goal of even higher instantaneous luminosities around $\mathcal{L} = 5 \cdot 10^{34} \text{ cm}^{-2} \text{ s}^{-1}$. Besides radiation damage, the main challenge for the CMS pixel detector then is the number of simultaneous proton-proton collisions in one LHC bunch crossing. It will result in high occupancy in the tracking detectors which might compromise the track finding in the reconstruction process.

One way to reduce the occupancy is to increase the detector granularity. In case of the CMS pixel detector this is planned by shrinking the size of the pixel cells in a newly designed silicon sensor by at least a factor of four. However, at the beginning the testing capabilities for new sensors are limited due to the non-availability of readout chips with a compatible bump-bonding pattern. The very first step towards a new sensor is therefore testing new ideas with sensor prototypes compatible with existing readout chips like the PS146 series used both in the current and the upgraded Phase I pixel detector. This approach was used in this work.

The performance of six optimized pixel sensor layouts based on the sensors currently in use in the barrel and forward pixel detectors of CMS has been investigated with an electron beam at the DESY Test Beam Facility for both unirradiated and irradiated samples. A beam telescope provided precise tracking of the particles traversing the sensor samples, which is required for the study of important sensor parameters like hit detection efficiency and spatial resolution on the level of the individual pixel cells.

The results show that the changes implemented in the different sensor layout variations show the intended effects and that there are no unforeseen surprises like non-working samples due to too aggressive sensor designs. Increased implant areas lead to better hit detection and better charge sharing with larger cluster sizes. Larger cluster sizes in turn allow a more accurate hit position calculation, which improves the spatial resolution of the sensors. Also the negative influence of the bias structure only present on the barrel pixel layouts on the electric field configuration and on the charge collection has been demonstrated.

The main goal of the sensor layout study was the identification of the pixel cell layout which is suited best for the requirements of the Phase II pixel detector and should thus be taken as starting point for further sensor developments with smaller pixel sizes. The conclusion from the results of the test beam campaign is that the design of a new pixel sensor layout is always a trade-off between implant size, pixel isolation scheme and biasing scheme. From the point of view of hit detection efficiency, a homogeneous pixel cell layout with a maximized implant size like in the FPixE layout derived from the forward pixel sensor is highly welcome while for safe detector operation a sufficient breakdown voltage that allows operation also after years in a radiation environment is mandatory. The electric fields at the cell edges and thus the risk for breakdown are higher when the isolation distances between the individual pixel cells are decreased in an attempt to maximize the implant size.

Another point is the need for sensors that are testable before bump bonding since only good sensors should be bump-bonded due to the high cost of the process. A basic test method is the

measurement of the IV characteristic of the sensor. The dedicated bias structure on the BPix layouts allows this measurement compared to the FPix solution with the open p-stop isolation scheme which does not yield reliable results.

OUTLOOK

The new Phase I pixel detector is on schedule for installation in the CMS experiment at the end of February 2017. The recommissioning phase of the LHC with beam will start in the first week of May and will provide the first proton-proton collisions for the new detector. Physics production will finally be resumed in June 2017.

As mentioned before, the challenges of the HL-LHC operating conditions require an increase of the granularity of the CMS tracking detectors. In case of the pixel detector this will be achieved by shrinking the pixel cell size of the silicon sensor in a module with a design comparable to the Phase I module described in the first part of this thesis. In the last two years, the CMS Phase II Pixel Upgrade Collaboration has therefore put a lot of effort in designing and optimizing more than 30 new pixel sensor layouts with smaller pixel sizes.

Since several new readout chips with different bump-bonding patterns will become available in 2017 that are intended for the investigation of the new sensors, the sensor layouts have pixel cells with either $50 \times 50 \mu\text{m}^2$, $100 \times 25 \mu\text{m}^2$ or $100 \times 30 \mu\text{m}^2$. Additionally there are sensor layouts with smaller pixel cells but a metal routing compatible with the existing PSI46DIGV21-RESPIN and PROC600 readout chips used for the Phase I modules which serve as backup solutions if there should be unforeseen problems with the first iterations of the new chips.

All sensors are produced with a single wafer layout dedicated only to the Phase II pixel upgrade. This decision allows using standard bump-bonding technologies for the production of the test samples since the necessary under-bump metallization (UBM) can be applied on the complete wafers. The wafer layout has been finalized recently and 35 wafers have been ordered. They are currently in production with the delivery to the CMS collaboration planned for March 2017. First bump-bonded samples will thus be available in the first half of the year and the first test beam campaign is already planned for July 2017.

BIBLIOGRAPHY

- [2SM15] CMS Tracker Upgrade Sharepoint: 2S Module Design Documents. Version: December 2015. <https://espace.cern.ch/Tracker-Upgrade/2S-Module/SitePages/Home.aspx> (cited on page 17.)
- [3M 00] 3M COMPANY: 3M Fluorinert Electronic Liquid FC-72: Product Information. Version: May 2000. http://solutions.3m.com/wps/portal/3M/en_US/Electronics_NA/Electronics/Products/Electronics_Product_Catalog/~//3M-Fluorinert-Electronic-Liquid-FC-72?N=8704931+3294001636&rt=rud (cited on page 37.)
- [A⁺12] AGUILAR, J. et al.: Infrastructure for Detector Research and Development towards the International Collider. (2012). <https://arxiv.org/abs/1201.4657> (cited on page 113.)
- [A⁺13] ALBERTI, G et al.: Development of a Thermal Control System with Mechanically Pumped CO₂ Two-Phase Loops for the AMS-02 Tracker on the ISS. (2013), Feb, Nr. arXiv:1302.4294. <https://cds.cern.ch/record/1517395> (cited on page 38.)
- [AAB⁺08] ALLKOEFER, Y. ; AMSLER, C. ; BORTOLETTO, D. ; CHIOCHIA, V. ; CREMALDI, L. ; CUCCIARELLI, S. ; DOROKHOV, A. ; HÖRMANN, C. ; HORISBERGER, R. ; KIM, D. ; KONECKI, M. ; KOTLINSKI, D. ; PROKOFIEV, K. ; REGENFUS, C. ; ROHE, T. ; SANDERS, D.A. ; SON, S. ; SWARTZ, M. ; SPEER, T.: Design and performance of the silicon sensors for the CMS barrel pixel detector. In: *Nuclear Instruments and Methods in Physics Research Section A: Accelerators, Spectrometers, Detectors and Associated Equipment* 584 (2008), Nr. 1, 25 - 41. <http://www.sciencedirect.com/science/article/pii/S0168900207018670>. – ISSN 0168–9002 (cited on page 121.)
- [Akg15] AKGUN, Bora: Pilot System for the Phase 1 Pixel Upgrade. (2015), Jul, Nr. CMS-CR-2015-139. <https://cds.cern.ch/record/2049174> (cited on page 36.)
- [Ali] Alice – A Large Ion Collider Experiment. <http://aliceinfo.cern.ch> (cited on page 7.)
- [AMS] AMS-02 - The Alpha Magnetic Spectrometer Experiment at the International Space Station. <http://www.ams02.org/> (cited on page 38.)
- [Atl] ATLAS – The Atlas Experiment. <http://atlas.web.cern.ch> (cited on page 7.)
- [ATL12] ATLAS COLLABORATION: Observation of a new particle in the search for the Standard Model Higgs boson with the ATLAS detector at the LHC. In: *Physics Letters B* 716 (2012), Nr. 1, 1 - 29. <http://www.sciencedirect.com/science/article/pii/S037026931200857X>. – ISSN 0370–2693 (cited on pages i, 3.)
- [Bar11] BARNEY, David: CMS slice raw illustrator files. <https://cms-docdb.cern.ch/cgi-bin/PublicDocDB/ShowDocument?docid=5581>. Version: September 2011 (cited on page 14.)
- [Bar15] BARTZ, Ed: TBMo8c Documentation. (2015), April. <https://cms-docdb.cern.ch/cgi-bin/DocDB/ShowDocument?docid=12626> (cited on pages 41, 71.)
- [BB48] BARDEEN, J. ; BRATTAIN, W. H.: The Transistor, A Semi-Conductor Triode. In: *Phys. Rev.* 74 (1948), Jul, 230–231. <http://dx.doi.org/10.1103/PhysRev.74.230>. – DOI 10.1103/PhysRev.74.230 (cited on page 19.)

- [BBF⁺13] BEHNKE, Ties ; BRAU, James E. ; FOSTER, Brian ; FUSTER, Juan ; HARRISON, Mike ; PATERSON, James M. ; PESKIN, Michael ; STANITZKI, Marcel ; WALKER, Nicholas ; YAMAMOTO, Hitoshi: The International Linear Collider Technical Design Report - Volume 1: Executive Summary. (2013). <https://arxiv.org/abs/1306.6327> (cited on page 8.)
- [BBH⁺02] BOLLA, G. ; BORTOLETTO, D. ; HORISBERGER, R. ; KAUFMANN, R. ; ROHE, T. ; ROY, A.: Sensor development for the CMS pixel detector. In: *Nuclear Instruments and Methods in Physics Research Section A: Accelerators, Spectrometers, Detectors and Associated Equipment* 485 (2002), Nr. 1-2, 89 - 99. <http://www.sciencedirect.com/science/article/pii/S0168900202005375>. – ISSN 0168–9002. – Proceedings of the 5th International Conference on Large Scale Applications and Radiation Hardness of Semiconductor Detectors (cited on page 104.)
- [BC10] BARNEY, David ; CITTOLIN, Sergio: CMS 3-D image for inclusion in presentations. <https://cms-docdb.cern.ch/cgi-bin/PublicDocDB/ShowDocument?docid=2715>. Version: July 2010 (cited on page 11.)
- [BCL⁺04] BRÜNING, Oliver S. ; COLLIER, Paul ; LEBRUN, P ; MYERS, Stephen ; OSTOJIC, Ranko ; POOLE, John ; PROUDLOCK, Paul: *LHC Design Report*. Geneva : CERN, 2004 <https://cds.cern.ch/record/782076> (cited on page 9.)
- [BCL07] BIGAS, M. ; CABRUJA, E. ; LOZANO, M.: Bonding techniques for hybrid active pixel sensors (HAPS). In: *Nuclear Instruments and Methods in Physics Research Section A: Accelerators, Spectrometers, Detectors and Associated Equipment* 574 (2007), Nr. 2, 392 - 400. <http://www.sciencedirect.com/science/article/pii/S0168900207002720>. – ISSN 0168–9002 (cited on page 58.)
- [BDJ⁺07] BEHNKE, Ties ; DAMERELL, Chris ; JAROS, John ; MIYAMOTO, Akiya ; DABROWSKI, Wladyslaw ; GAJEWSKI, Jan ; IDZIK, Marek ; KISIELEWSKA, Danuta ; KULIS, Szymon ; SUSZYCKI, Leszek et al.: ILC Reference Design Report Volume 4 - Detectors. (2007). <https://arxiv.org/abs/1306.6329> (cited on page 17.)
- [Bea13] BEAUDETTE, Florian: The CMS Particle Flow Algorithm. In: *Proceedings, International Conference on Calorimetry for the High Energy Frontier (CHEF 2013): Paris, France, April 22-25, 2013* (2013), 295-304. <https://arxiv.org/abs/1401.8155> (cited on pages 13, 16.)
- [Bet30] BETHE, H.: Zur Theorie des Durchgangs schneller Korpuskularstrahlen durch Materie. In: *Annalen der Physik* 397 (1930), 325 - 400. <http://dx.doi.org/10.1002/andp.19303970303> (cited on page 25.)
- [BGG⁺06] BROENNIMANN, Ch. ; GLAUS, F. ; GOBRECHT, J. ; HEISING, S. ; HORISBERGER, M. ; HORISBERGER, R. ; KÄSTLI, H.C. ; LEHMANN, J. ; ROHE, T. ; STREULI, S.: Development of an Indium bump bond process for silicon pixel detectors at PSI. In: *Nuclear Instruments and Methods in Physics Research Section A: Accelerators, Spectrometers, Detectors and Associated Equipment* 565 (2006), Nr. 1, 303 - 308. <http://www.sciencedirect.com/science/article/pii/S0168900206007741>. – ISSN 0168–9002. – PIXEL 2005 - Proceedings of the International Workshop on Semiconductor Pixel Detectors for Particles and Imaging (cited on page 110.)
- [BGGH] BEHNKE, T. ; GARUTTI, E. ; GREGOR, I.-M. ; HAAS, T.: Test Beams at DESY. <http://www.eudet.org/e26/e28/e182/e283/eudet-memo-2007-11.pdf>. – EUDET-Memo-2007-11 (cited on page 112.)
- [BHJ⁺14] BRAGA, D. ; HALL, G. ; JONES, L. ; MURRAY, P. ; PESARESI, M. ; PRYDDERCH, M. ; RAYMOND, M.: Characterization of the CBC2 readout ASIC for the CMS strip-tracker

- high-luminosity upgrade. In: *JINST* 9 (2014), P. C03001. <http://dx.doi.org/10.1088/1748-0221/9/03/C03001>. – DOI 10.1088/1748-0221/9/03/C03001 (cited on page 17.)
- [BKM11] BLOBEL, Volker ; KLEINWORT, Claus ; MEIER, Frank: Fast alignment of a complex tracking detector using advanced track models. In: *Computer Physics Communications* 182 (2011), Nr. 9, 1760 - 1763. <http://www.sciencedirect.com/science/article/pii/S0010465511001093>. – ISSN 0010-4655. – Computer Physics Communications Special Edition for Conference on Computational Physics Trondheim, Norway, June 23-26, 2010 (cited on page 117.)
- [BM14] BARTEK, Rachel ; MASCIOVECCHIO, Mario: HDI Testing Procedure for the Digital HDI using LabJack. (2014), Aug. <https://cds.cern.ch/record/1952337> (cited on pages 72, 73.)
- [BMD⁺14] BAUMBAUGH, A ; MONTE, L D. ; DRAKE, G ; FREEMAN, J ; HARE, D ; ROJAS, H H. ; HUGHES, E ; LOS, S ; MENDEZ, D M. ; PROUDFOOT, J ; SHAW, T ; TULLY, C ; VIDAL, R ; WHITMORE, J ; ZIMMERMAN, T: QIE10: a new front-end custom integrated circuit for high-rate experiments. In: *Journal of Instrumentation* 9 (2014), Nr. 01, C01062. <http://stacks.iop.org/1748-0221/9/i=01/a=C01062> (cited on page 16.)
- [BR97] BRUN, Rene ; RADEMAKERS, Fons: ROOT - An object oriented data analysis framework. In: *Nuclear Instruments and Methods in Physics Research Section A: Accelerators, Spectrometers, Detectors and Associated Equipment* 389 (1997), Nr. 1, 81 - 86. <http://www.sciencedirect.com/science/article/pii/S016890029700048X>. – ISSN 0168-9002 (cited on page 66.)
- [Bra] BRAVIN, Enrico: *LHC daily operation meetings: LHC Status 27.06.2016*. https://indico.cern.ch/event/538347/contributions/2186401/attachments/1298537/1938844/LHC_27.06.2016_EB.pdf (cited on page 9.)
- [C⁺08] CHATRCHYAN, S. et al.: The CMS experiment at the CERN LHC. In: *JINST* 3 (2008), P. S08004. <http://dx.doi.org/10.1088/1748-0221/3/08/S08004>. – DOI 10.1088/1748-0221/3/08/S08004 (cited on pages 10, 12.)
- [CBC⁺16] CASELLE, M. ; BLANK, T. ; COLOMBO, F. ; DIERLAMM, A. ; HUSEMANN, U. ; KUDELLA, S. ; WEBER, M.: Low-cost bump-bonding processes for high energy physics pixel detectors. In: *Journal of Instrumentation* 11 (2016), Nr. 01, C01050. <http://stacks.iop.org/1748-0221/11/i=01/a=C01050> (cited on page 59.)
- [CC74] CHELIKOWSKY, J. R. ; COHEN, M. L.: Electronic structure of silicon. In: *Phys. Rev. B* 10 (1974), Dec, 5095-5107. <http://dx.doi.org/10.1103/PhysRevB.10.5095>. – DOI 10.1103/PhysRevB.10.5095 (cited on page 21.)
- [CGS13] CHISTIANSSEN, J ; GARCIA-SCIVERES, M: RD Collaboration Proposal: Development of pixel readout integrated circuits for extreme rate and radiation. (2013), Jun, Nr. CERN-LHCC-2013-008. LHCC-P-006. <https://cds.cern.ch/record/1553467> (cited on page 43.)
- [Chi13] CHILINGAROV, A: Generation current temperature scaling. (2013), Jan, Nr. PH-EP-Tech-Note-2013-001. <http://cds.cern.ch/record/1511886> (cited on page 87.)
- [CKM⁺15] CONTARDO, D ; KLUTE, M ; MANS, J ; SILVESTRIS, L ; BUTLER, J: Technical Proposal for the Phase-II Upgrade of the CMS Detector. (2015), Jun, Nr. CERN-LHCC-2015-010. LHCC-P-008. CMS-TDR-15-02. <https://cds.cern.ch/record/2020886> (cited on pages 17, 18 and 106.)
- [CMSa] CMS – *The Compact Muon Solenoid Experiment*. <http://cms.web.cern.ch> (cited on page 7.)

- [CMSb] CMS *Luminosity - Public Results*. <https://twiki.cern.ch/twiki/bin/view/CMSPublic/LumiPublicResults> (cited on page 9.)
- [CMS98] CMS COLLABORATION: *The Tracker Project*. 1998 <https://cds.cern.ch/record/368412>. – CMS TDR 5 (cited on page 10.)
- [CMS12] CMS COLLABORATION: Observation of a new boson at a mass of 125 GeV with the CMS experiment at the LHC. In: *Physics Letters B* 716 (2012), Nr. 1, 30 - 61. <http://dx.doi.org/10.1016/j.physletb.2012.08.021>. – DOI 10.1016/j.physletb.2012.08.021. – ISSN 0370-2693 (cited on pages i, 3.)
- [Col16] COLOMBO, Fabio: *Packaging and assembly technologies for the pixel detector upgrade and measurement of $\tau\tau$ final states with the CMS experiment at the LHC*, Karlsruhe Institut für Technologie (KIT), PhD Thesis, 2016. <https://ekp-invenio.physik.uni-karlsruhe.de/record/48804> (cited on pages 61, 64, 69 and 70.)
- [Com23] COMPTON, Arthur H.: A Quantum Theory of the Scattering of X-rays by Light Elements. In: *Phys. Rev.* 21 (1923), May, 483–502. <http://dx.doi.org/10.1103/PhysRev.21.483>. – DOI 10.1103/PhysRev.21.483 (cited on page 27.)
- [CRSo2] CITTOLIN, Sergio ; RÁCZ, Attila ; SPHICAS, Paris: *CMS The TriDAS Project: Technical Design Report, Volume 2: Data Acquisition and High-Level Trigger. CMS trigger and data-acquisition project*. Geneva : CERN, 2002 (Technical Design Report CMS). <https://cds.cern.ch/record/578006> (cited on page 14.)
- [Cus] CUSSANS, David: Description of the JRA1 Trigger Logic Unit (TLU). <https://www.eudet.org/e26/e28/e42441/e57298/EUDET-MEMO-2009-04.pdf>. – EUDET-Memo-2009-04 (cited on page 114.)
- [D⁺00] DASU, S. et al.: *CMS The TriDAS project: Technical Design Report, Volume 1: The Trigger Systems*. 2000 <https://cds.cern.ch/record/706847> (cited on page 14.)
- [DAA⁺12] DOMINGUEZ, A ; ABBANEO, D ; ARNDT, K ; BACCHETTA, N ; BALL, A ; BARTZ, E ; BERTEL, W ; BILEI, G M. ; BOLLA, G ; CHEUNG, H W K. ; CHERTOK, M ; COSTA, S ; DEMARIA, N ; VAZQUEZ, Daniel D. ; ECKLUND, K ; ERDMANN, W ; GILL, K ; HALL, G ; HARDER, K ; HARTMANN, F ; HORISBERGER, R ; JOHNS, W ; KAESTLI, H C. ; KLEIN, K ; KOTLINSKI, D ; KWAN, S ; PESARESI, M ; POSTEMA, H ; ROHE, T ; SCHÄFER, C ; STARODUMOV, A ; STREULI, S ; TRICOMI, A ; TROPEA, P ; TROSKA, J ; VASEY, F ; ZEUNER, W: *CMS Technical Design Report for the Pixel Detector Upgrade*. (2012), Sep, Nr. CERN-LHCC-2012-016. CMS-TDR-11. <http://cds.cern.ch/record/1481838> (cited on pages 9, 16, 35, 36, 37, 39, 40, 41, 44, 45 and 47.)
- [DES16] *Test Beams at DESY*. Version: October 2016. <http://particle-physics.desy.de/e252106/> (cited on page 113.)
- [Die03] DIERLAMM, Alexander: *Studies on the Radiation Hardness of Silicon Sensors*, Universität Karlsruhe (TH), PhD Thesis, 2003. <https://ekp-invenio.physik.uni-karlsruhe.de/record/45039> (cited on page 106.)
- [Die16] DIERLAMM, Alexander: *Proton Irradiation: The Cyclotron and the Irradiation Setup*. Version: February 2016. <http://www.ekp.kit.edu/english/264.php> (cited on pages 106, 107.)
- [DKI⁺03] DESLATTES, Richard D. ; KESSLER, Ernest G. ; INDELICATO, P. ; BILLY, L. de ; LINDROTH, E. ; ANTON, J.: X-ray transition energies: new approach to a comprehensive evaluation. In: *Rev. Mod. Phys.* 75 (2003), Jan, 35–99. <http://dx.doi.org/10.1103/RevModPhys.75.35>. – DOI 10.1103/RevModPhys.75.35 (cited on page 89.)

- [Dom07] DOMINGUEZ, Aaron: The CMS pixel detector. In: *Nuclear Instruments and Methods in Physics Research Section A: Accelerators, Spectrometers, Detectors and Associated Equipment* 581 (2007), Nr. 1-2, 343 - 346. <http://www.sciencedirect.com/science/article/pii/S016890020701635X>. – ISSN 0168–9002. – VCI 2007 - Proceedings of the 11th International Vienna Conference on Instrumentation (cited on page 12.)
- [Ebe13] EBER, Robert: *Untersuchung neuartiger Sensorkonzepte und Entwicklung eines effektiven Modells der Strahlenschädigung für die Simulation hochbestrahlter Silizium-Teilchendetektoren*, Karlsruher Institut für Technologie (KIT), PhD Thesis, 2013. <https://ekp-invenio.physik.uni-karlsruhe.de/record/48328> (cited on pages 28, 46.)
- [EBH⁺10] ERDMANN, W. ; BERTEL, W. ; HORISBERGER, R. ; KÄSTLI, H.C. ; KOTLINSKI, D. ; KÖNIG, S. ; LANGENEGGER, U. ; MEIER, B. ; RADICCI, V. ; ROHE, T. ; STARODUMOV, A. ; STREULI, S.: Upgrade plans for the CMS pixel barrel detector. In: *Nuclear Instruments and Methods in Physics Research Section A: Accelerators, Spectrometers, Detectors and Associated Equipment* 617 (2010), Nr. 1-3, 534 - 537. <http://www.sciencedirect.com/science/article/pii/S0168900209019342>. – ISSN 0168–9002. – 11th Pisa Meeting on Advanced Detectors Proceedings of the 11th Pisa Meeting on Advanced Detectors (cited on page 35.)
- [Eid16] EIDGENÖSSISCHE TECHNISCHE HOCHSCHULE ZÜRICH (ETH): *MoReWeb - a software framework to analyze Module / ROC test data acquired using psi46expert or pXar*. Version: October 2016. <https://github.com/psi46/MoReWeb> (cited on page 54.)
- [Erd10] ERDMANN, W.: The CMS Pixel Detector. In: *International Journal of Modern Physics A* 25 (2010), Nr. 07, 1315-1337. <http://dx.doi.org/10.1142/S0217751X10049098>. – DOI 10.1142/S0217751X10049098 (cited on page 45.)
- [Erd15] ERDMANN, Wolfram: *BPIX Module Production Readiness Review: Introduction & Overview*. Version: February 2015. <https://indico.cern.ch/event/373338/contributions/883073/attachments/743488/1019882/2015-02-25-BPix-Module-Production.pdf>. – (not public) (cited on page 42.)
- [Erf09] ERFLE, Joachim: *Entwicklungen für neue Siliziumstreifensensoren und deren Qualitätskontrolle*, Universität Karlsruhe (TH), Diploma Thesis, 2009. <http://www-ekp.physik.uni-karlsruhe.de/pub/web/thesis/iekp-ka2009-27.pdf> (cited on page 46.)
- [EUT] *EUTelescope - A Generic Pixel Telescope Data Analysis Framework*. <http://eutelescope.web.cern.ch> (cited on page 116.)
- [FFF⁺13] FELD, Lutz ; FLECK, Martin ; FRIEDRICHS, Marcel ; HENSCH, Richard ; KARPINSKI, Waclaw ; KLEIN, Katja ; RITTICH, David ; SAMMET, Jan ; WLOCHAL, Michael: DC-DC powering for the CMS pixel upgrade. In: *Nuclear Instruments and Methods in Physics Research Section A: Accelerators, Spectrometers, Detectors and Associated Equipment* 732 (2013), 493 - 496. <http://www.sciencedirect.com/science/article/pii/S0168900213008863>. – ISSN 0168–9002. – Vienna Conference on Instrumentation 2013 (cited on page 39.)
- [Fin16] FINETECH GMBH & Co. KG: *Finetech FINEPLACER® femto Automated sub-micron Die Bonder*. Version: September 2016. <http://www.finetech.de/micro-assembly/products/diebonders1.html> (cited on page 62.)
- [Fre16] FREUND, Benedikt: *Private communication*. October 2016 (cited on page 64.)
- [GE] GAEDE, F. ; ENGELS, J.: Marlin et al. - A Software Framework for ILC detector R&D. <https://www.eudet.org/e26/e27/e584/eudet-report-2007-11.pdf>. – EUDET-Report-2007-11 (cited on page 115.)

- [Gia04] GIANOTTI, Fabiola: Physics at the LHC. In: *Physics Reports* 403-404 (2004), 379 - 399. <http://www.sciencedirect.com/science/article/pii/S0370157304003382>. – ISSN 0370–1573. – CERN - the second 25 years (cited on page 7.)
- [Hal11] HALL, G.: Conceptual study of a trigger module for the CMS Tracker at SLHC. In: *Nuclear Instruments and Methods in Physics Research Section A: Accelerators, Spectrometers, Detectors and Associated Equipment* 636 (2011), Nr. 1, Supplement, S201 - S207. <http://www.sciencedirect.com/science/article/pii/S0168900210009642>. – ISSN 0168–9002. – 7th International Hiroshima Symposium on the Development and Application of Semiconductor Tracking Detectors (cited on page 17.)
- [Har09] HARTMANN, Frank: *Evolution of Silicon Sensor Technology in Particle Physics*. Springer, 2009. – ISBN 978-3-540-25094-4 (cited on pages 19, 22 and 103.)
- [Hei12] HEITZ, Stefan: *Bump-Bonding-Technologie für das Upgrade des CMS-Pixeldetektors*, Karlsruher Institut für Technologie (KIT), Diploma Thesis, 2012. <https://ekp-invenio.physik.uni-karlsruhe.de/record/48178> (cited on page 58.)
- [HG^{BB+}10] HU-GUO, C. ; BAUDOT, J. ; BERTOLONE, G. ; BESSON, A. ; BROGNA, A.S. ; COLLEDANI, C. ; CLAUS, G. ; MASI, R. D. ; DEGERLI, Y. ; DOROKHOV, A. ; DOZIERE, G. ; DULINSKI, W. ; FANG, X. ; GELIN, M. ; GOFFE, M. ; GUILLOUX, F. ; HIMMI, A. ; JAASKELAINEN, K. ; KOZIEL, M. ; MOREL, F. ; ORSINI, F. ; SPECHT, M. ; SUN, Q. ; TORHEIM, O. ; VALIN, I. ; WINTER, M.: First reticule size MAPS with digital output and integrated zero suppression for the EUDET-JRA1 beam telescope. In: *Nuclear Instruments and Methods in Physics Research Section A: Accelerators, Spectrometers, Detectors and Associated Equipment* 623 (2010), Nr. 1, 480 - 482. <http://www.sciencedirect.com/science/article/pii/S0168900210006078>. – ISSN 0168–9002. – 1st International Conference on Technology and Instrumentation in Particle Physics (cited on page 113.)
- [HiL14] HiLUMI LHC COLLABORATION: HL-LHC Preliminary Design Report: Deliverable: D1.5. (2014), Nov. <https://cds.cern.ch/record/1972604> (cited on page 15.)
- [Hit15] HITI, Bojan: *Probe Station for Functionality Tests of Bare Modules for the Phase I Upgrade of the CMS Pixel Detector*, Karlsruher Institut für Technologie (KIT), Diploma Thesis, 2015. <https://ekp-invenio.physik.uni-karlsruhe.de/record/48731> (cited on pages 64, 65, 66, 67, 68 and 91.)
- [HLBS03] HUFFMAN, A. ; LABENNETT, R. ; BONAFEDE, S. ; STATLER, C.: Fine-pitch wafer bumping and assembly for high density detector systems. In: *Nuclear Science Symposium Conference Record* 5 (2003), Oct, 3522-3526 Vol.5. <http://dx.doi.org/10.1109/NSSMIC.2003.1352670>. – DOI 10.1109/NSSMIC.2003.1352670. – ISSN 1082–3654 (cited on page 59.)
- [Hof11] HOFFMANN, Karl-Heinz: Campaign to identify the future CMS tracker baseline. In: *Nuclear Instruments and Methods in Physics Research Section A: Accelerators, Spectrometers, Detectors and Associated Equipment* 658 (2011), Nr. 1, 30 - 35. <http://dx.doi.org/10.1016/j.nima.2011.05.028>. – DOI 10.1016/j.nima.2011.05.028. – ISSN 0168–9002. – RESMDD 2010 (cited on page 101.)
- [Hof13] HOFFMANN, Karl-Heinz: *Entwicklung von neuen Sensor Konzepten und Untersuchungen an strahlenharten Siliziumstreifensensoren für CMS am Large Hadron Collider in der Hochluminositätsphase*, Karlsruher Institut für Technologie (KIT), PhD Thesis, 2013. <https://ekp-invenio.physik.uni-karlsruhe.de/record/48272> (cited on pages 46, 102.)

- [Hor16] HORISBERGER, Roland: *Phase 1 Pixel Plenary: Status of PROC600 Chip*. Version: July 2016. https://indico.cern.ch/event/547429/contributions/2246208/attachments/1312262/1964110/PROC600v2_status_July2016_2.pdf. – (not public) (cited on page 41.)
- [Hos12] Hoss, Jan: *X-Ray Calibration of Pixel Detector Modules for the Phase I Upgrade of the CMS Experiment*, Karlsruhe Institut für Technologie (KIT), Diploma Thesis, September 2012. <https://ekp-invenio.physik.uni-karlsruhe.de/record/48180> (cited on page 24.)
- [ILO9] IBACH, H. ; LÜTH, H.: *Festkörperphysik*. Springer, 2009. – ISBN 978-3-540-85794-5 (cited on page 20.)
- [Int14] INTERGOVERNMENTAL PANEL ON CLIMATE CHANGE: *Climate Change 2013 - The Physical Science Basis: Working Group 1 - Contribution to the Fifth Assessment Report of the Intergovernmental Panel on Climate Change*. Cambridge University Press, 2014. – ISBN 110766182X (cited on page 38.)
- [JSB⁺16] JANSEN, Hendrik ; SPANNAGEL, Simon ; BEHR, Jörg ; BULGHERONI, Antonio ; CLAUS, Gilles ; CORRIN, Emlyn ; CUSSANS, David ; DREYLING-ESCHWEILER, Jan ; ECKSTEIN, Doris ; EICHHORN, Thomas ; GOFFE, Mathieu ; GREGOR, Ingrid M. ; HAAS, Daniel ; MUHL, Carsten ; PERREY, Hanno ; PESCHKE, Richard ; ROLOFF, Philipp ; RUBINSKIY, Igor ; WINTER, Marc: Performance of the EUDET-type beam telescopes. In: *EPJ Techniques and Instrumentation* 3 (2016), Nr. 1, 7. <http://dx.doi.org/10.1140/epjti/s40485-016-0033-2>. – DOI 10.1140/epjti/s40485-016-0033-2. – ISSN 2195-7045 (cited on page 113.)
- [Jun11] JUNKES, Alexandra: *Influence of radiation induced defect clusters on silicon particle detectors*, Hamburg U., PhD Thesis, 2011. <http://www-library.desy.de/cgi-bin/showprep.pl?thesis11-031> (cited on page 29.)
- [Kas06] KASAP, Safa O. (Publisher): *Springer handbook of electronic and photonic materials: with 168 tables*. New York : Springer, 2006. – ISBN 978-0-387-26059-4 (cited on page 21.)
- [Kra04] KRAMMER, Manfred: The silicon sensors for the Inner Tracker of the Compact Muon Solenoid experiment. In: *Nucl. Instrum. Methods Phys. Res., A* 531 (2004), 238-245. <http://cds.cern.ch/record/816579> (cited on page 28.)
- [Kud14] KUDELLA, Simon: *Gold-stud bump bonding interconnection technology for the CMS experiment*, Karlsruhe Institut für Technologie (KIT), Diploma Thesis, 2014. <https://ekp-invenio.physik.uni-karlsruhe.de/record/48571> (cited on pages 58, 60 and 106.)
- [Lan44] LANDAU, L.: On the energy loss of fast particles by ionization. In: *J. Phys.(USSR)* 8 (1944), P. 201-205 (cited on page 26.)
- [Lef09] LEFEVRE, C: *LHC: the guide (English version). Guide du LHC (version anglaise)*. <https://cds.cern.ch/record/1165534>. Version: Feb 2009 (cited on page 8.)
- [LHC] *LHCb – The Large Hadron Collider beauty experiment*. <http://lhcb.web.cern.ch> (cited on pages 7, 38.)
- [Lino3] LINDSTRÖM, G.: Radiation damage in silicon detectors. In: *Nuclear Instruments and Methods in Physics Research Section A: Accelerators, Spectrometers, Detectors and Associated Equipment* 512 (2003), Nr. 1-2, 30 - 43. [http://dx.doi.org/10.1016/S0168-9002\(03\)01874-6](http://dx.doi.org/10.1016/S0168-9002(03)01874-6). – DOI 10.1016/S0168-9002(03)01874-6. – ISSN 0168-9002. – Proceedings of the 9th European Symposium on Semiconductor Detectors: New Developments on Radiation Detectors (cited on page 30.)

- [Lip16] LIPINSKI, Martin: *Private communication*. October 2016 (cited on page 97.)
- [Luto7] LUTZ, G.: *Semiconductor Radiation Detectors: Device Physics*. Springer, 2007. – ISBN 978-3-540-71678-5 (cited on pages 19, 29.)
- [MAB⁺12] MICHELIS, S ; ALLONGUE, B ; BLANCHOT, G ; FACCIO, F ; FUENTES, C ; ORLANDI, S ; SAGGINI, S ; CENGARLE, S ; ONGARO, F: DC-DC converters in 0.35 μ m CMOS technology. In: *Journal of Instrumentation* 7 (2012), Nr. 01, C01072. <http://stacks.iop.org/1748-0221/7/i=01/a=C01072> (cited on page 39.)
- [MAD⁺12] MANS, J ; ANDERSON, J ; DAHMES, B ; BARBARO, P de ; FREEMAN, J ; GRASSI, T ; HAZEN, E ; MANS, J ; RUCHTI, R ; SCHIMDT, I ; SHAW, T ; TULLY, C ; WHITMORE, J ; YETKIN, T: CMS Technical Design Report for the Phase 1 Upgrade of the Hadron Calorimeter. (2012), Sep, Nr. CERN-LHCC-2012-015. CMS-TDR-10. <https://cds.cern.ch/record/1481837> (cited on page 15.)
- [Mar13] MARCASTEL, Fabienne: CERN's Accelerator Complex. La chaîne des accélérateurs du CERN. (2013), Oct. <https://cds.cern.ch/record/1621583>. – General Photo (cited on page 8.)
- [Mei14] MEIER, Frank: Physics Performance with the CMS Pixel Detector. (2014). <https://arxiv.org/abs/1412.5628> (cited on page 35.)
- [Mes15] MESCHÉDE, Dieter: *Gerthsen Physik*. Springer, 2015. – ISBN 978-3-662-45976-8
- [Mol99] MOLL, Michael: *Radiation Damage in Silicon Particle Detectors*, Universität Hamburg, PhD Thesis, 1999. <http://www-library.desy.de/cgi-bin/showprep.pl?desy-thesis99-040> (cited on pages 29, 31.)
- [Nat16a] NATIONAL INSTRUMENTS CORP.: *LabVIEW (Laboratory Virtual Instrument Engineering Workbench) System Design Software*. Version: September 2016. <http://www.ni.com/labview/> (cited on page 46.)
- [Nat16b] NATIONAL INSTRUMENTS CORP.: *LabWindows/CVI (C for Virtual Instrumentation) Development Environment*. Version: October 2016. <http://www.ni.com/lwcvl/> (cited on page 65.)
- [Nat16c] NATIONAL INSTRUMENTS CORP.: *Vision Development Module*. Version: October 2016. <http://www.ni.com/vision/software/> (cited on pages 61, 65.)
- [Nür13] NÜRNBERG, Andreas: *Studien an bestrahlten Siliziumsensoren für den CMS Spurdetektor am HL-LHC*, Karlsruher Institut für Technologie (KIT), PhD Thesis, 2013. <https://ekp-invenio.physik.uni-karlsruhe.de/record/48576> (cited on page 121.)
- [O⁺14] OLIVE, K. A. et al.: Review of Particle Physics. In: *Chin. Phys.* C38 (2014), P. 090001. <http://dx.doi.org/10.1088/1674-1137/38/9/090001>. – DOI 10.1088/1674-1137/38/9/090001 (cited on pages 9, 19, 21, 25, 26 and 27.)
- [PCH⁺92] PITZL, D. ; CARTIGLIA, N. ; HUBBARD, B. ; HUTCHINSON, D. ; LESLIE, J. ; O'SHAUGHNESSY, K. ; ROWE, W. ; SADROZINSKI, H.F.-W. ; SEIDEN, A. ; SPENCER, E. ; ZIOCK, H.J. ; FERGUSON, P. ; HOLZSCHEITER, K. ; SOMMER, W.F.: Type inversion in silicon detectors. In: *Nuclear Instruments and Methods in Physics Research Section A: Accelerators, Spectrometers, Detectors and Associated Equipment* 311 (1992), Nr. 1, 98 - 104. <http://www.sciencedirect.com/science/article/pii/016890029290854W>. – ISSN 0168-9002 (cited on page 44.)
- [Pri16] PRINTZ, Martin: *Analysis of n-in-p type silicon detectors for high radiation environment with fast analogue and binary readout systems*, Karlsruher Institut für Technologie (KIT), PhD Thesis, 2016. <https://ekp-invenio.physik.uni-karlsruhe.de/record/48797> (cited on pages 103, 104.)

- [R⁺10] ROHE, T. et al.: Signal height in silicon pixel detectors irradiated with pions and protons. In: *Nucl. Instrum. Meth.* A612 (2010), P. 493–496. <http://dx.doi.org/10.1016/j.nima.2009.08.012>. – DOI 10.1016/j.nima.2009.08.012 (cited on page 106.)
- [Ram39] RAMO, S.: Currents Induced by Electron Motion. In: *Proceedings of the IRE* 27 (1939), Sept, Nr. 9, P. 584–585. <http://dx.doi.org/10.1109/JRPROC.1939.228757>. – DOI 10.1109/JRPROC.1939.228757. – ISSN 0096–8390 (cited on page 28.)
- [RBC⁺04] ROHE, T ; BORTOLETTO, D ; CHIOCHIA, V ; CREMALDI, L M. ; CUCCIARELLI, S ; DOROKHOV, A ; HÖRMANN, C ; KIM, D ; KONECKI, M ; KOTLINSKI, D ; PROKOFIEV, K ; REGENFUS, C ; SANDERS, D A. ; SON, S ; SPEER, T ; SWARTZ, M: Fluence Dependence of Charge Collection of irradiated Pixel Sensors. In: *Nucl. Instrum. Methods Phys. Res., A* 552 (2004), Nov, Nr. physics/0411214. 1-2, 232-238. 11 p. <http://cds.cern.ch/record/807069> (cited on page 43.)
- [Rie14] RIESE, Felix: *Testsoftware und Datenbanken für das CMS-Pixeldetektor-Upgrade*, Karlsruher Institut für Technologie (KIT), Diploma Thesis, 2014. <https://ekp-invenio.physik.uni-karlsruhe.de/record/48583> (cited on pages 47, 49 and 51.)
- [Roh13] ROHE, Tilman: *Procurement Readiness Review of the BPIX silicon sensors: Sensor technology, radiation hardness and quality assurance*. Version: June 2013. <https://indico.cern.ch/event/259641/contributions/1590897/attachments/457793/634443/2013-06-CMS-PPR.ppt>. – (not public) (cited on page 44.)
- [Sab14] SABES, David: L1 track triggering with associative memory for the CMS HL-LHC tracker. In: *J. Instrum.* 9 (2014), Nr. 11, C11014. <https://cds.cern.ch/record/2025864> (cited on page 17.)
- [SBD⁺87] SUMMERS, G. P. ; BURKE, E. A. ; DALE, C. J. ; WOLICKI, E. A. ; MARSHALL, P. W. ; GEHLHAUSEN, M. A.: Correlation of Particle-Induced Displacement Damage in Silicon. In: *IEEE Transactions on Nuclear Science* 34 (1987), Dec, Nr. 6, P. 1133–1139. <http://dx.doi.org/10.1109/TNS.1987.4337442>. – DOI 10.1109/TNS.1987.4337442. – ISSN 0018–9499 (cited on page 29.)
- [Scho3] SCHAEEL, Stefan: The CMS silicon strip detector - mechanical structure and alignment system. In: *Nuclear Instruments and Methods in Physics Research Section A: Accelerators, Spectrometers, Detectors and Associated Equipment* 511 (2003), Nr. 1-2, 52 - 57. <http://www.sciencedirect.com/science/article/pii/S0168900203017509>. – ISSN 0168–9002. – Proceedings of the 11th International Workshop on Vertex Detectors (cited on pages 12, 13.)
- [Sch15] SCHELL, Daniel: *Evaluation of Sensor Materials and Technologies for the Innermost Layer of the CMS Pixel Detector at the HL-LHC*, Karlsruher Institut für Technologie (KIT), Diploma Thesis, 2015. <https://ekp-invenio.physik.uni-karlsruhe.de/record/48732> (cited on pages 106, 127.)
- [Sch16] SCHWANDT, J.: *Updates on layouts for the CMS submission of planar pixel sensors at HPK*. Version: March 2016. https://indico.cern.ch/event/514353/contributions/2027278/attachments/1249553/1841768/js_PPII_29032016.pdf. – (not public) (cited on page 43.)
- [SFK⁺12] SCHWANDT, J ; FRETWURST, E ; KLANNER, R ; PINTILIE, I ; ZHANG, J: Optimization of the radiation hardness of silicon pixel sensors for high x-ray doses using TCAD simulations. In: *Journal of Instrumentation* 7 (2012), Nr. 01, C01006. <http://stacks.iop.org/1748-0221/7/i=01/a=C01006> (cited on page 121.)
- [Sho38] SHOCKLEY, W.: Currents to Conductors Induced by a Moving Point Charge. In: *Journal of Applied Physics* 9 (1938), Nr. 10, 635-636. <http://scitation.aip.org/content/aip/journal/jap/9/10/10.1063/1.1710367> (cited on page 28.)

- [SMP15] SPANNAGEL, Simon ; MEIER, Beat ; PERREY, Hanno C.: The pxarCore Library - Technical Documentation, Reference Manual, and Sample Applications. (2015), October, Nr. CMS-NOTE-2016-001. <http://cds.cern.ch/record/2137512> (cited on pages 65, 66.)
- [Spa15] SPANNAGEL, Simon: *CMS Pixel Decoder*. Version: December 2015. <https://github.com/simonspa/CMSPixelDecoder> (cited on page 117.)
- [Spa16] SPANNAGEL, Simon: *Test Beam Measurements for the Upgrade of the CMS Pixel Detector and Measurement of the Top Quark Mass from Differential Cross Sections*. Hamburg, U. Hamburg, Dept. Phys., PhD Thesis, 2016. <http://bib-pubdb1.desy.de/search?cc=Publication+Database&of=hd&p=reportnumber:DESY-THESIS-2016-010> (cited on pages 43, 84, 85, 114 and 128.)
- [Spi05] SPIELER, Helmuth: *Semiconductor detector systems*. Oxford : Oxford Univ. Press, 2005 (Semiconductor Science and Technology). – ISBN 978-0-198-52784-8 (cited on page 23.)
- [Str11] STREULI, Silvan: Barrel Pixel Module Assembly Manual (for Phase 0 Modules). (2011), June. <https://cms-docdb.cern.ch/cgi-bin/DocDB/ShowDocument?docid=4899> (cited on page 76.)
- [Sze85] SZE, Simon M.: *Semiconductor Devices : Physics and Technology*. John Wiley & Sons, 1985. – ISBN 978-0-471-83704-6 (cited on page 23.)
- [TA13] TAPPER, A ; ACOSTA, Darin: CMS Technical Design Report for the Level-1 Trigger Upgrade. (2013), Jun, Nr. CERN-LHCC-2013-011. CMS-TDR-12. <https://cds.cern.ch/record/1556311> (cited on page 15.)
- [Tas16] TASKIRDI, Yavuz: *Studien zur Qualität der Modulproduktion am KIT für das Phase I Upgrade des CMS Pixel Detektors*, Karlsruher Institut für Technologie (KIT), Diploma Thesis, October 2016. <https://ekp-invenio.physik.uni-karlsruhe.de/record/48846> (cited on pages 88, 94 and 96.)
- [Tay11] TAYLOR, Lucas: *Using Russian navy shells*. Version: November 2011. <http://cms.web.cern.ch/news/using-russian-navy-shells> (cited on page 11.)
- [VC09] VERLAAT, Bart ; COLIJN, Auke-Pieter: CO₂ cooling developments for HEP detectors. In: *PoS VERTEX2009* (2009), 031. <http://pos.sissa.it/cgi-bin/reader/conf.cgi?confid=95> (cited on page 38.)
- [VG89] VAN GINNEKEN, A.: Nonionizing Energy Deposition in Silicon for Radiation Damage Studies. (1989). http://lss.fnal.gov/cgi-bin/find_paper.pl?fn-0522. – FERMILAB-FN-0522 (cited on page 29.)
- [WRFR06] WERMES, N. ; ROSSI, L. ; FISCHER, P. ; ROHE, T.: *Pixel Detectors, From Fundamentals to Applications*. Springer-Verlag, 2006. – ISBN 978-3-540-28332-4 (cited on page 19.)

LIST OF FIGURES

Figure 2.1	CERN accelerator complex	8
Figure 2.2	CMS Peak Luminosity per day in 2016	9
Figure 2.3	Three-dimensional view of the CMS detector	11
Figure 2.4	CMS all-silicon tracker and its subcomponents	12
Figure 2.5	Transverse cross section of the CMS detector	14
Figure 2.6	2S module for the Tracker Phase II Upgrade and its working principle	17
Figure 3.1	Energy band configuration and Fermi energy of conductors, semiconductors and insulators	20
Figure 3.2	Band structure of silicon in the reduced zone scheme	21
Figure 3.3	Doping of silicon with phosphorus or boron	23
Figure 3.4	pn-junction and formation of the depletion zone	24
Figure 3.5	Stopping power for positive muons in copper	25
Figure 3.6	Energy loss of a 500 MeV pion in silicon	26
Figure 3.7	Energy dependence of the photon interaction cross section in carbon	27
Figure 3.8	Basic design of a position-sensitive silicon particle detector	28
Figure 3.9	Displacement damage functions $D(E)$ in silicon	30
Figure 4.1	Comparison of the layouts of the current and the new Phase I pixel detector	36
Figure 4.2	Prototype of the new BPIX Layer 1 support structure	37
Figure 4.3	Material budget of the new CMS pixel detector as a function of pseudorapidity η	39
Figure 4.4	Phase I barrel pixel module for the detector layers 2 to 4	42
Figure 5.1	CMS production wafer with three pixel sensors and additional structures	44
Figure 5.2	Arrangement of four pixels from the CMS pixel sensor	45
Figure 5.3	IV measurement setup for CMS pixel sensors	47
Figure 5.4	IV characteristics of the three CMS pixel sensors from wafer 331154-10	49
Figure 5.5	IV characteristics of all CMS pixel sensors measured at IEKP	50
Figure 5.6	Histogram of all I_1 values at $U_1 = 100\text{ V}$	51
Figure 5.7	Histogram of all I_2 values at $U_2 = 150\text{ V}$	52
Figure 5.8	Histogram of all slope values I_2/I_1	53
Figure 5.9	Classification of pixel sensors by wafer position	54
Figure 6.1	Pixel module production workflow for the KIT-RWTH group	58
Figure 6.2	RTI SnPb bumping process	59
Figure 6.3	Overview of the Finetech FINEPLACER® femto flip-chip bonder	62
Figure 6.4	Force and temperature profiles used for the KIT flip-chip bonding process	63
Figure 6.5	Overview of the bare module probe station at IPE	65
Figure 6.6	Internal calibration mechanism of the ROC	67
Figure 6.7	Results from the electrical and bump-bonding tests of a ROC	68
Figure 6.8	Production rate and classification of the KIT bare modules	69
Figure 6.9	Distribution of bare module defects detected at KIT	70
Figure 6.10	Overview of the TBM gluing chuck designed by KIT	72
Figure 6.11	Overview of the HDI test station with needle card	73
Figure 6.12	Overview of the KIT module gluing line in the clean room	75
Figure 6.13	Distribution of the thicknesses of the base strip pairs used for KIT pixel modules	76
Figure 6.14	Indications and cause of problems during base strip gluing	77
Figure 6.15	Rubber stamp used for base strip gluing and base strip gluing test with glass dummy	78
Figure 6.16	HDI gluing test performed with dummy material	80

Figure 6.17	Wire-bonded KIT Phase I pixel module	81
Figure 6.18	Module cap preparation and gluing	82
Figure 7.1	Result from the SCurve test of a single pixel	84
Figure 7.2	KIT test setup used for electrical tests of complete modules	86
Figure 7.3	Distribution of the measured leakage currents of the KIT modules	88
Figure 7.4	KIT X-ray setup used for irradiation of complete modules	89
Figure 7.5	Hitmap of KIT module M4682 after X-ray irradiation	90
Figure 7.6	Distribution of defects detected by X-ray irradiation of KIT modules	92
Figure 7.7	Comparison of the KIT bump-bonding test with X-ray hitmaps	93
Figure 7.8	Distributions of measured pulse height values from the K_{α} line of silver	94
Figure 7.9	Distribution of measured pulse height values for the sixteen ROC positions of the KIT modules	96
Figure 7.10	Example of an energy calibration with X-rays and distribution of slope values from all modules calibrated in Aachen	97
Figure 8.1	Layout of the HPK campaign wafer	102
Figure 8.2	Layouts of the BPixB and the FPixF pixel sensors	103
Figure 8.3	Layouts of the pixel sensors from the HPK campaign wafer	105
Figure 8.4	IEKP irradiation setup at the Karlsruher Kompaktzyklotron (KAZ)	107
Figure 9.1	Single chip assembly on its carrier PCB	111
Figure 9.2	Schematic of the test beam generation at DESY	113
Figure 9.3	DATURA telescope setup at DESY	115
Figure 9.4	EUTelescope data analysis workflow	116
Figure 9.5	Profile cuts used for test beam data analysis	118
Figure 9.6	Illustration of the test board clock problem	120
Figure 9.7	Hit detection efficiencies of unirradiated and irradiated HPK pixel sensor samples	122
Figure 9.8	Comparison of cluster sizes of unirradiated and irradiated FPixF layouts	124
Figure 9.9	Spatial resolution of the BPixB sample (chip 62)	125

LIST OF TABLES

Table 4.1	Comparison of the simulated total material weight for both the barrel pixel and the forward pixel detector	39
Table 4.2	Comparison of important numbers for the current and the new Phase I pixel detector	40
Table 5.1	Yield of CMS pixel sensor IV measurements	55
Table 7.1	Results from module tests at KIT	91
Table 7.2	Final results of the KIT-RWTH module production	97
Table 8.1	Differences of the HPK pixel sensor layout variations	104
Table 9.1	HPK sensor samples available for investigation	112
Table 9.2	Naming and positions of the profile cuts	119
Table 9.3	Hit detection efficiencies of the HPK pixel sensor layouts	123
Table 9.4	Measured cluster sizes of the HPK pixel sensor layouts	124
Table 9.5	Measured average resolutions of the HPK pixel sensor layouts	126

ACKNOWLEDGEMENTS – DANKSAGUNG

The work presented in this thesis would not have been possible without the support of many colleagues. I would like to thank all of them! –

Diese Arbeit wäre nicht möglich ohne die Hilfe und Unterstützung vieler Kolleginnen und Kollegen. Ihnen allen sei an dieser Stelle herzlich gedankt!

Mein erster Dank gilt Herrn Prof. Dr. Thomas Müller für die Chance, meine Doktorarbeit am Institut für Experimentelle Kernphysik in einem spannenden Gebiet der Detektorentwicklung und -produktion durchzuführen.

Prof. Dr. Ulrich Husemann danke ich für die freundliche Aufnahme in die Pixelgruppe und die Übernahme des Korreferats.

Dr. Thomas Weiler danke ich für die Unterstützung bei der Modulproduktion, die Hilfestellung bei allen nur möglichen Fragen und die Korrektur dieser Arbeit.

Weiterer Dank gebührt

- Dr. Hans Jürgen Simonis für viele interessante Diskussionen auch abseits der Physik und die Administration des IEKP-Netzwerks,
- Dr. Alexander Dierlamm für die Hilfe bei sämtlichen Sensorfragen und die Korrektur dieser Arbeit,
- Benedikt Freund für seinen unermüdlichen Einsatz beim Bare Module Test am IPE und die Korrektur dieser Arbeit,
- meinen Mitstreitern Robert Eber, Andreas Nürnberg, Martin Printz, Fabio Colombo, Florian Kassel, Simon Kudella und Daniel Schell; ohne euch wäre die Zeit am IEKP nur halb so schön gewesen,
- den zahlreichen Bachelor- und Masterstudenten, die zum Gelingen der Pixelproduktion beigetragen haben, unter anderem Felix Riese, Rudolf Schimassek, Roland Koppenhöfer, Damir Raßloff, Pawel Jodiss, Jan Hoß, Simon Spannagel, Stefan Heitz, Bojan Hiti und Yavuz Taskirdi,
- Tobias Barvich für die kompetente technische Beratung und Umsetzung der zahlreichen Projekte,
- Anita Weddigen und Pia Steck für viele gebaute und gebondete Pixelmodule,
- Felix Bögelspacher für die Bestrahlung der Pixelsensoren,
- Brigitte Gering und Diana Fellner für die Erledigung aller organisatorischen Arbeiten,
- zu guter Letzt meinen Eltern Anneliese und Josef sowie meinen Großeltern Johanna und Hans Ernst für ihre unverzichtbare und anhaltende Unterstützung.

Der Landesgraduiertenförderung des Landes Baden-Württemberg und der Karlsruhe School of Elementary Particle and Astroparticle Physics: Science and Technology (KSETA) danke ich für die Unterstützung während der Promotion.

The measurements leading to these results have been performed at the Test Beam Facility at DESY Hamburg (Germany), a member of the Helmholtz Association (HGF).

This work is supported by the Initiative and Networking Fund of the Helmholtz Association, contract HA-101 (“Physics at the Terascale”).

WAS LANGE WÄHRT, WIRD ENDLICH GUT...

